UNIVERSITY OF OKLAHOMA

GRADUATE COLLEGE

SYNTHESIS AND REDOX BEHAVIOR OF GROUP 8 METALLOPORPHYRINS AND RELATED COMPOUNDS

A DISSERTATION

SUBMITTED TO THE GRADUATE FACULTY

in partial fulfillment of the requirements for the

Degree of

DOCTOR OF PHILOSOPHY

By

DENNIS AWASABISAH
Norman, Oklahoma
2015

SYNTHESIS AND REDOX BEHAVIOR OF GROUP 8 METALLOPORPHYRINS AND RELATED COMPOUNDS

A DISSERTATION APPROVED FOR THE
DEPARTMENT OF CHEMISTRY AND BIOCHEMISTRY

BY

_____
Dr. George B. Richter-Addo, Chair

_____
Dr. Kenneth M. Nicholas

_____
Dr. Daniel T. Glatzhofer

_____
Dr. Mark A. Nanny

_____
Dr. Robert Thomson

Dedications

I dedicate this work to my dad, the late Bonaventure Akowiak Awasabisah, my mum, Mary Azongpok Awasabisah, my wife, Maa Ahema Awasabisah and daughters, Phoebe and Denise Awasabisah.

Acknowledgements

I would like to express my sincere appreciation to my advisor, Dr. George Richter-Addo for being the best mentor I could ask for. Thanks for the insightful research discussions we have had and for challenging me to undertake independent work. You have taught me to ask the right questions and be critical of my own work. As you always put it, "People will never remember how long it took to complete a job, but they will always remember how well you did the job." Thanks for all your counsel.

I would also like to thank my advisory committee; Dr. Kenneth Nicholas, Dr. Daniel Glatzhofer, Dr. Mark Nanny, and Dr. Robert Thomson, for their guidance and support throughout my studies. I would also like to thank Dr. David Nagle and Dr. Robert Houser who previously served as members of my advisory committee. I learnt so much from you all.

Thanks to both past and present members of the GBRA group; Dr. Nan Xu, Dr. Jun (Eva) Yi, Dr. Myron W. Jones, Dr. Adam Warhausen, Guan Ye, Bing Wang, Erwin Abucayon, Samantha Powell, Neda Hessami and Wenhua Wang. It was such a great privilege to have worked with you. All the times we shared talking about science and life in general were priceless. I consider you all as part of my family and I wish to continue to keep in touch with you. Thanks Ye with help with the DFT calculations.

I would also like to thank our research collaborator, Dr. Michael J. Shaw for all the interesting research discussions we have had, and for his help in kick-starting my pursuit of the Ph.D. Chemistry degree program when I was a student at SIUE. I am grateful to Dr. Michael J. Shaw and Krishna P. Sharmah Gautam for their contribution in Chapter 2 and for providing preliminary data on the synthesis and electrochemistry of

the (por)Ru(NO)(OC(=O)Fc) complexes. My next special gratitude also goes to the research support staff at OU; to Dr. Douglas Powell for his help with my crystallographic work; Dr. Susan Nimmo for help with NMR spectroscopy; Dr. Steve Foster with help with mass spectrometry; Jim Cornell for all the glass-blowing jobs as well as Chad and Carl in the electronic shop for all their help.

Last but not least, I would like to thank my dear wife, Maa Ahema for her love, encouragement and patience throughout my academic career. I am truly blessed by her support through the years. Special thanks to my parents, and siblings; Diana, Cordelia, Martin and Tony for all the love and support they have shown me throughout my life and for teaching me to be disciplined.

Table of Contents

List of Tables

List of Figures

Abstract

This dissertation describes the Chemistry of Group 8 Metalloporphyrins and related compounds. Chapter one describes linkage isomerization in NO_x-coordinated metal complexes with emphasis on Group 8 metals, and part of this work was published in the series *Advances in Inorganic Chemistry*, Vol. 47. As already noted in the published work, the binding of small molecules such as nitric oxide (NO) to metals often imparts varied chemistry to the small molecules. Such chemistry is dependent on the coordination mode of the small molecule ligands, as the coordination mode affects the electronic distributions along the ligand atoms. In chapter one, the current knowledge of the linkage isomerization of NO_x ligands in metal complexes is outlined for both non-porphyrin and porphyrin systems. The modes of preparation and detection, and speculation on the consequences of such linkage isomerization on the resultant chemistry, are presented.

Chapter 2 describes the synthesis and redox behavior of the complexes (por)Ru(NO)(OR) (por = porphyrin, OR = alkoxide, carboxylate). These systems serve as potential structural models for the NO-inhibited heme enzyme catalase that contain (por)Fe(OR) active sites. The (por)Ru(NO)(OR) compounds were characterized by IR and ^{1}H NMR spectroscopy, and by X-ray crystallography. The X-ray crystallographic data reveal that the RuNO linkages are linear for these formally $\{RuNO\}^6$ species; for comparison, the (por)Ru(NO)Cl (por = OEP,T(*p*-OMe)PP) compounds also have linear RuNO bonds, whereas the related compounds (T(*p*-OMe)PP)Ru(NO)Et (∠RuNO = 153.4(5)°) and (TTP)Ru(NO)(C_6H_4F-*p*) (∠RuNO = 152°) have bent RuNO moieties. The alkyl/aryl ligands in the latter compounds are strongly σ donating to the metal with

concomitant bending of their *trans* RuNO units. Cyclic voltammetry and IR spectroelectrochemistry reveal reversible oxidations centered on the porphyrin rings in most of these (por)Ru(NO)(OR) complexes, a finding that supports the generation of porphyrin π-radical cations in oxidized natural (por)M(NO)(O-ligand) systems. The electrochemical reductions result in the eventual dissociation of the axial *O*-ligands with concomitant generation of the putative and unstable (por)Ru(NO) byproducts.

In Chapter 3, I explore the relationship between the stereochemistry and spin-states of a set of (por)Fe(OR) (R = aryl, alkyl) complexes using X-ray crystallography and solution measurements. The magnetic susceptibility data obtained by the Evans method show that most of these complexes are mainly high-spin species. X-ray crystal structures of these five-coordinate complexes show that the compounds are square pyramidal with axial *O*-bound ligands. The Fe−O bond lengths are ~1.9 Å and the Fe−N bonds are ~2 Å. The iron atoms of these compounds are displaced >0.3 Å above the 24-porphyrin atom mean planes. The crystallographic data support the high-spin properties observed in solution for these complexes. In some of the complexes, however, the X-ray crystal structures show severe distortion of the porphyrin macrocycles. Magnetic susceptibility measurements of those distorted porphyrin macrocycles show that they exhibit admixed spin-state properties in solution. The CV and IR spectroelectrochemistry of representative examples of these complexes show irreversible oxidations and reversible reductions. Furthermore, some of the five coordinate (por)Fe(O-aryl) and (por)Fe(*O*-alkyl) complexes in the powdered form react with NO to generate the six-coordinate (por)Fe(NO)(OR) compounds. A comparison of the IR data of the five-coordinate (por)Fe(OR) and six-coordinate (por)Fe(NO)(OR)

shows a *trans* influence of NO on the axial ligands, and this has been confirmed by DFT calculations. Finally, IR spectroelectrochemical experiments of a representative six-coordinate compound suggest a porphyrin-centered oxidation with electroreduction being accompanied by NO release.

In Chapter 4, I report on the preparation and characterization of some iridium phosphine complexes and I examine the reactivity of such complexes with small molecules. I present the reactivity of these complexes with alkyl nitrites leading to the formation of the related M{N(=O)OR} complexes of relevance to bioinorganic chemists.

Chapter 1: Linkage Isomerization in Metal complexes*

1.1 Introduction

The interactions of ambidentate ligands with transitions metals have often resulted in complexes with very interesting chemistry. For example, the complex $[(NH_3)_5Co(NO_2)]Cl_2$, first prepared by Jörgensen[1] in 1894, contains the ambidentate ligand NO_2 and the complex exists in two forms. Crystalline solids obtained for this compound showed a mixture of two different colored species; yellow and red, which were readily isolated with a pair of tweezers.[1] Later, Werner identified these two species as isomers arising from the different modes of binding of the NO_2 ligand to Co, either via the O or via the N atoms. This resulted in the birth of the concept of linkage isomerization in 1907.[2] About five decades later, Penland provided infrared spectroscopic data to show that the yellow $[(NH_3)_5Co(NO_2)]Cl_2$ complex had NO_2 bound to Co via its N atom, and the red isomer had NO_2 bonded to Co via the O atom.[3] By way of definition, linkage isomerization may be defined as the existence of two or more species that have the same molecular formula, and the same bonding ligands, but differ in the mode of attachment of at least one of the ligands (usually ambidentate) to the central atom.

Linkage isomerization in complexes containing several other ambidentate ligands including those of SCN^-, $SeCN^-$, CN^-,[4-6] and NO[5,7] has been reported. We wish to limit this review to linkage isomerization in NO_x complexes and to provide current knowledge in the area of linkage isomerization partly because of the myriad of

* This work has been published as a book Chapter in *Adv. Inorg. Chem.* **2015,** *67*, Chapter One pp. 1-86. Edited by Rudi van, Eldik and José, A. Olabe

applications and relevance of NO_x complexes. There are only a handful of recent reviews in the literature on linkage isomerization in NO_x complexes, including a review by Coppens and Novozhilova on photoinduced isomerization,[7] and a more recent forum paper on NO_x linkage isomerization in porphyrin complexes.[8] This review covers linkage isomerization deriving from isolable metal complex precursors. Thus, we will not cover the systems involving laser ablated atomic systems.[9]

The importance of linkage isomerization has been highlighted in a number of reviews.[8,10,11] A good understanding of the various modes of binding of an ambidentate ligand, and factors that influence these modes of binding will provide more insight in the kind of chemistry they present. For instance, nitric oxide (NO) is known to bind to the iron center of a heme enzyme to carry out its function as a hypotensive agent.[12-14] An increased knowledge of Fe−NO coordination has helped in designing better NO-releasing drugs for treatment of hypertension, as in the case of sodium nitroprusside (SNP).[15,16] Recently, a book chapter was dedicated to a review on medical application of solid NO complexes.[17] Also, the chemistry of NO_x complexes is relevant in understanding the mechanism of the denitrification process that forms part of the global nitrogen cycle,[18-21] and in understanding the action of the metal-dependent reduction of nitrite.[22]

NO_x species are generated by combustion processes in industries and automobiles, and may be produced naturally by lightning strikes. This has led to a rising interest in finding improved catalysts for removal of these toxic gases from the atmosphere.[23-25] In addition, and more recently, metastable linkage isomers of NO_x complexes have been generated to produce photoswitchable complexes which may be

applied in ultrafast optical switching and storage devices.[26-31] Recent work by Schuy,[32] Cervellino,[33] and Tahri [34] have shown how the nitroprusside anion $[(CN)_5Fe(NO)]^{2-}$ could be incorporated into silica gel pores to generate its corresponding linkage isomer for potential use in optical devices. Photoinduced linkage isomerism, Schaniel *et al*. have noted, is known to modify the polarizability of $[(CN)_5Fe(NO)]^{2-}$ so as to cause a macroscopic change of single crystal refractive index according to the Lorentz-Lorenz equation.[27]

1.1.1 Modes of binding of NO_x moieties in monometallic complexes

1.1.1.1 Nitric oxide (NO) complexes

NO is a colorless monomeric gas which is biosynthesized by the enzyme nitric oxide synthase (NOS).[35] NO is known to bind to transition metals in three main ways. The first is via the N end of the molecule to form the linear (Fig. 1.1 Ia) and bent (Fig. 1.1 Ib) nitrosyl (η^1-NO) modes, or via the O end to produce the isonitrosyl (η^1-ON) linkage isomer (Fig. 1.1 Ic).[36] Isonitrosyl complexes of SNP,[37] and some ruthenium nitrosyl complexes were detected in the solid state as metastable species just less than two decades ago by Coppens and coworkers.[38] The third mode of binding is the side-on NO (or the η^2-NO) binding mode to a metal as shown in Fig. 1.1 Id. Complexes containing this mode of binding were first demonstrated by Coppens and coworkers for their metastable SNP species.[37] Side-on NO species were obtained as short-lived species from photolysis of (OEP)Ru(NO)(O-*i*-C_5H_{11}) and (OEP)Ru(NO)(SCH_2CF_3) porphyrin complexes.[39] Theoretical evidence for the existence of the metastable modes of binding have been demonstrated for SNP[40-42] and for some (por)Fe(NO) models.[43]

I. Metal-NO binding modes

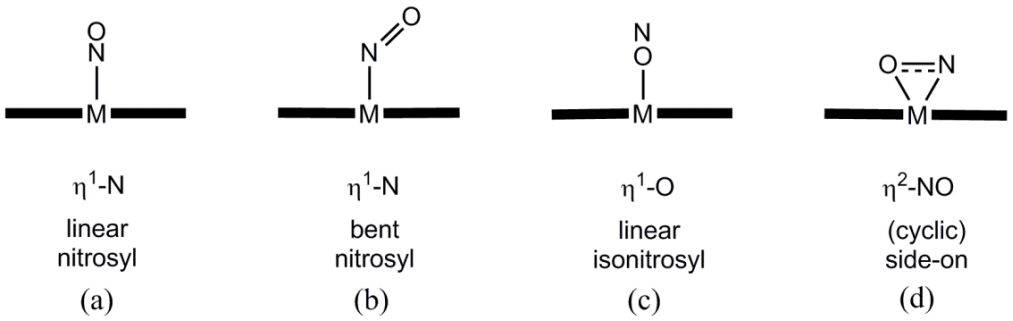

η^1-N linear nitrosyl (a)

η^1-N bent nitrosyl (b)

η^1-O linear isonitrosyl (c)

η^2-NO (cyclic) side-on (d)

II. Metal-NO_2 binding modes

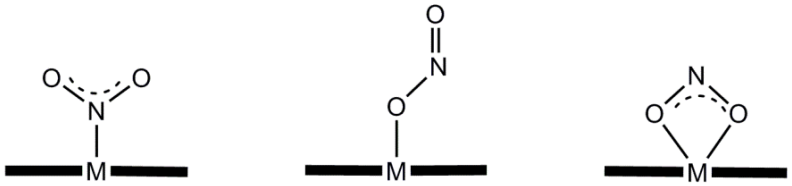

N-nitro (a)

O-nitrito (b)

O,O-bidentate (c)

III. Metal-NO_3 binding modes

O-nitrato (a)

O,O-nitrato (b)

Figure 1.1. Modes of binding of NO_x moieties in monometallic complexes.

1.1.1.2 NO_2 Complexes

The binding modes of NO_2 have been reviewed by Hitchman and Rowbottom.[44] Relevant to us in this review are the three nitrite binding modes shown in (Fig. 1.1 IIa-c). These are the *N*-nitro, *O*-nitrito and the *O,O*-bidentate modes. The *N*-nitro mode has the nitrite ligand bound to the metal via the N atom (Fig. 1.1 IIa). This appears to be the most common binding mode of NO_2 in its complexes, thus this binding mode is usually referred to as the ground state binding mode for nitrite, although clearly this is an oversimplification. In the nitrito binding mode, NO_2 is bound to the metal via the O atom as shown in Fig. IIb. Finally, in the *O,O*-binding mode, both oxygen atoms of nitrite are bound to the same metal to give an η^2-NO_2 configuration as shown in Fig. 1.1 IIc.

1.1.1.3 NO_3 Complexes

There are two common binding modes of the nitrate (NO_3^-) ligand. The first is binding via one oxygen atom to give the *O*-nitrato form (Fig. 1.1 IIIa) and the second is binding through two NO_3 oxygens to give the *O,O*-bidentate configuration (Fig. 1.1 IIIb). The monodentate mode of binding has been observed in some metalloporphyrin complexes including (OEP)Fe(NO_3),[45] (TF_8PP)Fe(NO_3),[46] T_{piv}PP)Fe(NO_3)$^-$,[47] and (TPP)Mn(NO_3).[48] Some examples of the *O,O*-bidentate binding mode in NO_3-coordinated metalloporphyrins include (TPP)Fe(NO_3)[49,50] and (T_{piv}PP)Fe(NO_3).[51] A review article on the coordination chemistry of the nitrate ligand was published in 1971 by Addison and Garner.[52]

1.1.2 Methods that induce linkage isomerization

Linkage isomerization in a complex usually requires an induction source. Such complexes have been generated as short-lived species, and in some cases, as long lived species by different methods. The first linkage isomer was photochemically generated by exposing samples of $[(NH_3)_5Co(NO_2)]Cl_2$ to sunlight.[2,53] Several linkage isomers of different metal complexes have been obtained by photoinduction using light sources in the UV-vis region.[7] Another means of obtaining linkage isomers is by thermal induction as in the conversion of the nitrito isomer of $[(NH_3)_5Co(NO_2)]Cl_2$ to the nitro isomer by warming[3] There are reports on the thermally-induced linkage isomerization in some nickel complexes.[54,55] In addition, sometimes changing the *trans* ligand and/or the other *cis* ligands in a complex may influence the mode of binding of an ambidentate ligand.[56,57]

1.1.3 Techniques for detecting linkage isomers

The first linkage isomer was spectroscopically characterized by Penland *et al.*[3] Some metastable linkage NO_x isomers have been detected via low temperature IR,[39,58] Raman spectroscopy, Mossbauer,[59,60] UV-vis, and NMR spectroscopies.[61,62] Current detection techniques include photocrystallography,[7,63-67] and differential scanning calorimetry (DSC).[68-70] DFT calculations have been invaluable in explaining the preferred modes of binding of the ligands in these complexes, as in the case of the observed linkage isomerization of NO in (por)Fe(NO).[43,58,71]

1.1.4 Factors that affect linkage isomerization

The factors that affect linkage isomerization of ambidentate ligand complexes of transition metals have previously been reviewed by Baluhura and Lewis,[72] some of these factors are summarized here.

First, the HSAB property of a metal can help predict in a simplistic sense which mode of binding to expect in a given complex (Fig. 1.2).[73-75]

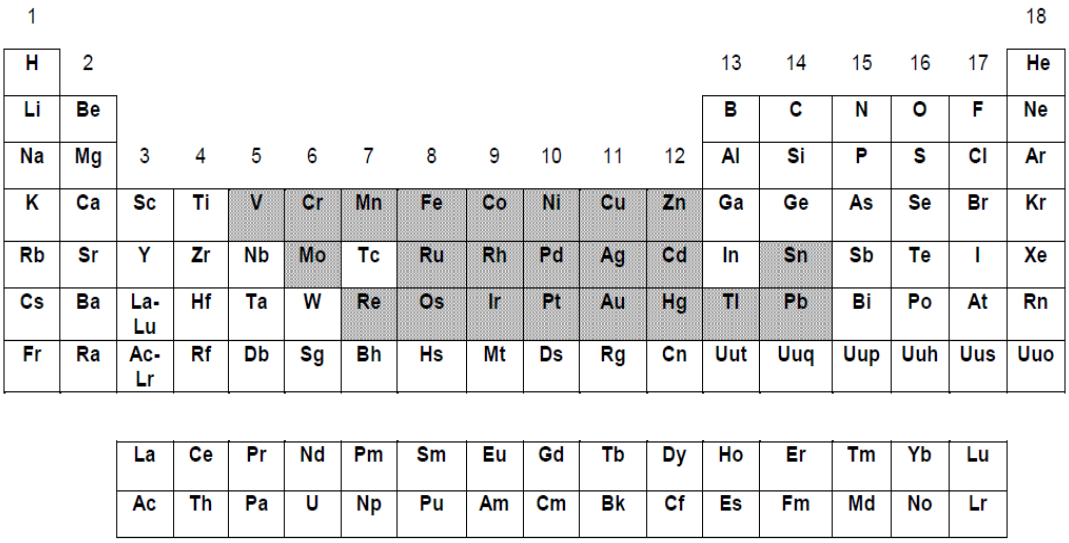

Figure 1.2. The periodic table showing metals (shaded) whose complexes have been reported to undergo linkage isomerization.

As a general rule of thumb, soft metals have the tendency to bind well with soft ligands and hard metals tend to form stronger bonds with hard ions.[74,76] However, the borderline metals are more prone to linkage isomerization because of the potential for various oxidation states, and thus, the different characters they exhibit.[72,76,77] The other ligands bound to the central metal in any complex also influence the mode of binding of ambidentate ligands depending on whether they are electron donating or electron withdrawing.

Any ligand that tends to decrease the positive charge on the metal or tends to increase the negative charge on the metal increases the tendency of the metal binding to the soft end of the ambidentate ligand.[73] For instance, in the complex $[(Bim)_3Fe(ONO)]^+$ ($(Bim)_3$ = tris(2-benzimidazolylmethyl)amine) the nitro group is reported to be *O*-bound to Fe (Fig. 1.3a) as evidenced by both IR spectroscopy and X-ray crystallography (Fig. 1.3).[78] In the related complex $[(PyN_4)Fe(NO_2)]^+$ (PyN_4 = 2,6-$C_5H_3N[CMe(CH_2NH_2)_2]_2$) NO_2 is *N*-bound as shown by IR spectroscopic data.[79] The ligand PyN_4 ligand is a better electron donor than $(Bim)_3$ such that Fe becomes relatively less positive in $[(PyN_4)Fe(NO_2)]^+$ to the extent that it has a better affinity for the soft end of ambidentate ligands rendering the mode of binding of NO_2 *N*-bound (Fig. 1.3).[78]

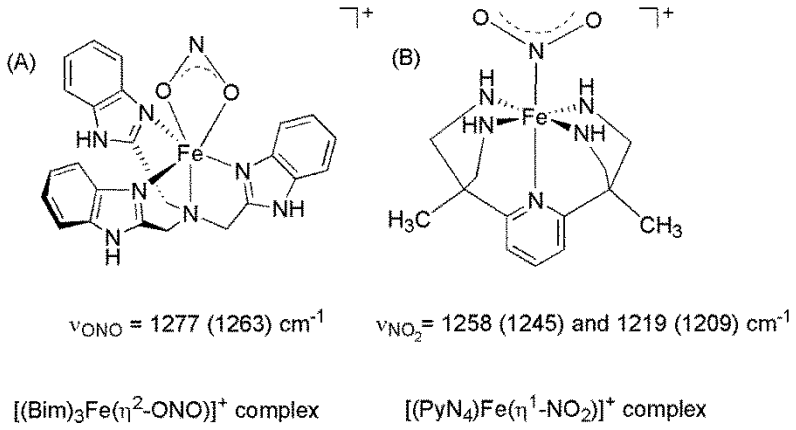

Figure 1.3. Comparison between the different modes of NO_2 binding in two Fe complexes: (A) $[(Bim)_3Fe(\eta^2\text{-ONO})]^+$ and (B) $[(PyN_4)Fe(\eta^1\text{-}NO_2)]^+$. The ligands Bim and PyN_4 influence the mode of binding in NO_2. IR data in parenthesis are for the ^{15}N-labeled NO_2 derivatives.

The size of the other ligands in the complex can also influence the mode of binding in ambidentate ligands. In complexes of NO_2 for instance, the nitrito isomer

may be preferred when the other ligands are bulky. It must be emphasized that in $[(Bim)_3Fe(ONO)]^+$ and $[(PyN_4)Fe(NO_2)]^+$ above, the $(Bim)_3$ and PyN_4 ligands, respectively, have comparable size around Fe to allow either mode of NO_2 binding and that steric factors do not appear to play a significant role in influencing the mode of NO_2 binding.

1.2 Linkage isomerism in non-porphyrin NO_x complexes

1.2.1 Group 6 (Cr and Mo) complexes

1.2.1.1 NO Complexes

The NO complexes of chromium that have been reported to date exist in the nitrosyl forms. In coordination complexes in particular, several compounds of configuration $\{Cr(NO)\}^5$ have been isolated; these have been reviewed recently.[80,81] In a 2005 review, Ford and coworkers noted that photolysis of some Fe, Mn, and Cr nitrosyl complexes often leads to the dissociation of the nitrosyl ligands.[82] For example, photolysis of the $[(H_2O)_5Cr(NO)]^{2+}$ complex under anaerobic conditions, and in the absence of trapping agents led to the dissociation of the NO ligand (Eq. 1.1). This process was determined to have a reverse rate constant, k_{on} of 2.5 x 10^8 $M^{-1}s^{-1}$ (Eq. 1.1).[81,83]

$$[(H_2O)_5Cr(NO)]^{2+} \xrightarrow[H_2O]{h\nu} [(H_2O)_6Cr]^{2+} + NO \qquad (\mathbf{1.1})$$

$$k_{on} = 2.5 \times 10^8\ M^{-1}s^{-1}$$

The compound Mo(dppe)(CO)(NO)(S_2CNMe_2) (dppe = 1,2-bis(diphenylphosphino)ethane) is an octahedral complex and is light-sensitive in solution.[84]

Irradiation of an acetonitrile solution of Mo(dppe)(CO)(NO)(S_2CNMe_2) (Fig. 1.4) with light of λ_{irr} = 546 nm resulted in the dissociation of the NO ligand with a quantum yield of 0.018.[84] However, irradiation of the related compound Mo(dppe)(CO)(NO)(S_2CNEt_2) in frozen matrices at low-irradiation wavelengths resulted in the generation of η^2-nitrosyl linkage isomers (Fig. 1.5).[85]

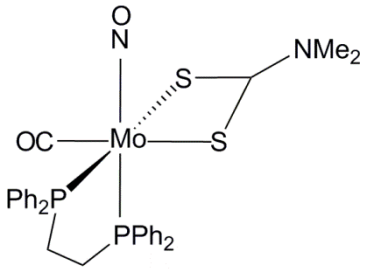

Figure 1.4. Structure of Mo(dppe)(CO)(NO)(S_2CNMe_2).

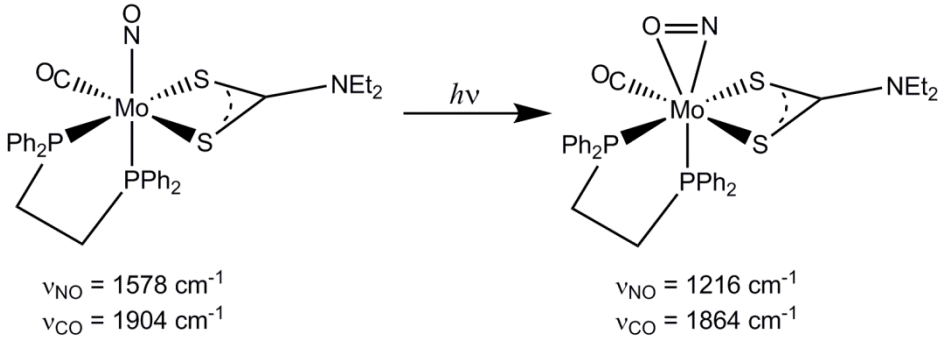

Figure 1.5. Linkage isomerization in Mo(dppe)(CO)(NO)(S_2CNEt_2).

Bitterwolf followed the photogenerated products (6.3% conversion) formed during the photolysis ($330 < \lambda_{irr} < 400$ nm) of Mo(dppe)(CO)(NO)(S_2CNEt_2) (ν_{NO} 1578 cm^{-1}, ν_{CO} 1904^{-1}) by difference IR spectroscopy, and observed two new bands at 1216

cm^{-1} and 1864 cm^{-1} (Fig. 1.6 I). The IR band at 1216 cm^{-1} was assigned to the side-on η^2-NO isomer of Mo(dppe)(CO)(NO)(S_2CNMe_2); this band shifts by $\Delta\nu$ = 362 cm^{-1} from the starting parent compound. The second band at 1864 cm^{-1} was assigned to ν_{CO} of the product; this band shifted by 40 cm^{-1} from the parent compound (Fig. 1.6 Ia top).[85]

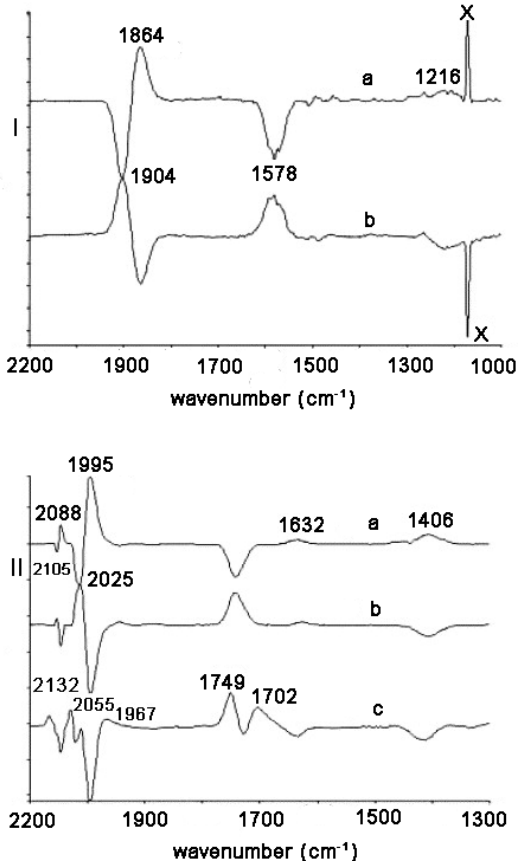

Figure 1.6. (Top): Difference spectra of Mo(dppe)(NO)(CO)(S_2CNEt_2) (I): (a) 10 min photolysis (330 nm < λ_{irr} < 400 nm) minus starting spectrum; (b) 10 min photolysis (λ_{irr} = 550 ± 35 nm) minus 10 min photolysis (330 nm < λ_{irr} < 400 nm) (Bottom): Difference spectra of [(dppe)Mo(NO)$(CO)_3$]PF_6: (II) (a) 10 min photolysis (λ_{irr} = 400 ± 35 nm) minus starting spectrum; (b) 10 min photolysis (λ_{irr} = 400 ± 35 nm) minus 10 min photolysis (λ_{irr} = 450 ± 35 nm); (c) 10 min photolysis (330 nm < λ_{irr} < 400 nm) minus 10 min photolysis (λ_{irr} = 400 ± 35 nm). Adapted with permission from ref.[85]

Bitterwolf also observed that the photolysis of the $[Mo(dppe)(CO)_3(NO)]PF_6$ complex in a PVC film ($\lambda_{irr} = 400 \pm 35$ nm) yielded both the η^2-NO and the isonitrosyl (*O*-bound) isomers with new observed bands at $\nu_{NO} = 1406$ cm^{-1} and $\nu_{NO} = 1632$ cm^{-1}, respectively (Fig. 1.6 II, bottom). The two photogenerated linkage isomers of $Mo(dppe)(CO)(NO)(S_2CNEt_2)$ and $[Mo(dppe)(CO)_3(NO)]PF_6$ reverted to their corresponding starting nitrosyl isomers upon back photolysis using $\lambda_{irr} = 550 \pm 35$ nm and 330 nm $< \lambda_{irr} <$ 400 nm, respectively.[85]

1.2.1.2 NO_2 complexes

The NO_2 complexes of Cr exist in the nitrito conformation and several nitrito complexes of cyclam derivatives [86] and amine derivatives [87] have been reported. An example is the *trans*-$[Cr(mbc)(ONO)_2]BF_4$ (mbc = 5,7-dimethyl-6-benzylcyclam) compound whose structure is shown in Fig. 1.7.[86]

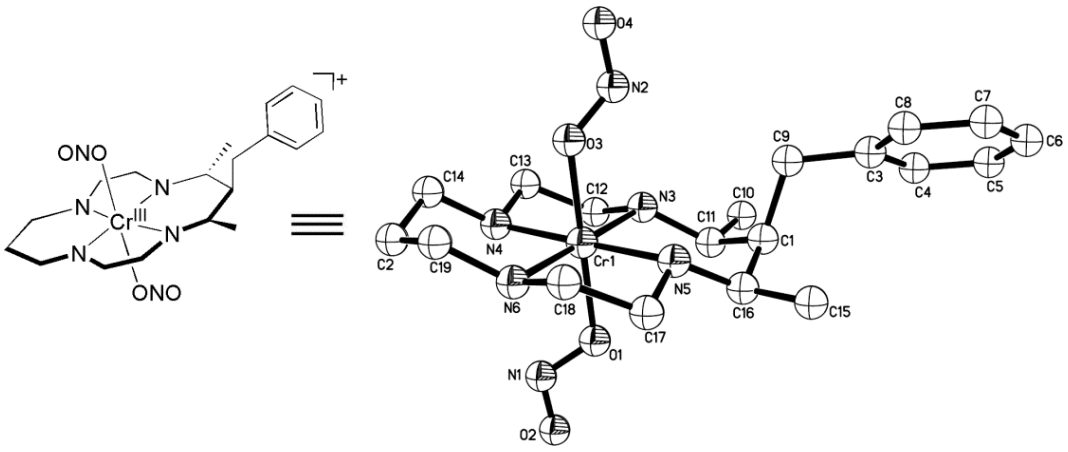

Figure 1.7. The molecular structure of the *trans*-$[Cr(mbc)(ONO)_2]BF_4$ compound.[86]

The Cr−NO_2 complexes reported to date do not appear to isomerize under photolysis conditions, but can decompose with release of NO when irradiated with light.[88] However, the complex $CpCr(NO)_2(NO_2)$ (Cp = cyclopentadiene) prepared by metathesis of $CpCr(NO)_2Cl$ with $NaNO_2$ in methanol, exists in both the nitro and nitrito forms in solution (Fig. 1.8), with the nitrito isomer favored both in solution and in the solid state.[89] The equilibrium is temperature-dependent as determined by ^{1}H NMR

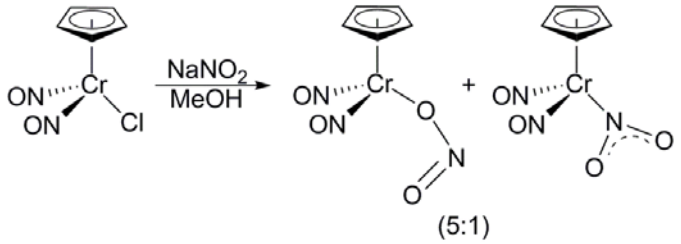

Figure 1.8. Preparation of the two isomers of $CpCr(NO)_2(NO_2)$. The nitrito isomer is the major product.

spectroscopy, with the nitrito isomer favored at high temperatures (ΔH_{eq} = 1.8(3) kcal mol^{-1}; ΔS = 9.3(9) eu).[89] In addition, ^{1}H NMR and quantitative IR spectroscopy indicate an equilibrium ratio of 5:1 (nitrito: nitro) mixture of $CpCr(NO)_2(NO_2)$.

The peaks in the IR spectrum were used to differentiate the two products with the nitrito isomer showing bands due to the "NO_2" group at 1425 and 1048 cm^{-1} and the minor nitro isomer displaying bands at 1385/ 1325 cm^{-1}. The X-ray crystal structure of the nitrito isomer was previously reported by Pasynskii and coworkers.[90] The X-ray powder diffraction data collected by Hubbard and coworkers for a finely-ground sample of $CpCr(NO)_2(NO_2)$ showed, in addition to the major nitrito isomer, additional features that were attributed to the minor nitro isomer.[89]

1.2.2 Group 7 (Mn and Re) complexes

1.2.2.1 NO complexes

Bitterwolf has studied the effects of light on linkage isomerization in some metal (Mn, Re) cylopentadienyl dicarbonyl nitrosyls of the form $[CpM(CO)_2(NO)]^+$ (M = Mn, Re) and $[(MeCp)Mn(CO)_2(NO)]^+$.[91] Fig. 1.9 shows the complexes that were investigated and illustrates how the photoinduced products were generated. In a typical experiment, the sample was dissolved in a triethyloctylammonium hexafluorophosphate solution and frozen to ca. 90 K in a glass cryostat and the IR of the sample was taken. The frozen matrix was then subjected to light of a set wavelength and the IR spectral data collected again to obtain difference IR spectra.

For $[CpMn(CO)_2(NO)]BF_4$ (**A** in Fig. 1.9), continuous irradiation of the sample (λ_{irr} = 450 ± 35 nm) for 10 min was required to detect the isomerization spectroscopically. The difference IR spectrum obtained during the photolysis of

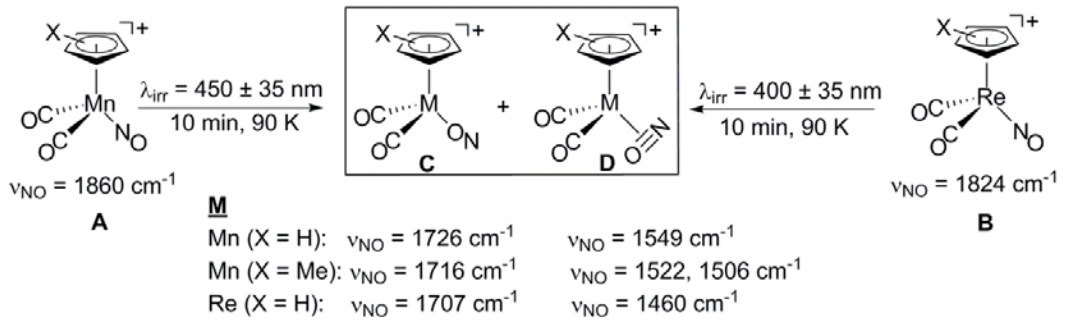

Figure 1.9. Photoinduced linkage isomerization in $[(CpM(CO)_2(NO)]BF_4$ (M = Mn, Re).

$[CpMn(CO)_2(NO)]BF_4$ showed two new bands (1726 and 1549 cm^{-1}) which are in the range of NO vibrations. Clearly these bands appear at lower frequencies than the ν_{NO} band of 1860 cm^{-1} of the starting compound, showing shifts of $\Delta\nu_{NO}$ =134 cm^{-1} and

$\Delta\nu_{NO}$ = 311 cm^{-1}, respectively and implying the possibility of NO linkage isomerization. The latter shift of $\Delta\nu_{NO}$ = 311 cm^{-1} is an indication of linkage isomerization from a nitrosyl configuration to the side-on NO linkage isomer.[92] The lower magnitude shift (i.e., $\Delta\nu_{NO}$ of 134 cm^{-1}) was suggested by Bitterwolf to have originated from the linkage isomerization from the nitrosyl to the isonitrosyl isomer.[91]

The analogous Re compound, $[CpRe(CO)_2(NO)]BF_4$, (**B** in Fig. 1.9) behaved similarly showing new ν_{NO} bands at 1707 ($\Delta\nu_{NO}$ = 117 cm^{-1}) and 1460 cm^{-1} ($\Delta\nu_{NO}$ = 364 cm^{-1}) for their respective isonitrosyl and η^2-NO isomers when the starting compound was irradiated with UV light of wavelength 400 ± 35 nm.[91] There were small shifts in the ν_{CO} bands of $[CpMn(CO)_2(NO)]BF_4$ to lower wavenumbers on moving from the ground state isomer to the photogenerated isomers suggesting that the NO linkage isomers were not as strong π acids as the ground state ligand.

Further, Bitterwolf also observed that during photolysis of a sample of $[(Me\text{-}Cp)Mn(CO)_2(NO)]PF_6$ (ν_{NO} = 1812 cm^{-1}) with UV light λ_{irr} = 450 ± 35 nm, in addition to the new isonitrosyl band at 1716 cm^{-1} in the difference IR, two other new distinct NO-related bands were observed at 1522 and 1506 cm^{-1}. The two latter bands were assigned to the ν_{NO} of the η^2-NO conformation of $[(MeCp)Mn(CO)_2(\eta^2\text{-}NO)PF_6]$ which probably exists as a pair of rotamers that arise due to the different orientations of the η^2-NO ligand relative to the cyclopentadienyl ring. In one instance the η^2-NO ligand is parallel to the cyclopentadienyl ring, and it is perpendicular in the other.[91] Such rotamer configurations have been proposed previously for $[CpFe(CO)_2(olefin)]^+$[93] and CpCr(CO)(NO)(alkyne).[94]

Schaniel observed the formation of an η^2-NO isomer as a photogenerated product species from photolysis of $K_3[Mn(CN)_5NO]\cdot 2H_2O$ (Fig. 1.10).[95] At 80 K,

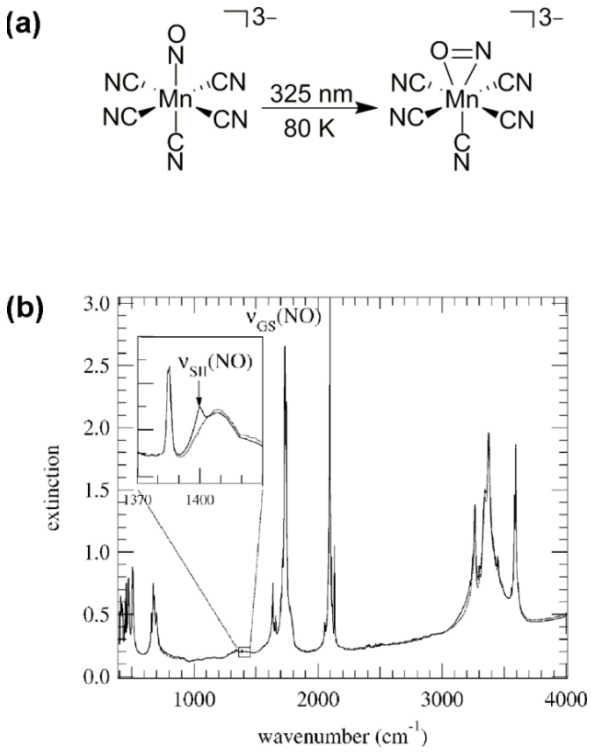

Figure 1.10. (a) Linkage isomerization of $[Mn(CN)_5NO]^{3-}$. (b) Infrared spectrum of $K_3[Mn(CN)_5NO]\cdot 2H_2O$ in GS and after irradiation with 325 nm light at $T = 80$ K. The insert shows the new peak assigned to the side-on linkage isomer SII. *Reproduced in part from ref.* [95] *with permission of The Royal Society of Chemistry.*

approximately 1% of the ground state $K_3[Mn(CN)_5NO]\cdot 2H_2O$ (ν_{NO} = 1733/ 1743 cm^{-1}) species isomerized to the side-on isomer after light of λ = 325 nm was applied; the IR spectrum of the photogenerated product showed a new band at 1399 cm^{-1} attributed to the linkage isomer.[95]

1.2.3 Group 8 (Fe, Ru and Os) complexes

1.2.3.1 NO complexes

One of the most widely studied iron nitrosyls is the nitroprusside anion $[(CN)_5Fe(NO)]^{2-}$ (Fig. 11). Since its first report in the literature by Playfair in 1848,[96]

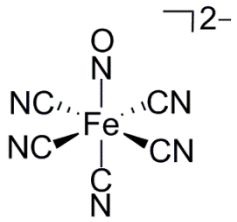

Figure 1.11. The nitroprusside anion.

several researchers have taken a keen interest in further investigations on its structural properties as well as its industrial and biological applications.[13,16,32,34,97] There are reports on the X-ray crystallographic structure of the nitroprusside[98] and spectroscopic characterization of its Ru and Os analogues with varying counter ions.[99] The application of X-ray crystallography for the determination of metastable species of the nitroprusside anion[100] was recently featured in American Chemical Society's *Chemical & Engineering News* magazine.[101]

The detection of the photogenerated metastable isomers of the $[(CN)_5Fe(NO)]^{2-}$ complex by Mössbauer spectroscopy was reported by Hauser in 1977.[59,60] In a definitive study, Coppens and coworkers identified the metastable species by X-ray crystallography as the $[(CN)_5Fe(\eta^1\text{-ON})]^{2-}$ and $[(CN)_5Fe(\eta^2\text{-NO})]^{2-}$ nitrosyl linkage isomers (Fig. 1.12).[37] Their IR spectroscopic work showed a decrease in the ν_{NO} from 1950 cm^{-1} for the nitrosyl isomer to 1666 cm^{-1} ($\Delta\nu_{NO}$ = 284 cm^{-1}). They assigned the

latter band to the side-on isomer. Another band was observed at 1835 cm^{-1} ($\Delta\nu_{NO}$ = 115 cm^{-1}) and was assigned to the isonitrosyl isomer.[37]

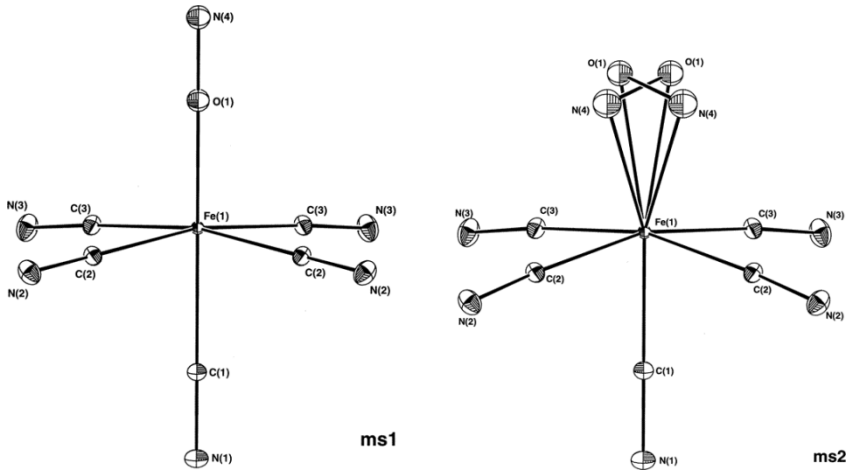

Figure 1.12. ORTEP plots of $[(CN)_5Fe(\eta^1\text{-ON})]^{2-}$ and $[(CN)_5Fe(\eta^2\text{-NO})]^{2-}$ at 50 K; 50% probability ellipsoids. *Adapted with permission from ref.* [37] *Copyright 1997 American* Chemical Society.

Güida and co-workers performed ^{15}NO, $N^{18}O$, and ^{54}Fe isotope labeling IR spectroscopic studies on the linkage isomerization of $[CN)_5Fe(NO)]^{2-}$ induced by photolysis.[102] They subjected the ground state $[(CN)_5Fe(NO)]^{2-}$ complex (ν_{NO} = 1943 cm^{-1}) to a 488.0 nm Ar^+ laser at 77 K and observed a new isotope sensitive IR band at 1834 cm^{-1} which was assigned to the isonitrosyl linkage isomer, $[(CN)_5Fe(\eta^1\text{-ON})]^{2-}$, a shift of $\Delta\nu_{NO}$ of 109 cm^{-1} from the ground state precursor. On the other hand, photolysis using 514.5 nm Ar^+ laser at 77 K afforded the $[(CN)_5Fe(\eta^2\text{-NO})]^{2-}$ linkage isomer that could also be generated by irradiation of the η^1-ON isomer with a Nd:YAG 1064 nm laser (Fig. 1.13). DFT calculations (B3LYP, 6-311+G) supported the isotopic IR shifts observed experimentally.[102]

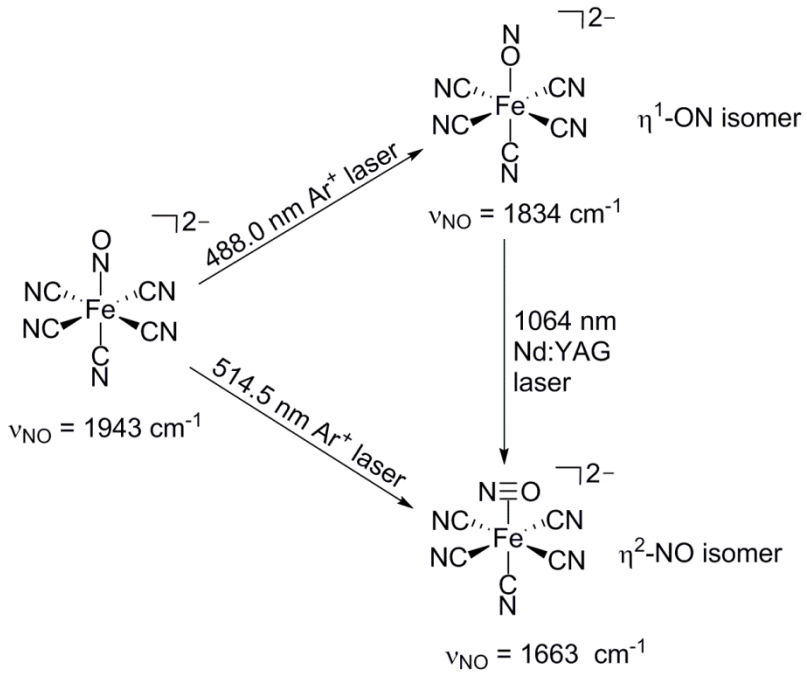

Figure 1.13. Linkage isomerization of $[(CN)_5Fe(NO)]^{2-}$ after photolysis.

Schaniel and coworkers studied the properties of the photoinduced η^1-ON and η^2-NO isomers in $Na_2[Fe(CN)_5NO]\cdot 2H_2O$ embedded in mesopores of silica xerogels by X-ray diffraction, steady-state low-temperature absorption, nanosecond transient absorption spectroscopy, and IR spectroscopy.[34] They determined that the electronic structures and activation energies of these η^1-ON and η^2-NO isomers were not dependent on the particle size (statistically distributed molecules or nanoparticles) and as such the isomers were essentially quasi-free inside the pores of the gel.[34]

We note that the related Ru complex $Na_2[(CN)_5Ru(NO)]$[103] and the Os complex $Na_2[(CN)_5Os(NO)]$[104] also exhibited linkage isomers after photolysis, producing their respective η^1-ON and η^2-ON linkage isomers as evidenced by their IR spectroscopic data (Table 1.1).

Table 1.1. IR spectral data (ν_{NO}) of some transition metal nitrosyl complexes and their linkage isomers.

Compound	M−NO	M−ON ($\Delta\nu_{NO}$)	M−η^2-NO ($\Delta\nu_{NO}$)	Ref.
$Mo(CO)(NO)(dppe)(S_2CNEt_2)$	1578		1216 (362)	85
$[Mo(CO)_3(NO)(dppe)]PF_6$	1740	1632 (108)	1406 (334)	85
$[CpMn(CO)_2(NO)]BF_4$	1860	1726 (134)	1549 (311)	91
$[(MeCp)Mn(CO)_2(NO)]PF_6$	1812	1716 (96)	1522 (290)	91
			1506 (306)	
$[CpRe(CO)_2(NO)]BF_4$	1824	1707 (117)	1460 (364)	91
$Na_2[Fe(CN)_5(NO)]\cdot 2H_2O$	1943	1834 (109)	1666 (277)	92,102
$Na_2[Ru(CN)_5(NO)]\cdot 2H_2O$	1932	1847 (85)	1648 (284)	103
		1839 (93)		
		1835 (97)		
$K_2[RuCl_5NO]$	1921	1765 (156)	1554 (367)	105
	1909		1550 (359)	
$K_2[RuCl_5NO]^a$	1893	1768 (125)		106
$[Ru(NH_3)_5(NO)]Cl_3$	1955	1823 (132)		107
$[Ru(NH_3)_4(NO)(OH)]Cl_2$	1847	1716 (131)		107
trans-$[Ru(Hox)NO(en)_2]Cl_2$	1900	1763 (137)		108
cis-$[Ru(Hox)(en)_2NO]Cl_2\cdot EtOH$	1917	1796 (121)		108
cis-$K[Ru(ox)_2(en)NO]$	1881	1779 (102)		108
trans-$[RuCl(en)_2NO]Cl_2$	1878	1744 (134)		109
cis-$[RuCl(en)_2NO]Cl_2$	1901	1775 (126)		109
	1879	1759 (120)		
trans-$[RuBr(en)_2NO]Br_2$	1877	1738 (139)		109
cis-$[RuBr(en)_2NO]Br_2$	1902	1777 (125)		109
	1881	1759 (122)		
trans-$[Ru(H_2O)(en)_2NO]Cl_3$	1904	1786 (118)		109
$[RuCl_3(en)NO]$ *fac* and *mer*	1865	1728 (137)		109
		1744 (121)		
$Na_2[Os(CN)_5(NO)]\cdot 5H_2O$	1897	1790 (107)	1546 (351)	104
		1788 sh (109)		

Abbreviations: dppe , 1,2-Bis(diphenylphosphino)ethane; ox, oxalate ion; en, ethylenediamine; *fac*, facial; *mer*, meridional. $\Delta\nu_{NO}$, difference between ν_{NO} of ground state isomer and ν_{NO} of corresponding metastable state.

Isonitrosyl η^1-ON linkage isomers have been observed during the photolysis of other ruthenium nitrosyl complexes such as $[RuX(en)_2(NO)]^{2+}$ (X = Cl, Br),[109] $[Ru(NH_3)_5(NO)]^{3+}$,[107] $[Ru(NH_3)_4(NO)(OH)]^{2+}$,[107] $[Ru(Hox)(NO)(en)_2]^{2+}$,[108]

$[RuCl_3(en)NO]$,[109] $[Ru(H_2O)(en)_2NO]^{3+}$, [109] and both the η^1-NO and η^2-NO linkage isomers have been observed in $[RuCl_5(NO)]^{2-}$ (Table 1.1).[105]

Recently, Woike and coworkers performed structural analysis on the two photoinduced linkage isomers of $[Ru(py)_4Cl(NO)](PF_6)_2 \cdot 0.5H_2O$ using photocrystallography.[110] Irradiation of a crystal of the ground state $[Ru(py)_4Cl(NO)](PF_6)_2 \cdot 0.5H_2O$ compound by a laser (λ = 473 nm) at 80 K resulted in a 92% conversion of the NO ligands from Ru−N−O (η^1-NO) to the Ru−O−N (η^1-ON) configuration. Upon further irradiation of the generated η^1-ON isomer with λ = 980 nm light, 48 % of the side-on (η^2-NO) isomer was produced (Fig. 1.14). The half-lives

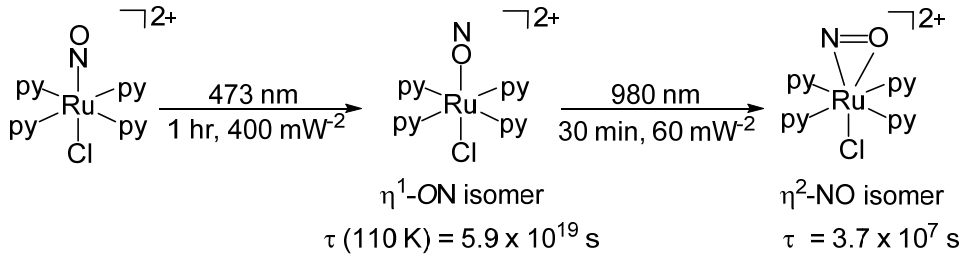

Figure 1.14. Linkage isomerization in $[Ru(py)_4Cl(NO)](PF_6)_2 \cdot 0.5H_2O$.

for the η^1-ON and η^2-NO isomers were determined to be 5.9 x 10^{19} s and 3.7 x 10^7 s, respectively, at 110 K. However, at temperatures above 200 K, or irradiation with light in the red spectral range, these metastable isomers reconverted to the ground state nitrosyl isomer.[110]

In addition to the isomerization of the NO ligand from nitrosyl to isonitrosyl, and then to the side-on isomers, X-ray crystallographic data of the parent and linkage isomers of $[Ru(py)_4Cl(NO)](PF_6)_2 \cdot 0.5H_2O$ revealed a shortening of the trans Ru−Cl

bond and the equatorial Ru−N bond distances in the linkage isomers. The Ru−O−N bond angle remained linear in the η^1-ON isomer. Woike and coworkers also performed DFT calculations that supported the experimental observations by X-ray crystallography.

Cormary *et al.*[111] used IR spectroscopy and single-crystal X-ray crystallography to study the effects of counterions, *trans* ligands to NO, and equatorial ligands on the linkage isomer conversion efficiency of a series of $[RuX(NO)(py)_4]Y_2 \cdot nH_2O$ (X = Cl and Y = PF_6, BF_4, Br, Cl; X = Br and Y = PF_6, BF_4, Br), $[RuCl(NO)(bpy)_2](PF_6)_2$, $[RuCl_2(NO)(tpy)](PF_6)$, and $[Ru(H_2O)(NO)(bpy)_2](PF_6)_3$, and observed that the lower the electron donating character of the *trans*-to-NO ligand (e.g., H_2O < Cl < Br), the higher the conversion yield. Also, complexes in which the counterions were closest to the NO ligand had a higher conversion of the photoinduced products.[111]

1.2.3.2 NO_2 complexes

Coppens and coworkers observed that laser irradiation of crystal samples of $[Ru(bpy)_2(NO)(NO_2)](PF_6)_2$, at 90 K produces a double isonitrosyl-nitrito linkage isomer (Fig. 1.15) and structurally identified the photogenerated linkage isomers by a combination of x-ray crystallography and infrared spectroscopy.[112]

At 200 K, the ground state $[Ru(bpy)_2(NO)(NO_2)](PF_6)_2$ compound displayed a ν_{NO} band at 1943 cm^{-1} and two ν_{NO2} bands were observed at 1430 and 1330 cm^{-1} in the IR spectrum. The photogenerated product at this temperature was structurally characterized as the nitrito-nitrosyl isomer, $[Ru(bpy)_2(NO)(ONO)]^{2+}$ or MS_{200K}. The

MS_{200K} photogenerated product showed a new ν_{NO} band at 1897 cm^{-1} and displayed the nitrito bands at 1495 and 983 cm^{-1}. However, at 90 K a five-minute photolysis of the

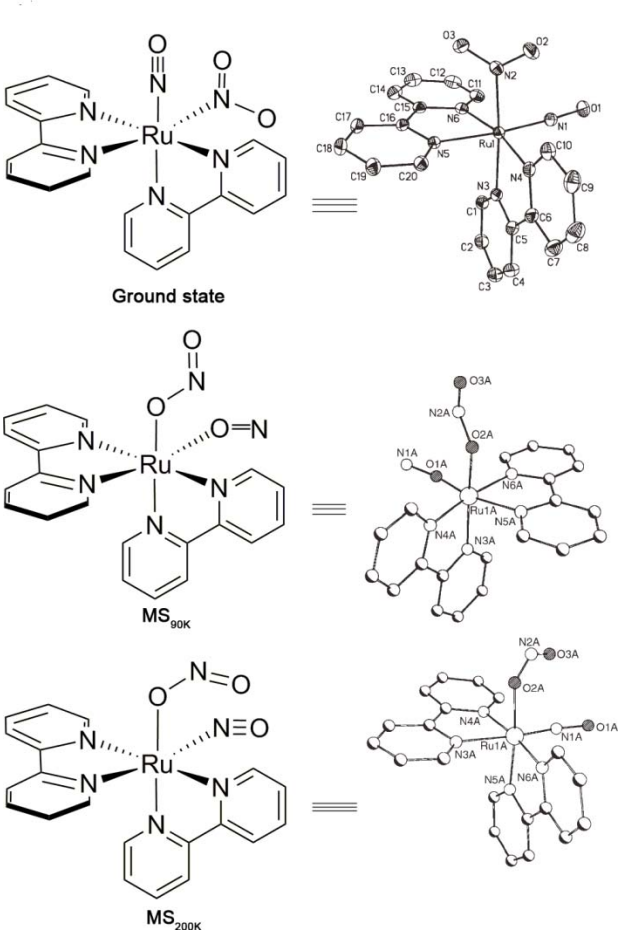

Figure 1.15. The ground state and metastable isomers of $[Ru(bpy)_2(NO)(NO_2)]^{2+}$ (charge not shown in figure). *Redrawn with permission from Ref.* [112]

ground state $[Ru(bpy)_2(NO)(NO_2)](PF_6)_2$ compound resulted in the production of another $[Ru(bpy)_2(ON)(ONO)]^{2+}$ (ν_{NO} = 1892 cm^{-1}) species which structurally differed from the MS_{200K} by the orientation of the nitrito group, as well as a major species identified as the nitrito-isonitrosyl compound, $[Ru(bpy)_2(ON)(ONO)]^{2+}$ or MS_{90K} (ν_{NO} = 1815cm^{-1}) (Fig. 1.16).

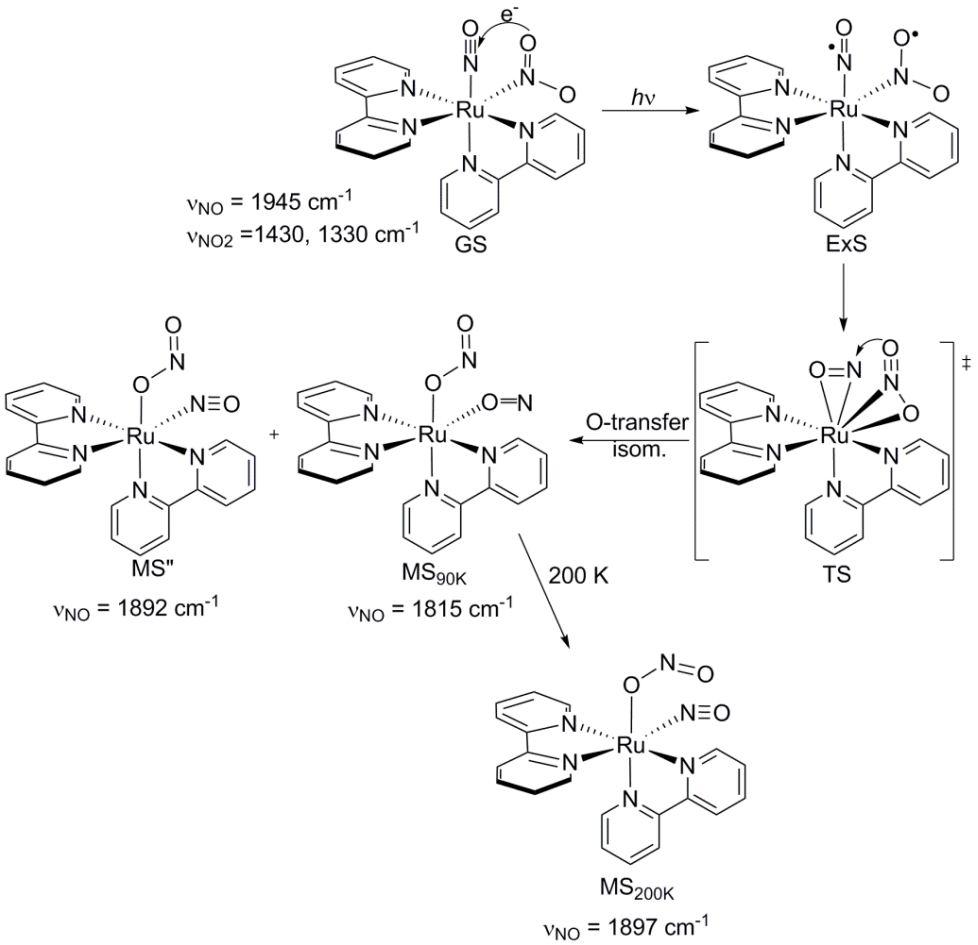

Figure 1.16. Proposed mechanism of the light-induced oxygen transfer reaction and the linkage isomerization. *Redrawn with permission from Ref.* [112]

Theoretical calculations suggest that the metastable states MS_{90K} and MS_{200K} corresponded to local minima on the potential energy surface.[112] Coppens and coworkers investigated the mechanism of the light-induced oxygen transfer reaction and proposed that at 90 K, and under light, there is an intramolecular redox reaction involving oxygen transfer from the nitro to the nitrosyl group to generate the six-coordinate compounds MS_{90}, MS" and MS_{200K} via isomerization of the side bound NO_2 transition state structure (TS).

Recently, Andriani and coworkers provided theoretical insights on the nature of the Ru−NO, Ru−ON, Ru−ONO and the Ru−NO_2 bonding in the $[Ru(bpy)_2(NO)(NO_2)]$-$(PF_6)_2$ compound using energy decomposition analysis [113] and observed that the nitrito-nitrosyl isomer, $[Ru(bpy)_2(NO)(ONO)]^{2+}$ and the nitro-nitrosyl isomer, $[Ru(bpy)_2(NO)(NO_2)]^{2+}$ were more stable than the nitrito-isonitrosyl, $[Ru(bpy)_2(ON)(ONO)]^{2+}$ compound.[114]

1.2.3.3 NO_3 complexes

Fanning and coworkers have prepared two forms of the complex, $[Fe(salen)NO_3]$ (salen = *N,N′*-ethylenebis(salicylideneaminato), namely, the monomeric $[Fe(salen)O_2NO]$, and the dimeric $[Fe(salen)ONO_2]_2$ complex by the reaction of the μ-oxo dimer complex, $[Fe(salen)]_2O$ with nitric acid (Fig. 1.17).[115]

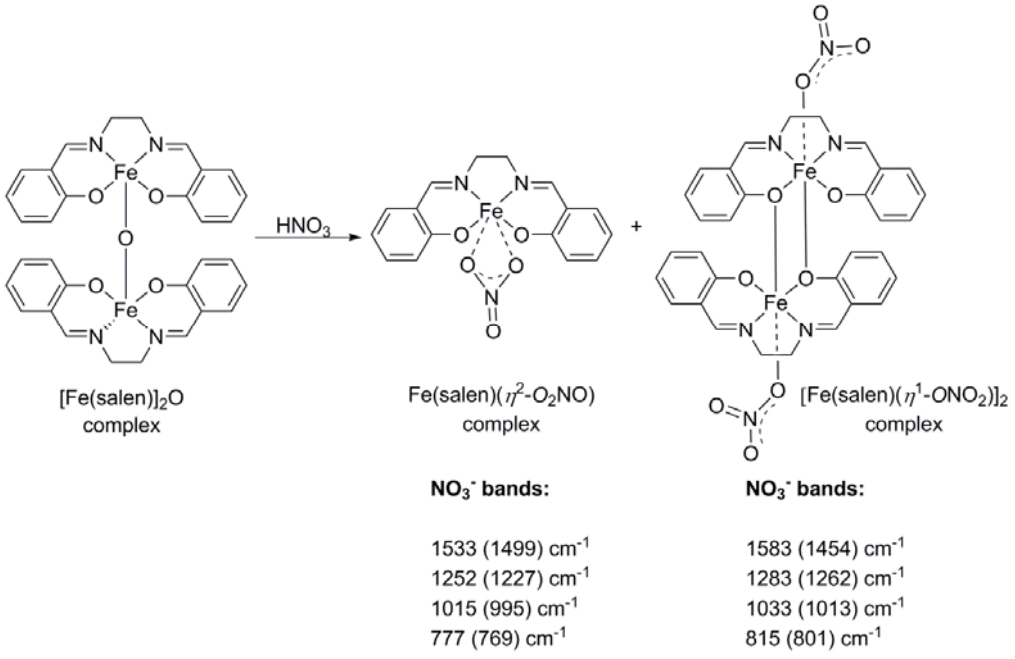

Figure 1.7. Preparation of the two forms of the complex $[Fe(salen)NO_3)]$. Numbers in brackets are $^{15}NO_3$ bands.

[Fe(salen)ONO_2]$_2$ was also prepared by treating a dichloromethane solution of [Fe(salen)]$_2$O with nitric oxide and then dioxygen.[116] IR spectroscopy data was used to distinguish the nitrate binding in each of the compounds. Specifically, [Fe(salen)NO_3)] displayed the following IR frequencies: 1533, 1252, 1015 and 777 cm^{-1} that were assigned to the bound nitrate ligand. The IR frequencies were isotope-sensitive with bands at 1499, 1227, 995, and 769 cm^{-1}, respectively in the ^{15}N-nitrate labeled compounds. Similarly, [Fe(salen)ONO_2]$_2$ displayed IR bands at 1583, 1283, 1033 and 815 cm^{-1}, and their respective isotope sensitive bands at 1454, 1262, 1013, and 801 cm^{-1}.[115] The nitrato ligand is bound to Fe in a bidentate *O,O*-nitrito fashion in Fe(salen)O_2NO and via one nitrato oxygen (η^1-ONO_2) in the [Fe(salen)ONO_2]$_2$ complex.

The molecular structure of [Fe(salen)ONO_2]$_2$ as determined by X-ray crystallography revealed the sixth coordination site of each of the Fe atoms was occupied by an oxygen atom belonging to the other salen ligand, forming a four-membered cyclic structure (Fig. 1.18).[116]

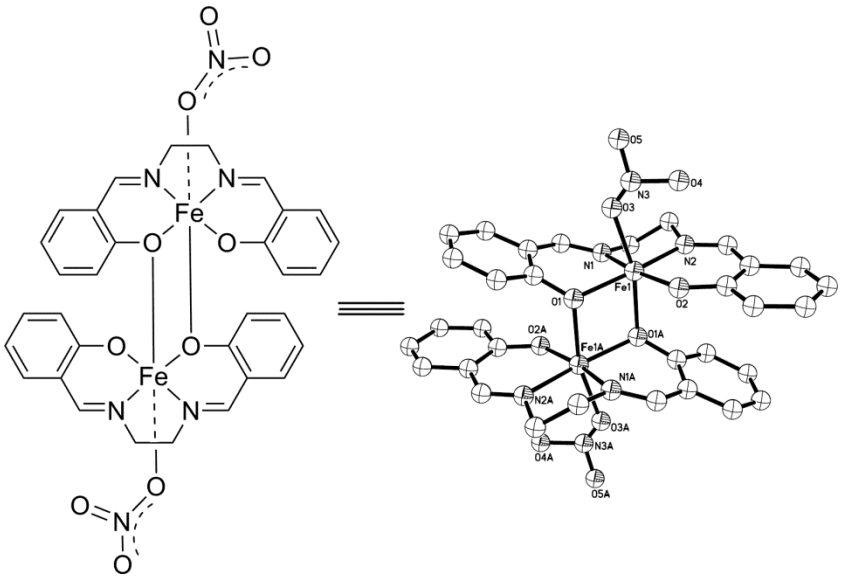

Figure 1.18. Molecular structure of $[Fe(salen)ONO_2]_2$.[116] Hydrogen atoms have been omitted for clarity.

1.2.4 Group 9 (Co, Rh and Ir) complexes

1.2.4.1 NO Complexes

It appears from the information gathered from the literature that the complex $K[IrCl_5NO]$ is the only known group 9 transition metal nitrosyl complex, to date, that undergoes NO linkage isomerization.[117] Irradiation of a Nujol mull sample of $K[IrCl_5NO]$ at 77 K with light of λ 309-413 nm generated a metastable species identified as the isonitrosyl isomer $K[IrCl_5(\eta^1\text{-ON})]$ as evidenced by a shift of the initial 2008 cm^{-1} band (in the IR spectrum) of the ground state $K[IrCl_5NO]$ complex to 1812 cm^{-1} for the metastable species. The linkage isomer thermally decays at 90 K or by irradiation with light in the range of λ 450-680 nm.[117]

1.2.4.2 NO_2 complexes

The most common NO_x complexes of Co are the Co-nitrites. In the solid form, the yellow N-bound nitro complex, $[(NH_3)_5Co(NO_2)]^{2+}$ is found to isomerize to the *O*-bound nitrito complex, $[(NH_3)_5Co(ONO)]^{2+}$ after irradiation with light.[53,118,119] Conversely, freshly prepared $[(NH_3)_5Co(ONO)]^{2+}$ complexes were converted to the $[Co(NH_3)_2(NO_2)]^{2+}$ isomer by warming a solid sample of the former to room temperature.[3,120]

Despite the fact that the Werner complexes have been intensively studied, there appears to still be controversy on the extent of reversibility of the nitro-nitrito isomerization of $[Co(NH_3)_2(NO_2)]^{2+}$,[120-124] a property of interest in these kinds of complexes (*vide infra*). Recently, Eslami showed by DSC experiments that the thermal isomerization of pure $[(NH_3)_5Co(ONO)]^{2+}$ to $[(NH_3)_5Co(NO_2)]^{2+}$ is a reversible process and is enthalpy driven and the reverse slightly entropy driven.[68,70] In addition, kinetic studies,[125] changes in X-ray diffraction patterns of solids[123,126,127] as well as isotope labeling experiments[128] seem to suggest that the linkage isomerization process is intramolecular that involves the formation of the 7-coordinate complex with N and one O of NO_2 coordinated to Co (Fig. 1.19). For instance, Grenthe and Nordin studied the nitrito-nitro linkage isomerization in *trans*-$[Co(en)_2(NCS)(ONO)]X$ (X = I^-, ClO_4^-, en = ethylenediamine) by X-ray crystallography and observed that the plane of the bound nitrite and the Co atom were approximately situated in the same plane before and after rearrangement, an indication that the isomerization process proceeded by an intramolecular mechanism via rotation rotation in the Co−O−N−O plane.[127]

The isomerization of the complex $[(NH_3)_5Co(NO_2)]^{2+}$ represented the first classical evidence for light- or thermally-induced linkage isomerization (Fig. 1.19).[1,129] Several derivatives of this complex with varying counterions since have been reported

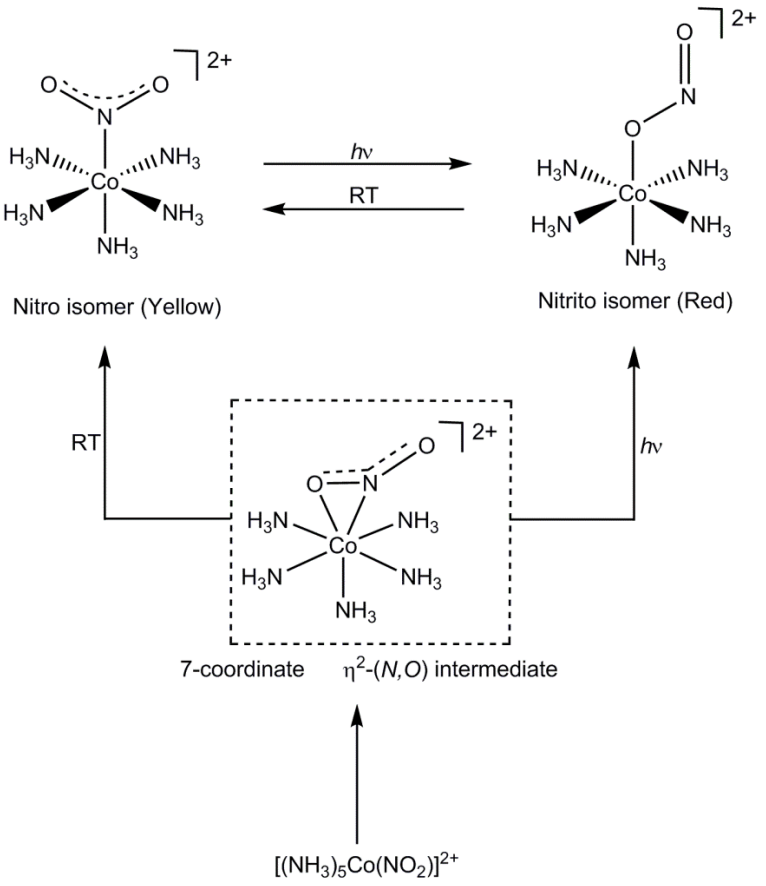

Figure 1.19. The $[(NH_3)_5Co(NO_2)]^{2+}$ complex, the first classical evidence for linkage isomerization. Linkage isomerism is normally promoted by light or change in temperature.

to undergo the nitro-nitrito linkage isomerization process. Several decades ago, Basolo reported nitrito-to-nitro linkage isomerizations in the related Rh(III) and Ir(III) complexes $[(NH_3)_5Rh(ONO)]^{n+}$ and $[(NH_3)_5Ir(ONO)]^{n+}$, as determined by absorption and IR spectroscopy[130] In the solid form, and at 35 °C the rate of nitrito-nitro

isomerization is 1.7 x 10^4 s^{-1} in $[(NH_3)_5Rh(ONO)]^{n+}$ and 6.8 x 10^4 s^{-1} in $[(NH_3)_5Ir(ONO)]^{n+}$. However, the rate of the nitrito-nitro isomerization of $[(NH_3)_5Ir(ONO)]^{n+}$ (4 .4 x 10^3 s^{-1}) in aqueous solutions, at 25 °C is lower than that of $[(NH_3)_5Rh(ONO)]^{n+}$ (9.6 x 10^4 s^{-1}).[130]

1.2.5 Group 10 (Ni, Pd and Pt) complexes

1.2.5.1 NO complexes

Coppens and coworkers reported the first experimental evidence for the presence of side-on nitrosyl bound isomer of any group 10 nitrosyl complex $\{MNO\}^{10}$.[65] In their work, they collected X-ray diffraction data sets on a crystal of Cp*Ni(NO) (Fig. 1.20) and subjected the same crystal at 25 K to 485 nm light from

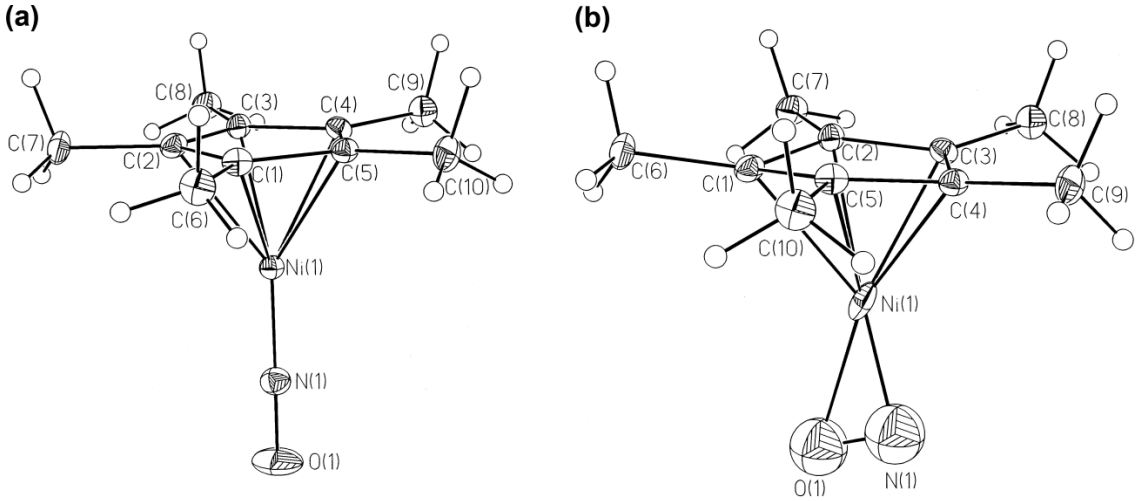

Figure 1.20. ORTEP drawing of: (a) Cp*Ni(NO)in the ground state (Selected bonding parameters: Ni−N = 1.620(3) Å, ∠NiNO = 179.2(3) and (b) Cp*Ni(η^2-ON) (Molecule a: Selected bonding parameters: Ni−N = 2.096(18) Å, ∠NiNO = 93(1). 50% probability ellipsoids are shown, except for those of the H atoms. *Adapted with permission from Ref.* [65] *Copyright 1998 American Chemical Society.*

an Ar^+ laser for 3 h. Analysis of the diffraction data before and after irradiation revealed the formation of a new species identified as the side-on η^2-NO bound nickel complex, accompanied by a shortening of the Ni-O distance, a slight shortening of the Ni−N distance, and a tightening of the Ni−N−O bond angle to 92(1)°. They also performed geometry optimizations on the metastable Cp*Ni(η^2-NO) structure using DFT calculations and found that it corresponded to a local minimum energy of 0.99 eV above that of the ground state isomer. The calculations also predicted a second local minimum at 1.85 eV above the ground state and the authors assigned this isomer to the isonitrosyl Cp*Ni(η^1-ON) species.[65]

Güida and coworkers have provided infrared spectra data to show two photogenerated metastable excited states (MSI and MSII) for the related CpNi(NO) complex.[131] They irradiated the parent CpNi(NO) with 488.0 nm and 514.5 nm light (Ar^+ laser line) at 77 K to generate the metastable species [Ni(η^1-ON)(η^5-Cp)] and [Ni(η^2-NO)(η^5-Cp)]. The IR spectra of the photogenerated species showed downward shifts of the ν_{NO} by 260 cm^{-1} and 460 cm^{-1}, consistent with the generation of the isonitrosyl (MSI) and side-on (MSII) species, respectively.

Schaniel *et al.* studied the photolysis products of some $[(NH_3)_4Pt(NO)X]^{n+}$ (X = Cl^-, SO_4^{2-}, NO_3^- complexes (Fig. 1.21).[132,133] They reported the first photogeneration

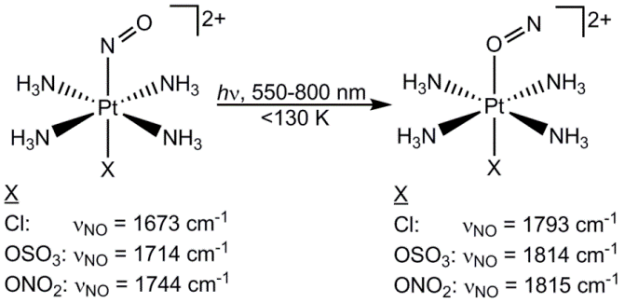

Figure 1.21. Nitrosyl-isonitrosyl isomerization in some $[(NH_3)_4Pt(NO)X]^{n+}$ complexes.

of nitrosyl linkage isomers in such Pt nitrosyl complexes, from irradiation of a powdered sample of the $[(NH_3)_4Pt(NO)Cl]^{2+}$ complex with light in the spectral range 550-800 nm. IR spectral data revealed a shift in the ν_{NO} band from 1673 cm^{-1} to 1793 cm^{-1} that they attributed to a nitrosyl-to-isonitrosyl linkage isomerization to a geometry between η^1-ON and η^2-ON.[132]

Schaniel *et al.* also observed similar linkage isomers in $[NH_3)_4Pt(NO)NO_3]^{2+}$ and $[NH_3)_4Pt(NO)OSO_3]^{+}$ complexes (Fig. 1.21) where the shifts in ν_{NO} (i.e., $\Delta\nu_{NO}$) were observed to be 70 cm^{-1} and 101 cm^{-1}, respectively, to higher frequencies; a feature attributed by the authors to a more positive NO ligand in the linkage isomers.[133] X-ray crystallographic data and DFT calculations of the ground state nitrosyl complex shows a bent Pt−N−O linkage in these $\{PtNO\}^8$ complexes with bond angles between 117 °and 120 °. The otherwise higher ν_{NO} bands in the metastable isomers on changing X from Cl to OSO_3 and ONO_2 were attributed to the significant *trans* effect of the O-bound ligands.[133] In addition changing the *trans* ligand from Cl to OSO_3 and ONO_2 resulted in a lower decay temperature by ~10 K as determined by DSC experiments.[133] Clearly, more research is needed to explain the higher ν_{NO}'s in the metastable isomers.

1.2.5.2 NO_2 complexes

The $[(NH_3)_4(NH_2)Pt(ONO)]^{2+}$ complex as the Cl^- salt is known and can be converted to the nitro isomer in the solid state by heating,[130] and the nitro isomer to the nitrito isomer in aqueous solution by photolysis using 254 or 313 nm light,[134] similar to the observation in the related $[(NH_3)_5Co(NO_2)]^{2+}$ complex. In 2001, Chaudhuri and coworkers provided evidence for a thermally induced nitro-to-*O,O*-nitrito linkage

isomerization in diamine complexes of nickel(II) such as *trans*-[$NiL_2(NO_2)_2$] (L = *N,N′*-dipropyl-1,2-diaminoethane) in the solid state as determined by X-ray crystallography.[54] See Fig. 1.22.

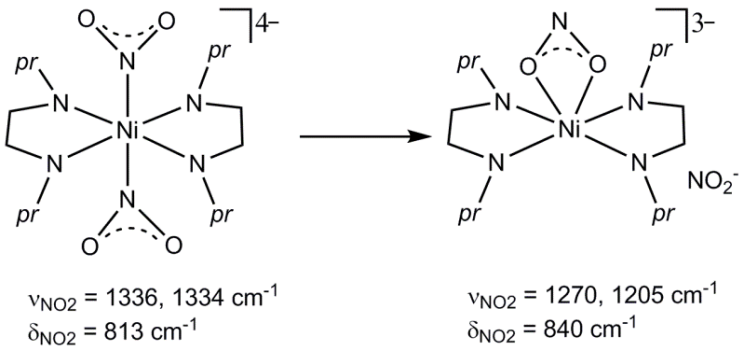

Figure 1.22. Linkage isomerization in *trans*-[$NiL_2(NO_2)_2$] (L = N,N'-dipropyl-1,2-diaminoethane).[54]

Raithby and coworkers have observed the reversible 100% conversion of the red [(dppe)Ni(η^1-NO_2)Cl] complex to its photoinduced yellow linkage isomer [(dppe)Ni(η^1-ONO)Cl] (Eq. 1.2).[135] Raman spectral data revealed a ν_{NO} band at 1333 cm^{-1} in the parent nitro compound and a 1404 cm^{-1} band in the nitrito isomer. The nitrito isomer was further identified by photocrystallography and was found to be stable between 100 and 160 K and observed to reconvert to the ground state at 300 K.

$$[(dppe)Ni(\eta^1\text{-}NO_2)Cl] \underset{300\ K}{\overset{400\ nm,\ 115\ K}{\rightleftharpoons}} [(dppe)Ni(\eta^1\text{-}ONO)Cl] \qquad \textbf{(1.2)}$$

Furthermore, Raithby and coworkers performed a combined thermal and photocrystallographic structural investigation of a nitro/ nitrito interconversion in the

[(Et_4dien)Ni(NO_2)$_2$] complex.[55] X-ray crystallographic analysis of a crystal of [(Et_4dien)Ni(NO_2)$_2$] prepared by treating $K_4[Ni(NO_2)_6]\cdot H_2O$ with Et_4diene, at 298 K shows a 78:22% mixture of the compounds [(Et_4dien)Ni(NO_2)(η^2-O_2N)] : [(Et_4dien)Ni(η^1-ONO)(η^2-ONO)] (Fig. 1.23). The mixture could be converted to the

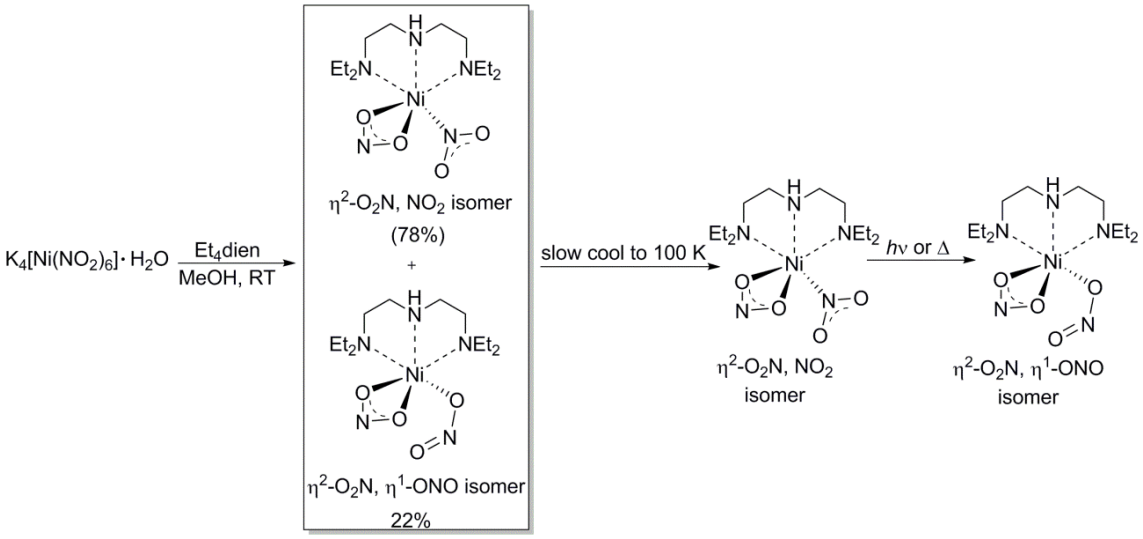

Figure 1.23. Synthesis of the [(Et_4dien)Ni(NO_2)(η^2-O_2N)] and [(Et_4dien)Ni(η^1-ONO)(η^2-ONO)] complexes and their conversion products.[55]

single nitro/η^2-nitrito isomer [(Et_4dien)Ni(NO_2)(η^2-O_2N)] by slow cooling to 100 K. Irradiation (at 100 K) with a 400 nm LED light, or heating of the latter complex to 370 K resulted in the η^1-nitrito, η^2-nitrito isomer, albeit at varying yield, with photolysis affording 86% of the η^1-nitrito, η^2-nitrito isomer and heating affording only 42% of the η^1-nitrito, η^2-nitrito isomer, as shown in Fig. 1.23.[55]

For a metastable system to be applicable as an effective photo- or thermal switchable device, very good linkage isomeric conversions are required. Raithby and coworkers extended their studies on solid-state interconversions of some group 10 nitro complexes by using larger ligands and heavier metals to explore the primary factors that

influence the linkage isomerization process.[56] They prepared sterically encumbered compounds and studied their conversions using both Raman spectroscopy and X-ray photocrystallographic techniques to characterize the resulting photogenerated products.

The solid-state facile isomerization of the [(dppe)Ni(η^1-NO_2)Cl] complex to its nitrito isomer (Fig. 1.24 a), Raithby noted, was possible due to the use of the bulky phosphine ligands which allowed the nitro group to sit in a sterically sheltered "reaction cavity" so that the interconversion could occur without disrupting the crystal packing.[56] To avoid any complexity in studying the effects of changing the size of the phosphine R substituent, the chloride ligand was replaced with another nitro ligand and the compounds *cis*-[(dcpe)Ni(η^1-NO_2)$_2$] and *cis*-[(dppe)Ni(η^1-NO_2)$_2$] were prepared. Irradiation of solid samples of *cis*-[(dcpe)Ni(η^1-NO_2)$_2$] and *cis*-[(dppe)Ni(η^1-NO_2)$_2$] with LED light of 400 nm resulted in 100% conversion to their respective dinitrito isomers (Fig. 1.24 b) although the *cis*-[(dppe)Ni(η^1-NO_2)$_2$] required a longer irradiation time (2 h) for conversion due to its relatively bulky phenyl rings as compared to a 1 h period for conversion for the less sterically encumbered *cis*-[(dcpe)Ni(η^1-NO_2)$_2$] compound.

Upon substituting the bidentate phosphine ligands by monodentate ligands, the *trans*-[(PCy_3)$_2$Ni(η^1-NO_2)$_2$] (and not *cis*) was obtained and displayed only ~82% conversion to the nitro isomer that was stable 130 K (*c.f.,* the higher 180 K for the bidentate complex). Thus, the change in geometry (*trans* vs *cis*) and ligation of the compounds had an effect on both the isomeric conversions and stabilities.[56] Interestingly, the authors observed that the rates of photoconversion of the dinitro

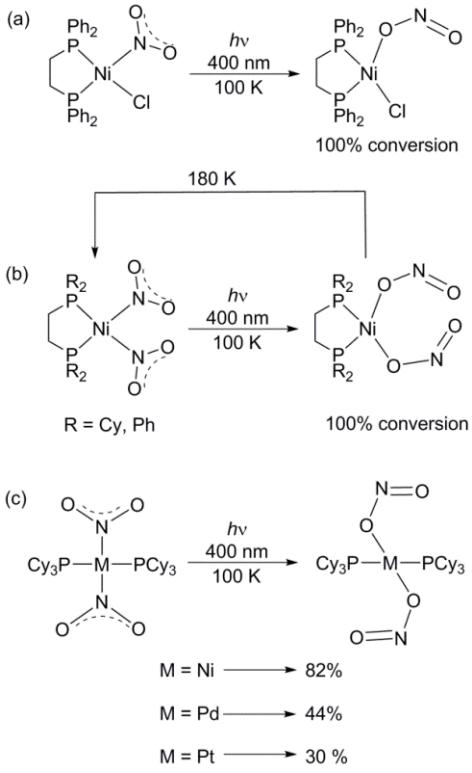

Figure 1.24. Photoisomerization reactions of some group 10 nitro complexes.[56] (a) mono nitro-to-nitrito; (b) bis nitro-to-nitrito; (c) bis nitro-to-nitrito and effects of metal substitution on yields.

complexes were lowered in going from the first row transition metal Ni to the second and third row Pd and Pt metals.[56] This observation may also be explained in terms of the HSAB theory where the more electronically dense Pt metal directs the mode of binding to the N-soft end of the nitro ligand such that only 30% conversion to the nitrito isomer was attained. Ni, which is the hardest of this metal triad saw the largest conversion of 82%. The authors also explained this observation in terms of reduction of cavity size in moving from Ni to Pt in the complexes (Fig. 1.24 c).[56]

An isomerization mechanism for these systems was proposed using the results of a computational study (B3LYP) on a model complex [(dmpe)Ni(NO_2)Cl] (dmpe = ethylenebis(dimethylphosphine). The proposed mechanism involves an initial rotation

of the nitro group about a vector perpendicular to the ligand plane leading to the *exo*-nitrito species. The latter species then rotates about the N−O single bond to yield the *endo*-nitrito species (Fig. 1.25). Calculations also revealed an energy barrier of 11-15 kcal mol^{-1} for the isomerization process with the intermediate siting in a very shallow minimum with barrier of 1-2 kcal mol^{-1} on either side.[56]

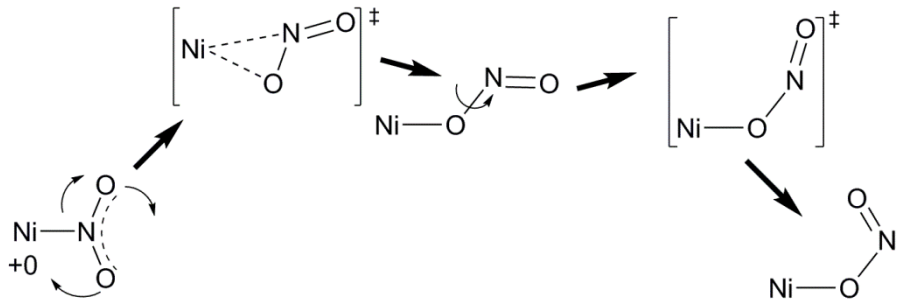

Figure 1.25. Proposed isomerization mechanism from theoretical calculations. The curved arrows indicate the general motions involved.[56]

1.3 Linkage isomerism in NO_x-coordinated metalloporphyrins

The chemistry of NO_x metalloporphyrins, namely the $[(por)M(NO_x)Y]^z$ complexes (M = metal; Y = no ligand, anion, or neutral ligand; z = charged or not charged), has received a lot of attention in the last few decades.[14] The $[(por)M(NO_x)Y]$ complexes are important in several areas. In biological systems, for example, $[(por)M(NO_x)Y]$ complexes have been used as model compounds for understanding the role of NO as a biological signaling molecule.[136,137] In addition, these model compounds have aided in understanding the function of heme cd_1-containing nitrite reductases, and in understanding the function of bacterial and fungal nitric oxide reductases (Fig. 1.26).[18,21]

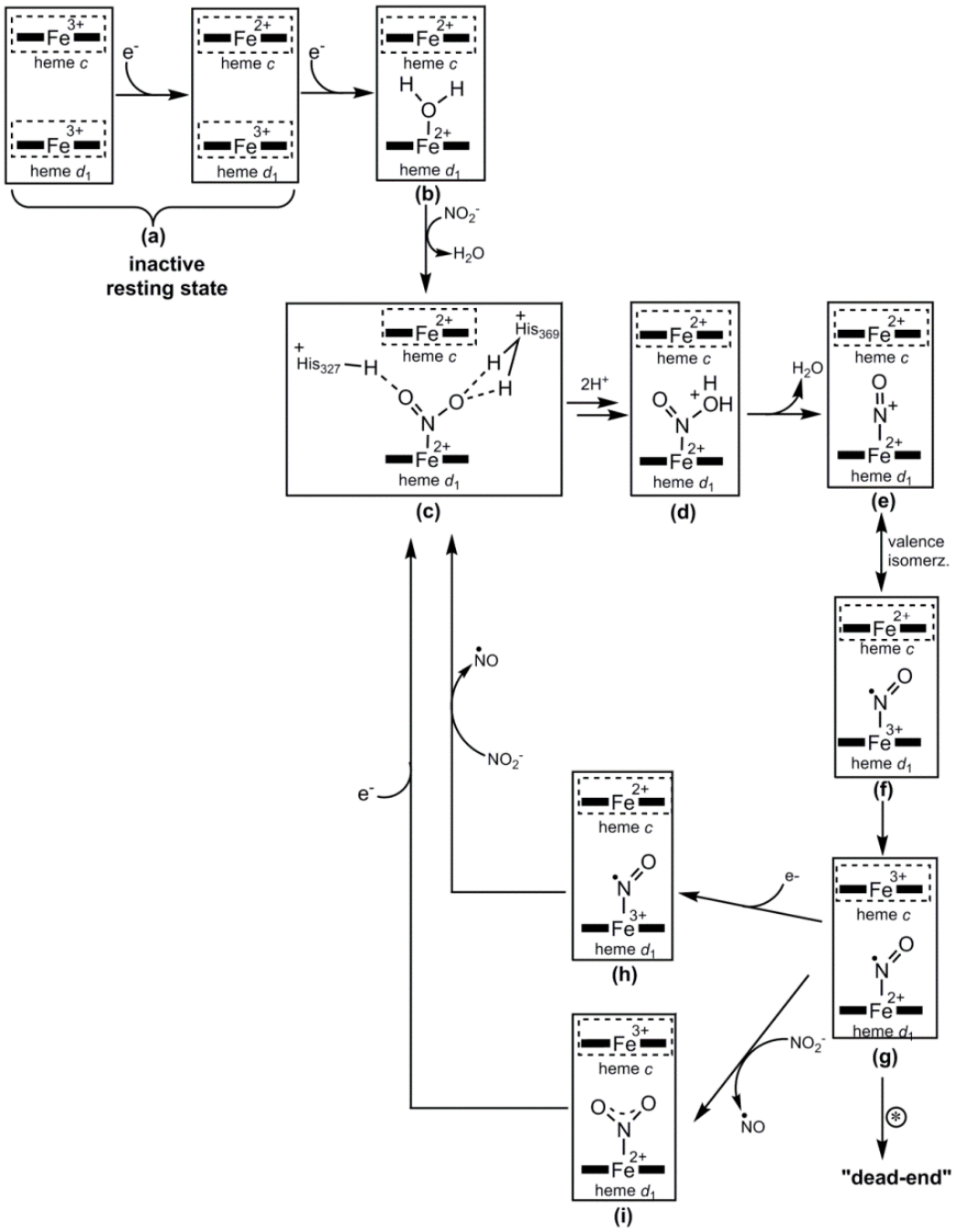

Figure 1.26. Proposed mechanism of nitrite reduction to NO by *c*d$_1$. (**a→b**) reductive activation of resting (inactive enzyme) and tyrosine displacement (not shown); (**b→c**) nitrite binding; (**c→d**) protonation of nitrite complex; (**d→e**) cleavage of N−O bond and elimination of H_2O; (**e→f**) intramolecular iron oxidation (valence isomerization); (**f→g→h→c** and **f→g→i→c**) redox reactions involving heme *c* and heme d_1 nitrosyl complex followed by rapid dissociation of NO; (*****) enzyme gets trapped in a "dead end" species in the absence of reducing substrate or nitrite. *Adapted with permission from Ref.* [21] *Copyright 2014 American Chemical Society.*

In this section, we present the chemistry of [(por)M(NO_x)Y] complexes concentrating on those that exhibit linkage NO_x isomerization. Key reports to be highlighted include recent work by Kurtikyan and coworkers on their use of microporous solvent-free layers of (por)M in experiments to study linkage isomers in the NO adducts,[(por)M(NO_x)Y] generated and work by Coppens and Richter-Addo and coworkers on light-induced linkage isomerization of (por)M(NO)Y complexes. It is our hope that this section, in addition to previous reviews,[7,8,11] will highlight important linkage isomerization processes in heme model chemistry, and open new areas of research and expand the scope and applications of linkage isomerization in [(por)M(NO_x)Y] complexes.

1.3.1 Manganese NO_x porphyrins

Kurtikyan, Ford and coworkers have used infrared and UV spectroscopy to probe the species formed in the interaction of NO_x molecules with microporous solvent-free layers of (por)M complexes (M = Mn,[138-140] Fe,[141-150] Co,[151-155]) at varying temperatures. Sample preparation of such (por)M layers and their interactions with NO_x have been described in detail elsewhere.[156,157] Importantly, in this sample preparation technique, the (por)M species are sublimed onto KBr, CsI or a CaF_2 substrates at low temperature to form "porphyrin sponges" which permit diffusion of volatile ligands into the bulk layer.[158] Using this method, clean IR spectra devoid of solvent interferences can be obtained for the precursor complexes and for the product species that form upon reacting with the incoming ligands. Another advantage of this technique is that the reaction temperature can be controlled so that thermally sensitive species can be identified at set temperatures. This makes this technique applicable in the detection

(e.g. by spectroscopic means) of metastable species, most of which are observed at cryogenic temperatures.[11,156]

Porous layer experiments were used to probe the mode of binding of NO in the 5-coordinate (TPP)Mn(NO) complex (Fig. 1.27).[138] In their work, Kurtikyan *et al.*

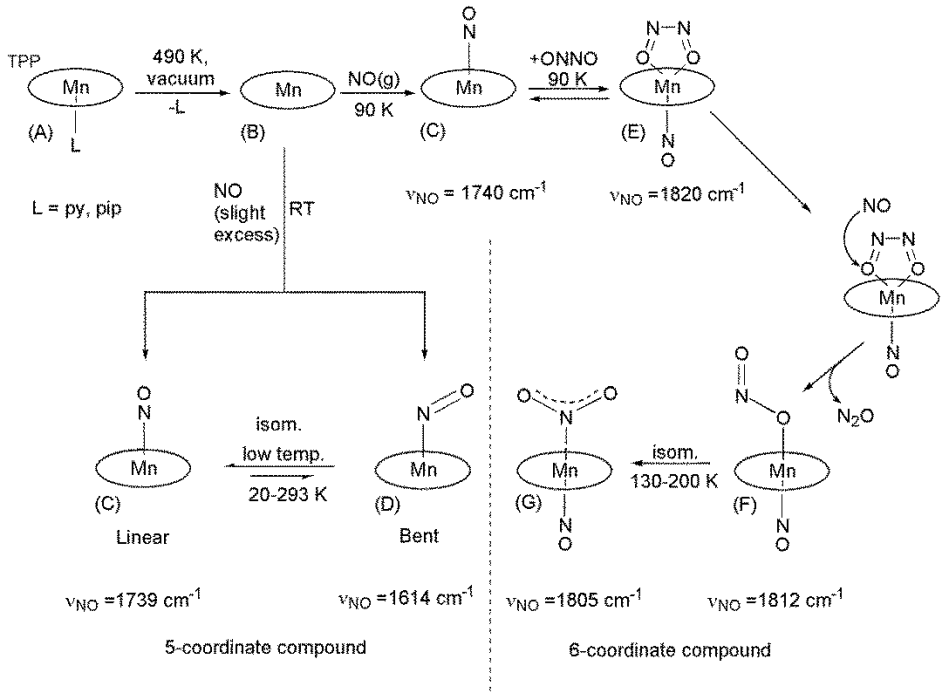

Figure 1.27. In situ preparation of the five coordinate (TPP)Mn(NO) and the six-coordinate (TPP)Mn(NO)(NO_2) complexes and their linkage isomers via NO diffusion onto microporous layers of (TPP)Mn.[138,140]

prepared a CsI porous layer of (TPP)Mn (Fig. 1.27, structure B) and treated it with slight excess of NO at room temperature. The IR spectrum obtained for the resulting species displayed two strong NO stretches at 1739 and 1614 cm^{-1} and ^{15}N isotope sensitive bands appearing at 1704 and 1585 cm^{-1}, respectively when ^{15}NO was used in place of NO (Fig. 1.28).[138]

Kurtikyan and coworkers assigned the band at 1739 cm^{-1} (1760 cm^{-1} in Nujol[159])

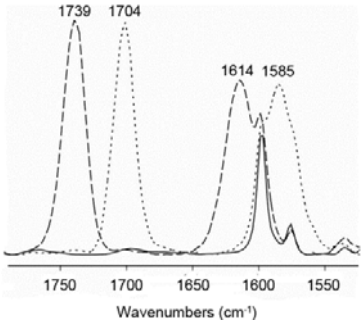

Figure 1.28. FTIR spectra of Mn(TPP) (solid line), Mn(TPP)(NO) (dashed line) and Mn(TPP)(^{15}NO) (dotted line). *Reproduced from ref.* [138] *with permission of the Royal Society of Chemistry.*

to the ν_{NO} of the linear nitrosyl configuration of (TPP)Mn(η^1-NO) in which NO is bound to Mn via its N atom (Fig. 1.27 C). The observed IR band is in accordance with the range normally found for ν_{NO} value in the linear M−N−O linkage in five coordinate $\{MNO\}^6$ systems.[71,137,160] They assigned the band at lower wavenumber (1614 cm^{-1}) to the bent nitrosyl linkage isomer (Fig. 1.27 D). They also identified the following experimental evidence as further support for their assignments of the two linkage isomers:

1. IR spectra data obtained from the product species did not provide evidence of the formation of the dinitrosyl complex (TPP)Mn(NO)$_2$ under the experimental conditions. If a dinitrosyl species were present, a ν_{NO} stretch higher than the mononitrosyl complex's 1739 cm^{-1} band would be observed, similar to the observation in the analogous (TPP)Fe(NO)$_{1,2}$ complexes (ν_{NO} = 1681 and ν_{NO} =1695 cm^{-1}, respectively). In addition, a dinitrosyl complex would be expected to have twice the intensity of absorption of the mononitrosyl complex,[161] which was not observed in their work. They also observed that NO loading of their (TPP)Mn(NO) complex did not favor dinitrosyl formation and that the relative

intensities of the two NO stretches (1739 and 1614 cm^{-1}) was independent of the NO deposited, an indication that no dinitrosyl complex was formed under their experimental conditions.[138]

2. No six-coordinate (TPP)Mn(NO)L (L = py, pip) species was detected. The (TPP)Mn complex was prepared from the solvated (TPP)MnL complex.[162] (Fig. 1.27 A) In the event that L is not completely removed during the porous layer preparation process, (TPP)MnL may react directly with NO to form (TPP)Mn(NO)L as shown in Eq. 1.3:

$$(TPP)MnL + NO \rightarrow (TPP)Mn(NO)L \quad \textbf{(1.3)}$$

$$(por)Fe(pip)_2 + NO \rightarrow (por)Fe(NO)(pip) + pip \quad \textbf{(1.4)}$$

A similar reaction has been reported in the analogous $(por)Fe(pip)_2$ (por = TPP and PPIX) as shown in Eq. 1.4. In a control experiment using (TPP)Mn(py) and (TPP)Mn(pip) as precursors for (TPP)Mn, similar ν_{NO} values (1739 and 1614 cm^{-1}) were obtained when the latter complex was exposed to NO. Kurtikyan and coworkers argued that if these IR bands resulted from the six-coordinate (TPP)Mn(NO)L their corresponding ν_{NO} would be different since py and pip have different σ and π donor and acceptor properties. Thus, neither of the observed ν_{NO} IR bands at 1739 and 1614 cm^{-1} correspond to the six-coordinate (TPP)Mn(NO)L complex.

3. IR spectral data did not support the formation of NO complexes due to partial oxidation of (TPP)Mn by trace NO_2. Such Mn(III) complexes, when formed, usually give a higher ν_{NO} at ca. 1830 cm^{-1},[163] which was not observed in their experiment.

4. Importantly, the relative intensities of the ν_{NO} bands changed with changes in temperature (20-293 K) suggesting the presence of thermally reversible isomers. Kurtikyan *et al.* observed that at 20 K the IR spectrum was dominated by the 1739 cm^{-1} band (Fig. 1.29). However, upon warming the cooled sample from

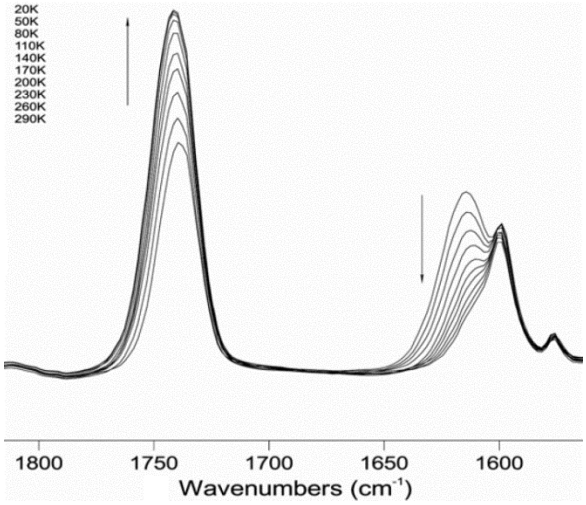

Figure 1.29. Temperature dependence of the (TPP)Mn(NO) FTIR spectra. Temperature was recorded in 30 K intervals from 20 to 290 K. *Figure reproduced from Ref.*[138] *with permission of the Royal Society of Chemistry.*

20 to 298 K the intensity of the 1614 cm^{-1} band decreased in the IR spectrum. Thus, the spectrum of the sample at room temperature showed a mixture of five-coordinate (TPP)Mn(NO) linkage isomers; the previously characterized linear isomer (TPP)Mn(η^1-NO) (1739 cm^{-1}) (Fig. 1.27)[71,137,163] and two other possible candidates, namely, either the bent η^1-NO or the η^1-ON configuration of (TPP)Mn(NO) giving rise to a ν_{NO} 1614 cm^{-1} band. Although, the η^2-NO isomer

is also a possible configuration, the observed IR spectrum and isotopic shifts did not correlate with the expected IR bands. In fact, earlier DFT calculations carried out by Wondimagegn and Ghosh on (por)Mn(NO) placed the η^2-NO isomer 1.67 eV higher than the η^1-NO isomer[71] thus disfavoring the η^2-NO isomer formation under this experimental conditions although it may have been formed in undetectable amounts.

In order to assign the correct configuration displaying the ν_{NO} = 1614 cm^{-1} band, Kurtikyan *et al.* then carried out DFT calculations for the gas phase (P)Mn(NO) and (P)Mn(ON) (P^{2-} = porphinato dianion) systems with linear and bent structures in the singlet, triplet and quintet spin states.[138] Data obtained using spin unrestricted BP86/TZVP, TPSS/DGDZVP and PBE/DGDZVP levels of theory without symmetry constraints showed that the linear *N*-bonded configuration in the singlet spin state gave the lowest energy, and the bent η^1-N in the triplet state gave the second lowest energy of 7-9 kcal mol^{-1} higher than the former. The triplet state with the linear NO also converged with energy ca. 13 kcal mol^{-1} higher than the singlet state. In addition, the calculated difference of NO stretch between the linear and bent, $\Delta\nu_{NO}$(calc.) and the difference obtained experimentally, $\Delta\nu_{NO}$(exp.) were comparable, with the former being ~120 cm^{-1} and the latter 125 cm^{-1}. Furthermore calculations with the Turbomole 6.3 program package [164] were used to confirm that the linear singlet was the lowest in energy, although the experimental energy difference (~1 kcal mol^{-1}) between the two observed species differed substantially from the calculated energy difference (7-9 kcal mol^{-1}) between the linear singlet and the bent triplet configurations.

Fig. 1.30 shows the molecular orbitals diagram and structure of (P)Mn(NO) in the singlet state and the structure in the triplet state. The Mn−NO bond involves a strongly covalent π-interaction between the Mn ($3d_{xz}$,$3d_{yz}$) orbital and the π* orbital of

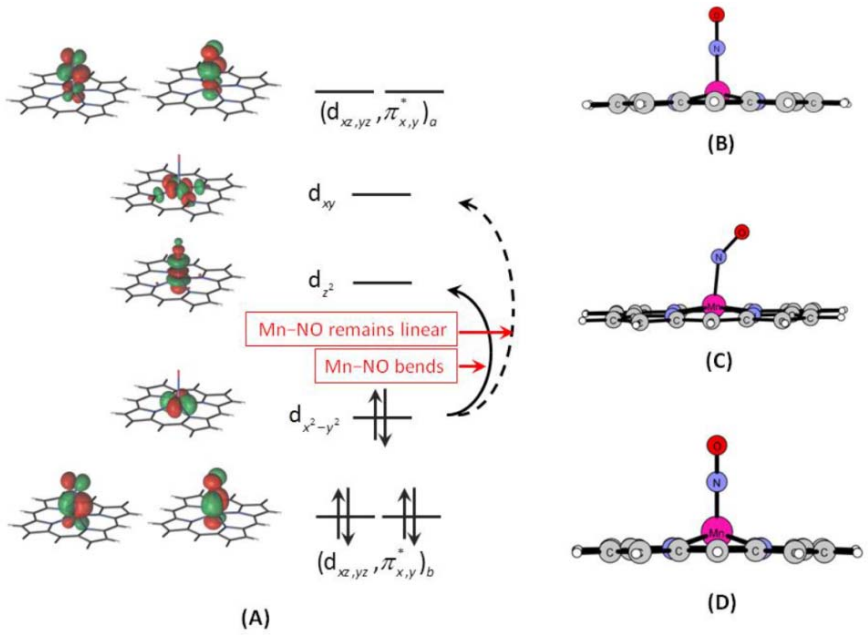

Figure 1.30. (A) Molecular orbital diagram of Mn(P)(NO) in its (S=0) state. Electronic transitions leading to two possible (S=1) states are indicated. (B) Structure of the (S=0) state; (C) Structure of the (S=1)$(d_{x^2-y^2})^1(d_{z^2})^1$ state; (D) Structure of the (S=1)$(d_{x^2-y^2})^1(d_{xy})^1$ state. *Reproduced from ref.* [138] *(supporting information) with permission of the Royal Society of Chemistry.*

NO to give the strongly delocalized bonding $(d_{xz,yz},\pi_{x,y}^*)_b$ (doubly occupied) and antibonding $(d_{xz,yz},\pi_{x,y}^*)_a$ (unoccupied) MOs, respectively.[138] In the linear configuration, σ-donation from NO into the Mn $3d_{z^2}$ orbital was observed to destabilize the unoccupied $3d_{z^2}$ orbital. Also, the $3d_{xy}$ orbital was found to be destabilized by σ-antibonding interaction with the four porphyrin nitrogens. Consequently, the nonbonding $3d_{x^2-y^2}$ orbital is doubly occupied in the singlet state. The DFT

calculations provided the linear singlet state configuration structure as shown in Fig. 1.30 B. Further calculations were carried out for the two other triplet states. After the calculations for the two triplet states the following deductions were made:

1. Transfer of one non-bonding $3d_{x^2-y^2}$ orbital electron into the σ-antibonding $3d_{xy}$ caused electron redistribution in the equatorial plane leading to the linear M−NO configuration.

2. Transfer of one non-bonding $3d_{x^2-y^2}$ electron into the σ-antibonding $3d_{z^2}$ orbital such that in removing the antibonding character (due to populated $3d_{z^2}$) the Mn−NO bond bends with concomitant decrease in overlap with NO σ-orbitals.

As it turned out, the linear triplet state structure was observed to occur at the highest energy. Thus, both experimental and theoretical data point towards the linear isomer and the bent isomer. Recent DFT calculations and NBO analysis of the Mn−NO bonding in (por)Mn(NO) showed that the Mn−N(O) bond has a triple bond character (Fig. 1.31) with a charge donation from NO to Mn.[165] This probably explains why the

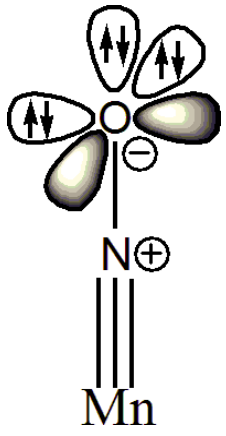

Figure 1.31. Schematic representation of the bonds in (por)Mn(NO). *Redrawn with permission from Ref.* [165]

linear (TPP)Mn(NO) complex is observed at lower temperature but some of it converts to the bent isomer at relatively high temperature. The calculations by Jaworska also showed that the oxygen atom is more negative and the nitrogen atom is more positive than in the free NO and these are factors supporting the linear Mn−N−O linkage in (TPP)Mn(NO).[165]

Earlier investigations by Martirosyan *et al.*[140] on Mn(II) porphyrin mediated NO disproportionation at low temperature showed linkage isomerization in one of the by-products, namely (TPP)Mn(NO)(ONO), to its nitro-nitrosyl isomer (TPP)Mn(NO)(NO_2) (Fig. 1.27F and G). In their experiment, the five coordinate (TPP)Mn(NO) produced at 90 K after reaction of (TPP)Mn with NO reacted further with three more equivalents of NO to release N_2O. A probe of the mechanism of the reaction revealed that two of these NOs reacted with each other at low temperature to produce a "nearly neutral N_2O_2 ligand", and the latter then complexed with (TPP)Mn(NO) to form a seven-coordinate intermediate proposed to be (TPP)Mn(NO)(ONNO) in which NO is bound to Mn via N, and the neutral N_2O_2 ligand is bonded to Mn via the two oxygens (Fig. 1.27E) (ν_{NO}= 1820, $\nu_{(NO)2}$ =1712 cm^{-1}). Martirosyan *et al.* explained that NO attack on one of the oxygens of the coordinated ONNO in (TPP)Mn(NO)(ONNO) leads to the formation of (TPP)Mn(NO)(ONO) and consequent release of N_2O.[140] More importantly in this review, is the observation that the (TPP)Mn(NO)(ONO) species isomerized to the nitrosyl nitro isomer when the former was warmed from 130 K to room temperature. The IR spectra of the two isomers showed that the nitro-nitrosyl isomer had a relatively higher ν_{NO} band (1812 cm^{-1}) than the nitrito-nitrosyl isomer (1805 cm^{-1}) demonstrating the stronger σ-donation of the

nitrito group than the nitro group. It will be interesting to determine if the shift in IR bands compare with the Mn−N(O) lengths and to see whether there is the possibility of a bent Mn−N−O configuration in the X-ray structure at higher temperatures. It is interesting to note that the isomerization of (TPP)Mn(NO)(ONO) to (TPP)Mn(NO)(NO_2) at 200 K is an irreversible transformation. The (TPP)Mn(NO)(NO_2) formed readily converts to the five coordinate (TPP)Mn(ONO) at room temperature by a mechanism that is not well understood.

Unlike (TPP)Mn(NO), the five-coordinate (TPP)Mn(ONO) complex undergoes linkage isomerization to (TPP)Mn(NO_2) following laser flash photolysis of a toluene solution of (TPP)Mn(ONO).[166] The proposed mechanism involves the photoinduced dissociation of the axial ligand to (TPP)Mn and NO_2. (TPP)Mn and NO_2 then recombine to form (TPP)Mn(NO_2). The latter complex readily isomerizes back to the structurally characterized ground state (TPP)Mn(ONO) compound (Fig. 1.32).[48]

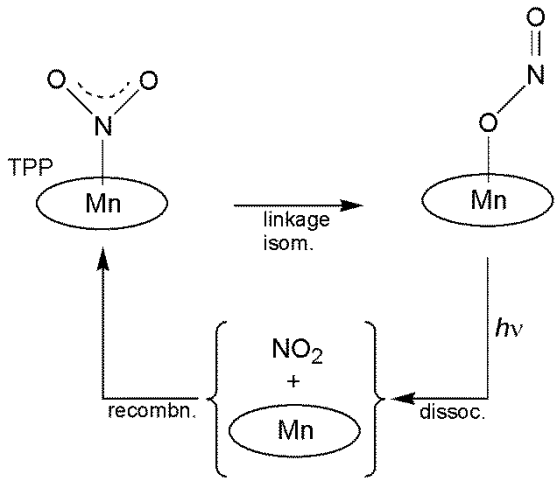

Figure 1.32. Proposed mechanism for photoinduced linkage isomerization reactions of toluene solution of (TPP)Mn(ONO).[8] *Reproduced with permission from Ref.* [8] *Copyright 2010 American Chemical Society.*

1.3.2 Ruthenium and iron NO_x porphyrin complexes

The group 8 transition metal NO_x porphyrin complexes are arguably some of the most widely studied biologically relevant heme models. Several review articles on NO_x-coordinated metalloporphyrins were published in the last decade.[8,14,137,156,167-169] The complex (por)Fe(*O*-ligand), for example is a prosthetic group in heme catalase, an enzyme known to catalyze the dismutation of hydrogen peroxide to water and oxygen.[170] Heme catalase is however, inhibited by NO.[171] In order to understand the inhibition mechanism of NO in catalase, structural models of the neutral NO-inhibited catalase active sites containing varying axial *O*-bound ligands have been prepared and characterized for some $\{MNO\}^6$ complexes including (TTP)M(NO)(O-*i*-C_5H_{11}) (M= Ru, Os) [172], (T(*p*-OMe)PP)Ru(NO)(OY) (Y= C_6HF_4, C(=O)CF_3),[173] (OEP)Os(NO)(OR) (R=Et, *i*-pr, hexyl, cyclohexyl).[174]

Both spectroscopic and X-ray data obtained for the six-coordinate ruthenium nitrosyl porphyrins mentioned above reveal that NO is bound to Ru via the N. However, upon subjecting some of these compounds to light of the correct wavelength, different conformations of NO linkages may be generated. In this regard, Richter-Addo and Coppens reported the first spectroscopic evidence for the η^1-ON and η^2-NO linkage in nitrosyl metalloporphyrins, namely (OEP)Ru(NO)(O-*i*-C_5H_{11}) (OEP)Ru(NO)(SCH_2CF_3) , (OEP)Ru(NO)Cl and $[(OEP)Ru(NO)(py)]^+$.[39]

In their work, Richter-Addo and Coppens and coworkers subjected a KBr pellet sample of (OEP)Ru(NO)(O-*i*-C_5H_{11}) at 200 K to light ($330 < \lambda < 460$ nm) generated from a Xe lamp;[43] difference IR spectroscopy was used to identify the species generated (Fig. 1.33 a).

Richter-Addo and Coppens and coworkers observed new isotope-sensitive infrared bands at 1645 and 1497 cm^{-1} in the difference IR spectrum (Fig. 1.33a) when a

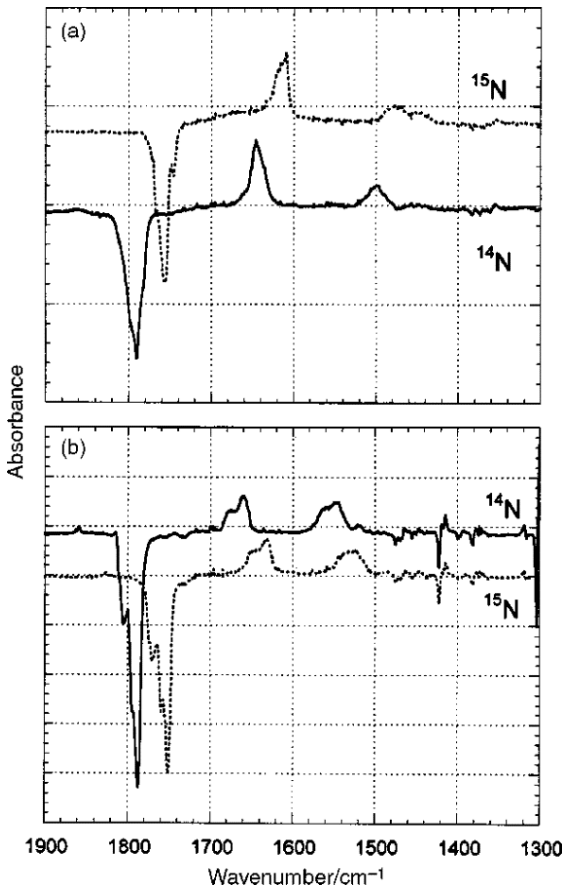

Figure 1.33. Difference spectra (spectrum after irradiation minus spectrum prior to irradiation for 15 min) for the ^{14}N and ^{15}N labeled compounds (a) (OEP)Ru(NO)(O-*i*-C_5H_{11}) and (b) (OEP)Ru(NO)(SCH_2CF_3). The bimodal structure of some of the shifted bands is attributed to crystalline disorder and two possible orientations of the NO group. Conversion percentages are estimated as 1 and 1.5% for (a) and (b), respectively. *Reproduced from ref.* [39] *with permission of the Royal Society of Chemistry.*

KBr sample of (OEP)Fe(NO)(O-*i*-C_5H_{11}) at 20 K was subjected to irradiation. The two bands at 1645 and 1497 cm^{-1} were assigned to ν_{NO} for the metastable η^1-ON and η^2-NO isomers of (OEP)Ru(NO)(O-*i*-C_5H_{11}), respectively (Fig. 1.33 a). The metastable isomer formation was observed to be temperature dependent. The η^1-ON isomer in

(OEP)Ru(NO)(O-*i*-C_5H_{11}) is observable up to a temperature of 160 K, whereas the η^2-NO isomer is observable only below 80 K. The two metastable isomers reverted to the ground state η^1-NO on warming the sample back to room temperature. Only 1% of the starting (OEP)Ru(NO)(O-*i*-C_5H_{11}) was estimated to be converted to the two metastable isomers.

Similar metastable linkage isomers were observed in (OEP)Ru(NO)(Cl), $[(OEP)Ru(NO)(py)]^+$ and (OEP)Ru(NO)(SCH_2CF_3). In the latter complex, irradiation of a KBr sample with light at 60 K gave two products identified as (OEP)Ru(η^1-ON)(SCH_2CF_3) (ν_{NO} = 1660 cm^{-1}) and (OEP)Ru(η^2-NO)(SCH_2CF_3) (ν_{NO} = 1546 cm^{-1}) (Fig. 1.34 b) in their difference IR spectrum.[39] As in the case of the (OEP)Ru(NO)(O-*i*-C_5H_{11}) complex, a low percent conversion of 1.5 % of the (OEP)Ru(NO)(SCH_2CF_3)

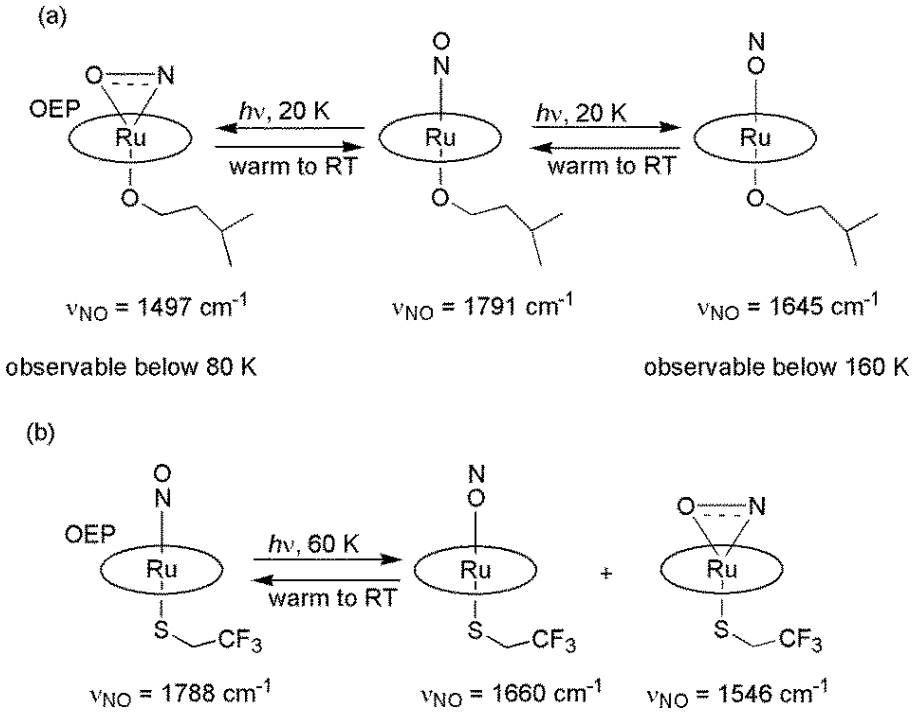

Figure 1.34. Formation of the η^1-ON and η^2-NO isomers in some six coordinate ruthenium nitrosyl porphyrins. (a) (OEP)Ru(NO)(O-*i*-C_5H_{11}) and (b) (OEP)Ru(NO)(SCH_2CF_3).

complex was estimated during its conversion to its corresponding metastable isomers.

DFT calculations on a model of the six coordinate (P)Ru(η^2-NO)Cl (S = 0) shows asymmetry in the Ru(η^2-NO) moiety (Fig. 1.35a).[71,175] In Fig. 1.35, if the Ru(η^2-NO) plane were defined as *xz* then in the HOMO-4 the Ru d_{xz} orbital can be envisioned to effectively π-bond with the NO π* orbital in the *xz* plane. Ghosh and Wondimagegn observed that the HOMO-3 revealed that the Ru d_{yz} orbital only π-bonds with one end of the NO π* orbital via the nitrogen end causing the unsymmetrical nature of the Ru−η^2-NO geometry.[175]

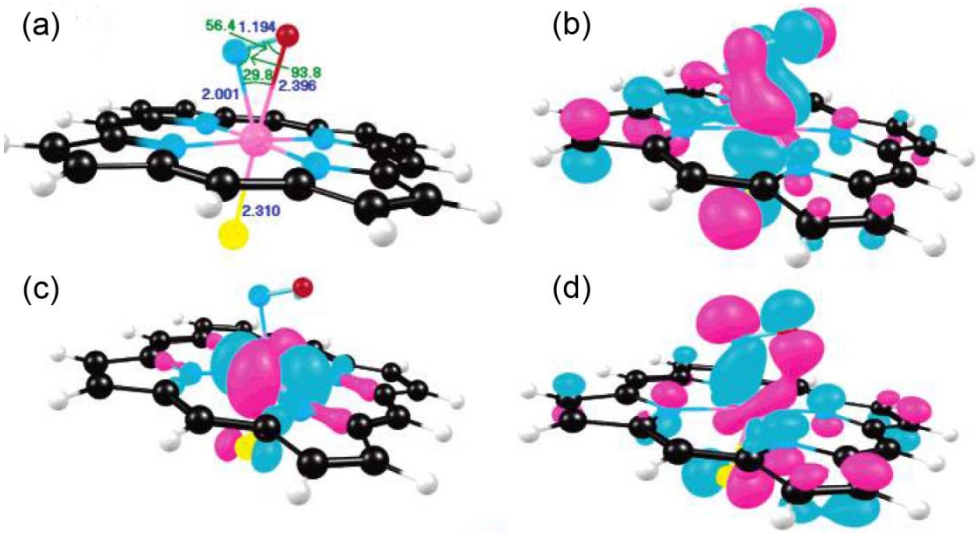

Figure 1.35. (a) optimized structure (Å, °; (b) - (d)) the three primary Ru 4d-based MOs of (P)Ru(NO)Cl (S = 0). *Adapted with permission from Ref.* [175] *Copyright 2005 American Chemical Society.*

In another report, Cheng *et al.* observed the first photoinduced linkage isomers of two (por)Fe(NO) complexes (por = OEP, TTP).[43] The (por)Fe(NO) is a $\{MNO\}^7$ system and as such a bent Fe−N−O geometry would be expected for the ground state η^1-NO isomer. Crystal structures of (TPP)Fe(NO),[176] (T_{piv}PP)Fe(NO),[177] (PPIX-

DME)Fe(NO),[178] and (OEP)Fe(NO),[179] for instance, show that each of these complexes possesses a bent Fe−N−O moiety. The five coordinate (OEP)Fe(η^1-NO) and (TTP)Fe(η^1-NO), however, were shown to undergo light-induced linkage isomerization to their corresponding isonitrosyl linkage isomers.

In their work, Cheng *et al.* subjected a KBr sample of (OEP)Fe(NO) (ν_{NO} of 1672 cm^{-1}) to light of wavelength $350 < \lambda < 550$ nm (300 W xenon arc lamp).[43] The difference IR spectrum of the resulting product displayed a new ν_{NO} band at 1532 cm^{-1} (Fig. 1.36). This band was assigned to the (OEP)Fe(η^1-ON) isomer where NO is bonded to Fe via the O atom (Fig. 1.37).

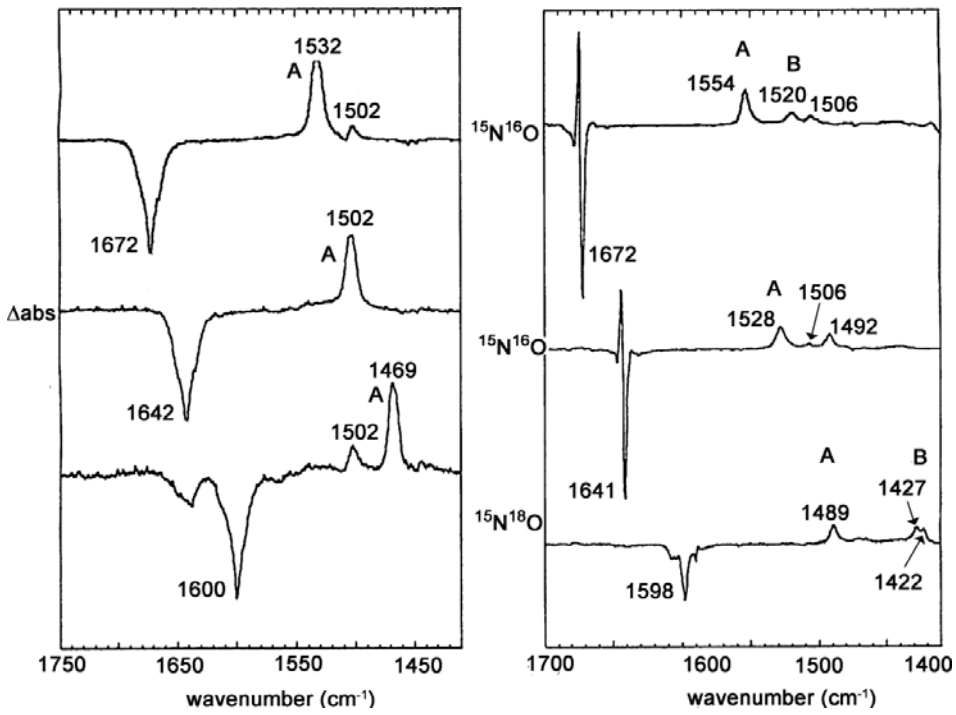

Figure 1.36. Infrared difference spectra formed by subtracting the spectra of the complex after illumination (at 25 K) from the infrared spectra of the complex in the dark. (Left) (TTP)Fe(NO); (right) (OEP)Fe(NO). Negative and positive features represent IR bands that are depleted, or new or increased in intensity upon illumination, respectively. The differential feature of the highest frequency band of (OEP)Fe(NO) is due to a slight change in peak profile. *Reproduced with permission from Ref.* [43] *Copyright 2000 American Chemical Society.*

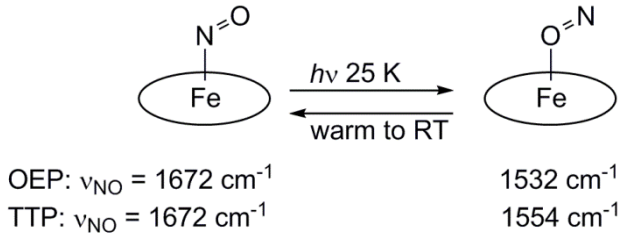

Figure 1.37. Formation of the η^1-*O*N isomers of (OEP)Fe(NO) and (TTP)Fe(NO).[43]

In the (TTP)Fe(NO) sample (ν_{NO} of 1672 cm^{-1}) a new IR band at 1554 cm^{-1} was observed in the difference spectrum when (TTP)Fe(NO) was irradiated with light of similar wavelength and the new band was assigned to the ν_{NO} of the *O*-bound isonitrosyl group in (TTP)Fe(NO). Importantly, the shifts in the ν_{NO} of both (OEP)Fe(NO) and (TTP)Fe(ON) were also observed to be isotope sensitive. Ford proposed a mechanism of this isomerization process which suggests the formation of a caged pair intermediate involving (por)Fe and NO as shown in Fig. 1.38.[168]

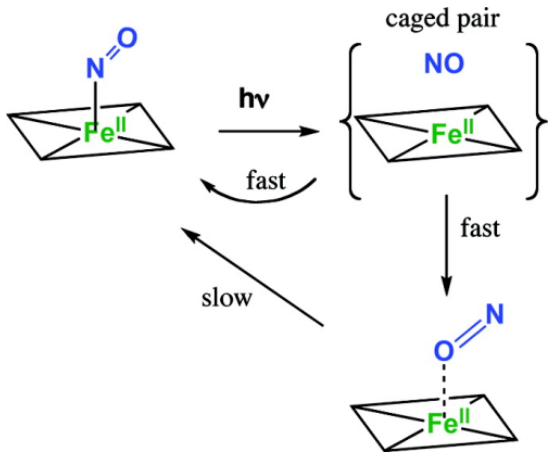

Figure 1.38. Likely scenario for the photochemical formation of the isonitrosyl complex Fe(TPP)(ON) in a solid or low-temperature matrix. The rectangle represents a porphyrinato ligand. *Reproduced with permission from Ref.* [168] *Copyright 2010 American Chemical Society.*

It is important to note that only small fractions of the metastable species were generated in this experiment. In addition, some theoretical calculations performed on a (P)Fe(NO) system indeed showed that the metastable (P)Fe(η^1-ON) was a likely linkage isomer and it corresponded to a local minimum with energy of 1.59 eV above the ground state (P)Fe(NO) complex.[43]

The metastable species generated during the photolysis of the six coordinate (TPP)Fe(NO)(NO_2) complex have been investigated by Coppens and Richter-Addo.[58,180] In their work, they irradiated a KBr sample of the nitro-nitrosyl iron tetraphenylporphyrin complex, (TPP)Fe(NO)(NO_2) with light at different experimental temperatures and observed that new metastable species were generated. Fig. 1.39 shows a schematic diagram for their experiment. Two linkage isomers of (TPP)Fe(NO)(NO_2),

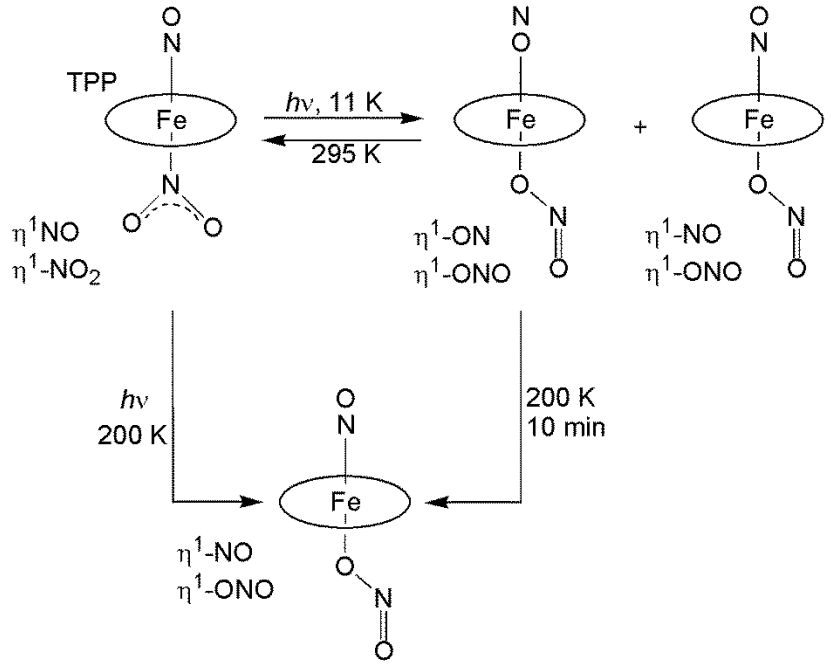

Figure 1.39. Photoinduced isomerization of (TPP)Fe(NO)(NO_2) at different temperatures

namely, the nitrito-nitrosyl complex (TPP)Fe(NO)(ONO), and the nitrito-isonitrosyl complex (TPP)Fe(ON)(ONO) were both observed when the sample was cooled to 11 K and irradiated with light. The assignments of the two metastable species were made based on infrared spectral data. The ground state complex, (TPP)Fe(NO)(NO_2) displayed ν_{NO}, ν_{as}, ν_s, and $\delta_{(ONO)}$ bands at 1883, 1464, 1303 and 806 cm^{-1}, respectively.

The difference IR spectrum obtained for the photogenerated species displayed bands at 1510 and 935 cm^{-1} which were assigned, respectively to ν_{as} and ν_s of the coordinated ONO group in (TPP)Fe(NO)(ONO). In addition a new IR band was observed at 1699 cm^{-1}, and was assigned to the coordinated isonitrosyl group in (TPP)Fe(ON)(ONO). Interestingly, the 1699 cm^{-1} band persisted in the IR spectrum up to a temperature of 50 K. It was observed that the nitrito-nitrosyl complex, (TPP)Fe(NO)(ONO) was exclusively produced after the photo-generated isomers at 11 K were warmed to 200 K, suggesting a change in binding mode from η^1-ON to η^1-NO. Also worthy of note is the fact that only one isomer, namely, the nitrito-nitrosyl isomer (TPP)Fe(NO)(ONO) was generated when the ground state isomer at 200 K was irradiated with light. This suggests that the double linkage isomerization species is the less stable of the metastable species.

To probe further, DFT calculation for model compounds in the gas phase were performed. In all, ten different conformations were explored and were categorized based on the mode of binding of the axial ligands and the orientation of the axial ligands relative to each other. In the first category, two different conformations of the ground state isomer converged in which NO_2 and NO are in the same axial plane (GS$\parallel$) or where NO_2 and NO are perpendicular to each other (GS$\perp$) (Fig. 1.40).

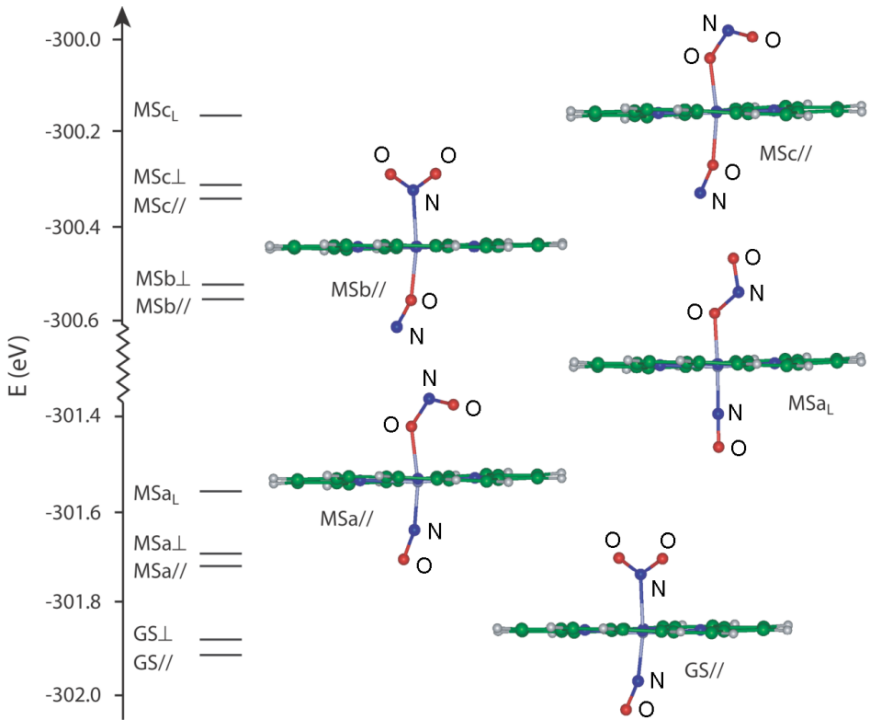

Figure 1.40. Calculated energies and representative structures for the linkage isomers of (porphine)Fe(NO)(NO_2). The axial nitrogen and oxygen atoms are colored blue and red, respectively. ‖ = axial ligand planes are coplanar; ⊥= axial ligand planes are mutually perpendicular. MSa_L and MSc_L are the isomers displaying linear FeNO and FeON groups, respectively. *Reproduced with permission from Ref.* [180] *Copyright 2004 American Chemical Society.*

In the second category, three different nitrito-nitrosyl metastable isomers were observed as MSa‖, MSa⊥, and MSa_L. In the latter conformation the FeNO moiety is linear. The third category is the single linkage isonitrosyl isomer where two conformations are possible (MSb‖ and MSb⊥). In the final category, three double linkage isomerization isomers, namely MSc‖, MSc⊥ and MSc_L conformations were obtained. These isomers have both NO and NO_2 bound to Fe via oxygen. As depicted in Fig. 1.40 the MSc metastable isomers were the highest in energy, followed by MSb and then MSa. This ranking parallels the experimental data which suggests that the nitrito-

nitrosyl metastable isomer is more stable (stable at 200 K) than the nitro-isonitrosyl metastable isomer (stable at 50 K). It is necessary to point out that in each category the most stable conformation were those that had the axial planes coplanar to each other. In general, the double-linkage isomer conformations were the highest in energy and were calculated to be 1.58 eV higher than the corresponding ground state conformation. This value is comparable to the 1.59 eV energy difference computed for the η^1-NO-to-η^1-ON linkage isomerism in (P)Fe(NO).

1.3.3 Cobalt NO_x porphyrins

Vitamin B_{12}, the cobalt containing corrin complex, is a natural biologically relevant enzyme. Vitamin B_{12} is known to play an important role in the enzymatic reactions involving Co−C bond breaking and bond making.[181,182] However, some of these enzymatic reactions are inhibited by NO_x molecules.[183-188]

Cobalt porphyrin complexes are usually employed as synthetic models for vitamin B_{12} because of their ease of synthesis and the ability to obtain unambiguous structural and spectroscopic data. Some of the (por)Co complexes themselves are known to play important roles in the activation and reduction of NO. For example, [(2-TMPPyP)Co]$^{5+}$[189] and (TPP)Co supported on TiO_2[190,191] have been used as catalyst for the reduction of NO

The five-coordinate nitrosyl porphyrin complexes, (por)Co(NO) [por = OEP,[192,193] TPP,[194-196] TTP,[154] T(*p*-OMe)PP, T(*p*-CH_3)PP, T(*m*-OCH_3)PP), T(*p*-OCF_3)PP, T(*p*-CF_3)PP and T(*p*-CN)PP[197]] are known.

Laser photolysis of (OEP)Co(NO) and (TPP)Co(NO) in 2-methyltetrahydrofuran solution revealed that these porphyrin complexes underwent denitrosylation[198] and no linkage isomeric intermediates of (por)Co(NO) were reported, although available kinetic data does not preclude Co−NO geometry isomerism.[199] To date, there is no report on the observance of either of the two other metastable forms (η^1-NO and η^2-NO) of (por)Co(NO). However the known five coordinate (TPP)Co(NO_2) complex readily linkage-isomerizes to the nitrito species, (TPP)Co(ONO) when benzene solution of the former was photoexcited with a 50 *n*s laser.[200] The isomerization is reported to occur by an intermolecular process as follows (Fig. 1.41).

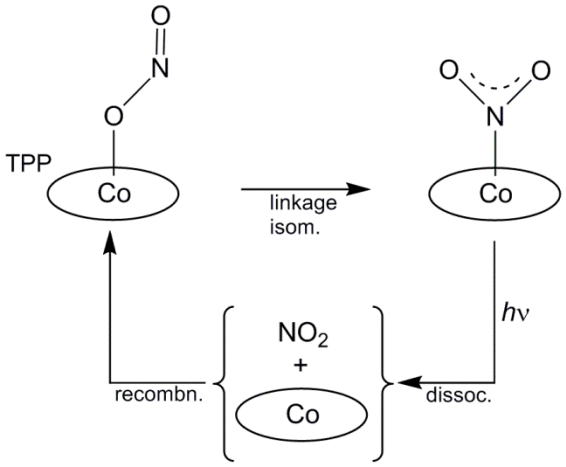

Figure 1.41. Proposed mechanism for linkage isomerization reactions after photolysis of benzene solution of (TPP)Co(ONO). *Reproduced with permission from Ref.* [8] *Copyright 2010 American Chemical Society.*

First, the photoexcitation of (TPP)Co(NO_2) causes cleavage of the Co−NO_2 bond leading to complete separation of NO_2 and (TPP)Co (Eq. 1.5) (TPP)Co and NO_2 then recombine to form the five coordinate nitrito (TPP)Co(ONO) complex (Eq. 1.6).[200]

$(TPP)Co^{III}(NO_2) + h\nu \rightarrow (TPP)Co + (NO_2)$ (complete separation) **(1.5)**

$(TPP)Co^{III} + (NO_2) \rightarrow (TPP)Co(ONO)$ (recombination process) **(1.6)**

$(TPP)Co(ONO) \rightarrow (TPP)Co(NO_2)$ (linkage isomerization) **(1.7)**

Silaghi-Dumitrescu and coworkers have determined, using UBP86 and UB3LYP calculation with LANL2DZ and 6-32G** sets that, although the nitro-isomer is stable in all metal oxidation states, the nitrito-isomer in the $(P)Co(NO_2)$ (P = por, Pz) compound was more favored by lower metal oxidation states.[57] It was observed that the Co(III) complexes favored the nitro-isomer. However, between por and Pz complexes they observed that $(Pz)Co(NO_2)$ gave the most favored nitrito-compound possible due to the reduced size of the metal-chelating cavity of the porphyrazine macrocycle,[57] an indication of steric effects from the nitro group (Table 1.2).

Table 1.2. Linkage isomers of some NO_x porphyrin complexes and their structural/ IR (KBr, unless otherwise stated) spectroscopic data. GS = ground state; ^{L} linear; ^{B} bent; ^{a} Nujol; ^{b} CsI; ^{c} ligand that isomerizes.

Compound (GS)	η^1-NO_x	η^1-O_xN or η^1-NO_x	η^2-NO	∠M-N-O / ° for GS [references]
	$\nu(NO_x)$(cm^{-1}) [references]	$\nu(NO_x)$ (cm^{-1}) [references]	ν(NO) (cm^{-1}) [references]	
(TPP)Mn(NO)	$1760^{L,a}$ or 1739^{L}, $1614^{B,L}$[138]			
(TPP)Mn(NO)-(ONO^{c})	1812,1480, 971 [139,140]	1805, 1421, 1304 [140]		
(OEP)Ru(NO)-(O-*i*-C_5H_{11})	1791 [39]	1645 [39]	1497 [39]	
(OEP)Ru(NO)-(SCH_2CF_3)	1788 [39]	1660 [39]	1546 [39]	
(OEP)Fe(NO)	1672 [43]	1532 [43]		144.4(2), 142.74(8) [179]
(TPP)Fe(NO)	1672 [43]	1554 [43]		149.2(6) [176]
(TPP)Fe(NO)-(NO_2^{c})	1883, 1464, 1303 [180]	1510, 935 [180]		

1.3.4 Hyponitrite complexes of transition metal porphyrins

The metal-mediated two-electron reduction of NO to the less toxic species N_2O (Eq. 1.8), N_2 and ammonia in the global nitrogen cycle by bacteria and fungi, or in catalytic converters in automobiles has received a great deal of attention.

$$2NO + 2H^{+} + 2e^{-} \longrightarrow N_2O + H_2O \qquad \textbf{(1.8)}$$

Several review articles on this process, and the effects of NO_x in the environment and on biological systems have recently been published.[21,201-203] In bacteria nitric oxide reductases (NOR) (i.e. the enzyme responsible for the reduction of NO), for instance, the enzymatic active site is composed of a bimetallic iron center; a heme iron center in close proximity with a nonheme iron center, and both centers are known to work coherently in the reduction of NO to N_2O. Three mechanisms; namely, the *cis-heme* b_3 mechanism, the *cis-*Fe_B mechanism and the *trans* mechanism (Fig. 1.42) have been suggested as possible pathways for this reduction process.[204]

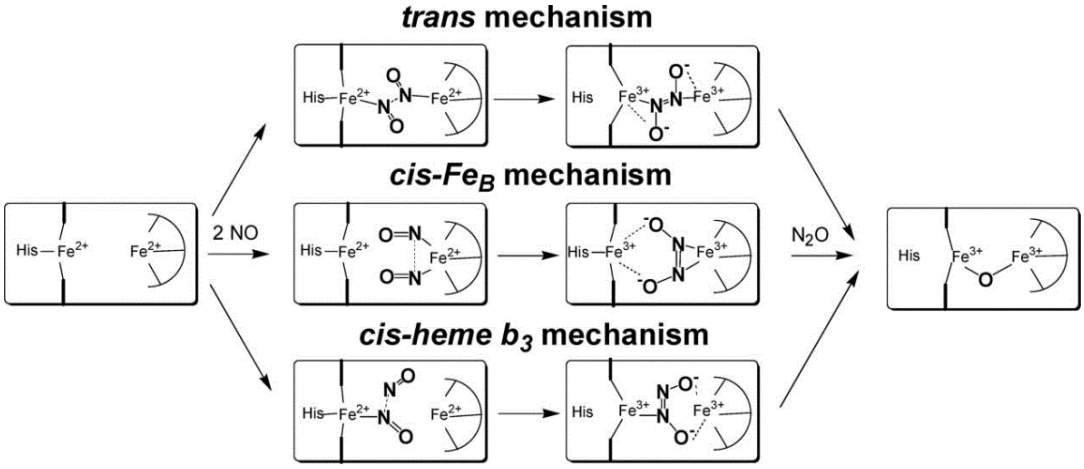

Figure 1.42. Putative mechanisms of nitric oxide reductase (NOR). General mechanisms involve: (i) initial coordination of NO at diiron center; (ii) coupling of two NO molecules (formation of a N−N bond) to form a hyponitrite intermediate, (iii) cleavage of an N−O bond and the release of N_2O.[204] *Reproduced from Ref.* [204] *with permission of The Royal Society of Chemistry.*

Each of the proposed mechanisms begins first by the coupling of two NO molecules by the two different iron centers (a heme iron center and a nonheme iron center) leading to the initial formation of a hyponitrite intermediate complex. The manner in which the diiron centers couple with the two NO molecules to form the

hyponitrite complex, and how this affects the breaking of the N−O has been a question of serious experimental and theoretical scrutiny. The N−O bond of the hyponitrite complex is proposed to be one of the bonds that break during NO reduction leading to the release of N_2O and H_2O.

In the *cis-heme b_3* mechanism model, it has been proposed that one NO molecule reacts with the heme iron center to form the $\{FeNO\}^7$ complex activating it for attack by a second free NO molecule to generate the *cis*-N bound Fe-hyponitrite intermediate complex (Fig. 1.43 A).[204] Reduction of the [Fe-N_2O_2] complex to the

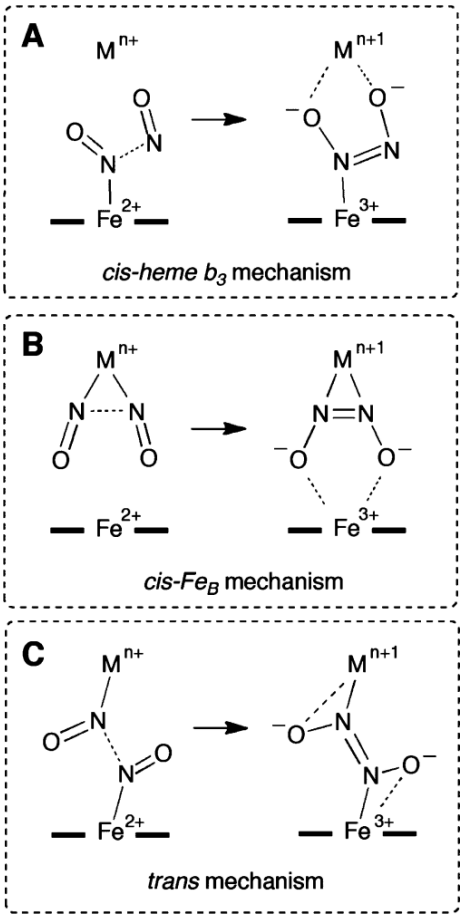

Figure 1.43. Intermediates in the three putative mechanisms for NO reduction by nitric oxide reductase. *Reproduced with permission from Ref.* [8] *Copyright 2010 American Chemical Society.*

hyponitrite ion followed by cleavage of one of the N−O bonds of the hyponitrite then results in the release of N_2O and H_2O as by-product. In the *cis-*Fe_B mechanism, however, the two NO molecules interact with the Fe of nonheme complex to generate the dinitrosyl nonheme complex. The dinitrosyl nonheme Fe complex formed then complexes with the heme-Fe^{3+} to generate the bimetallic intermediate in which the nonheme Fe coordinates with the hyponitrite on the nitrogens and the heme Fe coordinates at the two oxygens (Fig. 1.43 B). In contrast, in the *trans* mechanism each of the iron centers react with one NO molecule to form the $\{FeNO\}^7$ heme complex and the nonheme complex. Subsequently, the two $\{FeNO\}^7$ complexes couple via their nitrogens to generate the *trans* N-bound complex as shown in Fig. 1.43 C.[204]

Related to the mechanism of action of NOR on NO is the action of the heme copper oxidases (HCO) which is composed of a heme a_3 active site in close proximity to a copper active site.[205] The proposed mechanism of action of HCO in NO reduction entails an initial "fast binding" of one NO molecule to the His-heme a_3 site (**2** in Fig. 1.44) followed by another slow binding of the second NO molecule to the Cu_B center. These two NO-coordinated metal intermediate complexes couple together via the N of the coordinated NO molecules to generate (in the presence of H^+) the protonated hyponitrite bimetallic complex (**3** in Fig. 1.44).The generation of N_2O in this mechanism is promoted by another H^+ ion and H_2O is produced as a byproduct. Like the NORs the proposed hyponitrite complex in the HCO has been a subject of scrutiny. Recently, Varotsis and coworkers performed DFT calculations (B3LYP/6-31G*) on the hyponitrite ion complex models for which resonance Raman (RR) spectroscopy was used to identify key vibrational frequencies.[206] Vibrational bands at 626 and 1334 cm^{-1}

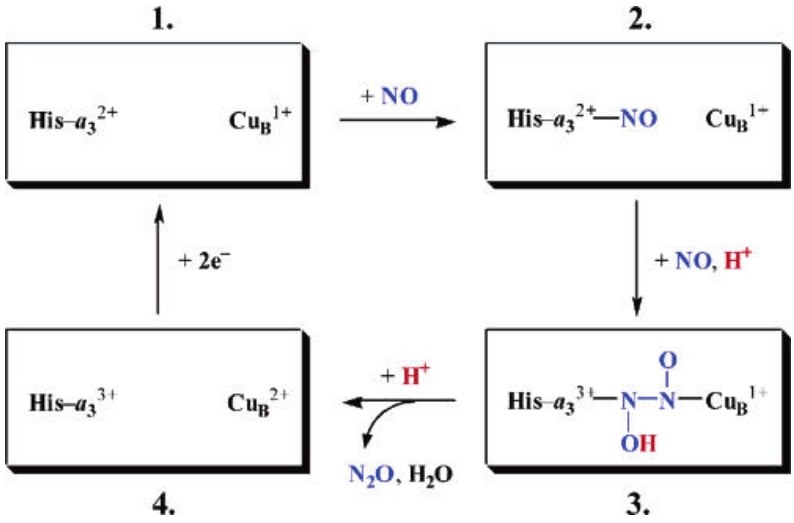

Figure 1.44. Proposed mechanism for the reduction of NO to N_2O by ba_3-oxidase. *Reproduced with permission from ref.* [207] *Copyright 2005 American Chemical Society.*

were observed in the calculated RR spectrum of the model complex and these were assigned to the heme a_3 Fe−N−OH bending and the N−N (in the mono-hyponitrite intermediate) stretching frequencies, respectively. The 1334 cm^{-1} band is lower than the reported 1392 cm^{-1} band observed in the Raman spectrum of $Na_2N_2O_2$ [208] suggesting a single N−N character in the proposed intermediate. Thus, a protonated hyponitrite intermediate complex (**3** in Fig. 1.44) is a likely intermediate in the NO reduction by HCO.

We note that in the proposed mechanism of action of NOR and HCO, one thing is common, namely, formation of the N−N bond via coupling of two NO molecules at a bimetallic center. In this regard we deem it worthwhile to digress and discuss briefly the chemical and electronic properties of the NO dimer (ONNO), and its reduced forms.

1.3.4.1 The nitric oxide dimer and its reduced forms

The neutral nitric oxide dimer, N_2O_2 is a diamagnetic molecule and is formed from nitric oxide in the condensed phase at low temperatures as shown in Eq. 1.9.

$$2NO \underset{}{\overset{\text{low temp}}{\rightleftharpoons}} N_2O_2 \qquad \textbf{(1.9)}$$

The NO dimer is unstable with an estimated binding energy of 2 kcal mol^{-1}[209] and can exist in the *trans* or the *cis* form (Fig. 1.45). Several experimental studies,

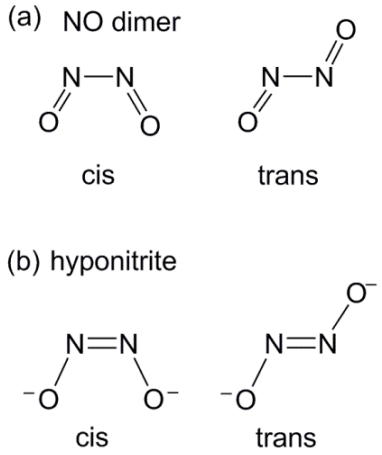

Figure 1.45. *cis* and *trans* (**a**) NO dimer, (**b**) hyponitrite dianion.

including gaseous infrared[210-212] and UV spectroscopic studies[213] show that the *cis*-ONNO isomer is the most stable form. The N−N bond length in the *cis*-ONNO has been calculated to be 1.77 Å[214] and 1.62 Å.[215] The experimental N−N bond length (2.263 Å) determined via rotational transition frequency for $^{14}NO–^{14}NO$, $^{15}NO–^{15}NO$ and $^{14}NO–^{15}NO$[210], and X-ray diffraction experiments (2.18 Å)[216] both show that this bond distance is longer than a N−N single bond (1.45 Å). The cause of lengthening of the

N−N bond in N_2O_2 was explained by Harcourt using *ab initio* valence bond calculation (STO-5G basis set).[217] The lengthening was associated with the strong repulsion between the lone-pair electrons on the sp^2 hybridized nitrogens.[217] Harcourt also explained that the orbitals that form the N−N σ-bond are mostly 2p in character and tend to orient at right angles to the N−O bond axes and this tends to affect the N−N bond length.

The reduced monoanion $(NO)_2^-$ and dianion $(NO)_2^{2-}$ forms of N_2O_2 have relatively different electronic and structural properties. For example, Snis and Panas have shown by DFT calculations that the N−N bond length decreases drastically on moving from the neutral to the monoanion and dianion hyponitrite (*cis*-NO dimer: 1.991 Å; *cis*-$N_2O_2^-$: 1.206 Å; and *cis*-$N_2O_2^{2-}$: 1.292 Å) with a corresponding increase in the N−N frequency.[218] The calculations by Snis and Panas is complemented by experimental results from Mckellar, Bohle and Felmann who observed N−N bond lengths of 2.2630(12), 1.256(2) and 1.20(3) for the neutral *cis*-N_2O_2, *trans*-$Na_2N_2O_2$ and *cis*-$Na_2N_2O_2$, respectively.[210,219-221] Furthermore, the *trans* isomer was found to be the most stable isomer of the dianion hyponitrites. Several hyponitrite salts have been prepared and isolated, and are known to be quite stable. The methods available for the preparation of hyponitrites are sparse in the literature. There are three main procedures for generating the hyponitrite salts of sodium (Fig. 1.46). In particular, the isomeric forms of $Na_2N_2O_2$ can be selectively prepared. The *cis*-$Na_2N_2O_2$ salt can be produced by reaction of sodium metal with nitric oxide in liquid NH_3, or by reacting Na_2O with N_2O at high temperatures.[220,222] The *trans*-$Na_2N_2O_2$ isomer is prepared by treating an aqueous $NaNO_2$ solution with sodium amalgam at 0 °C.[223,224] In fact, the sodium

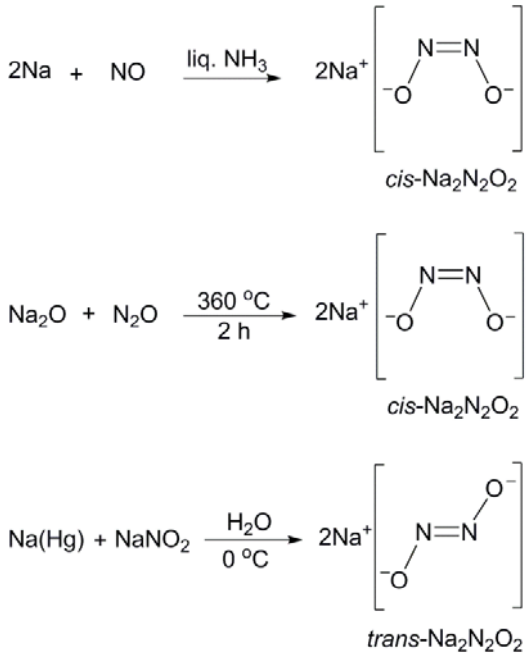

Figure 1.46. Preparation methods for *cis*-$Na_2N_2O_2$[220,222] and *trans*-$Na_2N_2O_2$.[223,224]

hyponitrite salts have been converted to other metal (Ag, Mg, Co, Pb) salts (Fig. 1.47 and Table 1.3).

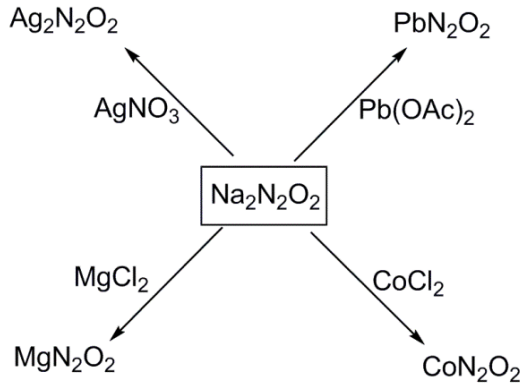

Figure 1.47. Preparation of other hyponitrite salts from $Na_2N_2O_2$.

Table 1.3. Vibrational spectroscopic data for some hyponitrite salts

Molecule	νN=N (cm^{-1})	ν_{as}N−O (cm^{-1})	ν_s N−O (cm^{-1})	δNNO (cm^{-1})	References
NO (in Ar)		1875[a]			36
Cis-N_2O_2 (gas)		1788[a]	1860[a]		211
trans-N_2O_2 (in CO_2)		1740[a]			225
trans-$Na_2N_2O_2$	1392[b]	1035[a]	958[b]	629[a]	208,222
cis-$Na_2N_2O_2$	1314[a]	1047[a]	830[a]		222
$Hg_2N_2O_2$		1138[a]		618[a]	208
MgN_2O_2		1051[a]	862[a]	585[a]	226
$Ag_2N_2O_2$		1058[a]		571[a]	208
PbN_2O_2		1128[a]	990[a]	683[a]	226
BaN_2O_2		*ca.*1015[a]	996[a]	*ca.* 515[a]	226
CoN_2O_2		1150 (br)[a]	896[a]	ca. 670[a]	226

[a] Infrared spectroscopy; [b] Raman spectroscopy. br = broad

To this end we have identified and categorized the preparation methods for hyponitrite compounds into three main categories depending on the number of nitrogen nitrogen atoms contributed by the different reacting molecules in the formation of the N−N bond (Table 1.4).

Table 1.4. Selected structural data for NO, the NO dimer, and sodium hyponitrite.

Molecule	N−N (Å)	N−O (Å)	N−N−O (°)	Ref
NO		1.15		36
cis-N_2O_2	2.2630(12)	1.1515(3)	97.17(5)	210
trans-$Na_2N_2O_2$	1.256(2)	1.3622(11)	112.14(9)	219
cis-$Na_2N_2O_2$	1.20(3)	1.40(3), 1.39(3)	119.8(2),119.2(4)	220,221

In the first category (**Category 1**) the hyponitrite complex is prepared from reaction between a molecule bearing only one nitrogen and another without a nitrogen atom. Examples include metal-mediated reduction of NO_x[227-232] or oxidation of hydroxylamine to hyponitrite.[233] In these reactions a transition metal complex plays a

role in coupling two NO molecules or activating one NO for attack by another NO molecule. In the second category (**category 2**) the hyponitrite complex is prepared from two or more molecules in which, at least each of the reacting molecules bears a nitrogen atom. Here, unlike **category 1**, no metal is involved. A typical example is the reaction between nitrous acid (or its derivative) with hydroxylamine (or its derivative).[234] In the third category (**category 3**), the hyponitrite compound is prepared from reactions in which at least one of the reacting molecules contains the two N atoms used in the formation of the hyponitrite N−N bond, or in which there is a direct transfer of the hyponitrite unit to another group. An example of **category 3** hyponitrite synthesis is the transfer of the hyponitrite unit in an organic diazenium diolate, hyponitrous acid or a hyponitrite salt to a metal.[219,235-237] Fig. 1.48 shows representative examples of the three categories of preparation of hyponitrite complexes.

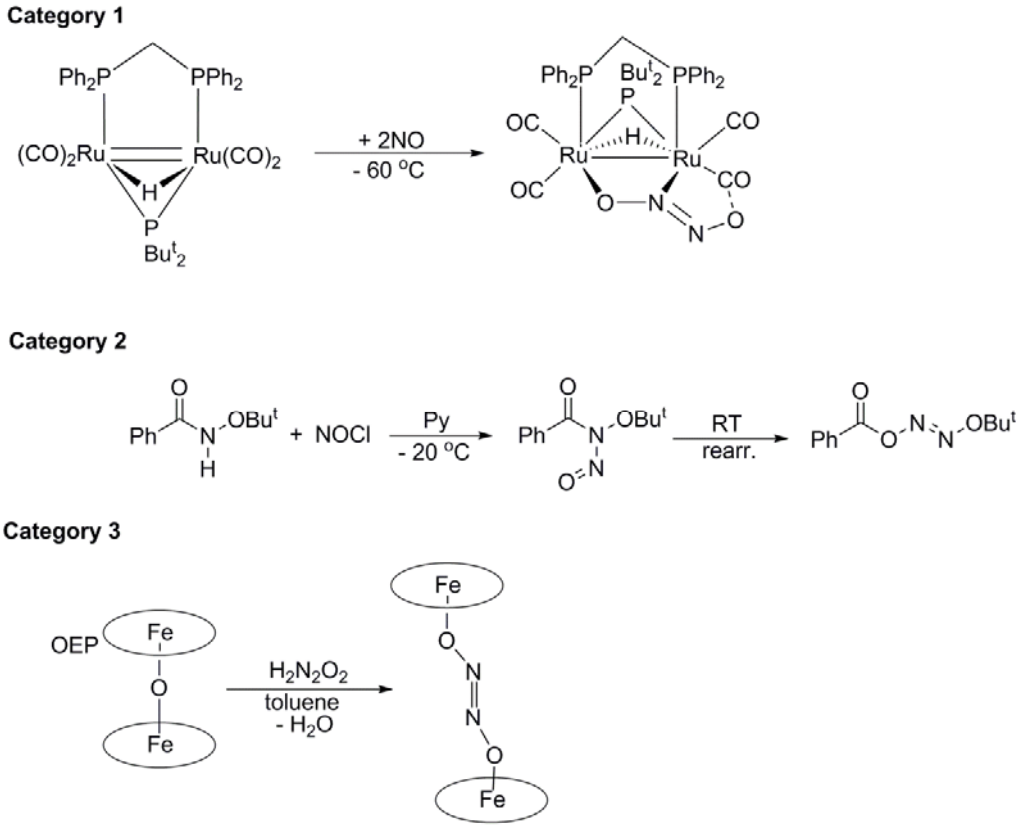

Figure 1.48. Representative examples of the three categories of preparation procedures for hyponitrite compounds. See text for explanation.

1.3.4.2 Metal hyponitrite binding modes

The first crystal structure of a transition metal hyponitrite complex was reported for the red $[(NH_3)_5Co(\mu\text{-}N_2O_2)Co(NH_3)_5]^{4+}$ complex by Hoskins *et al.*[238] in 1969 and vibrational spectra and redetermination of the X-ray structure was reported by Villalba, *et al.* in 2006.[239] The X-ray crystal structure of the $[(NH_3)_5Co(\mu\text{-}N_2O_2)Co(NH_3)_5]^{4+}$ complex shows the *cis*-hyponitrite binding mode (structure **B**, Fig. 1.49) where one Co metal is bound via N, and the other Co via O. Fig. 1.49 shows schematic representations of some structurally characterized metal hyponitrite binding modes in inorganic coordination compounds obtained by X-ray crystallography.

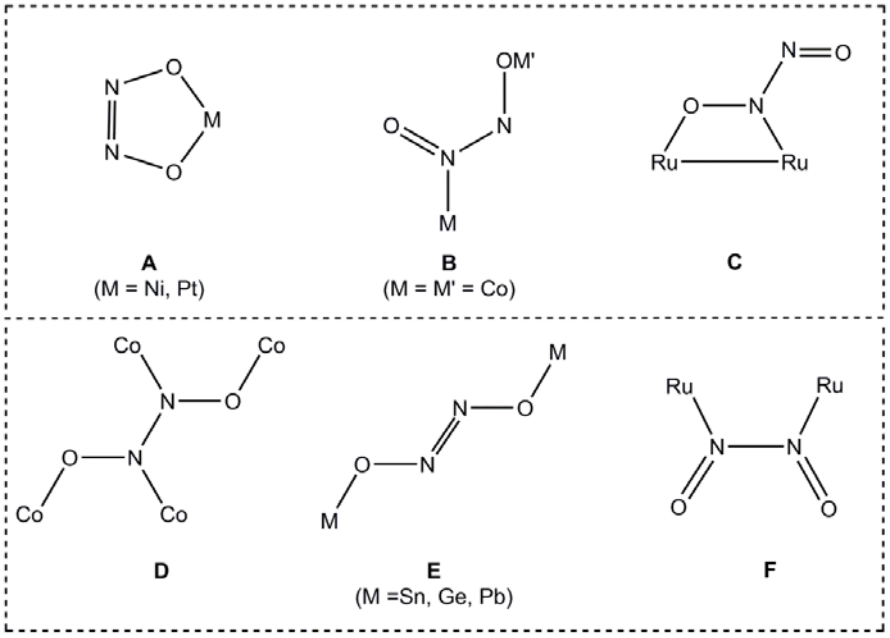

Figure 1.49. Structurally characterized metal hyponitrite binding modes in inorganic coordination compounds.

The X-ray structure of the *cis*-hyponitrite *O,O*-binding mode has been determined for $(PPh_3)_2Pt(N_2O_2)$,[236,240] and (dppf)Ni(N_2O_2).[235] Quite recently, Hayton and coworkers reported the crystal structure of the related (*bipy*)Ni(N_2O_2) complex which also possesses the *cis*-N_2O_2 moiety (structure **A**).[241] The crystal structure of the *trans*-hyponitrite N,O-binding mode (structure **C**) was reported by Böttcher and coworkers for the bimetallic ruthenium complex $Ru_2(CO)_4(\mu\text{-H})(\mu\text{-PBu}^t_2)(\mu\text{-X})(\mu\text{-}N_2O_2)$ (X = dppm[227], dppen, dpppha, dpppra, dppbza).[242] To date the crystal structure reported for the complex $[(NO)_2Co(\mu\text{-}NO_2)]_2(\mu\text{-}N_2O_2)$ remains the only example of metal complex possessing a hyponitrite ligand with the structure **D** linkage which was only isolated by Bau and coworkers at low yields.[243] It will be interesting to see the original spectroscopic data of this complex. Some examples of the structure **E** hyponitrite complexes include $[(OEP)Fe]_2(\mu\text{-ONNO})]$,[237] $[(PPh_3)_2Sn]_2(\mu\text{-ONNO})$,[244]

$[(PPh_3)_2Pb]_2(\mu$-ONNO), and $[(PPh_3)_2Pb]_2(\mu$-ONNO).[245] Table 1.5 shows selected structural data for these compounds.

Returning to the discussion on the reduction of NO to N_2O by the bimetallic active sites in the heme containing NORs and the HCOs, we note that although the mechanisms of these transformations have been vigorously studied experimentally, the elucidation of the reduction pathway still remains a challenging problem. DFT calculations by Varotsis and coworkers (discussed above) and other calculations performed by Blomberg and coworkers on the ba_3-type HCO[246] and the bacterial NOR model[247] continue to provide information on the viability of these mechanisms (Fig. 1.42).

Table 1.5. Selected structural data of some hyponitrite complexes. Structural data of some hyponitrite complexes.

Compound	N−O	N−N	M−O	M−N	∠N−N−O	∠M−O−N	∠M−N−N	∠M−N−O	Ref
$[(NO)_2Co(\mu\text{-}NO_2)](\mu\text{-}N_2O_2$	1.316	1.265	1.958	1.991	112.5	120.9			[243]
$[(OEP)Fe]_2(\mu\text{-}ONNO)]$	1.375(2)	1.250(3)			108.5(2)				[237]
$[(PPh_3)_2Sn]_2(\mu\text{-}ONNO)$	1.365(3)- 1.372(3)	1.231(5)-1.240(5)	2.062(2)-2.069(2)		110.8(3)-111.6(3)				[243]
$[(PPh_3)_2Pb]_2(\mu\text{-}ONNO)$	1.368(8)- 1.355(8)	1.246(9)	2.198(4)-2.188(5)		111.2(5)-112.4(5)	114.0(4)			[245]
$[(PPh_3)_2Ge]_2(\mu\text{-}ONNO)$	1.388(8)	1.225(8)	1.824(5)		108.5(6)	110.6(4)			[245]
$(PPh_3)_2Pt(N_2O_2)$	1.370(8)- 1.363(8)	1.230(9)-1.363(8)	2.013(4)-2.023(5)		118.9(7)-118.5(7)	112.3(5)			[236]
$(dppf)Ni(N_2O_2)$	1.400(6)- 1.385(5)	1.236(6)	1.820(4)-1.818(4)		115.4(4)-115.4(5)	112.2(3)-112.9(3)			[235]
$Ru_2(CO)_4(\mu\text{-}H)(\mu\text{-}PBu^t_2)(\mu\text{-}dppm)(\mu\text{-}\eta^2\text{-}ONNO)$	1.329(3)- 1.370(3)	1.265(3)	2.125(2)	2.014(2)	115.9[a] 110.1[a]	104.6[a]	124.7[a]	119.4[a]	[242]
$Ru_2(CO)_4(\mu\text{-}H)(\mu\text{-}PBu^t_2)(\mu\text{-}dppen)(\mu\text{-}\eta^2\text{-}N_2O_2)$	1.330(2)- 1.374(3)	1.267(3)	2.153(2)	2.020(2)	115.8[a]	103.7[a]	125.3[a]	118.8[a]	[242]
$Ru_2(CO)_4(\mu\text{-}H)(\mu\text{-}PBu^t_2)(\mu\text{-}dpppha)(\mu\text{-}\eta^2\text{-}N_2O_2)$	1.335(4)- 1.373(4)	1.260(4)	2.168(3)	1.993(3)	117.0[a]	103.0[a]	125.3[a]	117.6[a]	[242]
$Ru_2(CO)_4(\mu\text{-}H)(\mu\text{-}PBu^t_2)(\mu\text{-}dpppra)(\mu\text{-}\eta^2\text{-}N_2O_2)$	1.339(9)- 1.401(9)	1.268(10)	2.157(6)	1.989(8)	115.1[a]	102.6[a]	126.3[a]	118.6[a]	[242]
$Ru_2(CO)_4(\mu\text{-}H)(\mu\text{-}PBu^t_2)(\mu\text{-}dppbza)(\mu\text{-}\eta^2\text{-}N_2O_2)$	1.346(3)- 1.374(3)	1.260(3)	2.161(2)	2.005(2)	115.8[a]	103.0[a]	126.1[a]	118.1	[242]

[a] Data obtained from data file deposited at the CCDC website.

We would like to point out that following the report of the crystal structure of binuclear center in the NOR from *P. aeruginosa* (Fig. 1.50)[248] there now seems to be a much better precedence for clearly defining the mechanism of reaction at the bimetallic center of NOR. Blomberg and Siegbahn[249] recently performed quantum mechanical calculations (B3LYP and B3LYP*) of a model of the Fe and Cu binuclear active center

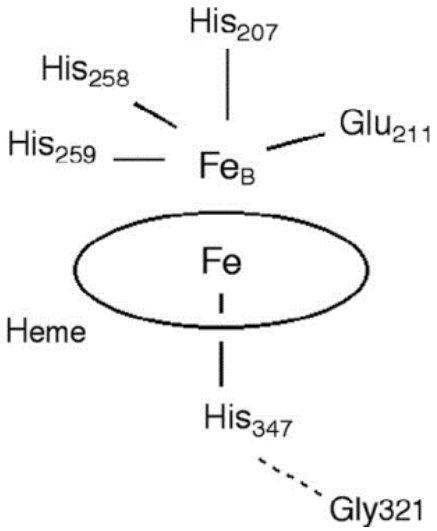

Figure 1.50. Sketch of the binuclear center in NOR from *P. aeruginosa*.[248]

in NOR from *P. aeruginosa* which strongly suggest the *cis*-b_3 mechanism. They calculated a barrier for the formation of the *cis*-hyponitrite intermediate heme complex to be 19.8 kcal mol^{-1} higher than the oxidized diiron active site; a value quite close to the estimated 16 kcal mol^{-1} value obtained experimentally.[250,251]

In related work, Richter-Addo and coworkers reported a DFT study on a mono-metal heme model system of the proposed mono-heme hyponitrite intermediate by calculating the effects of addition of an electron or a proton to a six-coordinate (P)Fe(NONO)(Im) system.[252] In their neutral (P)Fe(NONO)(Im) (theoretically obtained

by coupling via attack of NO on (P)Fe(NO)(Im)), two products, depending on the relative orientation of NONO and Im axial planes, namely $[(P)Fe(NONO)(Im)]_{\parallel}$ and $[(P)Fe(NONO)(Im)]_{\perp}$ were calculated to have similar energies. The calculated N−N bond distances obtained for the models compounds were 1.960 and 1.957 Å, respectively.

As indicated in Eq. 1.8, the reduction of NO to N_2O by NOR requires electrons and protons. To model the role of the transferable electron from the supposedly nonheme center, and the effect of the electron transfer on the geometry of the proposed hyponitrite complex through changes in bond distance and electron densities, Richter-Addo and coworkers subjected the anionic $[(P)Fe(NONO)(Im)]_{\perp}^{-}$ to theoretical calculations. Quite interestingly, the addition of one electron contributed in strengthening the N−N bond as evidenced by a decrease in the N−N bond distance in the neutral $[(P)Fe(NONO)(Im)]_{\perp}$, for instance, from 1.957 to 1.708 Å in the anionic $[(P)Fe(NONO)(Im)]_{\perp}^{-}$ structure. Yet this N−N = 1.708 Å bond length is relatively long and does not correspond with the expected ~1.45 Å bond length for an N−N single bond, or an N=N double bond in the hyponitrite complex.[8,253] This then poses a question on the role of the nonheme center in stabilizing the hyponitrite ligand in the complex and how this affects NO reduction. Blomberg and Sieghahn have performed some theoretical studies which supports the possibility that the nonheme Fe coordinates with the NO of the six-coordinate (heme)Fe(NO)Im complex via isonitrosyl linkage ((nonheme)Fe−O) bond = 2.19 Å), which then activates the bound NO for attack by a second NO molecule.[249]

Spin density diagrams of $[(P)Fe(NONO)(Im)]_{\perp}^{0}$ and $[(P)Fe(NONO)(Im)]_{\perp}^{-}$ (Fig. 1.51) obtained using (B3LYP/TZVP) revealed interesting observations. First, Richter-Addo and coworkers observed a greater localization of the highest occupied spin orbital

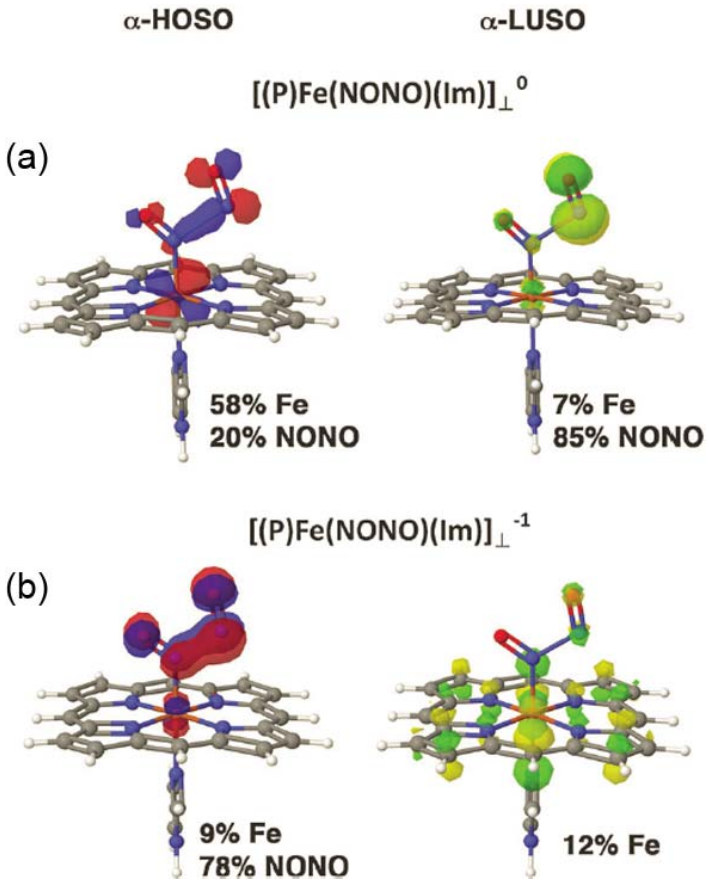

Figure 1.51. The highest occupied spin orbitals (α-HOSO) and lowest unoccupied spin orbitals (α LUSO) of the neutral $[(P)Fe(NONO)(Im)]_{\perp}$ (a) and the anionic $[(P)Fe(NONO)(Im)]_{\perp}^{-}$ (b) complexes. [252] *Reproduced from ref.* [252] *with permission from the Royal Society of Chemistry.*

(HOSO) of $[(P)Fe(NONO)(Im)]_{\perp}^{-}$ on the hyponitrite moiety with 78% NN bonding character with appreciable of 43% localized on the NN unit (Fig. 1.51 b left). Secondly, 9% Fe character was observed in the HOSO of the $[(P)Fe(NONO)(Im)]_{\perp}^{-}$. These two

observations led them to believe that the electron was added to the lowest unoccupied spin orbital (LUSO) of the precursor in Fig. 1.52a right.

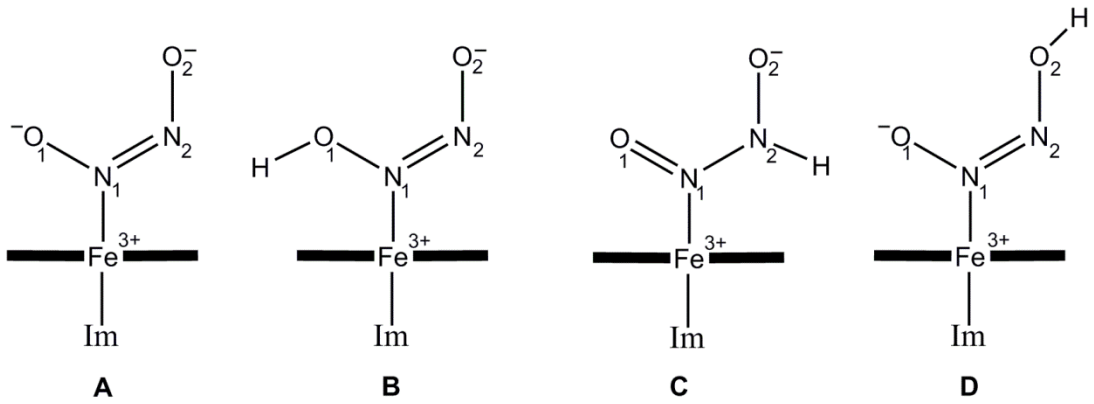

Figure 1.52. Sketches of the non-protonated $[(P)Fe(NONO)(Im)]_{\perp}^{-}$ (**A**) and their protonated products (**B**-**D**).

They then proceeded to determine the effects of addition of a proton to their $[(P)Fe(NONO)(Im)]^{-}$ system. There are three possible areas of proton: attack at O1, N2, or O2 which would lead to protonated products **B**, **C**, and **D**, respectively (Fig. 1.52).

Geometric optimization of the starting non-protonated anionic $[(P)Fe(NONO)(Im)]_{\perp}^{-}$ model and its corresponding protonated forms revealed an interesting observation. Firstly, the addition of a proton to any of the three possible protonation sites resulted in changes in the bond lengths (Fig. 1.52, Fig. 1.53 and Table 1.6). Protonation of the O1 atom saw a significant shortening of the N−N bond length from 1.708 Å to a bond distance (1.339 Å) between a single bond and a double bond. The "nitrosyl" (N1−O1) bond length increased by 0.204 Å to 1.421 Å and the N2−O2 bond length changed only by 0.035 Å. Clearly, the N1−O1 bond in the

[(P)Fe(NOHNO)(Im)]⊥ (**B**) has a single bond character. Addition of a proton to the uncoordinated N atom (N2) gave a complex **C** which was calculated to have a N−N

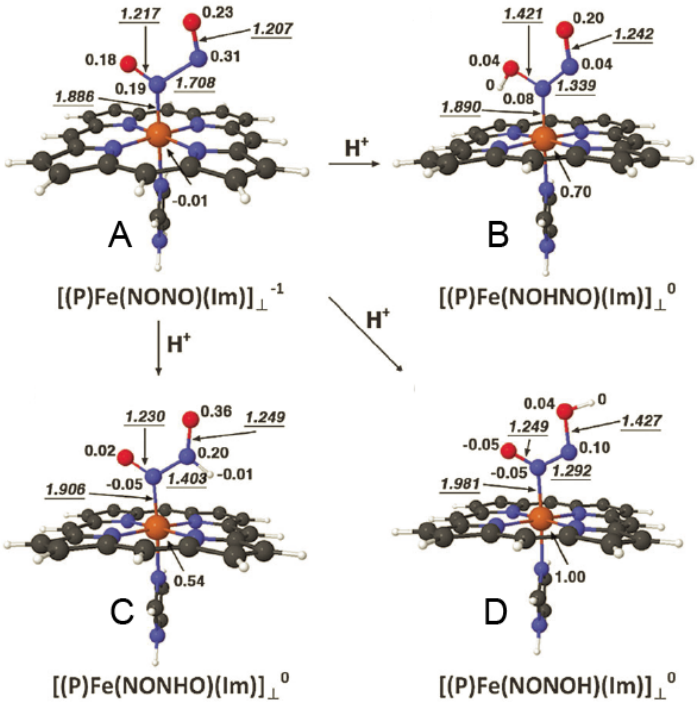

Figure 1.53. Calculated geometries and selected atomic spin densities (BP86/TZVP) of three products resulting from protonation of [(por)Fe(NONO)(Im)]⊥. Bond distances are in italics underline. *Reproduced from Ref.* [252] *with permission from the Royal Society of Chemistry.*

bond distance of 1.403 Å. Unlike **B**, there was only a small increase in the (N1−O1) (0.013 Å) to 1.230 Å and thus, exhibits a double bond character as depicted in Fig. 1.53 C. Protonation at O2 generated a product (**D**) which was observed to have the shortest N−N bond distance. Clearly, the 1.292 Å bond distance calculated for the N−N bond is indicative of a double bond character in N1−N2 in **D**. However, there was no significant change in the relative orientation of the NONO and Im ligand planes. Interestingly, there was a significant increase in the Fe−N1 bond distance from 1.886 Å to 1.981 Å in **D** and the N2−O2 bond length from 1.207 Å to 1.427 Å. Thus, the Fe−N bond and the

N2−O2 bonds became weaker upon O_2 protonation of the anionic $[(por)Fe(NONO)(Im)]_{\perp}^{-}$ and those bonds may be the sites of reduction of NO to N_2O and H_2O.

Table 1.6. Selected calculated bond distances in the non-protonated (**A**) and protonated (**B-D**) [(P)Fe(NONO)(Im)] systems obtained using BP86/TZVP.

Structure	N1−N2 (ΔN1−N2)[a]	N1−O1 (ΔN1−N1)[a]	N2−O2 (ΔN2−O2)[a]	Fe−N1 (ΔFe−N1)[a]
A	1.708 (0)	1.217 (0)	1.207 (0)	1.886 (0)
B	1.339 (−0.369)	1.421 (0.204)	1.242 (0.035)	1.890 (0.004)
C	1.403 (−0.305)	1.230 (0.013)	1.249 (0.042)	1.906 (0.020)
D	1.292 (−0.416)	1.249 (0.032)	1.427 (0.22)	1.981 (0.005)

[a] Difference in bond length calculated by subtracting the bond distance of interest of the protonated structure from that of the corresponding anionic structure (**A**) in Å. Negative values mean bond shortened.

The second observation after protonation of the anionic $[(por)Fe(NONO)(Im)]_{\perp}^{-}$ model is the increase in the spin density of Fe from −0.01 in the nonprotonated model to 0.70, 0.54, and 1.00, (using BP86/TZVP) for **B**, **C** and **D**, respectively (Fig. 1.53). This observation is consistent with the proposed change in oxidation state of Fe of low-spin +2 to +3 after addition of proton (Fig. 1.44).[204]

In 2009, our research group's interest in the interaction of NO_x molecules with metalloporphyrins was extended to investigating the role of the heme active site independent of the nonheme site in the mechanism of action of the NORs. To this end, Richter-Addo and coworkers sought to prepare and isolate the hyponitrite-bridged porphyrin complex $[(OEP)Fe]_2(\mu\text{-}N_2O_2)$. The $[(OEP)Fe]_2(\mu\text{-}N_2O_2)$ complex was

successfully prepared by treating a toluene solution of (OEP)Fe(OMe) or the oxo-dimer complex, $[(OEP)Fe]_2(\mu\text{-}O)$ with hyponitrous acid (Eq. 1.10 and 1.11) which may be viewed as a **category 3** hyponitrite complex synthesis. See Section 1.3.4.1.

$$2[(OEP)Fe(OMe)] + H_2N_2O_2 \longrightarrow [(OEP)Fe]_2(\mu\text{-}ONNO) + MeOH \qquad (\mathbf{1.10})$$

$$[(OEP)Fe]_2O + H_2N_2O_2 \longrightarrow [(OEP)Fe]_2(\mu\text{-}ONNO) + H_2O \qquad (\mathbf{1.11})$$

In their effort to structurally characterize our $[(OEP)Fe]_2(\mu\text{-}ONNO)$ complex Richter-Addo and coworkers resorted, initially, to spectroscopy. They performed IR spectroscopic analysis on the $[(OEP)Fe]_2(\mu\text{-}ONNO)$ complex and observed a new isotope-sensitive IR band at 982 cm^{-1} in the IR spectrum which was unambiguously assigned to the ν_{as} of the NO (ν_{as} for ^{15}NO is 973 cm^{-1}[18] and the reported ν_{as} of $H_2N_2O_2$ is 1014/ 1003 cm^{-1}) without trace of the 875 cm^{-1} band from the Fe−O−Fe starting compound. In a follow-up collaborative work with Lehnert and coworkers, they reported a weak isotope-sensitive band at 436 cm^{-1} in the IR spectrum assigned to the bound hyponitrite ligand.[254] In addition, NRVS experiments, in conjunction with DFT calculations, were utilized to assign the additional single isotope-sensitive band observed at 322 cm^{-1} and associated it with the Fe−ONNO−Fe unit.[254]

They succeeded in obtaining the desired X-ray crystal structure of the $[(OEP)Fe]_2(\mu\text{-}ONNO)$ complex which crystallized as a tetrakis-(dichloromethane) solvent (Fig. 1.54).

The crystal structure of $[(OEP)Fe]_2(\mu\text{-}ONNO)$ demonstrates one example of *trans* hyponitrite bridge bimetallic complex proposed as an intermediate in the reduction of NO to N_2O, except that their system is composed of two heme bimetallic

centers instead of the proposed heme and nonheme bimetallic centers. Regardless, we note here that the [(OEP)Fe]$_2$(μ-ONNO) complex is, to date, the only reported crystal structure of a *trans* hyponitrite-bridge bimetallic porphyrin complex. Key structural features of the crystal structure are worthy of note.

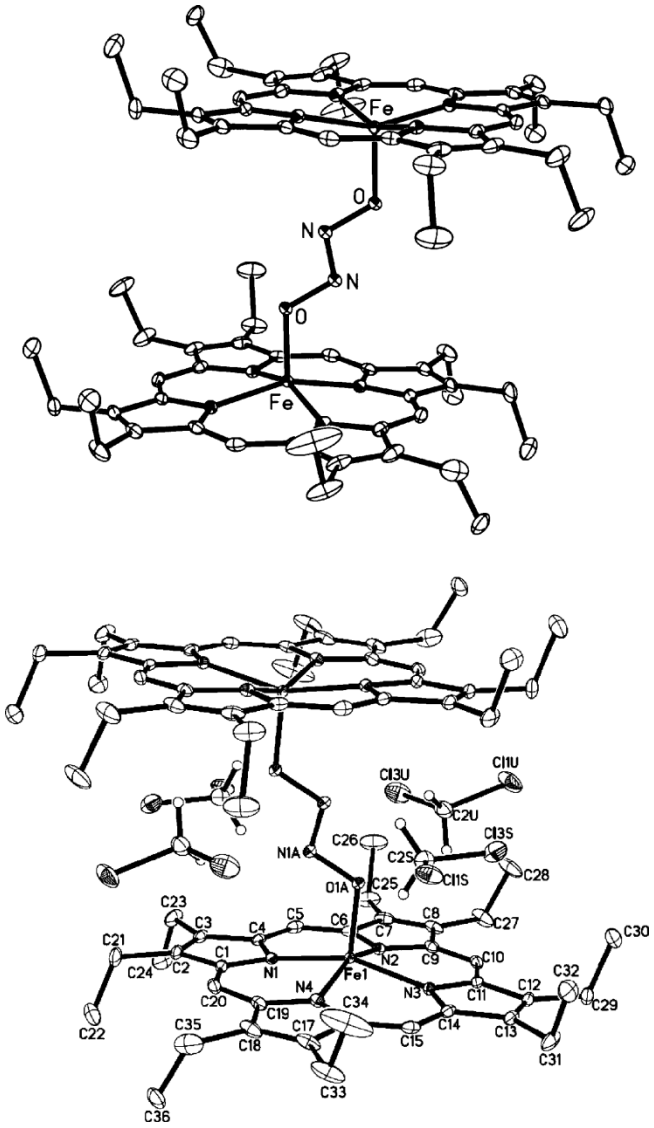

Figure 1.54. Molecular structure of [(OEP)Fe]$_2$(μ-ONNO). Top: H atoms and the CH_2Cl_2 solvates have been omitted for clarity. Bottom: With CH_2Cl_2 solvates but without non-solvate H atoms. *Reproduced with permission from Ref.* [8] *Copyright 2010 American Chemical Society.*

First, the N_2O_2 ligand is bound to each of the iron centers via the O which has been proposed to be a possible mode of binding in the NOR and HCO as discussed above. Richter-Addo and coworkers also observed in this crystal structure a N−N bond length of 1.250(3) Å (cf., N−N double bond = 1.25 Å; N−N bond in *trans*-$Na_2N_2O_2$ is 1.256(2) Å[219]); an indication of double bond character.

In addition, it was observed from the crystal structure that the two iron centers are separated from each other by a distance of 6.7 Å (Fig. 1.55). In contrast, the distance between the heme Fe center and nonheme Fe center in the crystal structure of the NOR *Pseudom. aeruginosa* thermophilus cyt ba_3 obtained at 2.7 Å resolution was reported to

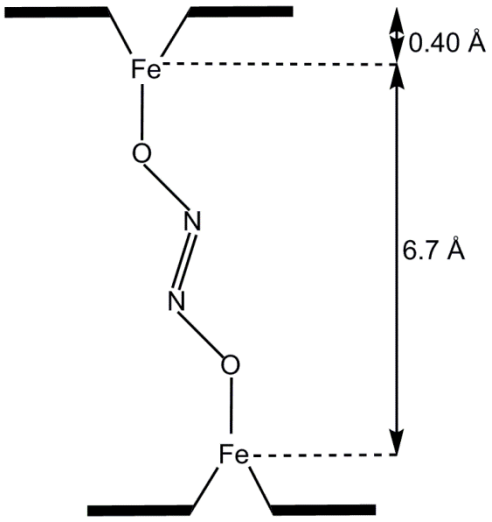

Figure 1.55. The Fe−Fe distance in the $[(OEP)Fe]_2(\mu$-ONNO) complex.

be 3.9 Å, and the Fe−Cu distance obtained in the crystal structure of thermophilus cyt ba_3 was determined to be 4.4 Å.[255] Furthermore, it was noted that the Fe atoms in the porphyrin centers are displaced from the 4N mean plane by 0.40 Å. Scheidt and coworkers have done extensive studies on five-coordinate porphyrinato iron(III)

complexes and have come to the generalization that the spin state and stereochemistry of the iron(III) center is governed by the nature and number of axial ligands; namely, weak field ligands lead to five coordinate high-spin complexes and high field ligands generally lead to high-spin six-coordinate complexes.[256] By this generalization, it was envisioned that the iron centers in the $[(OEP)Fe]_2(\mu$-ONNO) complex were each in the +3 oxidation states. To confirm this, EPR experiments were employed to study the spin state of the complex. EPR data of a frozen CH_2Cl_2 sample of the $[(OEP)Fe]_2(\mu$-ONNO) complex at liquid helium temperature (4 K) were collected. Quite unexpectedly, the EPR signal showed signals consistent with a high-spin complex (S = 5/2) (Fig. 1.56). The $[(OEP)Fe]_2(\mu$-ONNO) complex was expected to be EPR-silent due to bridging of the two iron centers. Indeed, by doing a quantification of the EPR signal of $[(OEP)Fe]_2(\mu$-ONNO) complex against the standard $(F_8TPP)FeCl$ at 4 K, Richter-Addo and coworkers obtained EPR signals suggesting that the EPR signal observed in the $[(OEP)Fe]_2(\mu$-ONNO)] complex was due to ~20 mol% impurity , (OEP)Fe(OH) (Fig. 1.56 and 1.57) Attempts at avoiding the formation of the (OEP)Fe(OH) impurity proved futile.

Richter-Addo and coworkers then proceeded to perform SQUID susceptibility measurements on the $[(OEP)Fe]_2(\mu$-ONNO) complex which showed a constant magnetic moment above 100 K implying that the ferric centers in the hyponitrite are only weakly magnetically coupled, an indication that the hyponitrite probably exhibits dianionic character. A μ_{eff} value of 5.53 μBM value was obtained per dimer at 250 K.[254]

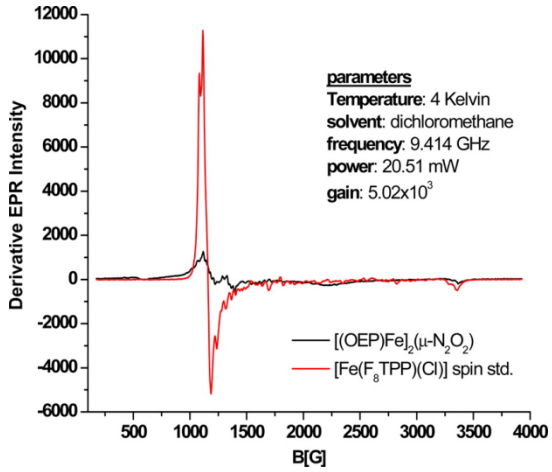

Figure 1.56. EPR spectrum of $[(OEP)Fe]_2(\mu\text{-ONNO})$ [254] versus the S = 5/2 spin standard [Fe(F_8TPP)Cl] recorded at 4 K. The solutions are 3mM in iron centers. *Reproduced with permission from Ref.* [254] *Copyright 2014 American Chemical Society.*

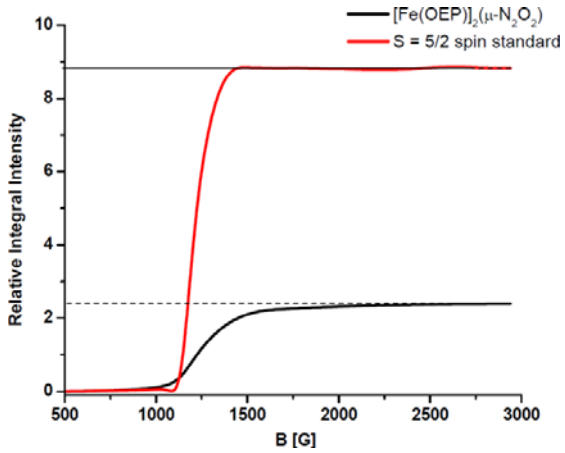

Figure 1.57. Integration of the EPR spectrum of $\{[(OEP)Fe]_2(\mu\text{-}N_2O_2)\}$ versus that of the S = 5/2 spin standard [(F_8TPP)Fe]Cl recorded at the identical concentration (3 mM) in CH_2Cl_2 solution at 4K. The signal observed for $[(OEP)Fe]_2(\mu\text{-}N_2O_2)]$ is due to the presence of about 20 mol% of a high-spin ferric impurity, likely [Fe(OEP)(OH)], that is commonly observed in preparations of $\{[(OEP)Fe]_2(\mu\text{-}N_2O_2)\}$. *Reproduced with permission from Ref.* [254] *Copyright 2014 American Chemical Society.*

DFT calculations for the $[(P)Fe]_2(\mu\text{-}N_2O_2)]$ model complex using B3LYP functional with TZVP basis set was employed to confirm the structure of $[(OEP)Fe]_2(\mu$-

N_2O_2)].[254] We note that their calculations predicted an energy gap of ~2 kcal mol^{-1} between the *trans*-N_2O_2 product and the *cis*-N_2O_2 product, an indication that both isomers may form.

Calculations of the bond orders in the Fe−O−N−N−O−Fe using the Nalewajski-Mrozek scheme was used to confirm a double bond character in the N−N bond (Fig. 1.58). In the *trans* high-spin model, Richter-Addo and coworkers observed a positive charge on Fe (+1.61) and a negative charge (−0.62) on the oxygen of the hyponitrite ligand.[237]

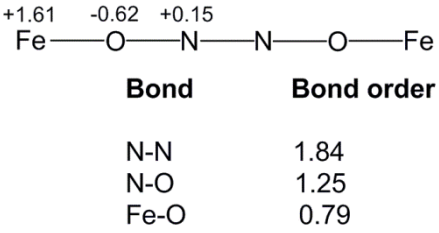

Figure 1.58. Calculated atomic charges and bond orders for the FeONNOFe moiety.[237]

Furthermore, the frontier spin orbital diagram which was obtained from the unrestricted open-shell calculation suggests that the interaction in both the highest occupied spin orbitals was responsible for N−N bond in the hyponitrite moiety (Fig. 1.59).[237]

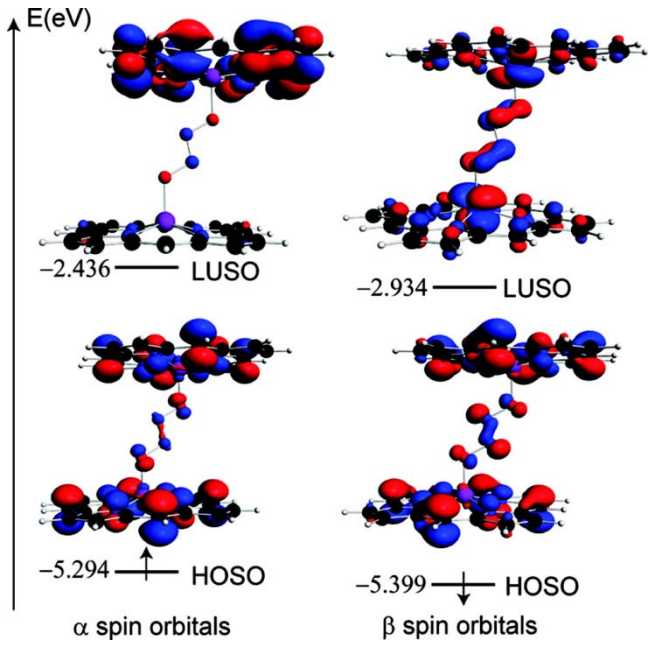

Figure 1.59. Frontier spin orbitals for high-spin $[(P)Fe]_2(\mu\text{-}N_2O_2)$. HOSO and LUSO denote the highest occupied and the lowest unoccupied spin orbitals, respectively. *Reproduced with permission from Ref.* [237] *Copyright 2009 American Chemical Society.*

In addition, molecular orbital diagram calculated with B3LYP/TZVP for the BP86/TZVP-optimized structure revealed that the strongest component of coupling of the hyponitrite to the iron originates from the π-donation from the occupied π* orbital of the hyponitrite, orthogonal to the ONNO plane, into the appropriate t_2g-type d orbitals of the iron(III) as depicted in Fig. 1.60. The hyponitrite π* orbital is mostly located in the terminal oxygens of the hyponitrite anion and could therefore be considered to bear partial lone-pair character on the oxygen atoms.[237]

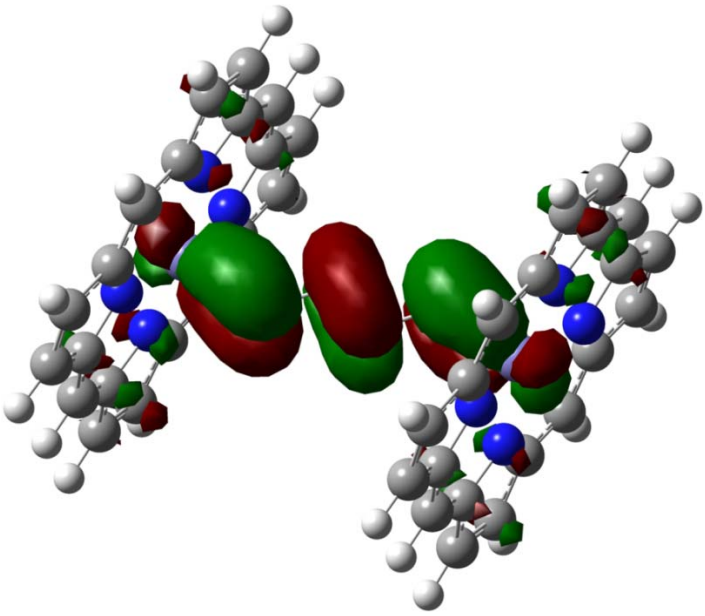

Figure 1.60. Key occupied molecular orbital (β<193>, the β HOMO) of {[Fe(P)]$_2$(μ-N_2O_2)} (S = 3) that illustrates the π-coupling between the iron centers across the hyponitrite bridge. This MO has 21% Fe and 65% hyponitrite charge contributions. Calculated with B3LYP/TZVP for the BP86/TZVP-optimized structure. *Reproduced with permission from ref.* [254] *Copyright 2014 American Chemical Society.*

With the structure of the *trans*-bridged hyponitrite complex [(OEP)Fe]$_2$(μ-N_2O_2)] established by spectroscopy, EPR and theoretical calculations,[237,254] Richter-Addo and coworkers sought to investigate the mechanism by which [(OEP)Fe]$_2$(μ-N_2O_2)] releases N_2O and H_2O. Specifically, they wanted to explore the effects of H^+ ion on the decomposition of [(OEP)Fe]$_2$(μ-N_2O_2)] complex. The treatment of a toluene solution of the [(OEP)Fe]$_2$(μ-N_2O_2)] complex with hydrochloric acid resulted in the formation of (OEP)FeCl, H_2O and N_2O (Fig. 1.61). The N_2O produced was easily detected by IR spectroscopy.[237] Isotope sensitive bands were observed at 2236/2213 and 1298/1266 cm^{-1} and these were assigned to the ν_{as} and ν_s of N_2O, respectively. The corresponding isotopic $^{15}N_2O$ ν_{as} bands were observed at 2167/2144 cm^{-1}, but the ν_s band was not detected because it was outside the detection window.[237]

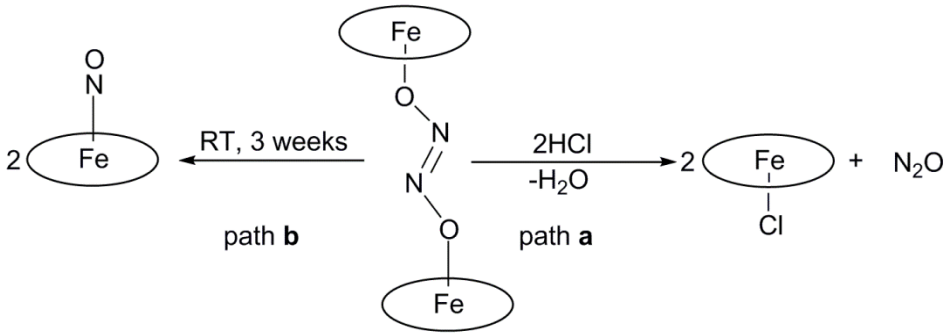

Figure 1.61. (Path **a**) decomposition of $[(OEP)Fe]_2(\mu\text{-}ONNO)]$ by addition of HCl; (path **b**) thermal decomposition of $[(OEP)Fe]_2(\mu\text{-}ONNO)]$ at room temperature.

We note also that the complex $[(OEP)Fe]_2(\mu\text{-}ONNO)]$ is thermally unstable. At room temperature, and in solution, or even in the crystalline form $[(OEP)Fe]_2(\mu\text{-}ONNO)]$ readily decomposes to the known (OEP)Fe(NO) complex (Path b in Fig. 1.61).[254] The resulting (OEP)Fe(NO) product was detected by EPR which shows a three-line hyperfine splitting signals consistent with ferrous heme. The decomposed product was confirmed by UV spectroscopy. Absorption measurements taken at 30 °C for a CH_2Cl_2 solution of $[(OEP)Fe]_2(\mu\text{-}ONNO)]$ shows the isosbestic conversion of the 620 nm Q band of $[(OEP)Fe]_2(\mu\text{-}ONNO)]$ to the characteristic bands at 565 and 595 nm for (OEP)Fe(NO).[257] We would like to point out also that the related $[(PPDME)Fe]_2(\mu\text{-}N_2O_2)$ compound similarly decomposes to the five-coordinate (PPDME)Fe(NO) complex, N_2O and H_2O.[254]

As already discussed above the binuclear center in NOR from *P. aeruginosa*, for instance possesses a histidine protein at the axial position.[248] Richter-Addo and coworkers wanted to explore further the function of the histidine moiety in the decomposition of $[(OEP)Fe]_2(\mu\text{-}ONNO)]$.

In this regard, they treated the [(OEP)Fe]$_2$(μ-ONNO)] complex with 1-methylimidazole (1-MeIm) and studied the rate of decomposition of the resulting complexes ([(OEP)Fe]$_2$(μ-ONNO)(1-MeIm)n; n = 1 or 2) (Fig. 1.62). It was discovered that in the presence of 13-fold excess 1-MeIm, the [(OEP)Fe]$_2$(μ-ONNO)] complex completely converted to the (OEP)Fe(NO) complex in 80 minutes. In contrast, without 1-MeIm, the [(OEP)Fe]$_2$(μ-ONNO)] converts to the (OEP)Fe(NO) complex in 6 hours. They envisioned that at higher 1-MeIm concentration the hyponitrite ligand may be displaced in which case the EPR active (OEP)Fe(1-MeIm)$_2$ complex could form. Quite interestingly, the latter complex was not observed in the EPR spectrum. Thus, it is likely that the presence of the N-donor histidine at the axial position of the heme iron complex may play a role in speeding up the rate of reduction of NO to N_2O in NORs.

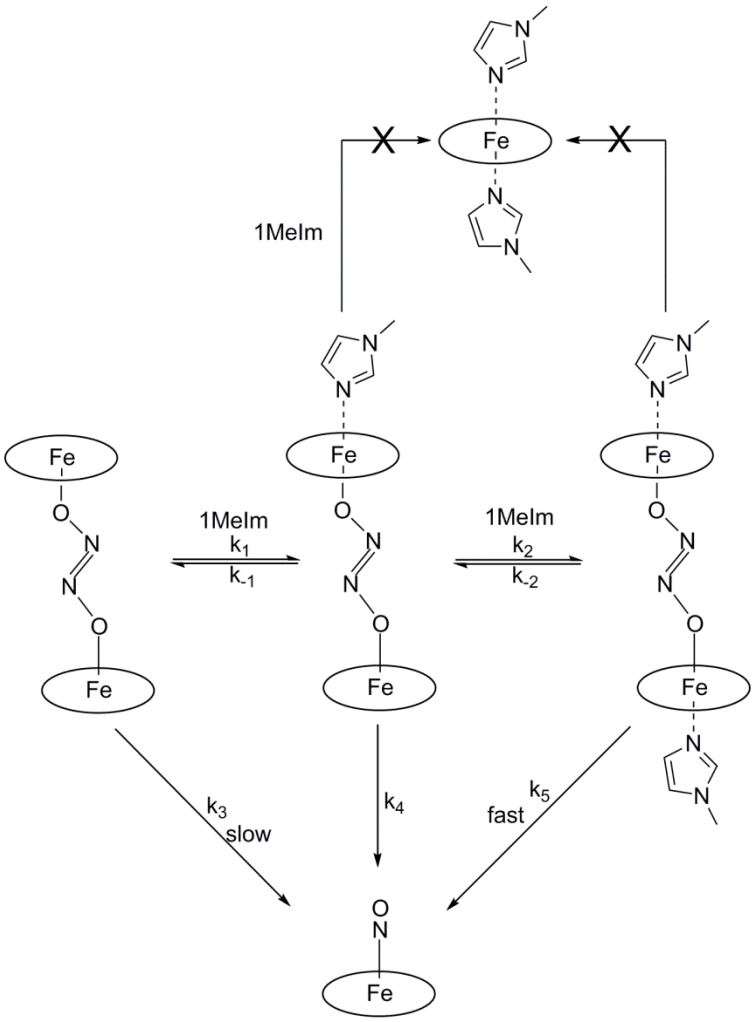

Figure 1.62. Decomposition of $[(OEP)Fe]_2(\mu\text{-ONNO})]$ in the presence of 1-Methylimidazole. $k_5 > k_3$. *Modified with permission from ref.* [254] *Copyright 2014 American Chemical Society.*

Richter-Addo and coworkers then wanted to probe what the mechanism of decomposition of $[(OEP)Fe]_2(\mu\text{-ONNO})]$ to (OEP)Fe(NO) would be. Fig. 1.63 shows the proposed decomposition pathway of $[(OEP)Fe]_2(\mu\text{-ONNO})$.[254]

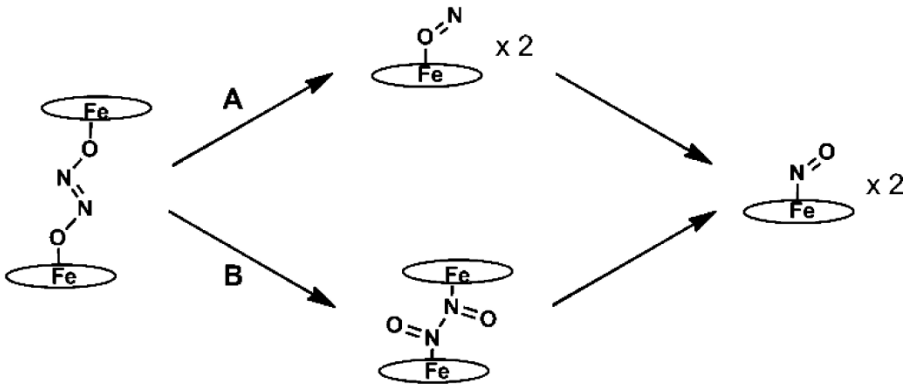

Figure1.63. Potential decomposition pathways of $[(OEP)Fe]_2(\mu\text{-ONNO})$. *Reproduced with permission from Ref.* [254] *Copyright 2014 American Chemical Society.*

Two pathways were proposed (Fig. 1.63) for the decomposition of $[(OEP)Fe]_2(\mu\text{-ONNO})$ to (OEP)Fe(NO). In the first pathway (A) they envisioned a direct breaking of the N−N bond in of $[(OEP)Fe]_2(\mu\text{-ONNO})$] leading to the formation of the metastable (OEP)Fe(η^1-ON) complex (discussed above).[43] The latter complex then linkage-isomerizes to the more stable nitrosyl complex (OEP)Fe(NO). They also considered another pathway, Path B. In this pathway, they hypothesize that the *O*,*O*-hyponitrite bridged complex first isomerizes to the *N*,*N*-bound trans isomer and the N−N bond of the latter complex cleaves yielding the (OEP)Fe(NO) complex. To probe this further, they resorted to DFT calculations to help elucidate the probable path of decomposition. DFT data obtained for model $[(P)Fe]_2(\mu\text{-}N_2O_2)$ seems to favor decomposition of $[(P)Fe]_2(\mu\text{-}N_2O_2)$ via path B, since there is a better match with the experimentally determined free reaction energy although path A is also a possibility.

1.4 Heme Proteins

The biological effects of nitrites have been known for many decades. Earlier work by Gamgee, Haldene, Makgill, and Mavrogordato in this area has contributed immensely in understanding the action of NO_x on blood.[258-260] For example, it was discovered more than a century ago that NO_x contribute to methemoglobinemia conditions in animals.[259] Although high concentrations of NO_x molecules are toxic, NO_x molecules are also practically relevant. In the food industry, nitrite, for example is used in preserving and curing meat.[169] In biological systems there are enzymes known to reduce NO_x to less toxic molecules. A typical example of such enzymes is the nitrite reductases (NiR) which are responsible for the one electron reduction of NO_2^- to NO (Eq. 1.12).

$$NO_2^- + 2H^+ + e^- \longrightarrow NO + H_2O \qquad (\mathbf{1.12})$$

There are two main types of NiRs involved in the reduction of nitrites, namely, the heme-containing cytochrome *cd*$_1$ NiR which was obtained and first purified from *Thiosphaera pantotropha*.[261] The second kind of NiR is the copper-containing NiR which was first isolated from *Alcaligenes xylosoxidans* NCIB 11015, a bacterial isolated from a soil in Japan. Other Cu NiR have been isolated from, *Achromobacter cycloclastes, Alcaligenes faecalis* S-6, *Bacillus halodenitrificans*, *Haloferax denitrificans*, *Nitrosomonas europaea*, *Pseudomonas aureofaciens*, *Rhodobacter sphaeroides*, and *Hyphomicrobium* sp.[262] (and references therein). In mammalian systems, nitrites are reduced by deoxyHb[263] and by ferrous myoglobin[264,265] to nitric

oxide. In synthetic iron porphyrins, Ford and coworkers have demonstrated how nitrites inhibit the reductive nitrosylation process by forming ferric-nitrites species.[266]

The mode of NO_2 binding to the irons centers (Fig. 1.1 II) in these NiRs has been of interest to many researchers. We note that, many of the structurally characterized proteins and related heme complexes of NO_2 have NO_2 bound to the metal via N.[137,267-270]

Although earlier Gamgee provided spectroscopic data to show how the color of blood was changed by treating with nitrites,[258]there was no crystal structure of a Mb-nitrite or Hb-nitrite of the proposed adduct.[8] More than a century later after Gamgee's report, the first crystal structure of a horse heart myoglobin adduct of nitrite,[271] and later, the X-ray structure of the green pigment in nitrite-cured meat[272] were reported by Richter-Addo and coworkers. The nitrite-bound adduct crystals of hh Mb were obtained either by allowing a $NaNO_2$ solution to soak into crystals of aqua-metMb or by treating a solution of metMb with $NaNO_2$ and then growing the crystals from the solution. Thus, the method of preparation of the crystals, either by soaking the nitrite into the preformed crystal or by growing crystals from a solution of Mb^{III}(nitrite) did not affect the mode of binding of the nitrite. Richter-Addo and coworkers observed, for the first time, a *O*-nitrito-binding mode of the nitrite in their hh Mb^{III}(ONO) complex (Fig. 1.64 A).

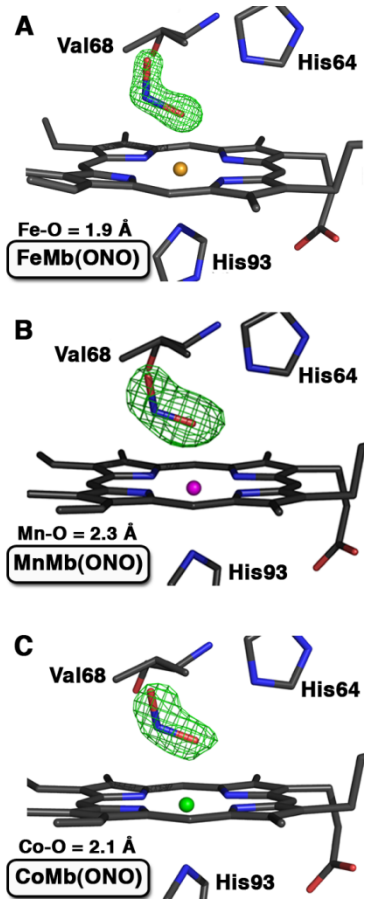

Figure 1.64. *Fo−Fc* omit electron density maps (contoured at 3σ) and final models of the heme environments of the O-bound nitrite adducts of (A) wild-type horse heart ferric Mb (1.20 Å resolution; PDB access code 2FRF),[271] (B) Mn^{III}-substituted Mb (1.60 Å resolution; PDB access code 2O5O),[160] and (C) Co^{III}-substituted Mb (1.60 Å resolution; PDB access code 2O5S).[160] *Reproduced with permission from Ref.* [8] *Copyright 2010 American Chemical Society.*

Key features of the crystal structure of the hh Mb^{III}(ONO) complex are worthy of note. The Fe−O bond distance in the crystal structure of hh Mb^{III}(ONO) is 1.94 Å and the Fe−O−N moiety is essentially bent with a bond angle of 116°. The Fe−N(His93) bond length is 2.07 Å. We note that whereas the ferric (d^5) Mb−ONO complex was formed, the corresponding ferrous (d^6) Mb−ONO complex was not obtained following similar experimental procedure. In contrast the Fe−NO_2 modes of binding have been observed in both the ferric and ferrous forms in synthetic porphyrin complexes and the

nitrito binding mode has been observed in (TPP)Fe(NO)(NO_2) in the metastable state following irradiation of the ground state isomer at low temperatures (see Section 1.2.3).[180] However, in another work, Richter-Addo and coworkers succeeded in obtaining the crystal structure of the ferrous (d^6) Mb^{II}(ONO)* (* = photoreduced product) complex by photoreduction of the Mb^{III}(ONO) precursor (Eq. 1.13) using a correlated microspectrophotometry and synchrotron X-ray (3 x 10^{10} photons/s; λ = 1.0 Å) photoreduction technique at 100 K.[273]

$$Mb^{III}(ONO) + e^- \longrightarrow Mb^{II}(ONO/NO_2)^* \qquad (\mathbf{1.13})$$

The UV spectrum of the resulting photoreduced species differed from the precursor in the following ways. First, the Soret band was red-shifted with accompanying change in shape of the bands in the region of 500−600 nm. Secondly, there was an increase in intensity of the 570 nm band, an indication that a change in identity of the photoreduced product had occurred. Indeed X-ray crystal structure of the photoreduced product of Mb^{III}(ONO) confirmed a retention of the nitrito binding mode (Fig. 1.65).[273]

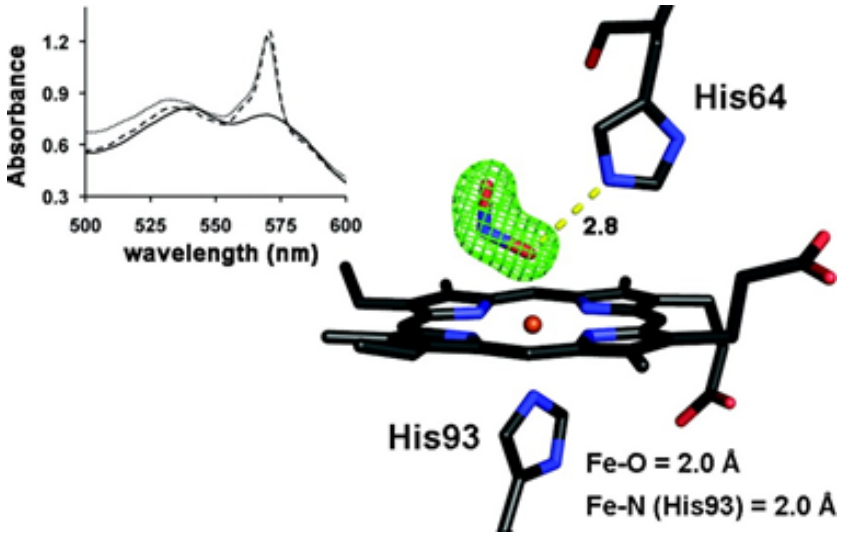

Figure 1.65. Single-crystal optical spectra (500−600 nm region, ~25 μm incident light focal spot size) of a crystal of ferric $Mb^{III}(ONO)$ during exposure to high-intensity X-rays. The dark line is the original spectrum before X-ray exposure. The dashed line is the spectrum after exposure of the crystal to X-rays for 161 images at 15 s/image. The gray line is the spectrum at the end of data collection (365 images at 15 s/image). $F_o - F_c$ omit electron density map (contoured at 5σ) and final model of the heme environment (1.55 Å resolution structure) of the ferrous $Mb^{II}(ONO)$* product obtained after exposure of the ferric precursor to high-intensity X-rays using images 161−365 for the structure determination. The bonds to Fe have been omitted for the sake of clarity, and the H-bond between the nitrito ligand and the distal His64 residue is shown as a yellow dashed line (distance in angstroms). Protein Data Bank entry 3LR9. *Reproduced with permission from ref.* [273] *Copyright 2010 American Chemical Society*.

The nitrito mode of binding was also observed in the Mn^{III}Mb-nitrite complex (Fig. 1.64 B) and quite unexpectedly in the d^6 Co^{III}Mb-nitrite complex (Fig. 1.64 C). In synthetic Co porphyrin complexes the nitro configuration has been observed in the ground state.[200]

Richter-Addo and coworkers observed the nitrito mode of binding in the related ferric human Hb.[274] The crystal structure of this complex (Fig. 1.66) reveals two conformations of the nitrito ligand; *trans* in the α-subunit and *cis*-like in the β-subunit.

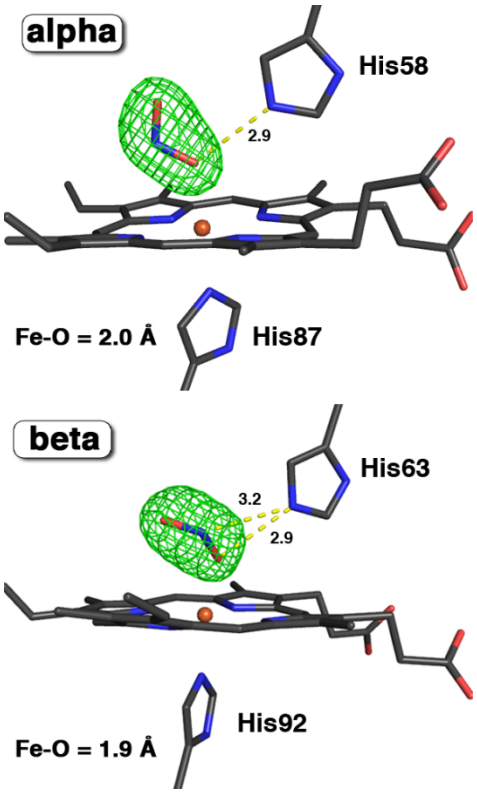

Figure 1.66. $F_o - F_c$ omit electron density maps (contoured at 3σ) and final models of the heme environments of the O-bound nitrite adduct of ferric human Hb (1.80 Å resolution; PDB access code 3D7O). *Reproduced with permission from Ref.* [274] *Copyright 2008 American Chemical Society.*

It is interesting to note that in each of the crystal structures of the Fe^{III}Mb(ONO), Fe^{III}Hb(ONO), Mn^{III}Mb(ONO), and Co^{III}Mb(ONO) complexes there is a histidine residue which is in hydrogen-bonding distance with the bound nitrito oxygen, a feature which was not observed in the related synthetic complexes. Thus, it was proposed that H-bonding with the histidines may be responsible for the observance of this "rare" nitrite heme complexes. Indeed, in the crystal structure of the nitrite adduct of the H64V mutant of Mb, they observed only the very weak nitro binding mode (Fig. 1.67 A)[275] demonstrating how the lack of a distal histidine affects the mode of binding of nitrite to the metal center of these heme proteins.

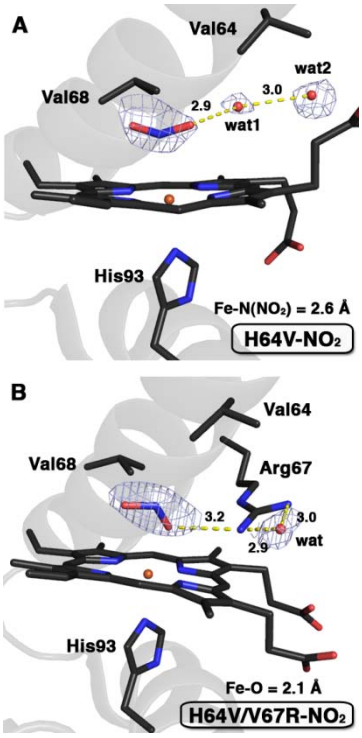

Figure 1.67. $F_o - F_c$ omit electron density maps (contoured at 3σ) and final models of the heme environments of (A) the N-bound nitrite adduct of the ferric Mb H64V mutant (1.95 Å resolution; PDB access code 3HEP) and (B) the O-bound nitrite adduct the ferric Mb H64V/V67R double mutant (2.0 Å resolution; PDB access code 3HEO).[275] *Adapted with permission from Ref.* [275] *Copyright 2009 American Chemical Society.*

When the H64V mutant of Mb was further mutated to the H64V/V67R mutant, thus introducing hydrogen bonding, the nitrite binding mode was observed signifying the role of the histidine H in directing the mode of binding in the Mb^{III}(ONO) heme proteins. Fig. 1.68 summarizes the effects of the H-donor histidine (or arginine) side chain on directing the mode of NO_2 binding.

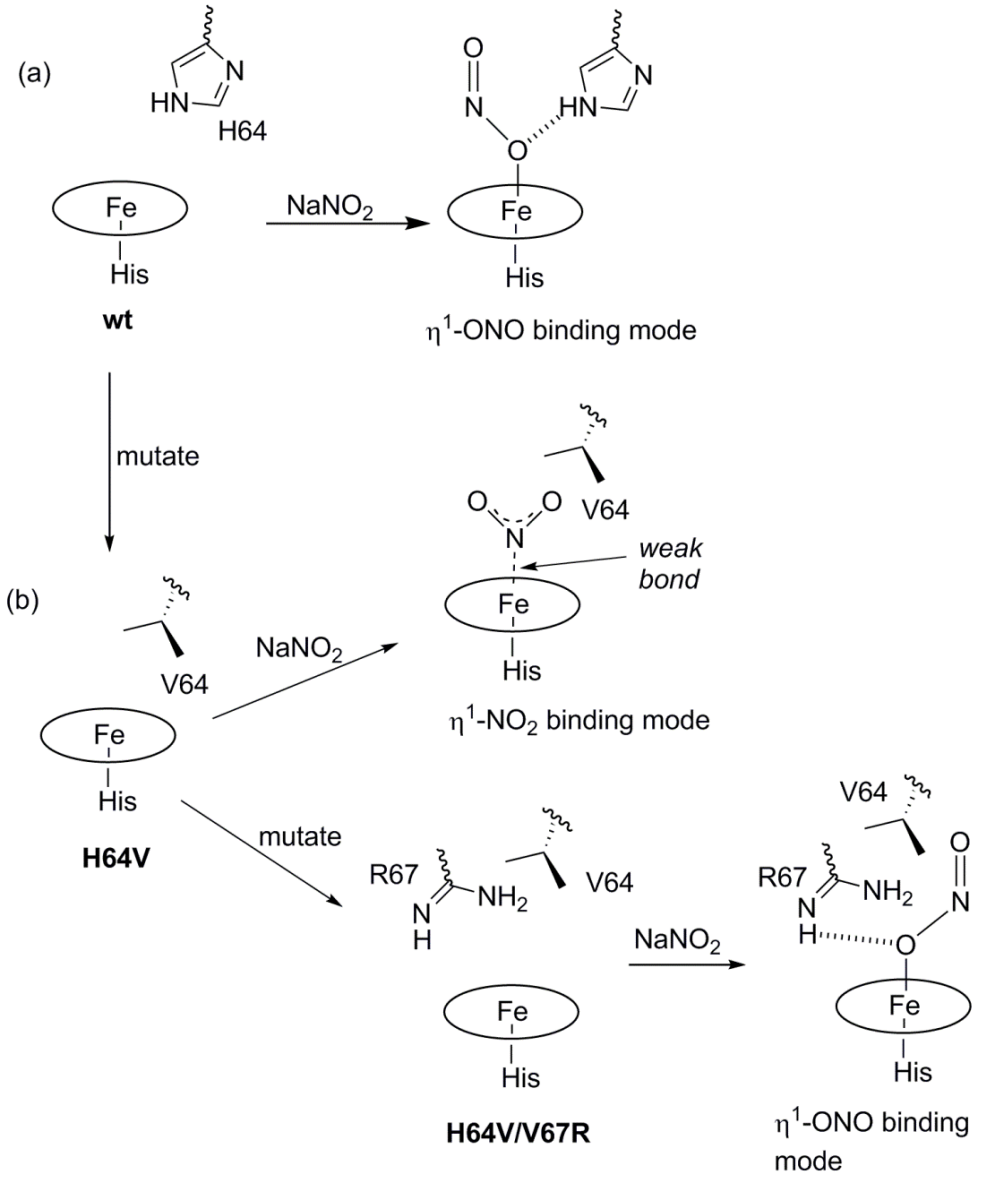

Figure 1.68. Sketches of the active sites of wild-type Mb (a), H64V mutant (left) and nitrite adducts demonstrating the effects of H-bonding and non-H-bonding residue on mode of NO_2 binding to Fe.

In a related report, Richter-Addo and coworkers performed experiments on distal pocket control of nitrite binding in a Mb complex prepared from a wild-type protein and a chlorin macrocycle.[276] They utilized the known chlorin compound FeMPPaCl (MPPa = pyropheophorbide-*a* methyl ester) and inserted the resulting

compound into apoMb. The resulting MbChl(NO_2) adduct showed two absorption bands at 419 nm and 652 nm in the UV/Vis spectrum. These bands were indications that NO_2 was linked to Fe via N. The former band has also been observed in a CH_2Cl_2 solution of the related FeMPPa(NO_2) complex, and a similar band at 417 nm was observed in a CH_2Cl_2 solution of the relatively unstable (TPP)Fe(NO_2) complex.[277,278] Indeed, the crystal structure of the proposed adduct confirmed that NO_2 was N-bound in the FeMPPaCl adduct (Fig. 1.69 A). More importantly, the Fe−N(nitrite) bond distance of 2.0 Å is in the range of those reported for the N-bound nitrite adducts of cyt c NiR (1.9 Å; 1.60 Å resolution),[279,280] nitrophorin 4 (2.0 Å; 1.4 Å resolution), [281] cyt cd_1 NiR (2.0 Å; 1.8 Å resolution),[268] and sulfite reductases hemoprotein (2.0 Å; 2.1 Å resolution).[269]

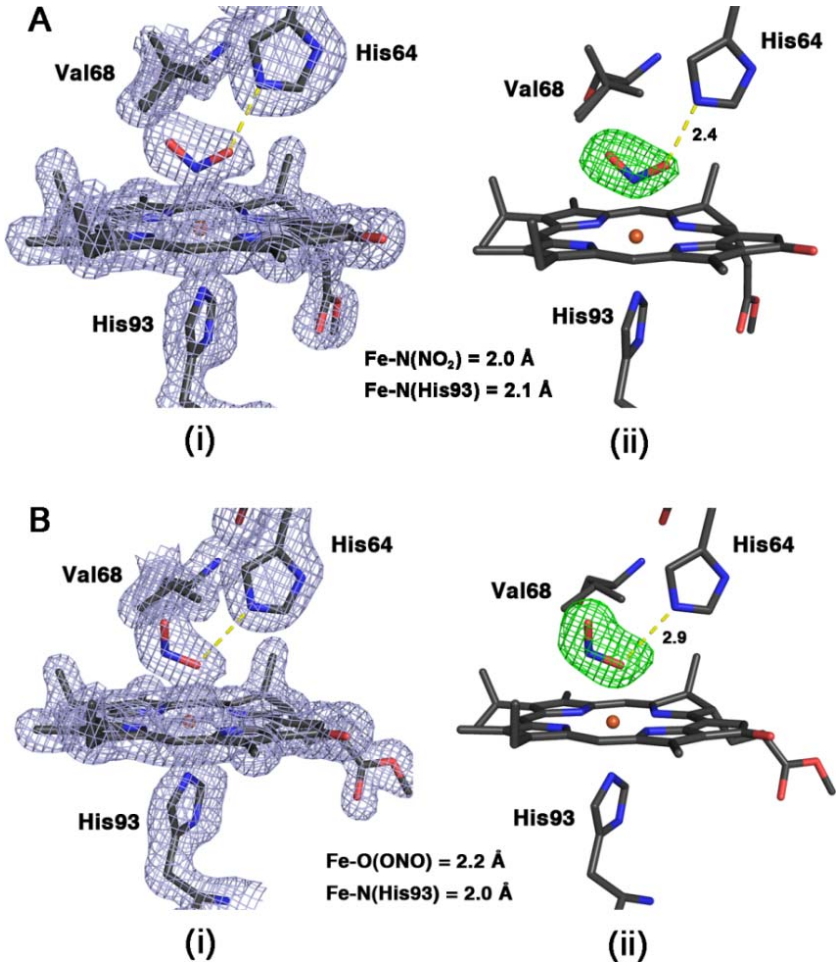

Figure 1.69. A. The heme site of the 1.65 Å resolution structure of MbChl(NO_2). (i) The 2 F_o−F_c electron-density map (contoured at 1σ) and the final model; (ii) The F_o−F_c omit electron density map (contoured at 3σ) and the final model. B. The heme site of the 1.65 Å resolution structure of MbChl(ONO) (i) The 2 F_o−F_c electron density map (contoured at 1σ) and the final model; ii) The F_o−F_c omit electron density map (contoured at 3σ) and the final model. *Reproduced with permission from ref.* [276]

Interestingly, when a solution of the aquometchlorin-substituted Mb (MbChl(H_2O) was treated with sodium nitrite, the *O*-nitrito complex, MbChl(ONO) was obtained as evidenced by shift in the λ = 417 and 656 nm to 422 and 662 nm, respectively. The X-ray crystal structure of the adduct confirmed the nitrito isomer as shown in Fig. 1.69 B. A comparison of the two crystal structures reveal that in the MbChl(ONO) structure the portion of the chlorin macrocycle near the protein exterior is

shifted slightly toward the distal side without causing significant change in the positions of the amino acids that contact the macrocycle plane and the chlorin ester group moved from the proximal position in MbChl(NO_2) further toward the exterior of the protein in MbChl(ONO), losing the direct hydrogen-bonding interaction with the Ser92 molecule.

Finally, we note that MbNO has been shown to possess a higher-energy isonitrosyl metastable form MbON.[282]

1.5 Conclusion

The discovery that several compounds undergo NO_x ligand isomerization provides opportunities for varied reactivities of these NO_x liganded species as a function of NO_x coordination mode. Clearly, this field is in its infancy and in need of systematic studies of relevance to NO_x combination/recombination processes and chemical/biological reactivities, and biological signaling capacity.

1.6 References

(1) Jörgensen, S. M. *Z. Anorg. Chem.* **1894**, *5*, 147-196.

(2) Werner, A. *Ber. Dtsch. Chem. Ges.* **1907**, *40*, 765-788.

(3) Penland, R. B.; Lane, T. J.; Quagliano, J. V. *J. Am. Chem. Soc.* **1956**, *78*, 887-889.

(4) Norbury, A. H.; Sinha, A. I. P. *Quart. Rev. Chem. Soc.* **1970**, *24*, 69-94.

(5) Burmeister, J. L. *Coord. Chem. Rev.* **1968**, *3*, 225-245.

(6) Burmeister, J. *Coord. Chem. Rev.* **1990**, *105*, 77-133.

(7) Coppens, P.; Novozhilova, I.; Kovalevsky, A. *Chem. Rev.* **2002**, *102*, 861-884.

(8) Xu, N.; Yi, J.; Richter-Addo, G. B. *Inorg. Chem.* **2010**, *49*, 6253-6266.

(9) Andrews, L.; Citra, A. *Chem. Rev.* **2002**, *102*, 885-912.

(10) Dieckmann, V.; Eicke, S.; Springfeld, K.; Imlau, M. *Materials* **2012**, *5*, 1155-1175.

(11) Bitterwolf, T. E. *Coord. Chem. Rev.* **2006**, *250*, 1196-1207.

(12) Esplugues, J. V. *Br. J. Pharmacol.* **2002**, *135*, 1079-1095.

(13) Moncada, S.; Palmer, R. M.; Higgs, E. A. *Pharmacol. Rev.* **1991**, *43*, 109-142.

(14) Cheng, L.; Richter-Addo, G. B. In: Kadish, K. M., Smith, K. M., Guilard, R., Eds.; *The Porphyrin Handbook;* Vol. 4; Academic Press: New York, 2000; Ch. 33*,* pp 219-291.

(15) Friederich, J. A.; Butterworth, J. F. *Anesth. Analg.* **1995**, *81*, 152-162.

(16) Butler, A. R.; Glidewell, C. *Chem. Soc. Rev.* **1987**, *16*, 361-380.

(17) Allan, P.; Morris, R. In *Nitrosyl Complexes in Inorganic Chemistry, Biochemistry and Medicine II*; Mingos, D. M. P., Ed.; Springer Berlin Heidelberg: 2014; Vol. 154, p 225-256.

(18) Averill, B. A. *Chem. Rev.* **1996**, *96*, 2951-2964.

(19) Hochstein, L. I.; Tomlinson, G. A. *Annu. Rev. Microbiol.* **1988**, *42*, 231-261.

(20) Firestone, M. K.; Davidson, E. A. *Microbiological basis of NO and N_2O Production and Consumption in Soil*. Wiley: New York, NY, 1989; pp 7-21.

(21) Maia, L. B.; Moura, J. J. G. *Chem. Rev.* **2014**.

(22) Heinecke, J.; Ford, P. C. *Coord. Chem. Rev.* **2010**, *254*, 235-247.

(23) Farrauto, R. J.; Heck, R. M. *Catal. Today* **1999**, *51*, 351-360.

(24) Limousy, L.; Mahzoul, H.; Brilhac, J. F.; Garin, F.; Maire, G.; Gilot, P. *Appl. Catal. B Environ.* **2003**, *45*, 169-179.

(25) Harrison, B.; Diwell, A. F.; Hallett, C. *Platin. Met. Rev.* **1988**, *32*, 73-83.

(26) Schaniel, D.; Mockus, N.; Woike, T.; Klein, A.; Sheptyakov, D.; Todorova, T.; Delley, B. *Phys. Chem. Chem. Phys.* **2010**, *12*, 6171-6178.

(27) Schaniel, D.; Imlau, M.; Weisemoeller, T.; Woike, T.; Krämer, K. W.; Güdel, H. U. *Adv. Mater.* **2007**, *19*, 723-726.

(28) Woike, T.; Kirchner, W.; Schetter, G.; Barthel, T.; Hyung-sang, K.; Haussühl, S. *Opt. Commun.* **1994**, *106*, 6-10.

(29) Goulkov, M.; Schaniel, D.; Woike, T. *J. Opt. Soc. Am. B* **2010**, *27*, 927-932.

(30) Imlau, M.; Haussühl, S.; Woike, T.; Schieder, R.; Angelov, V.; Rupp, R. A.; Schwarz, K. *Appl. Phys. B* **1999**, *68*, 877-885.

(31) Akl, J.; Billot, C.; Lacroix, P. G.; Sasaki, I.; Mallet-Ladeira, S.; Malfant, I.; Arcos-Ramos, R.; Romero, M.; Farfan, N. *New J. Chem.* **2013**, *37*, 3518-3527.

(32) Schuy, A.; Woike, T.; Schaniel, D. *J. Sol-Gel Sci. Technol.* **2009**, *50*, 403-408.

(33) Cervellino, A.; Schefer, J.; Keller, L.; Woike, T.; Schaniel, D. *J. Appl. Crystallogr.* **2010**, *43*, 1040-1045.

(34) Tahri, Z.; Lepski, R.; Hsieh, K.-Y.; Bendeif, E.-E.; Pillet, S.; Durand, P.; Woike, T.; Schaniel, D. *Phys. Chem. Chem. Phys.* **2012**, *14*, 3775-3781.

(35) Alderton, W. K.; Cooper, C. E.; Knowles, R. G. *Biochem. J.* **2001**, *357*, 593-615.

(36) Richter-Addo, G. B.; Legzdins, P. *Metal Nitrosyls;* Oxford University Press Inc.; New York, USA, 1992.

(37) Carducci, M. D.; Pressprich, M. R.; Coppens, P. *J. Am. Chem. Soc.* **1997**, *119*, 2669-2678.

(38) Fomitchev, D. V.; Coppens, P. *Inorg. Chem.* **1996**, *35*, 7021-7026.

(39) Fomitchev, D. V.; Coppens, P.; Li, T.; Bagley, K. A.; Chen, L.; Richter-Addo, G. B. *Chem. Commun.* **1999**, 2013-2014.

(40) Delley, B.; Schefer, J.; Woike, T. *J. Chem. Phys.* **1997**, *107*, 10067-10074.

(41) Schefer, J.; Woike, T.; Imlau, M.; Delley, B. *Eur. Phys. J. B* **1998**, *3*, 349-352.

(42) Schefer, J.; Woike, T.; Haussühl, S.; Díaz, M. T. F. *Z. Kristallogr.* **1997**; *212*, 29.

(43) Cheng, L.; Novozhilova, I.; Kim, C.; Kovalevsky, A.; Bagley, K. A.; Coppens, P.; Richter-Addo, G. B. *J. Am. Chem. Soc.* **2000**, *122*, 7142-7143.

(44) Hitchman, M. A.; Rowbottom, G. L. *Coord. Chem. Rev.* **1982**, *42*, 55-132.

(45) Ellison, M. K.; Shang, M.; Kim, J.; Scheidt, W. R. *Acta Crystallogr. C* **1996**, *52*, 3040-3043.

(46) Schopfer, M. P.; Mondal, B.; Lee, D.-H.; Sarjeant, A. A. N.; Karlin, K. D. *J. Am. Chem. Soc.* **2009**, *131*, 11304-11305.

(47) Nasri, H.; Ellison, M. K.; Shaevitz, B.; Gupta, G. P.; Scheidt, W. R. *Inorg. Chem.* **2006**, *45*, 5284-5290.

(48) Suslick, K. S.; Watson, R. A. *Inorg. Chem.* **1991**, *30*, 912-919.

(49) Phillippi, M. A.; Baenziger, N.; Goff, H. M. *Inorg. Chem.* **1981**, *20*, 3904-3911.

(50) Wyllie, G. R. A.; Munro, O. Q.; Schulz, C. E.; Robert Scheidt, W. *Polyhedron* **2007**, *26*, 4664-4672.

(51) Munro, O. Q.; Scheidt, W. R. *Inorg. Chem.* **1998**, *37*, 2308-2316.

(52) Addison, C. C.; Logan, N.; Wallwork, S. C.; Garner, C. D. *Quart. Rev., Chem. Soc.* **1971**, *25*, 289-322.

(53) Adell, B. *Z. Anorg. Allg. Chem.* **1955**, *279*, 219-224.

(54) Laskar, I. R.; Das, D.; Mostafa, G.; Lu, T.-H.; Keng, T.-C.; Wang, J.-C.; Ghosh, A.; Chaudhuri, N. R. *New J. Chem.* **2001**, *25*, 764-768.

(55) Hatcher, L. E.; Warren, M. R.; Allan, D. R.; Brayshaw, S. K.; Johnson, A. L.; Fuertes, S.; Schiffers, S.; Stevenson, A. J.; Teat, S. J.; Woodall, C. H.; Raithby, P. R. *Angew. Chem.* **2011**, *123*, 8521-8524.

(56) Warren, M. R.; Easun, T. L.; Brayshaw, S. K.; Deeth, R. J.; George, M. W.; Johnson, A. L.; Schiffers, S.; Teat, S. J.; Warren, A. J.; Warren, J. E.; Wilson, C. C.; Woodall, C. H.; Raithby, P. R. *Chem. Eur. J.* **2014**, *20*, 5468-5477.

(57) Silaghi-Dumitrescu, R.; Uta, M.-M.; Makarov, S. V. *Rev. Roum. Chim.* **2010**, *55*, 897-903.

(58) Novozhilova, I. V.; Coppens, P.; Lee, J.; Richter-Addo, G. B.; Bagley, K. A. *J. Am. Chem. Soc.* **2006**, *128*, 2093-2104.

(59) Hauser, U.; Oestreich, V.; Rohrweck, H. *Z. Phys. A* **1977**, *280*, 17-25.

(60) H auser, U.; Oestreich, V.; Rohrweck, H. *Z. A* **1977**, *280*, 125-130.

(61) Ooms, K. J.; Wasylishen, R. E. *Can. J. Chem.* **2006**, *84*, 300-308.

(62) Jackson, W. G.; Lawrence, G. A.; Lay, P. A.; Sargeson, A. M. *J. Chem. Soc., Chem. Commun.* **1982**, 70-72.

(63) Coppens, P.; Vorontsov, I. I.; Graber, T.; Gembicky, M.; Kovalevsky, A. Y. *Acta Crystallogr. A* **2005**, *61*, 162-172.

(64) Cole, J. *Acta Cryst. A* **2008**, *64*, 259-271.

(65) Fomitchev, D. V.; Furlani, T. R.; Coppens, P. *Inorg. Chem.* **1998**, *37*, 1519-1526.

(66) Raithby, P. R. *Crystallogr. Rev.* **2007**, *13*, 121-142.

(67) Coppens, P.; V. Fomitchev, D.; D. Carducci, M.; Culp, K. *J. Chem. Soc., Dalton Trans.* **1998**, 865-872.

(68) Eslami, A. *Thermochim. Acta* **2004**, *409*, 189-193.

(69) Eslami, A.; Hasani, N. *J. Therm. Anal. Calorim.* **2013**, *111*, 193-201.

(70) Eslami, A.; Hasani, N. *Thermochim. Acta* **2014**, *575*, 114-121.

(71) Wondimagegn, T.; Ghosh, A. *J. Am. Chem. Soc.* **2001**, *123*, 5680-5683.

(72) Baluhura, R. J.; Lewis, N. A. *Coord. Chem. Rev.* **1976**, *20*, 109-153.

(73) Pearson, R. G. *J. Am. Chem. Soc.* **1963**, *85*, 3533-3539.

(74) Pearson, R. G. *J. Chem. Educ.* **1968**, *45*, 581.

(75) Duffus John, H. *Pure Appl. Chem.* **2002**, *74*, 793.

(76) Ahrland, S.; Chatt, J.; Davies, N. R. *Quart. Rev. Chem. Soc.* **1958**, *12*, 265-276.

(77) Jorgensen, C. K. *Inorg. Chem.* **1964**, *3*, 1201-1202.

(78) Tsou, C.-C.; Yang, W.-L.; Liaw, W.-F. *J. Am. Chem. Soc.* **2013**, *135*, 18758-18761.

(79) Pitarch López, J.; Heinemann, F. W.; Prakash, R.; Hess, B. A.; Horner, O.; Jeandey, C.; Oddou, J.-L.; Latour, J.-M.; Grohmann, A. *Chem. Eur. J.* **2002**, *8*, 5709-5722.

(80) Hayton, T. W.; Legzdins, P.; Sharp, W. B. *Chem. Rev.* **2002**, *102*, 935-992.

(81) Døssing, A. *Rev. Inorg. Chem.* **2013**, *33*, 129.

(82) Ford, P. C.; Wecksler, S. *Coord. Chem. Rev.* **2005**, *249*, 1382-1395.

(83) Nemes, A.; Pestovsky, O.; Bakac, A. *J. Am. Chem. Soc.* **2001**, *124*, 421-427.

(84) Kunkely, H.; Vogler, A. *Inorg. Chem. Commun.* **2004**, *7*, 767-769.

(85) Bitterwolf, T. E. *Inorg. Chem. Commun.* **2006**, *9*, 39-41.

(86) DeRosa, F.; Bu, X.; Ford, P. C. *Inorg. Chem.* **2005**, *44*, 4157-4165.

(87) Fee, W. W.; Garner, C. S.; Harrowfield, J. N. M. *Inorg. Chem.* **1967**, *6*, 87-93.

(88) DeLeo, M. A.; Ford, P. C. *Coord. Chem. Rev.* **2000**, *208*, 47-59.

(89) Hubbard, J. L.; Zoch, C. R.; Elcesser, W. L. *Inorg. Chem.* **1993**, *32*, 3333-3338.

(90) Eremenko, I. L.; Pasynskii, A. A.; Kalinnikov, V. T.; Struchkov, Y. T.; Aleksandrov, G. G. *Inorg. Chim. Acta* **1981**, *52*, 107-111.

(91) Bitterwolf, T. E. *J. Photochem. Photobiol. A* **2004**, *163*, 209-213.

(92) Chacón Villalba, M. E.; Güida, J. A.; Varetti, E. L.; Aymonino, P. J. *Inorg. Chem.* **2003**, *42*, 2622-2627.

(93) Faller, J. W.; Johnson, B. V. *J. Organomet. Chem.* **1975**, *88*, 101-113.

(94) Herberhold, M.; Alt, H.; G. Kreiter, C. *J. Organomet. Chem.* **1972**, *42*, 413-418.

(95) Schaniel, D.; Woike, T. *Phys. Chem. Chem. Phys.* **2009**, *11*, 4391-4395.

(96) Playfair, L. *Abstr. Pap. Commun. Roy. Soc. London* **1843**, *5*, 846-847.

(97) Page, I. H.; Corcoran, A. C.; Dustan, H. P.; Koppanyi, T. *Circulation* **1955**, *11*, 188-198.

(98) Manoharan, P. T.; Gray, H. B. *J. Am. Chem. Soc.* **1965**, *87*, 3340-3348.

(99) Swinehart, J. H. *Coord. Chem. Rev.* **1967**, *2*, 385-402.

(100) Pressprich, M. R.; White, M. A.; Vekhter, Y.; Coppens, P. *J. Am. Chem. Soc.* **1994**, *116*, 5233-5238.

(101) *Chem&Eng News*. http://cen.xraycrystals.org/nitroprusside-ion.html. Accessed August 11 2014.

(102) Villalba, M. E. C.; Güida, J. A.; Varetti, E. L.; Aymonino, P. J. *Spectrochim. Acta A* **2001**, *57*, 367-373.

(103) Güida, J. A.; Piro, O. E.; Schaiquevich, P. S.; Aymonino, P. J. *Solid State Commun.* **1997**, *101*, 471-475.

(104) Güida, J. A.; Piro, O. E.; Aymonino, P. J. *Inorg. Chem.* **1995**, *34*, 4113-4116.

(105) Güida, J. A.; Ramos, M. A.; Piro, O. E.; Aymonino, P. J. *J. Mol. Struct.* **2002**, *609*, 39-46.

(106) Woike, T.; Zöllner, H.; Krasser, W.; Haussühl, S. *Solid State Commun.* **1990**, *73*, 149-152.

(107) D Da Silva, S. C.; Franco, D. W. *Spectrochim. Acta A* **1999**, *55*, 1515-1525.

(108) Morioka, Y.; Ishikawa, A.; Tomizawa, H.; Miki, E.-i. *J. Chem. Soc., Dalton Trans.* **2000**, 781-786.

(109) Ookubo, K.; Morioka, Y.; Tomizawa, H.; Miki, E. *J. Mol. Struct.* **1996**, *379*, 241-247.

(110) Cormary, B.; Malfant, I.; Buron-Le Cointe, M.; Toupet, L.; Delley, B.; Schaniel, D.; Mockus, N.; Woike, T.; Fejfarova, K.; Petricek, V.; Dusek, M. *Acta Crystallogr. B* **2009**, *65*, 612-623.

(111) Cormary, B.; Ladeira, S.; Jacob, K.; Lacroix, P. G.; Woike, T.; Schaniel, D.; Malfant, I. *Inorg. Chem.* **2012**, *51*, 7492-7501.

(112) Kovalevsky, A. Y.; King, G.; Bagley, K. A.; Coppens, P. *Chem. Eur. J.* **2005**, *11*, 7254-7264.

(113) Su, P.; Li, H. *J. Chem. Phys.* **2009**, *131*, 014102.

(114) Andriani, K. F.; Caramori, G. F.; Doro, F. G.; Parreira, R. L. T. *Dalton Trans.* **2014**, *43*, 8792-8804.

(115) Fanning, J. C.; Resce, J. L.; Lickfield, G. C.; Kotun, M. E. *Inorg. Chem.* **1985**, *24*, 2884-2889.

(116) Resce, J. L.; Fanning, J. C.; Day, C. S.; Uhm, S.-J.; Croisy, A. F.; Keefer, L. K. *Acta Crystallogr. C* **1987**, *43*, 2100-2104.

(117) Güida, J. A. *Inorg. Chem. Commun.* **2013**, *33*, 75-77.

(118) Balzani, V.; Ballardini, R.; Sabbatini, N.; Moggi, L. *Inorg. Chem.* **1968**, *7*, 1398-1404.

(119) Wendlandt, W. W.; Woodlock, J. H. *J. Inorg. Nucl. Chem.* **1965**, *27*, 259-260.

(120) Beattie, I. R.; Satchell, D. P. N. *Trans. Faraday Soc.* **1956**, *52*, 1590-1593.

(121) Jackson, W. G. *J. Chem. Educ.* **1991**, *68*, 903.

(122) Phillips, W. M.; Choi, S.; Larrabee, J. A. *J. Chem. Educ.* **1990**, *67*, 267.

(123) Masciocchi, N.; Kolyshev, A.; Dulepov, V.; Boldyreva, E.; Sironi, A. *Inorg. Chem.* **1994**, *33*, 2579-2585.

(124) Boldyreva, E. V. *Mol. Crys. Liq. Cryst. Section A.* **1994**, *242*, 17-52.

(125) Pearson, R. G.; Henry, P. M.; Bergmann, J. G.; Basolo, F. *J. Am. Chem. Soc.* **1954**, *76*, 5920-5923.

(126) Grenthe, I.; Nordin, E. *Inorg. Chem.* **1979**, *18*, 1109-1116.

(127) Grenthe, I.; Nordin, E. *Inorg. Chem.* **1979**, *18*, 1869-1874.

(128) Murmann, R. K.; Taube, H. *J. Am. Chem. Soc.* **1956**, *78*, 4886-4890.

(129) Adell, B. *Z. Anorg. Allg. Chem.* **1971**, *386*, 122-128.

(130) Basolo, F.; Hammaker, G. S. *Inorg. Chem.* **1962**, *1*, 1-5.

(131) Schaiquevich, P. S.; Güida, J. A.; Aymonino, P. J. *Inorg. Chim. Acta* **2000**, *303*, 277-281.

(132) Schaniel, D.; Woike, T.; Delley, B.; Biner, D.; Kramer, K. W.; Gudel, H.-U. *Phys. Chem. Chem. Phys.* **2007**, *9*, 5149-5157.

(133) Schaniel, D.; Woike, T.; Behrnd, N.-R.; Hauser, J. r.; Krämer, K. W.; Todorova, T.; Delley, B. *Inorg. Chem.* **2009**, *48*, 11399-11406.

(134) Sabbatini, N.; Moggi, L.; Varani, G. *Inorg. Chim. Acta* **1971**, *5*, 469-472.

(135) Warren, M. R.; Brayshaw, S. K.; Johnson, A. L.; Schiffers, S.; Raithby, P. R.; Easun, T. L.; George, M. W.; Warren, J. E.; Teat, S. J. *Angew. Chem. Int. Ed.* **2009**, *48*, 5711-5714.

(136) Goodrich, L. E.; Paulat, F.; Praneeth, V. K. K.; Lehnert, N. *Inorg. Chem.* **2010**, *49*, 6293-6316.

(137) Wyllie, G. R. A.; Scheidt, W. R. *Chem. Rev.* **2002**, *102*, 1067-1090.

(138) Kurtikyan, T. S.; Hayrapetyan, V. A.; Martirosyan, G. G.; Ghazaryan, R. K.; Iretskii, A. V.; Zhao, H.; Pierloot, K.; Ford, P. C. *Chem. Commun.* **2012**, *48*, 12088-12090.

(139) Martirosyan, G. G.; Azizyan, A. S.; Kurtikyan, T. S.; Ford, P. C. *Chem. Commun.* **2004**, 1488-1489.

(140) Martirosyan, G. G.; Azizyan, A. S.; Kurtikyan, T. S.; Ford, P. C. *Inorg. Chem.* **2006**, *45*, 4079-4087.

(141) Hovhannisyan, A. A.; Mehrabyan, M. M.; Kurtikyan, T. S. *Russ. Chem. Bull.* **2013**, *62*, 1630-1635.

(142) Kurtikyan, T. S.; Ford, P. C. *Angew. Chem. Int. Ed.* **2006**, *45*, 492-496.

(143) Kurtikyan, T. S.; Ford, P. C. *Chem. Commun.* **2010**, *46*, 8570-8572.

(144) Kurtikyan, T. S.; Gulyan, G. M.; Martirosyan, G. G.; Lim, M. D.; Ford, P. C. *J. Am. Chem. Soc.* **2005**, *127*, 6216-6224.

(145) Kurtikyan, T. S.; Hovhannisyan, A. A.; Gulyan, G. M.; Ford, P. C. *Inorg. Chem.* **2007**, *46*, 7024-7031.

(146) Kurtikyan, T. S.; Hovhannisyan, A. A.; Hakobyan, M. E.; Patterson, J. C.; Iretskii, A.; Ford, P. C. *J. Am. Chem. Soc.* **2007**, *129*, 3576-3585.

(147) Kurtikyan, T. S.; Hovhannisyan, A. A.; Iretskii, A.; Ford, P. C. *Aust. J. Chem.* **2009**, *62*, 1226-1230.

(148) Kurtikyan, T. S.; Hovhannisyan, A. A.; Iretskii, A. V.; Ford, P. C. *Inorg. Chem.* **2009**, *48*, 11236-11241.

(149) Kurtikyan, T. S.; Martirosyan, G. G.; Lorkovic, I. M.; Ford, P. C. *J. Am. Chem. Soc.* **2002**, *124*, 10124-10129.

(150) Martirosyan, G. G.; Kurtikyan, T. S.; Azizyan, A. S.; Iretskii, A. V.; Ford, P. C. *J. Inorg. Biochem.* **2013**, *121*, 129-133.

(151) Kurtikyan, T. S.; Eksuzyan, S. R.; Goodwin, J. A.; Hovhannisyan, G. S. *Inorg. Chem.* **2013**, *52*, 12046-12056.

(152) Kurtikyan, T. S.; Eksuzyan, S. R.; Hayrapetyan, V. A.; Martirosyan, G. G.; Hovhannisyan, G. S.; Goodwin, J. A. *J. Am. Chem. Soc.* **2012**, *134*, 13861-13870.

(153) Kurtikyan, T. S.; Gulyan, G. M.; Dalaloyan, A. M.; Kidd, B. E.; Goodwin, J. A. *Inorg. Chem.* **2010**, *49*, 7793-7798.

(154) Kurtikyan, T. S.; Markaryan, E. R.; Mardyukov, A. N.; Goodwin, J. A. *Inorg. Chem.* **2007**, *46*, 1526-1528.

(155) Kurtikyan, T. S.; Stepanyan, T. G. *Russ. Chem. Bull.* **1998**, *47*, 695-698.

(156) Kurtikyan, T. S.; Ford, P. C. *Coord. Chem. Rev.* **2008**, *252*, 1486-1496.

(157) Urban, M. W.; Nakamoto, K.; Basolo, F. *Inorg. Chem.* **1982**, *21*, 3406-3408.

(158) Byrn, M. P.; Curtis, C. J.; Hsiou, Y.; Khan, S. I.; Sawin, P. A.; Tendick, S. K.; Terzis, A.; Strouse, C. E. *J. Am. Chem. Soc.* **1993**, *115*, 9480-9497.

(159) Wayland, B. B.; Olson, L. W. *Inorg. Chim. Acta* **1974**, *11*, L23-L24.

(160) Zahran, Z. N.; Chooback, L.; Copeland, D. M.; West, A. H.; Richter-Addo, G. B. *J. Inorg. Biochem.* **2008**, *102*, 216-233.

(161) Lorković, I.; Ford, P. C. *J. Am. Chem. Soc.* **2000**, *122*, 6516-6517.

(162) Kobayashi, H.; Yanagawa, Y. *Bull. Chem. Soc. Jpn.* **1972**, *45*, 450-456.

(163) Wayland, B. B.; Olson, L. W.; Siddiqui, Z. U. *J. Am. Chem. Soc.* **1976**, *98*, 94-98.

(164) Ahlrichs, R.; Bär, M.; Häser, M.; Horn, H.; Kölmel, C. *Chem. Phys. Lett.* **1989**, *162*, 165-169.

(165) Jaworska, M.; Lodowski, P. *Struct. Chem.* **2012**, *23*, 1333-1348.

(166) Hoshino, M.; Nagashima, Y.; Seki, H.; De Leo, M.; Ford, P. C. *Inorg. Chem.* **1998**, *37*, 2464-2469.

(167) Richter-Addo, G. B. *J. Porphyr. Phthalocya.* **2000**, *04*, 354-357.

(168) Ford, P. C. *Inorg. Chem.* **2010**, *49*, 6226-6239.

(169) Møller, J. K. S.; Skibsted, L. H. *Chem. Rev.* **2002**, *102*, 1167-1178.

(170) Gaudin, C. F. M.; Grigg, J. C.; Arrieta, A. L.; Murphy, M. E. P. *Biochemistry* **2011**, *50*, 5443-5452.

(171) Clark, D.; Durner, J.; Navarre, D. A.; Klessig, D. F. *Mol. Plant Microbe Interact.* **2000**, *13*, 1380-1384.

(172) Yi, G.-B.; Khan, M. A.; Richter-Addo, G. B. *Inorg. Chem.* **1997**, *36*, 3876-3885.

(173) Awasabisah, D.; Xu, N.; Sharmah Gautam, K. P.; Powell, D. R.; Shaw, M. J.; Richter-Addo, G. B. *Dalton Trans.* **2013**, *42*, 8537-8540.

(174) Cheng, L.; Powell, D. R.; Khan, M. A.; Richter-Addo, G. B. *Inorg. Chem.* **2001**, *40*, 125-133.

(175) Ghosh, A. *Acc. Chem. Res.* **2005**, *38*, 943-954.

(176) Scheidt, W. R.; Frisse, M. E. *J. Am. Chem. Soc.* **1975**, *97*, 17-21.

(177) Cheng, L.; Powell, D. R.; Khan, M. A.; Richter-Addo, G. B. *Chem. Commun.* **2000**, 2301-2302.

(178) Wyllie, G. R. A.; Silvernail, N. J.; Oliver, A. G.; Schulz, C. E.; Scheidt, W. R. *Inorg. Chem.* **2014**, *53*, 3763-3768.

(179) Scheidt, W. R.; Duval, H. F.; Neal, T. J.; Ellison, M. K. *J. Am. Chem. Soc.* **2000**, *122*, 4651-4659.

(180) Lee, J.; Kovalevsky, A. Y.; Novozhilova, I. V.; Bagley, K. A.; Coppens, P.; Richter-Addo, G. B. *J. Am. Chem. Soc.* **2004**, *126*, 7180-7181.

(181) Greenberg, S. S.; Xie, J.; Zatarain, J. M.; Kapusta, D. R.; Miller, M. J. *J. Pharmacol. Exp. Ther.* **1995**, *273*, 257-265.

(182) Jenkinson, K. M.; Reid, J. J.; Rand, M. J. *Eur. J. Pharmacol.* **1995**, *275*, 145-152.

(183) Brouwer, M.; Chamulitrat, W.; Ferruzzi, G.; Sauls, D.; Weinberg, J. *Blood* **1996**, *88*, 1857-1864.

(184) Wolak, M.; Stochel, G.; Hamza, M.; van Eldik, R. *Inorg. Chem.* **2000**, *39*, 2018-2019.

(185) Rochelle, L. G.; Morana, S. J.; Kruszyna, H.; Russell, M. A.; Wilcox, D. E.; Smith, R. P. *J. Pharmacol. Exp. Ther.* **1995**, *275*, 48-52.

(186) Rajanayagam, M. A. S.; Li, C. G.; Rand, M. J. *Brit. J. Pharmacol.* **1993**, *108*, 3-5.

(187) Li, C. G.; Rand, M. J. *Clin. Exp. Pharmacol. Physiol.* **1993**, *20*, 633-640.

(188) Bauer, J. A. *Anti-Cancer Drugs* **1998**, *9*, 239-244.

(189) Cheng, S.-H.; Su, Y. O. *Inorg. Chem.* **1994**, *33*, 5847-5854.

(190) Mochida, I.; Suetsugu, K.; Fujitsu, H.; Takeshita, K. *J. Chem. Soc., Chem. Commun.* **1982**, 166-167.

(191) Tsuji, K.; Imaizumi, M.; Oyoshi, A.; Mochida, I.; Fujitsu, H.; Takeshita, K. *Inorg. Chem.* **1982**, *21*, 721-725.

(192) Fujita, E.; Chang, C. K.; Fajer, J. *J. Am. Chem. Soc.* **1985**, *107*, 7665-7669.

(193) Fujita, E.; Fajer, J. *J. Am. Chem. Soc.* **1983**, *105*, 6743-6745.

(194) Scheidt, W. R.; Hoard, J. L. *J. Am. Chem. Soc.* **1973**, *95*, 8281-8288.

(195) Wayland, B. B.; Minkiewixz, J. V.; Abd-Elmageed, M. E. *J. Am. Chem. Soc.* **1974**, *96*, 2795-2801.

(196) Groombridge, C. J.; Larkworthy, L. F.; Mason, J. *Inorg. Chem.* **1993**, *32*, 379-380.

(197) Richter-Addo, G. B.; Hodge, S. J.; Yi, G.-B.; Khan, M. A.; Ma, T.; Van Caemelbecke, E.; Guo, N.; Kadish, K. M. *Inorg. Chem.* **1996**, *35*, 6530-6538.

(198) Hoshino, M.; Arai, S.; Yamaji, M.; Hama, Y. *J. Phys. Chem.* **1986**, *90*, 2109-2111.

(199) Zavarine, I. S.; Kini, A. D.; Morimoto, B. H.; Kubiak, C. P. *J. Phys. Chem. B* **1998**, *102*, 7287-7292.

(200) Seki, H.; Okada, K.; Iimura, Y.; Hoshino, M. *J. Phys. Chem. A* **1997**, *101*, 8174-8178.

(201) Fukuto, J. M.; Carrington, S. J.; Tantillo, D. J.; Harrison, J. G.; Ignarro, L. J.; Freeman, B. A.; Chen, A.; Wink, D. A. *Chem. Res. Toxicol.* **2012**, *25*, 769-793.

(202) Lundberg, J. O.; Weitzberg, E.; Gladwin, M. T. *Nat Rev Drug Discov* **2008**, *7*, 156-167.

(203) Lundberg, J. O.; Weitzberg, E.; Cole, J. A.; Benjamin, N. *Nat. Rev. Microbiol.* **2004**, *2*, 593-602.

(204) Moënne-Loccoz, P. *Nat. Prod. Rep.* **2007**, *24*, 610-620.

(205) Zumft, W. G. *J. Inorg. Biochem.* **2005**, *99*, 194-215.

(206) Varotsis, C.; Ohta, T.; Kitagawa, T.; Soulimane, T.; Pinakoulaki, E. *Angew. Chem. Int. Ed.* **2007**, *46*, 2210-2214.

(207) Pinakoulaki, E.; Ohta, T.; Soulimane, T.; Kitagawa, T.; Varotsis, C. *J. Am. Chem. Soc.* **2005**, *127*, 15161-15167.

(208) Kuhn, L.; Lippincott, E. R. *J. Am. Chem. Soc.* **1956**, *78*, 1820-1821.

(209) Wade, E. A.; Cline, J. I.; Lorenz, K. T.; Hayden, C.; Chandler, D. W. *J. Chem. Phys.* **2002**, *116*, 4755-4757.

(210) McKellar, A. R. W.; Watson, J. K. G.; Howard, B. J. *Mol. Phys.* **1995**, *86*, 273-286.

(211) Dinerman, C. E.; Ewing, G. E. *J. Chem. Phys.* **1970**, *53*, 626-631.

(212) Dinerman, C. E.; Ewing, G. E. *J. Chem. Phys.* **1971**, *54*, 3660-3661..

(213) Billingsley, J.; Callear, A. B. *Trans.Faraday Soc.* **1971**, *67*, 589-597.

(214) Skaarup, S.; Skancke, P. N.; Boggs, J. E. *J. Am. Chem. Soc.* **1976**, *98*, 6106-6109.

(215) Benzel, M. A.; Dykstra, C. E.; Vincent, M. A. *Chem. Phys. Lett.* **1981**, *78*, 139-142.

(216) Lipscomb, W. N.; Wang, F. E.; May, W. R.; Lippert, E. L. *Acta Crystallogr.* **1961**, *14*, 1100-1101.

(217) Harcourt, R. D. *J. Mol. Struc. Theochem.* **1990**, *206*, 253-264.

(218) Snis, A.; Panas, I. *Chem. Phys.* **1997**, *221*, 1-10.

(219) Arulsamy, N.; Bohle, D. S.; Imonigie, J. A.; Sagan, E. S. *Inorg. Chem.* **1999**, *38*, 2716-2725.

(220) Feldmann, C.; Jansen, M. *Angew. Chem. Int. Ed. Engl.* **1996**, *35*, 1728-1730.

(221) Feldmann, C.; Jansen, M. *Z. Anorg. Allg. Chem.* **1997**, *623*, 1803-1809.

(222) Goubeau, J.; Laitenberger, K. *Z. Anorg. Allg. Chem.* **1963**, *320*, 78-85.

(223) Addison, C. C.; Gamlen, G. A.; Thompson, R. *J. Chem. Soc. (Resumed)* **1952**, 338-345.

(224) Hughes, M. N. *Quart. Rev. Chem. Soc.* **1968**, *22*, 1-13.

(225) Fateley, W. G.; Bent, H. A.; Crawford, B. *J. Chem. Phys.* **1959**, *31*, 204-217.

(226) Le, F. R.; Oh, W.; Reece, I.; Werner, R. *Aust. J. Chem.* **1957**, *10*, 361-364.

(227) Böttcher, H.-C.; Graf, M.; Mereiter, K.; Kirchner, K. *Organometallics* **2004**, *23*, 1269-1273.

(228) Cenini, S.; Ugo, R.; La Monica, G.; Robinson, S. D. *Inorg. Chim. Acta* **1972**, *6*, 182-184.

(229) Lorenzelli, V.; Busca, G.; Sheppard, N.; Al-Mashta, F. *J. Mol. Struct.* **1982**, *80*, 181-186.

(230) Ramprasad, R.; Hass, K. C.; Schneider, W. F.; Adams, J. B. *J. Phys. Chem. B* **1997**, *101*, 6903-6913.

(231) Azambre, B.; Zenboury, L.; Koch, A.; Weber, J. V. *J. Phys. Chem. C* **2009**, *113*, 13287-13299.

(232) Franz, K. J.; Lippard, S. J. *J. Am. Chem. Soc.* **1999**, *121*, 10504-10512.

(233) Yamashita, K.; Oba, H. *Jpn. Kokai Tokkyo Koho* **1975**, *JP 50123624 A* (Patent).

(234) Koenig, T.; Deinzer, M. *J. Am. Chem. Soc.* **1966**, *88*, 4518-4520.

(235) Arulsamy, N.; Bohle, D. S.; Imonigie, J. A.; Levine, S. *Angew. Chem. Int. Ed.* **2002**, *41*, 2371-2373.

(236) Arulsamy, N.; Bohle, D. S.; Imonigie, J. A.; Moore, R. C. *Polyhedron* **2007**, *26*, 4737-4745.

(237) Xu, N.; Campbell, A. L. O.; Powell, D. R.; Khandogin, J.; Richter-Addo, G. B. *J. Am. Chem. Soc.* **2009**, *131*, 2460-2461.

(238) Hoskins, B. F.; Whillans, F. D.; Dale, D. H.; Hodgkin, D. C. *J. Chem. Soc. D, Chem. Commun.* **1969**, 69-70.

(239) Villalba, M. E. C.; Navaza, A.; Güida, J. A.; Varetti, E. L.; Aymonino, P. J. *Inorg. Chim. Acta* **2006**, *359*, 707-712.

(240) Bhaduri, S.; Johnson, B. F. G.; Pickard, A.; Raithby, P. R.; Sheldrick, G. M.; Zuccaro, C. I. *J. Chem. Soc., Chem. Commun.* **1977**, 354-355.

(241) Wright, A. M.; Wu, G.; Hayton, T. W. *J. Am. Chem. Soc.* **2012**, *134*, 9930-9933.

(242) Mayer, T.; Mayer, P.; Böttcher, H.-C. *J. Organomet. Chem.* **2012**, *700*, 41-47.

(243) Bau, R.; Sabherwal, I. H.; Burg, A. B. *J. Am. Chem. Soc.* **1971**, *93*, 4926-4928.

(244) Mayer, T.; Beck, W.; Böttcher, H.-C. *Z. Anorg. Allg. Chem.* **2011**, *637*, 345-347.

(245) Mayer, T.; Böttcher, H.-C. *Z. Anorg. Allg. Chem.* **2012**, *638*, 1071-1074.

(246) Blomberg, L. M.; Blomberg, M. R. A.; Siegbahn, P. E. M. *Biochim. Biophys. Acta* **2006**, *1757*, 31-46.

(247) Blomberg, L. M.; Blomberg, M. R. A.; Siegbahn, P. E. M. *Biochim. Biophys. Acta* **2006**, *1757*, 240-252.

(248) Hino, T.; Matsumoto, Y.; Nagano, S.; Sugimoto, H.; Fukumori, Y.; Murata, T.; Iwata, S.; Shiro, Y. *Science* **2010**, *330*, 1666-1670.

(249) Blomberg, M. R. A.; Siegbahn, P. E. M. *Biochemistry* **2012**, *51*, 5173-5186.

(250) Lachmann, P.; Huang, Y.; Reimann, J.; Flock, U.; Ädelroth, P. *J. Biol. Chem.* **2010**, *285*, 25531-25537.

(251) Forte, E.; Urbani, A.; Saraste, M.; Sarti, P.; Brunori, M.; Giuffrè, A. *Eur. J. Biochem.* **2001**, *268*, 6486-6491.

(252) Yi, J.; Morrow, B. H.; Campbell, A. L. O. C.; Shen, J. K.; Richter-Addo, G. B. *Chem. Commun.* **2012**, *48*, 9041-9043.

(253) Huheey, J. E.; Keiter, E. A.; Keiter, R. L. *Inorganic Chemistry: Principles of Structure and Reactivity,* Harper Collins, New York, 1993, p. A31.

(254) Berto, T. C.; Xu, N.; Lee, S. R.; McNeil, A. J.; Alp, E. E.; Zhao, J.; Richter-Addo, G. B.; Lehnert, N. *Inorg. Chem.* **2014**, *53*, 6398-6414.

(255) Soulimane, T.; Buse, G.; Bourenkov, G. P.; Bartunik, H. D.; Huber, R.; Than, M. E. *EMBO J. 2000*; *19*, 1766-1776.

(256) Scheidt, W. R.; Reed, C. A. *Chem. Rev.* **1981**, *81*, 543-555.

(257) Ellison, M. K.; Scheidt, W. R. *J. Am. Chem. Soc.* **1999**, *121*, 5210-5219.

(258) Gamgee, A. *Philos. Trans. R. Soc. London* **1868**, *158*, 589-625.

(259) Haldane, J.; Makgill, R. H.; Mavrogordato, A. E. *J Physiol* **1897**, *21*, 160-189.

(260) Haldane, J. *J Hyg.* **1901**, *1*, 115-122.

(261) Moir, J. W. B.; Baratta, D.; Richardson, D. J.; Ferguson, S. J. *Eur. J. Biochem.* **1993**, *212*, 377-385.

(262) Suzuki, S.; Kataoka, K.; Yamaguchi, K.; Inoue, T.; Kai, Y. *Coord. Chem. Rev.* **1999**, *190–192*, 245-265.

(263) Doyle, M. P.; Pickering, R. A.; DeWeert, T. M.; Hoekstra, J. W.; Pater, D. *J. Biol. Chem.* **1981**, *256*, 12393-12398.

(264) Huang, Z.; Shiva, S.; Kim-Shapiro, D. B.; Patel, R. P.; Ringwood, L. A.; Irby, C. E.; Huang, K. T.; Ho, C.; Hogg, N.; Schechter, A. N.; Gladwin, M. T. *J. Clin. Invest.* **2005**, *115*, 2099-2107.

(265) Sulc, F.; Immoos, C. E.; Pervitsky, D.; Farmer, P. J. *J. Am. Chem. Soc.* **2004**, *126*, 1096-1101.

(266) Fernandez, B. O.; Lorkovic, I. M.; Ford, P. C. *Inorg. Chem.* **2004**, *43*, 5393-5402.

(267) Wasser, I. M.; de Vries, S.; Moënne-Loccoz, P.; Schröder, I.; Karlin, K. D. *Chem. Rev.* **2002**, *102*, 1201-1234.

(268) Williams, P. A.; Fulop, V.; Garman, E. F.; Saunders, N. F. W.; Ferguson, S. J.; Hajdu, J. *Nature* **1997**, *389*, 406-412.

(269) Crane, B. R.; Siegel, L. M.; Getzoff, E. D. *Biochemistry* **1997**, *36*, 12120-12137.

(270) Einsle, O.; Messerschmidt, A.; Huber, R.; Kroneck, P. M. H.; Neese, F. *J. Am. Chem. Soc.* **2002**, *124*, 11737-11745.

(271) Copeland, D. M.; Soares, A. S.; West, A. H.; Richter-Addo, G. B. *J. Inorg. Biochem.* **2006**, *100*, 1413-1425.

(272) Yi, J.; Richter-Addo, G. B. *Chem. Commun.* **2012**, *48*, 4172-4174.

(273) Yi, J.; Orville, A. M.; Skinner, J. M.; Skinner, M. J.; Richter-Addo, G. B. *Biochemistry* **2010**, *49*, 5969-5971.

(274) Yi, J.; Safo, M. K.; Richter-Addo, G. B. *Biochemistry* **2008**, *47*, 8247-8249.

(275) Yi, J.; Heinecke, J.; Tan, H.; Ford, P. C.; Richter-Addo, G. B. *J. Am. Chem. Soc.* **2009**, *131*, 18119-18128.

(276) Yi, J.; Thomas, L. M.; Richter-Addo, G. B. *Angew. Chem.* **2012**, *124*, 3685-3687.

(277) Finnegan, M. G.; Lappin, A. G.; Scheidt, W. R. *Inorg. Chem.* **1990**, *29*, 181-185.

(278) Wei, Z.; Ryan, M. D. *Inorg. Chim. Acta* **2001**, *314*, 49-57.

(279) Lukat, P.; Rudolf, M.; Stach, P.; Messerschmidt, A.; Kroneck, P. M. H.; Simon, J.; Einsle, O. *Biochemistry* **2008**, *47*, 2080-2086.

(280) Polyakov, K. M.; Boyko, K. M.; Tikhonova, T. V.; Slutsky, A.; Antipov, A. N.; Zvyagilskaya, R. A.; Popov, A. N.; Bourenkov, G. P.; Lamzin, V. S.; Popov, V. O. *J. Mol. Biol.* **2009**, *389*, 846-862.

(281) He, C.; Ogata, H.; Knipp, M. *Biochemistry* **2010**, *49*, 5841-5851.

(282) Nutt, D. R.; Karplus, M.; Meuwly, M. *J. Phys. Chem. B* **2005**, *109*, 21118-21125.

Chapter 2: Synthesis, Characterization and Redox Behavior of Stable Ruthenium Nitrosyl Complexes with Axial O-Bound Ligands*

2.1 Introduction

Hemoproteins containing (por)Fe(*O*-ligand) (H_2por = porphyrin macrocycle) active sites are important in enzymes such as heme catalase[1,2] and in the heme acquisition HasAp[3] and IsdB[4] proteins. Further, hemoglobin variants such as Hb M Boston [α58(E7)His→Tyr][5] contain axial *O*-coordinated tyrosine ligands bound to Fe, whereas the Hb M Milwaukee [β67(E 11)Val→Glu][6] variant contains an Fe-coordinated distal carboxylate ligand.[7]

Ferrocene-containing compounds have found use in selected biological applications. For example, ferrocene and its derivatives have been used as conjugates with amino acids, peptides, proteins, DNA, RNA, PNA, carbohydrates and hormones,[8,9] and conjugates of ferrocene with some drugs including, antibiotics such as penicillins and cephalosporins have shown similar antibacterial activity as amoxicillin, carbenicillin and cephalothin.[10,11] Other drugs such as ferrocenyl aspirin,[12] the antimalarial drugs ferroquine,[13-15] as well as ferrocifen (anticancer drug tamixofen) drugs[16] have ferrocenyl moieties incorporated into them and have potential for improved biological activity. Moreover, ferrocenylethyl maleimide groups have been incoorperated into cytochrome $P450_{cam}$ (C334A) as electroactive sulfydryl-specific reagent and have shown excellent redox properties.[17,18]

* Sections of this chapter were taken from the article, "Awasabisah, *et al*., *Dalton Trans.* **2013**, *42*, 8537-8540" with permission from The Royal Society of Chemistry.

Heme catalase catalyzes the dismutation of H_2O_2 to dioxygen and H_2O.[4] The vasodilator nitric oxide (NO) binds to heme catalase and inhibits the enzyme.[19] It is interesting to note that although the X-ray structure of the NO adduct of heme catalase has been reported,[20] the metal-NO geometry could not be determined accurately due to the low occupancy (~50%) of the NO ligand at the reported resolution of the structure. Indeed, only one crystal structure of a neutral model (por)Fe(NO)(*O*-ligand) complex has been reported to date,[21] but this compound was not stable in solution precluding its detailed spectroscopic and electrochemical characterization.

To begin to gain an understanding of the properties of the general class of group 8 metalloporphyrins of the form (por)M(NO)(*O*-ligand) we have prepared, characterized and investigated the redox behaviors of several ruthenium nitrosyl porphyrin complexes, (T(*p*-OMe)PP)Ru(NO)(OC_6HF_4), (T(*p*-OMe)PP)Ru(NO)(OC(=O)R) (R = CF_3, CH_3, $CH(CH_3)_3$, $C(CH_3)_3$, *p*-NO_2-C_6H_4), (T(*p*-OMe)PP) = tetra(*p*-methoxyphenyl)porphyrinato) and (por)Ru(NO)(OC(=O)Fc) (por: T(*p*-OMe)PP); TTP: tetra(*p*-tolyl)porphyrinato); Fc = ferrocenyl group) complexes. We have also determined the redox behavior of these compounds. This chapter describes the synthesis, characterization and electrochemical studies of these compounds.

2.2 Experimental Section

All reactions were performed under an atmosphere of nitrogen using standard Schlenk glassware and/ or in an Innovative Technology Labmaster 100 Dry Box unless stated otherwise. Solvents for reactions were collected under a nitrogen atmosphere

from a solvent purification system (Innovative Technology, Inc. Newburyport, MA, PS-400-5MD) using a glass syringe.

2.2.1 Chemicals

The compounds (por)Ru(NO)(O-*i*-C_5H_{11}) (por = H_2T(*p*-OMe)PP = tetra(*p*-methoxyphenyl)porphyrin, H_2TTP = tetra(*p*-tolyl)porphyrin) were prepared as reported in literature for the preparation of the related (TPP)Ru(NO)(O-*i*-C_5H_{11}) compound.[22] Chloroform-*d* ($CDCl_3$, 99.96 atom %D) was purchased from Cambridge Isotope Laboratories, deaerated, and dried under 4 Å molecular sieves. The compounds 2,3,5,6-tetrafluorophenol (C_6HF_4OH, 97%), trifluoroacetic acid ($CF_3C(=O)OH$, 99%), trimethylacetic acid ($(CH_3)_3CC(=O)OH$, 99%), isobutyric acid ($(CH_3)_2CHC(=O)OH$, 99%), *p*-nitrobenzoic acid (*p*-NO_2-$C_6H_4C(=O)OH$, 98%), ferrocene (Fc, 98%), acetylferrocene (AcFc, 95%), ferrocenecarboxylic acid, FcC(=O)OH, 97%), tetrabutylammonium hexafluorophosphate (NBu_4PF_6, ≥99%) and anhydrous methanol (99.8%) were purchased from Sigma-Aldrich and used as received. Acetic acid ($CH_3C(=O)OH$, 99.7%) was purchased from EMD Chemicals and used as received. Dichloromethane for electrochemical experiments was purchased from Sigma-Aldrich and distilled from CaH_2 under N_2 prior to use.

2.2.2 Instrumentation/ Spectroscopy

Infrared spectra were recorded on a Bio-Rad FT-155 and/or a Tensor 27 FTIR spectrometer. ^{1}H NMR spectra were obtained on a Varian 300 MHz spectrometer at 20 °C and the signals referenced to the residual signal of the solvent employed ($CHCl_3$ at

7.24 ppm). ^{19}F NMR spectral signals were referenced to $C_6H_5CF_3$ set to −63.72 ppm. Coupling constants are reported in Hz. ESI mass spectra were obtained on a Micromass Q-TOF mass spectrometer by Dr. Steven Foster. Elemental analyses were obtained by the staff of Atlantic Microlab, Norcross, GA.

Cyclic voltammetric measurements were performed using a BAS CV 50W instrument (Bioanalytical Systems, West Lafayette, IN). In all the electrochemical experiments, a three-electrode cell was utilized and consisted of a 3.0-mm diameter Pt disk working electrode, a Pt wire counter electrode, and a Ag/AgCl reference electrode. Solutions were deaerated before use by passing a stream of N_2 gas through the solution for a minimum of 10 min. A blanket of N_2 was maintained over the solution while performing the experiments. The electrochemical experiments were performed in solutions containing 0.1 M NBu_4PF_6 and 1.0 mM of the analyte. Ferrocene, Fc (1.0 mM) was used as internal standard for the electrochemical experiments and potentials were referenced to the Fc/Fc^+ couple at 0.00 V. In cases where the Fc/Fc^+ couple overlapped with the responses of the analyte, the sample was referenced to the $AcFc/AcFc^+$ couple, which was in turn referenced to the Fc/Fc^+ couple. A Bruker Vector 22 and/ or a Tensor 27 FTIR spectrometer equipped with a mid-IR fiber-optic dip probe and liquid nitrogen cooled MCT detector (RemSpec Corporation, Sturbridge, MA, USA) was used for the infrared spectroelectrochemistry. The electrochemical experiments were performed in triplicate to determine reproducibilities. X-ray diffraction data were collected by Dr. Douglas R. Powell using a diffractometer with a Bruker APEX ccd area detector[23,24] and graphite-monochromated Mo Kα radiation (λ = 0.71073 Å).

2.2.3 Syntheses

*2.2.3.1 Preparation of (T(p-OMe)PP)Ru(NO)(OC(=O)CH$_3$) (**1**)*

To a stirred dichloromethane solution (10 mL) of (T(*p*-OMe)PP)Ru(NO)(O-*i*-C_5H_{11}) (50.3 mg, 0.053 mmol) at room temperature was added excess glacial acetic acid (0.2 mL) and the resulting mixture heated to reflux. During this period the color of the solution changed from red to brown-green. After 1 hour of refluxing the solution was allowed to cool to room temperature and the volume slowly reduced in vacuo to *ca.* 3 mL. Hexane (10 mL) was added and the solution slowly removed in vacuo to *ca.* 5mL to result in the precipitation of a solid. The supernatant was removed with a Pasteur pipette, and the residue washed twice with hexane. The resulting product was then dried in vacuo to give (T(*p*-OMe)PP)Ru(NO)(OC(=O)CH_3) (35 mg, 72% isolated yield). Slow evaporation of a CH_2Cl_2/ cyclohexane (3:1 ratio; 5 mL) solution of the product at room temperature provided suitable crystals for X-ray diffraction studies. IR (CH_2Cl_2, cm^{-1}): ν_{NO} = 1852 s, ν_{CO} = 1647 m, 1654 m (sh). IR (KBr, cm^{-1}): ν_{NO} = 1843 s, ν_{CO} = 1665; also 1606 m, 1511 m, 1461 w, 1440 w, 1350 m, 1244 s, 1174 s, 1019 s, 1009 m, 809 m, 798 m, 712 w, 610 w. ^{1}H NMR ($CDCl_3$, 300 MHz): δ 9.00 (s, 8H, *pyrrole*-H of T(*p*-OMe)PP), 8.15 (*app d*, *J* = 8.7 Hz, *J* = 7.8 Hz, 8H, *o*/ *o′*-H of T(*p*-OMe)PP), 7.29 (*app* d, *J* =7.5 Hz, *J* = 7.2 H, 8H, *m*/ *m′*-H of T(*p*-OMe)PP), 4.10 (s, 12H, OCH_3), −1.47 (s, 3H, CH_3). ESI mass spectrum (TOF): *m/z* 946.3 [M + Na^+] (45%), *m/z* 864.3 [(T(*p*-OMe)PP)Ru(NO)]$^+$ (100%). Anal. Cald for $C_{50}H_{39}N_5O_7Ru{\cdot}0.5CH_2Cl_2$: C, 62.83; H, 4.18; N, 7.25. Found: C, 62.96; H, 4.09; N, 7.38.

*2.2.3.2 Preparation of (T(p-OMe)PP)Ru(NO)(OC(=O)CH(CH$_3$)$_2$) (**2**)*

To a stirred dichloromethane solution (10 mL) of (T(*p*-OMe)PP)Ru(NO)(O-*i*-C_5H_{11}) (50.1 mg, 0.053 mmol) at room temperature was added excess isobutyric acid and the mixture was refluxed for 1 h. During this period the color of the solution changed from red to brown-green. The solution was then allowed to cool, and the volume reduced under vacuum to ~2 mL. Hexane (10 mL) was added and the product mixture was placed in a −20 ° C freezer overnight. The resulting precipitate was collected by filtration and dried under vacuum to give 39 mg (77% isolated yield) of the product. Slow evaporation of a CH_2Cl_2/cyclohexane (2:1 ratio; 5 mL) solution of the product at room temperature under nitrogen gave suitable crystals for X-ray diffraction studies. IR (CH_2Cl_2, cm^{-1}): ν_{NO} = 1850, ν_{CO} = 1637 w, 1642 w (sh). IR (KBr, cm^{-1}): ν_{NO} = 1837 s, ν_{CO} = 1654 m, 1663 m; also 1606 s, 1528 m, 1510 s, 1492 w, 1459 w, 1437 w, 1348 m, 1287 m, 1243 s, 1174 s, 1107 w, 1068 w, 1018 s, 1009 s, 848 w, 807 m, 800 m, 787 w, 715 w, 606 m, 539 m. ^{1}H NMR ($CDCl_3$, 300 MHz): δ 8.99 (s, 8H, *pyrrole*-H of T(*p*-OMe)PP), 8.21 (dd, *J* = 8.6 Hz, *J* = 2.4 Hz, 4H *o*-H of (T(*p*-OMe)PP), 8.08 (dd, *J* z= 8.1 Hz, *J* = 2.4 Hz, 4H of *o′*-H of (T(*p*-OMe)PP), 7.28 (*app* d, *J* = 10.2 Hz, *J* = 2.4 Hz, 8H, *m*-H of (T(*p*-OMe)PP), 4.10 (s, 12H, OCH_3), −0.93-(−0.90) (m, *J* = 6.3 Hz, 1H, CH), −1.72 (d, *J* = 6.3 Hz, 6H, CH_3). ESI mass spectrum (TOF): *m/z* 974.3 [M + Na$^+$] (40%), *m/z* 864.3, [(T(*p*-OMe)PP)Ru(NO)]$^+$ (100%). Anal. Cald for $C_{52}H_{43}N_5O_7Ru{\cdot}0.2CH_2Cl_2$: C, 64.77; H, 4.52; N, 7.24. Found: C, 64.80; H, 4.71; N, 7.19.

*2.2.3.3 Preparation of (T(p-OMe)PP)Ru(NO)(OC(=O)C(CH$_3$)$_3$) (**3**)*

To a stirred dichloromethane solution (10 mL) of (T(*p*-OMe)PP)Ru(NO)(O-*i*-C_5H_{11}) (50.1 mg, 0.053 mmol) at room temperature was added excess trimethylacetic acid and the mixture refluxed for 1 h. During this period the color of the solution changed from red to brown-green. The solution was allowed to cool and the volume reduced under vacuum to ~2 mL. Hexane (10 mL) was added and the solution placed in a −20 ° C freezer overnight. The resulting precipitate was collected by filtration and dried under vacuum to give 38 mg of the product (75% isolated yield). IR (CH_2Cl_2, cm^{-1}): ν_{NO} = 1849 s , ν_{CO} = 1640; IR (KBr, cm^{-1}): ν_{NO} = 1839 s, ν_{CO} = 1659 m, 1653 m; also 1607 m, 1512 m, 1496 w, 1438 w, 1349 m, 1290 m, 1244 s, 1175 s, 1019 s, 1010 m, 849 w, 808 m, 800 m, 788 w, 714 w, 608 w. ^{1}H NMR ($CDCl_3$, 300 MHz): δ 8.98 (s, 8H, *pyrrole*-H of T(*p*-OMe)PP), 8.20 (d, *J* = 7.2 Hz, 4H *o*-H of (T(*p*-OMe)PP), 8.06 (d, *J* = 7.5 Hz (*o′*-H of (T(*p*-OMe)PP), 7.30 (*app* d, *J* = 8.7 Hz, 8H, *m*-H of (T(*p*-OMe)PP), 4.09 (s, 12H, OCH_3), −1.66 (s, CH_3). ESI mass spectrum (TOF): *m/z* 988.4 [M + Na^+] (30%). *m/z* 864.3 [(T(*p*-OMe)PP)Ru(NO)]$^+$ (100%).

*2.2.3.4 Preparation of (T(p-OMe)PP)Ru(NO)(OC(=O)(C$_6$H$_4$-p-NO$_2$) (**4**)*

To a dichloromethane (10 mL) solution of (T(*p*-OMe)PP)Ru(NO)(O-*i*-C_5H_{11}) (33.0 mg, 0.035 mmol) was added *p*-nitrobenzoic acid (10 mg, 0.059 mmol). The mixture was stirred overnight during which time the color of the solution changed from red to brown. The solution was reduced to *ca.* 5 mL, and hexane (15 mL) was added. The solution was then placed in a −20 °C freezer overnight. The resulting solid was collected by filtration, washed twice with hexane and dried in vacuo to give (T(*p*-

OMe)PP)Ru(NO)(OC(=O)C_6H_4-*p*-NO_2) (29 mg, 81% isolated yield). IR (CH_2Cl_2, cm^{-1}): ν_{NO} = 1858 s, ν_{NO_2} = 1523 s, ν_{CO} = 1651w; IR (KBr, cm^{-1}): ν_{NO} = 1849 s, ν_{NO_2} = 1521 s, 1302 s, ν_{CO} = 1656 m; also 1606 s, 1511 s, 1495 m,1463 w, 1439 w, 1411 m,1349 m, 1288 s, 1245 s, 1175s, 1107 w, 1073 w, 1019 s, 1013 m, 849 w, 811 m, 799 m, 724 w, 714 w, 609 w. ^{1}H NMR ($CDCl_3$, 300 MHz): δ 9.04 (s, 8H, *pyrrole*-H of T(*p*-OMe)PP), 8.20 (*app* d, *J* = 8.1 Hz, 4H, *o*-H of (T(*p*-OMe)PP), 8.01 (*app* d, *J* = 8.7 Hz, 4H, *o′*-H of (T(*p*-OMe)PP), 7.27 (*app* d, *J* = 9.3 Hz, *J* = 7.2 Hz, 8H, *m*-H of (T(*p*-OMe)PP), 7.03 (d, *J* = 8.4 Hz, 2H, *o*-H of (C_6H_4-*p*-NO_2), 4.55 (d, *J* = 8.4 Hz, 2H, *m*- H of (C_6H_4-*p*-NO_2), 4.10 (s, 12H, OCH_3). Anal. Cald for $C_{55}H_{40}N_6O_9Ru{\cdot}CDCl_3$: C, 58.47; H, 3.68; N, 7.30. Found: C, 58.50; H, 3.71; N, 6.64.

*2.2.3.5 Preparation of (T(p-OMe)PP)Ru(NO)(OC(=O)Fc) (**5**)*

This compound was initially synthesized and investigated by the Shaw group at SIUE.

To a CH_2Cl_2 (10 mL) solution of (T(*p*-OMe)PP)Ru(NO)(O-*i*-C_5H_{11}) (31.0 mg, 0.033 mmol) in a Schlenk tube was added excess ferrocenecarboxylic acid, FcC(=O)OH (30.0 mg, 0.13 mmol). The mixture refluxed overnight in the dark during which time the solution changed from red to brown-green. The solution was cooled to room temperature, and the solvent removed in vacuo. The resulting residue was washed with anhydrous diethyl ether (5 mL); for this residue, it was necessary to use a spatula to scrape off the solid stuck on the inner walls of the reaction vessel. The supernatant was removed, and the resulting solid washed thoroughly with diethyl ether until the supernatant was no longer colored. The resulting solid was dried in vacuo to give 30 mg

(84 %) isolated yield of the product. IR (CH_2Cl_2, cm^{-1}): ν_{NO} = 1850 s, ν_{CO} = 1634 m. IR (KBr, cm^{-1}): ν_{NO} = 1840 s; also ν_{CO} = 1647 m; also 1606 m, 1511 s, 1495 m, 1464 w, 1454 w, 1374 w, 1350 m, 1288 s, 1245 s, 1174 s, 1106 w, 1072 w, 1020 s, 848 w, 811 m, 798 m, 712 w, 608 w. ^{1}H NMR ($CDCl_3$): δ 9.02 (s, 8H, *pyrrole*-H of T(*p*-OMe)PP), 8.92 (br s, 2H, Cp-*H* to adjacent C(=O)), 8.17 (*app* d, *J* = 9.9 Hz, *J*=10.5 Hz, 8H, *o*/ *o′*-H of T(*p*-OMe)PP), 8.07 (br s, 2H, Cp-*H* adjacent to C(=O)), 7.28 (*app* d, *J*= 8.1 Hz, 8H, *m*-H of (T(*p*-OMe)PP), 4.12 (br s, 5H, Cp-H), 4.10 (s, 12H, OCH_3). Anal. Cald for $C_{50}H_{45}N_5O_6FeRu{\cdot}0.5CH_2Cl_2$: C, 62.92; H, 4.08; N, 6.17. Found: C, 62.36; H, 4.24; N, 5.98.

*2.2.3.6 Preparation of (TTP)Ru(NO)(OC(=O)Fc) (**6**)*

To a dichloromethane (15 mL) solution of (TTP)Ru(NO)(O-*i*-C_5H_{11}) (100 mg, 0.10 mmol) in a Schlenk tube was added excess ferrocenecarboxylic acid, FcC(=O)OH (50.1 mg, 0.21 mmol). The mixture was refluxed for 24 hr during which time the solution changed from red to red-brown. The solution was cooled to room temperature, and the solvent slowly removed in vacuo. The resulting residue was washed with anhydrous diethyl ether (10 mL); for this residue, it was necessary to use a spatula to scrape off the solid stuck on the inner walls of the reaction vessel. The supernatant was removed and the resulting residue washed with twice with anhydrous diethyl ether. The resulting solid was dried in vacuo to give 83 mg (77 % isolated yield) of the product. IR (CH_2Cl_2, cm^{-1}): ν_{NO} = 1851 s, ν_{CO} = 1634 m. IR (KBr, cm^{-1}): ν_{NO} = 1839 s; also ν_{CO} = 1646 m; also 1529 w, 1490 w, 1450 w, 1351 m, 1288 s, 1213 w, 1180 m, 1168 m, 1108 w, 1073 w, 1018 s, 798 s, 716 w, 523 m, 512 m. ^{1}H NMR ($CDCl_3$): δ 9.02 (s, 8H, *pyrrole-H* of TTP), 8.15 (*app* d, *J* = 7.8 Hz, *J* = 2.1 Hz, 8H, *o*/ *o′-H* of TTP), 7.55 (*app*

d, J = 8.1 Hz, J = 1.8 Hz, 8H, *m*-H of (TTP), 3.01 (s, 2H, Cp-*H* adjacent to C(=O)), 2.70 (s, 12H, CH_3), 2.38 (s, 5H, Cp-*H*), 1.70 (s, 2H, Cp-*H* adjacent to C(=O)). Anal. Cald for $C_{59}H_{45}N_5O_3FeRu \cdot 0.3CH_2Cl_2$: C, 67.55; H, 4.36; N, 6.64. Found: C, 67.38; H, 4.66; N, 6.22.

2.2.3.7 Preparation of (T(p-OMe)PP)Ru(NO)(OC_6HF_4) (7)

To a stirred dichloromethane (10 mL) solution of (T(*p*-OMe)PP)Ru(NO)(O-*i*-C_5H_{11}) (50 mg, 0.053 mmol) at room temperature was added excess 2,3,5,6-tetrafluorophenol (45.7 mg, 0.284 mmol). The color of the solution changed from red to green on stirring for 30 min. After 4 h of stirring, the volume of the solvent was reduced in vacuo to 2 mL, then 10 mL of hexane was added to aid precipitation of a solid. The supernatant was discarded, and the resulting solid washed with methanol (3 x 15 mL) and the supernatant discarded each time. The solid was dried overnight in vacuo. Further purification of the solid was accomplished as follows: The solid was dissolved in a minimum amount of CH_2Cl_2 and applied on a neutral alumina (in hexane) column. The column was first eluted with hexane to remove trace unreacted species and byproducts. A green band was then eluted with CH_2Cl_2; this green band was collected and dried in vacuo to afford 43.6 mg (80% isolated yield) of the product. IR (CH_2Cl_2, cm^{-1}): ν_{NO} = 1850 s. IR (KBr, cm^{-1}): ν_{NO} = 1844 s; also 1735 w, 1685 w, 1654 m, 1636 m, 1606 m, 1559 m, 1540 w, 1507 s, 1501 s, 1472 s, 1458 m, 1438 w, 1349 m, 1305 w, 1288 m, 1245 s, 1176 s, 1093 s, 1019 s, 1010 m, 932 m, 848 w, 901 s, 718 m, 607 w. ^{19}F NMR (282 MHz, $CDCl_3$, 20 °C): δ −146.7 (m, 2F) and δ −162.2 (m, 2F). ^1H NMR (300 MHz, $CDCl_3$, 20 °C): δ 9.01 (s, 8H, *pyrrole*-H of T(*p*-OMe)PP), 8.17 (d, J = 7.2

Hz, 4H, *o*-H of (T(*p*-OMe)PP), 8.08 (d, $J_{H\text{-}H}$ = 7.5 Hz, 4H, *o′*-H of (T(*p*-OMe)PP), 7.30 (*app* t (overlapping d's), 8H, *m*/ *m′*-H of (T(*p*-OMe)PP)), 5.29 (m, 1H, *H*-C_6F_4), 4.10 (s, 12H, OCH_3). ESI mass spectrum (TOF): *m/z* = 1052.3 [M + Na^+] (10%), *m/z* = 864.3 [(T(*p*-OMe)PP)Ru(NO)]$^+$ (100%). Anal. Calc. ($C_{54}H_{37}N_5O_6F_4Ru{\cdot}CH_3OH$): C, 62.26; H, 3.89; N, 6.60 %. Found: C, 62.29; H, 3.61, N 6.74%.

*2.2.3.8 Preparation of (T(p-OMe)PP)Ru(NO)(OC(=O)CF$_3$) (**8**)*

A stirred dichloromethane (10 mL) solution of (T(*p*-OMe)PP)Ru(NO)(O-*i*-C_5H_{11}) (50 mg, 0.053 mmol) was treated with excess trifluoroacetic acid (~0.2 mL, ~3 mmol). After stirring for 1 h, the color of the solution changed from red to green. The volume of the solution was reduced to 2 mL in vacuo, and 10 mL hexane was added to aid precipitation of a solid. The supernatant was discarded and the resulting solid was washed with methanol (3 x 15 mL) and the supernatant discarded each time. The crude solid was dried overnight in vacuo. Further purification of the crude solid was accomplished by dissolving it in a minimum amount of CH_2Cl_2 and applying it on a neutral alumina (in hexane) column. The column was first eluted with hexane to remove trace unreacted species and byproducts, and then CH_2Cl_2 was then used to elute a green band which was collected and dried overnight under vacuum to 44.0 mg (85% isolated yield) of the product. IR (CH_2Cl_2, cm^{-1}): ν_{NO} = 1866 s; ν_{CO} = 1717 m. IR (KBr, cm^{-1}): ν_{NO} = 1861 s, ν_{CO} = 1719 m; also 1606 s, 1512 s, 1493 w, 1463 w, 1348 m, 1245 s, 1175 s, 1020 s, 1009 m, 810 m, 800 m, 713 w.). IR (CH_2Cl_2, cm^{-1}): ν_{NO} = 1866 s; ν_{CO} = 1717 m. IR (KBr, cm^{-1}): ν_{NO} = 1861 s, ν_{CO} = 1719 m; also 1606 s, 1512 s, 1493 w, 1463 w, 1348 m, 1245 s, 1175 s, 1020 s, 1009 m, 810 m, 800 m, 713 w. ^{19}F NMR (282 MHz,

$CDCl_3$, 20 °C): δ −78.1 (s, 3F, CF_3). ^{1}H NMR (300 MHz, $CDCl_3$, 25°C): δ 9.04 (s, 8H, *pyrrole*-H of T(*p*-OMe)PP), 8.20 (d, *J* = 7.8 Hz , 4H, *o*-H of (T(*p*-OMe)PP), 8.10 (d, *J* = 8.1 Hz, 4H, *o′*-H of (T(*p*-OMe)PP), 7.30 (*app* d, *J* = 9.0 Hz, *J* = 8.7 Hz, 8H, *m*/ *m′*-H of (T(*p*-OMe)PP), 4.10 (s, 12H, OCH_3). ESI mass spectrum (TOF): m/z = 1000.1 [M + Na^+] (5%), *m/z* = 864.1 [(T(*p*-OMe)PP)Ru(NO)]$^+$ (100%). Anal. Calc. ($C_{50}H_{36}N_5O_7F_3Ru{\cdot}CH_2Cl_2$): C, 57.69; H, 3.61; N, 6.60 %. Found: C, 57.62; H, 3.34; N, 6.60%.

2.3 Results and Discussion

2.3.1 Synthesis

The precursor compounds (por)Ru(NO)(O-*i*-C_5H_{11}) (por = T(*p*-OMe)PP), TTP) used for the preparation of the derivatives in this study have been reported previously.[22,25-27] The nitrosyl aryloxide ruthenium porphyrin complex (T(*p*-OMe)PP)Ru(NO)(OC_6HF_4) (**7**) was prepared by treating a CH_2Cl_2 solution of the precursor (T(*p*-OMe)PP)Ru(NO)(O-*i*-C_5H_{11}) compound with C_6HF_4OH (Eq. 2.1). Similarly, the compounds (T(*p*-OMe)PP)Ru(NO)(OC(=O)R) (R = CF_3 (**8**), CH_3 (**1**), $CH(CH_3)_2$ (**2**), $C(CH_3)_3$ (**3**), *p*-NO_2-C_6H_4 (**4)** and (por)Ru(NO)(OC(=O)Fc) (por = (T(*p*-OMe)PP) (**5**) and TTP (**6**)) were prepared by treating dichloromethane solutions of the precursor (por)Ru(NO)(O-*i*-C_5H_{11}) compounds with their corresponding carboxylic acids (Eq. 2.2 and 2.3).

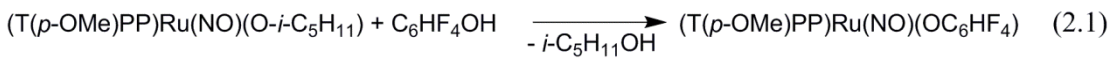

(2.1)

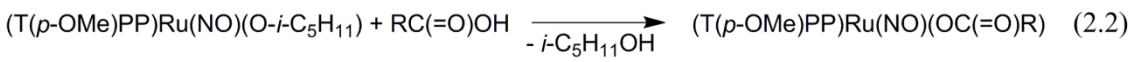

(2.2)

R = CH_3, $CH(CH_3)_2$, $C(CH_3)_3$, C_6H_4-*p*-NO_2

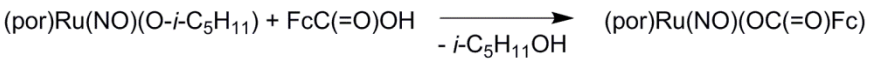

(2.3)

por = T(*p*-OMe)PP, TTP

The reactions proceed by a replacement of isoamyl alkoxide by the corresponding aryloxide or carboxylate as shown in Eq. 2.1, 2.2 and 2.3. Isolated yields ranging from 53% to 85% were obtained for the products. IR monitoring of the reactions (*vide infra*) revealed that the aliphatic carboxylic acids reacted with the precursor (por)Ru(NO)(O-*i*-C_5H_{11}) compound in less than an hour, whereas the aromatic carboxylic acids required longer reaction times to produce the desired derivatives. In particular, reactions of (T(*p*-OMe)PP)Ru(NO)(O-*i*-C_5H_{11}) with FcC(=O)OH were slower and required at least 12 h to go to completion. We attribute the slow formation of the ruthenium ferrocenecarboxylate nitrosyl complexes (**5** and **6**) to the weak acidity of ferrocenecarboxylic acid.[28-30] The products are moderately stable as solids in air at room temperature showing no signs of decomposition over several weeks as judged by IR and ^{1}H NMR spectroscopy.

2.3.2 Mass Spectrometry

The mass spectra (TOF) of all the compounds did not show the parent ions. For example, for compound (T(*p*-OMe)PP)Ru(NO)(OC_6HF_4) (**7**), the ion fragment; [(T(*p*-

OMe)PP)Ru(NO)]$^+$ (m/z 864.3) was observed, due to loss of the $C_6HF_4O^-$. The [M + Na]$^+$ peaks for the compounds were observed (see experimental).

2.3.3 Infrared Spectroscopy and Monitoring Reactions

The compounds were characterized by IR spectroscopy, and Table 2.1 lists the IR nitrosyl frequencies for the complexes and selected six-coordinate ruthenium porphyrin complexes containing the alkoxide and nitrosyl linkages. Clearly, all the *O*-bound Ru nitrosyl porphyrin complexes listed, including compounds used in this study have ν_{NO} stretching frequencies consistent with linear metal-nitrosyl linkages.[31]

The IR spectrum of the alkoxide complex **7** in CH_2Cl_2 shows a strong band at 1850 cm^{-1} assigned to ν_{NO} (KBr pellet, 1844 cm^{-1}) and the observed ν_{NO} band is in the range of those of other six-coordinate (por)Ru(NO)(OR) complexes (Table 2.1).[31] The IR spectrum of compound **1** in CH_2Cl_2 shows a strong band at 1852 cm^{-1} assigned to ν_{NO} and a ν_{CO} band at 1647 cm^{-1} (1654 sh). As a KBr pellet, compound **1** displays these bands at 1843 cm^{-1} and 1665 cm^{-1}. Similarly, IR spectrum of **8** in CH_2Cl_2 reveals a strong band at 1866 cm^{-1} and a medium intensity band at 1717 cm^{-1} assigned to the ν_{NO} and the ν_{CO} bands, respectively.

Table 2.1 Infrared nitrosyl and carbonyl stretching frequencies of some *O*-bound ruthenium nitrosyl complexes.

Compound	ν_{NO} KBr (CH_2Cl_2) /cm^{-1}	ν_{CO} KBr (CH_2Cl_2) /cm^{-1}	Ref
(T(*p*-OMe)PP)Ru(NO)(OC_6HF_4) (**7**)	1844 (1850)		32
(OEP)Ru(NO)(OPh)	(1821)		33
(OEP)Ru(NO)(O-2,6-($NHC(=O)CF_3$)C_6H_3)	1845 (1842)	1722 (1727)	33
(OEP)Ru(NO)(O-*o*-($NHC(=O)CF_3$)C_6H_4)	1835 (1830)	1718 (1731)	33
(OEP)Ru(NO)(O-NHC(=O)-C_6H_4-*o*-OH)	1835	1637 w	33
(TPP)Ru(NO)(O-2,6-($NHC(=O)CF_3$)$_2C_6H_3$)	1848	1718	33
(TPP)Ru(NO)(O-*o*-($NHC(=O)CF_3$)C_6H_4)	1845	1718	33
(T(*p*-OMe)PP)Ru(NO)(O-*i*-C_5H_{11})	1801 (1808)		*a*
(TPP)Ru(NO)(O-*i*-C_5H_{11})	1800 (1809)		34
(TTP)Ru(NO)(O-*i*-C_5H_{11})	1809		22
(OEP)Ru(NO)(O-*i*-C_5H_{11})	1788 (1800)		34
(OEP)Ru(NO)(OCH_3)	1780		35
(TTP)Ru(NO)(OCH_3)	1800		36
(OEP)Ru(NO)(OEt)	1791		37
(T(*p*-OMe)PP)Ru(NO)($OC(=O)CF_3$) (**8**)	1861 (1866)	1719 (1717)	32
(T(*p*-OMe)PP)Ru(NO)($OC(=O)CH_3$) (**1**)	1843 (1852)	1665 (1647, 1654 sh)	*a*
(T(*p*-OMe)PP)Ru(NO)($OC(=O)CH(CH_3)_2$) (**2**)	1837 (1850)	1663, 1654 sh (1637, 1642 sh)	*a*
(T(*p*-OMe)PP)Ru(NO)($OC(=O)C(CH_3)_3$) (**3**)	1839 (1849)	1659, 1653 sh (1640)	*a*
(T(*p*-OMe)PP)Ru(NO)(OC(=O)(C_6H_4-*p*-NO_2) (**4**)	1849 (1858)	1656 (1651)	*a*
(T(*p*-OMe)PP)Ru(NO)(OC(=O)Fc) (**5**)	1840 (1850)	1647 (1634)	*a*
(TTP)Ru(NO)(OC(=O)Fc) (**6**)	1839 (1851)	1646 (1634)	*a*

[a] This work

As a KBr pellet, **8** displays these bands at 1861 cm^{-1} and 1719 cm^{-1} in the corresponding IR spectrum. The higher ν_{NO} and ν_{CO} bands in **8** are consistent with the axial $CF_3C(=O)O$ ligand being a relatively poor σ-donor compared with the less electronwithdrawing $CH_3C(=O)O$ ligand. It is widely accepted that poor σ-donors and electron withdrawing groups contribute to decrease in electron density in the d_π orbital of metals and as a result reduce the extent of π-backbond donation into the empty π* orbital of the *trans* NO ligand.[35] This is the case for all the six-coordinate ruthenium porphyrin compounds studied in this work.

The compounds **2** and **3** displayed ν_{NO} bands (in CH_2Cl_2) at 1850 cm^{-1} and 1849 cm^{-1}, respectively. Their respective ν_{CO} bands (in CH_2Cl_2) were observed at 1637 (1642 sh) cm^{-1} and 1640 cm^{-1}. As KBr pellet, compound **2** displayed a strong ν_{NO} band at 1837 cm^{-1} and a medium intensity ν_{CO} band at 1663 (1654 sh) cm^{-1}. KBr samples of compound **3** displayed a ν_{NO} band 1839 cm^{-1} and a ν_{CO} band 1659 (1654 sh) cm^{-1}.

It is clear from the ν_{NO} of compounds **1**, **2** and **3** that substitution of a H with CH_3 in the carboxylate groups does not have a significant effect on the *trans* influence of the RC(=O)O group on NO although we observed a *cis*-effect[38] based on the chemical shift of the *pyrrole-H* of the porphyrin macrocycle. For example, *pyrrole-H* signals were observed at 9.00, 8.99 and 8.98 ppm for **1**, **2** and **3**, respectively (Table 2.2, *vide infra*). We also note that these ν_{NO} wavenumbers are higher than that determined for the starting (T(*p*-OMe)PP)Ru(NO)(O-*i*-C_5H_{11}) compound (1801 cm^{-1} in CH_2Cl_2).

The IR (in CH_2Cl_2) spectrum of **4** displayed a strong ν_{NO} band at 1858 cm^{-1} and a medium intensity band at 1651 cm^{-1} assigned to ν_{CO}. The IR spectrum, as KBr pellet, shows a strong band at 1849 cm^{-1} assigned to ν_{NO} and is 12 cm^{-1} lower than the ν_{NO} of **8**.

Table 2.2. ^{1}H NMR data due to porphyrin macrocycle of compounds **1-8**.

Compound	*Pyr-H*	*o-H*	*m-H*	*p*-OC*H*$_3$
1	9.00	8.15	7.29	4.10
2	8.99	8.21, 8.08	7.28	4.10
3	8.98	8.20, 8.06	7.30	4.09
4	9.04	8.20, 8.01	7.27	4.10
5	9.02	8.17, 8.07	7.28	4.10
6	9.02	8.15	7.55	
7	9.01	8.17, 8.08	7.30	4.10
8	9.04	8.20, 8.10	7.30	4.10

The ν_{CO} band was also observed in the IR spectrum at 1656 cm^{-1} and is 29 cm^{-1} lower than the reported ν_{CO} for *p*-nitrobenzoic acid.[39] In addition, bands at 1521 cm^{-1} and 1302 cm^{-1} were observed in the IR spectrum of (T(*p*-OMe)PP)Ru(NO)(OC(=O)C$_6$H$_4$-*p*-NO$_2$) and were assigned to the symmetric and asymmetric stretching frequencies (ν_{NO_2}), respectively or the nitro groups.

As already mentioned, the reaction involving (por)Ru(NO)(O-*i*-C$_5$H$_{11}$) and FcC(=O)OH to form (por)Ru(NO)(OC(=O)Fc) (**5** and **6**) required longer time time, typically >24 hours, in refluxing dichloromethane. We were able to characterize by infrared spectroscopy, an intermediate that suggests that the reaction may proceed by protonation of the Ru−(O-*i*-C$_5$H$_{11}$) group by the ferrocenecarboxylic proton and it is likely that the dissociation of the ferrocenecarboxylic acid proton (or protonation of the isoamyl alkoxide) is the first step of this reaction based on the IR spectrum (see below). Note that the pK_as of FcC(=O)OH have been determined in different media; (pK_a = 6.09 in 50% EtOH),[28] (pK_a = 7.76 in 80% MeCN),[29] pK_a = 4.20 in H$_2$O).[30] We expect the attack of the ferrocenecarboxylate anion on the Ru center to be the second step which leads to the product, eliminating *i*-C$_5$H$_{11}$OH. (Scheme 2.1).

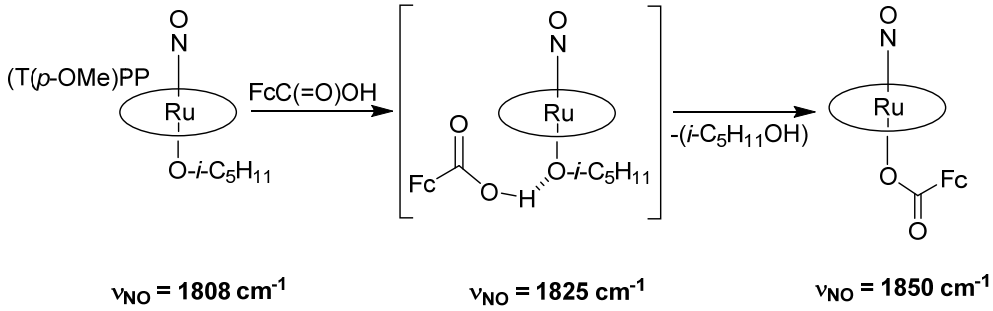

Scheme 2.1. Proposed formation of the [(T(*p*-OMe)PP)Ru(NO)(O-*i*-C_5H_{11})(HOC(=O)Fc)] intermediate during the reaction of (T(*p*-OMe)PP)Ru(NO)(O-*i*-C_5H_{11}) with FcC(=O)OH.

Indeed, IR monitoring of the reaction involving (T(*p*-OMe)PP)Ru(NO)(O-*i*-C_5H_{11}) and FcC(=O)OH suggests the complex [(T(*p*-OMe)PP)Ru(NO)(O-*i*-C_5H_{11})(HOC(=O)Fc)] as the intermediate (Scheme 2.1).

As shown in Fig. 2.1 the IR spectrum of a mixture of the precursor (T(*p*-OMePP)Ru(NO)(O-*i*-C_5H_{11}) and FcC(=O)Fc) in CH_2Cl_2 obtained after 5 minutes of stirring at room temperature shows a new ν_{NO} band at 1825 cm^{-1} (labelled *) which is 27 cm^{-1} higher than that of the starting (T(*p*-OMe)PP)Ru(NO)(O-*i*-C_5H_{11}) compound. We assign the 1825 cm^{-1} band to the ν_{NO} of the intermediate adduct [(T(*p*-OMe)PP)Ru(NO)(O-*i*-C_5H_{11})(HOC(=O)Fc)]. Similarly, we observed a ν_{NO} band at 1830 cm^{-1} in the [(T(*p*-OMe)PP)Ru(NO)(O-*i*-C_5H_{11})(HOC(=O)$CH(CH_3)_2$)] reaction (not shown) by reaction of the precursor (T(*p*-OMe)PP)Ru(NO)(O-*i*-C_5H_{11}) with $CH_3C(=O)OH$.

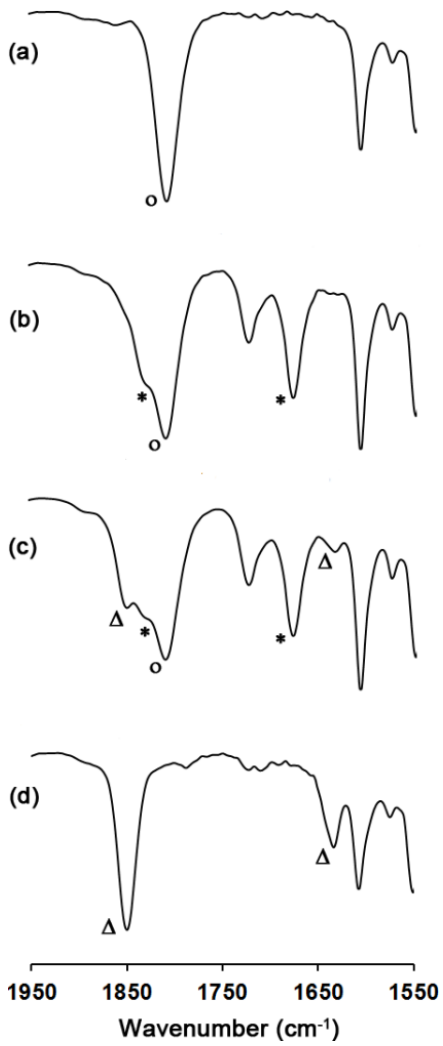

Figure 2.1. IR monitoring (in CH_2Cl_2) of the reaction involving (T(*p*-OMe)PP)Ru(NO)(O-*i*-C_5H_{11}) (ν_{NO} = 1808 cm^{-1} labelled **o** in **spectrum a**) with ferrocenecarboxylic acid, FcC(=O)OH to give (T(*p*-OMe)PP)Ru(NO)(OC(=O)Fc) (ν_{NO} =1850 cm^{-1}, ν_{CO} = 1634 cm^{-1} labelled Δ in **spectrum d**; after 12 h, and workup). **Spectrum a:** before addition of FcC(=O)OH. **Spectrum b**: after addition of FcC(=O)OH and stirring for 5 minutes showing the intermediacy of [(T(*p*-OMe)PP)Ru(NO)(O-*i*-C_5H_{11})(HOC(=O)Fc)] (labelled *; ν_{NO} =1825 cm^{-1}, ν_{CO} = 1677 cm^{-1}), starting (T(*p*-OMe)PP)Ru(NO)(O-*i*-C_5H_{11}) and starting FcC(=O)OH; **spectrum c**: After 1 h of reaction showing mixture of product, intermediate, and reactants.

In the related (OEP)Os(NO)(OEt) complex, the starting ν_{NO} band at 1759 cm^{-1} (CH_2Cl_2) shifted by 69 cm^{-1} to 1828 cm^{-1} (CH_2Cl_2) when it was protonated to the [(OEP)Os(NO)(HOEt)]BF_4 complex. The shift was attributed to less Os−NO

backbonding in the cationic product.[40] We propose that the Ru−NO backbonding will similarly diminish in the [(T(*p*-OMe)PP)Ru(NO)(HO-*i*-C_5H_{11})(OC(=O)Fc)] such that the ν_{NO} occurs at a higher wavenumber than (T(*p*-OMe)PP)Ru(NO)(O-*i*-C_5H_{11}). In a control experiment, we prepared the complex [(T(*p*-OMe)PP)Ru(NO)(HO-*i*-C_5H_{11})]BF_4 by treating the precursor [(T(*p*-OMe)PP)Ru(NO)(O-*i*-C_5H_{11})] compound with HBF_4 and observed a new band at 1880 cm^{-1} ($\Delta\nu_{NO}$ = 72 cm^{-1}) assigned to ν_{NO}. This large shift may be attributed to a complete proton transfer from HBF_4 to (T(*p*-OMe)PP)Ru(NO)(O-*i*-C_5H_{11}) in contrast to a partial protonation in the case of the carboxylate intermediates.

The compound **6** displays similar IR spectral features as compound **5** (Table 2.1). The ν_{NO} (KBr) values of the carboxylate complexes parallel their respective pK_as (obtained from ref. [41]) of the conjugate acids of the carboxylate ligand, with **8** (pK_a = 0.5) displaying the highest ν_{NO}. Thus, in order of decreasing ν_{NO} values, the compounds may be arranged as: **8** (pK_a = 0.5) > **4** (pK_a = 3.441) > **5** ≈ **6** (pK_a = 4.2)[30] > **1** (pK_a = 4.756) ≈ **2** (pK_a = 4.853) ≈ **3** (pK_a = 5.031).

To the best of our knowledge, the ν_{NO} band of 1861 cm^{-1} obtained for the compound **8**[32] is the highest ν_{NO} reported for a neutral six coordinate ruthenium nitrosyl porphyrin complex. This high ν_{NO} band is attributed to the stronger electron withdrawing effect of the trifluoroacetate group than the other ligands. In addition, the ν_{CO} band in **8** is downshifted to 1719 cm^{-1} from the ν_{NO} = 1783 cm^{-1} of the starting FcC(=O)OH compound.

2.3.4 ^{1}H NMR and ^{19}F NMR Spectroscopy

^{1}H NMR and ^{19}F NMR spectroscopy were used to characterize the compounds and to help ascertain their purity. The ^{1}H NMR spectrum of **7** in $CDCl_3$ showed the expected peaks due to the porphyrin macrocycle (Table 2.2), and a multiplet at 5.29 ppm assigned to $C_6\mathit{H}F_4O$. In comparison, a multiplet at 6.00 ppm was observed in the ^{1}H NMR spectrum of (OEP)Ru(NO)($SC_6\mathit{H}F_4$) in $CDCl_3$.[42] The ^{19}F NMR spectrum of **8** in $CDCl_3$ shows two multiplets at −146.7 ppm and −162.2 ppm; the corresponding two multiplets for $C_6H\mathit{F}_4OH$ are at −140.7 ppm and −163.6 ppm. The ^{19}F NMR spectrum of **8** thus suggests that the ligand is bound to the metal in solution. The ^{1}H NMR spectrum of **7** in $CDCl_3$ displayed peaks due solely to the porphyrin macrocycle (Table 2.2), and the ^{19}F NMR spectrum displayed a single peak at −78.1 ppm due to the axial $C\mathit{F}_3C(=O)O$ ligand.

The ^{1}H NMR spectrum of compound **1** in $CDCl_3$, displayed the expected peaks due to porphyrin macrocycle (Table 2.2) as well as a single peak at a shielded region of −1.47 ppm assigned to the bound $C\mathit{H}_3C(=O)O$ ligand. Similarly, **2** and **3** showed the expected peaks due to the porphyrin macrocycles in their ^{1}H NMR spectra (Table 2.2), and the additional signals resulting from the various carboxylate ligands. The ^{1}H NMR spectrum of compound **2** showed a doublet at −1.72 ppm assigned to $(C\mathit{H}_3)_2CHC(=O)O$ which is higher upfield compared to the $C\mathit{H}_3$ signal in **1**. This is expected considering the methyl group in **2** is one bond further from the carbonyl functional group. In addition, a multiplet centered at −0.92 ppm was observed and assigned to $(CH_3)_2C\mathit{H}C(=O)O$. Not surprisingly, compound **3** showed a singlet at −1.66 ppm and was assigned to the axial $(C\mathit{H}_3)_3CC(=O)O$ ligand.

Compound **4** showed the peaks due to the porphyrin macrocycle (Table 2.2) and two doublets at 4.55 ppm and 7.03 ppm in the ^{1}H NMR spectrum which were assigned to the H of *p*-NO_2-C_6H_4C(=O)O adjacent to NO_2 (*m-H*) and the H at the *ortho*-position (*o-H*), respectively. The doublet at 4.55 ppm is particularly quite surprising since the ^{1}H NMR of the starting carboxylic acid (*p*-NO_2-C_6H_4C(=O)OH) shows only one signal; a multiplet at 8.50 ppm (assigned to the aromatic Hs) and a single broad peak observed at 6.60 ppm (assigned to carboxylic *H*). The upfield shift of the two aromatic protons in **4** is an indication of ligand binding to the Ru and the phenyl ring of *p*-NO_2-C_6H_4C(=O)O aligning in the direction of the magnetic field with one set of protons (at 4.55 ppm) more shielded than the other (at 7.03 ppm).

The ^{1}H NMR spectrum of compound **5** displayed peaks due to the porphyrin macrocycle and three additional peaks at 8.92 ppm and 8.07 ppm assigned to the cyclopentadienyl-*H* adjacent to the carboxyl group (i.e Cp'-*H*), and a peak at 4.12 ppm assigned to the unsubstituted cyclopentadienyl-*H* group (i.e Cp-*H*) of the FcC(=O)O ligand (Fig. 2.2).

Clearly, there is a large shift of the proton signals of the two Cp'-*H* protons of **5** to the deshielded region. A comparison of this spectrum with the ^{1}H NMR spectrum of the neutral FcC(=O)OH in $CDCl_3$ showed that this shift ($\Delta\delta$) is +4 ppm for the more downfield Cp'-*H* signal and +3.6 ppm for upfield Cp'-*H* signal. These large downfield shifts (*cf.* with FcC(=O)OH) may be attributed to the alignment of the hydrogens of the

FcC(=O)O ligand in solution in the direction of the applied magnetic field.

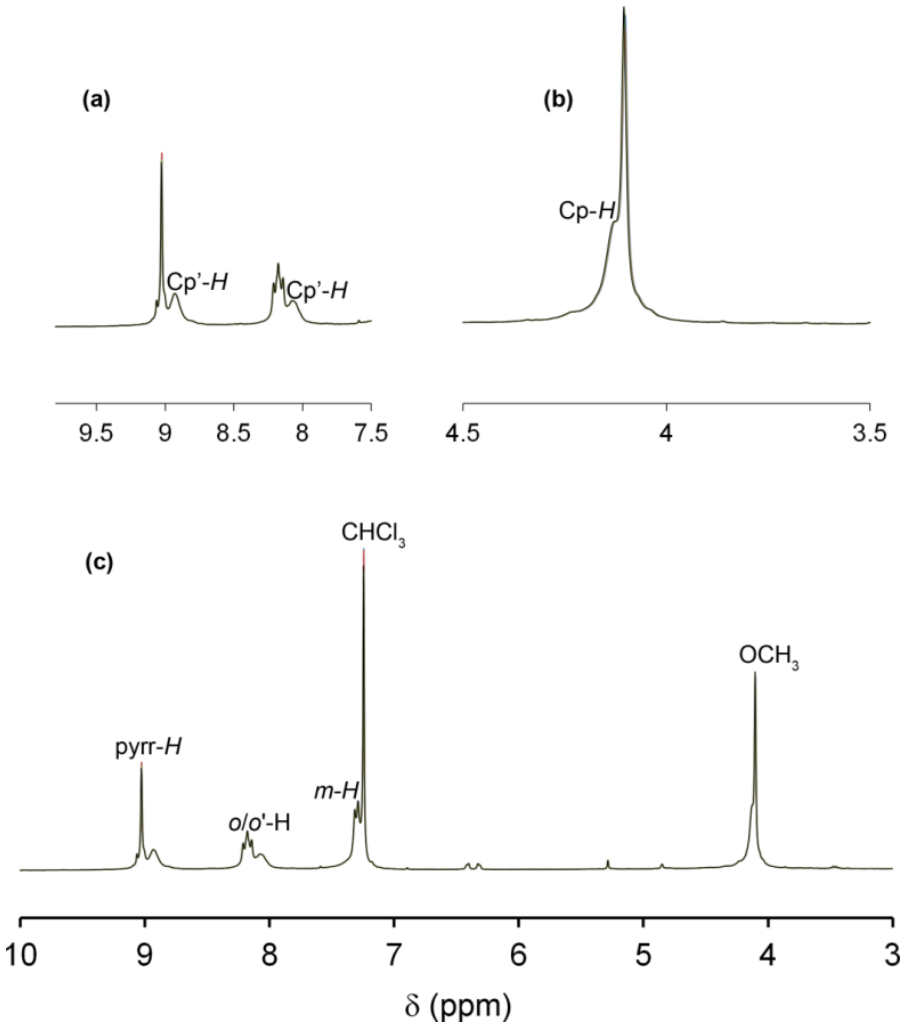

Figure 2.2. The ^{1}H NMR spectra of (T(*p*-OMe)PP)Ru(NO)(OC(=O)Fc) (**5**). (a) and (b) are expanded spectra showing the peaks due to the hydrogens on the substituted cyclopentadienyl ring (Cp'-*H*) and the unsubstituted cyclopentadienyl ring (Cp-*H*), respectively of the FcC(=O)O ligand (c) Full spectrum from 3-10 ppm.

Furthermore, similar unexpected proton chemical shifts have been observed in some cyclophanes[43] and some porphyrin compounds. For example, in the porphyrin dimer, bis-(octaethylporphyrinyl)ethylene, the ethylene proton signals were observed at 9.69 and 7.66 ppm for the *cis* and *trans* isomers, respectively. The downward shift of the chemical shift of the ethylene proton was attributed to the "face-to-face" spacial

orientation of the porphyrin macrocycle in the *cis* isomer such that the ethylene protons are located in the same plane of ring current of the porphyrin macrocycle.[44] A similar effect has been observed in the nickel complex of the bis-(octaethylporphyrinyl)ethylene compound.[45,46] Interestingly, the Cp-*H* signal of the FcC(=O)O ligand in **5** displays a peak at 4.12 ppm which is a downfield shift ($\Delta\delta$ = + 0.2 ppm) from the Cp-*H* signal of the neutral FcC(=O)OH compound implying a reduced ring current effect imposed by the porphyrin macrocyle on the unsubstituted Cp in compound **5**.

The ^{1}H NMR spectrum of **6** similarly showed peaks due to the porphyrin macrocycle (Table 2.2). However, quite unexpectedly, the signals due to the Cp-*H* and Cp'-*H* in **6** were observed at higher upfield regions than those of the free FcC(=O)OH ligand. That is, the Cp'-*H* adjacent C(=O) signals were observed at upfield regions of 2.70 ppm and 1.70 ppm; and the unsubstituted Cp-*H* signal was observed at 2.38 ppm. Similar upfield shifts of the Cp-*H* have been observed in the ^{1}HNMR spectrum of the complexes (por)Sn(OC(=O)Fc)$_2$ (por = OEP[47], TPP[48]).

We would like to note that the *cis*-effect based on the chemical shifts of the pyrrole-*H* is evident in these complexes. As shown in Table 2.2, the chemical shifts of the pyrrole-*H* parallel the σ-donating ability of the axial *O*-bound ligand. For example, in **1** the *pyr-H* signal was observed at 9.00 ppm. In the related complex **8**, the *pyr-H* signal was observed at a higher chemical shift of 9.04 ppm which parallels the electrondonating abilities of $CH_3C(=O)O$ and $CF_3C(=O)O$, the former being the better electrondonating group. Similarly, compounds **4** and **7** displayed *pyr-H* signals at 9.04 and 9.01 ppm, respectively. Furthermore, the chemical shifts decrease by alkyl

substitution of the axial ligand and increases by 0.04 ppm when hydrogen atoms are substituted for fluorine atoms (*cf.* **1** and **8**).

2.3.5 X-ray Crystallography

The crystal structures of compounds **1**, **2**, **8**, **5**, **6**, and **7** were obtained by X-ray crystallography. Selected bond lengths (Å) and bond angles (°) for the molecular structures and selected six-coordinate (por)Ru(NO)(*O*-ligand) are listed in Table 2.3.

Table 2.3. Selected bond lengths (Å), Ru displacement (in Å x 100) and bond angles (°) in **1**, **2**, **5**, **6**, **7** and **8**.

Compound	Ru−N(O)	Ru−O(axial)	∠Ru−N−O	∠Ru−O−C(axial)	Δ_{N4}Ru
1	1.850(12)	1.909(10)	169.6(14)	132.7(10)	4
2	1.874(15)	1.805(11)	174.1(12)	127.3(13)	0
5	1.753(2)	1.9959(19)	179.7(3)	131.79(19)	10
6	1.738(6)	1.971(5)	169.5(7)	135.0(5)	10
7[a]	1.739(3)	2.000(3)	173.1(3)	127.5(2)	0
8[a]	1.986(11)	1.773(11)	178.3(9)	134.0(9)	11

[a] Ref. [32] Δ_{N4}Ru: Displacement of Ru from the porphyrin 4N mean plane.

The solid-state structures of these formally {RuNO}^{6} derivatives[49] listed in Table 2.3 reveal a near linear Ru−N−O linkages with bond angles ranging between 169 and 180° (Fig. 2.3a, 2.4a, 2.5, 2.6, 2.7 and 2.9). For example, X-ray crystal structure of **1** reveals a near linear Ru−N−O linkage of 169.6(14)° (Fig. 2.3a).

(a)

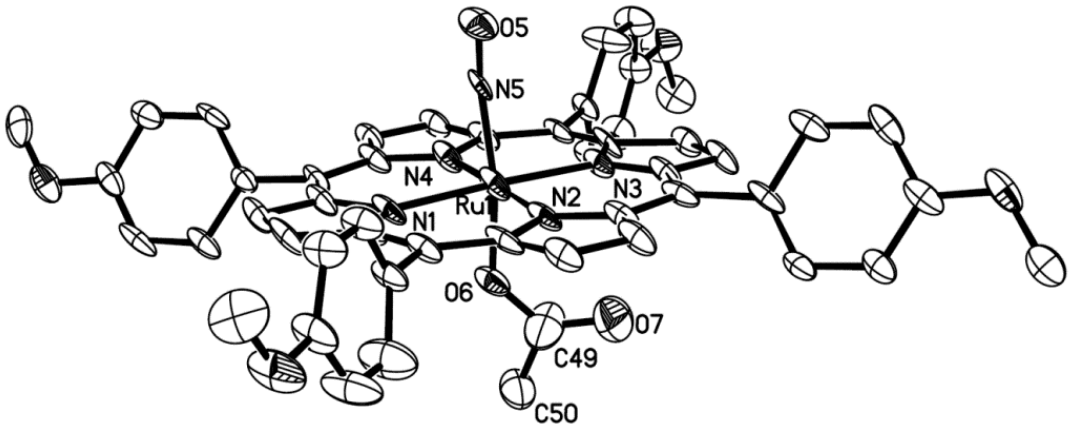

(b)

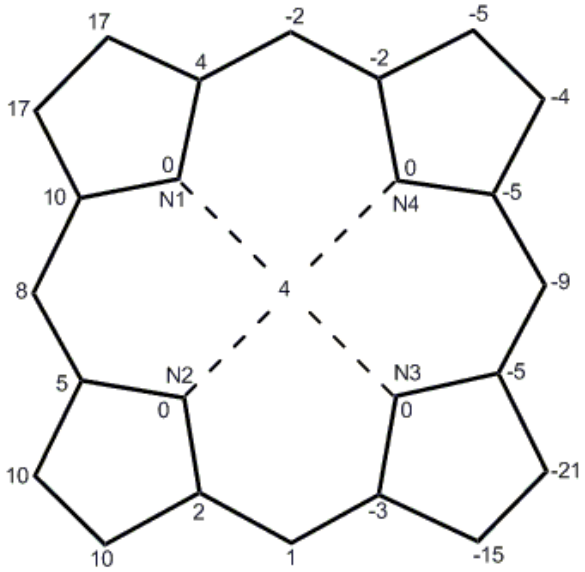

Figure 2.3. (a) Molecular structure of compound **1**. Hydrogen atoms and disordered molecules have been omitted for clarity. (b) Perpendicular atom displacements (in Å × 100) of the porphyrin core from the porphyrin 4N mean plane.

(a)

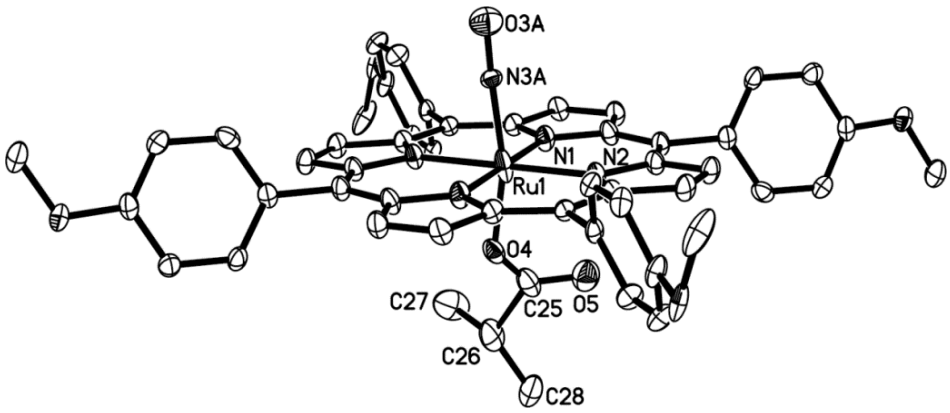

(b)

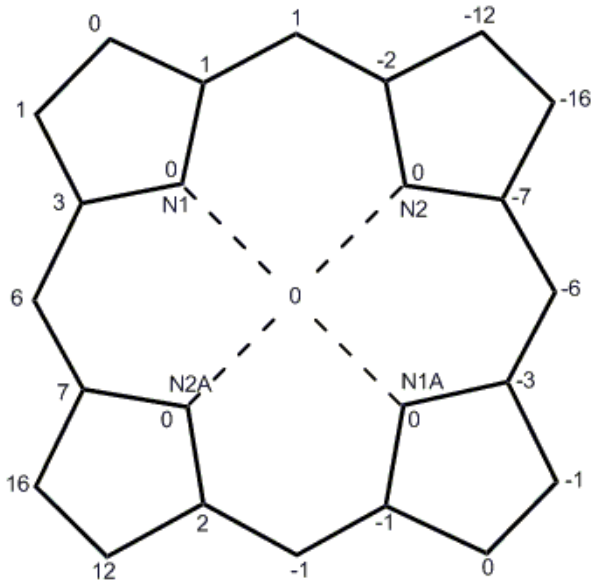

Figure 2.4. (a) Molecular structure of **2**. Hydrogen atoms and disordered molecules have been omitted for clarity. (b) Perpendicular atom displacements (in Å × 100) of the porphyrin core from the porphyrin 4N mean plane.

(a)

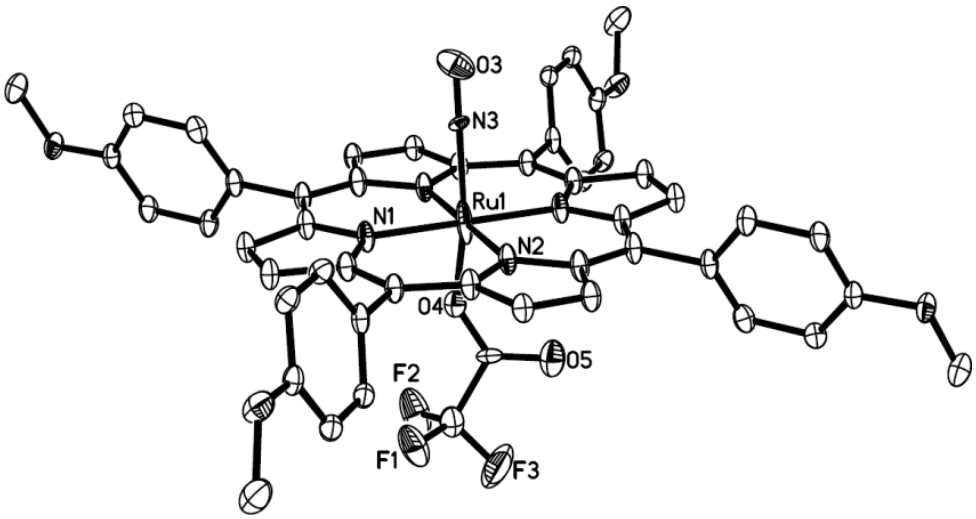

(b)

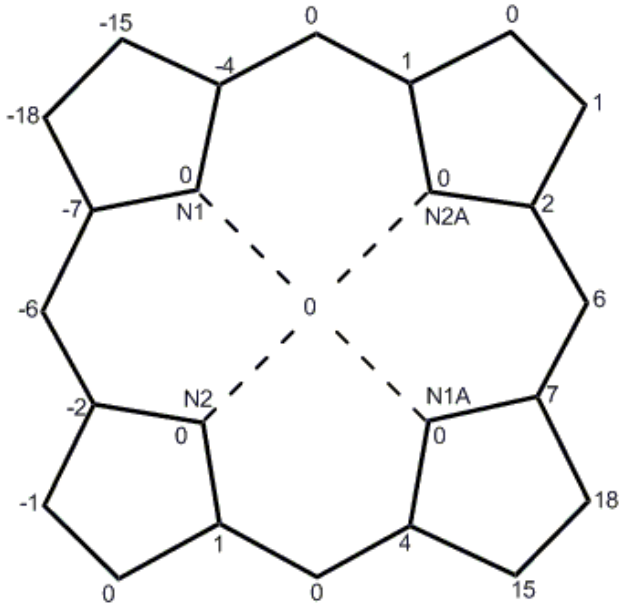

Figure 2.5. (a) Molecular structure of compound **8**. Hydrogen atoms have been omitted for clarity. (b) Perpendicular atom displacements (in Å × 100) of the porphyrin core from the porphyrin 4N mean plane.

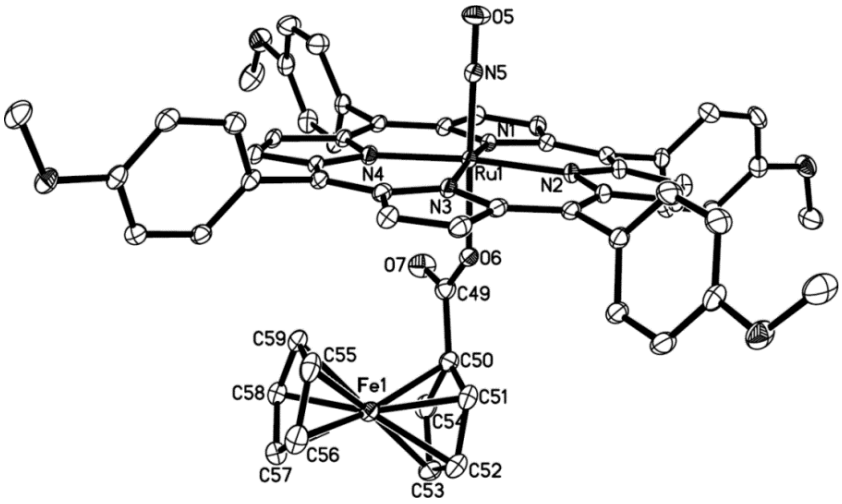

Figure 2.6. Molecular structure of compound **5**. Hydrogen atoms have been omitted for clarity.

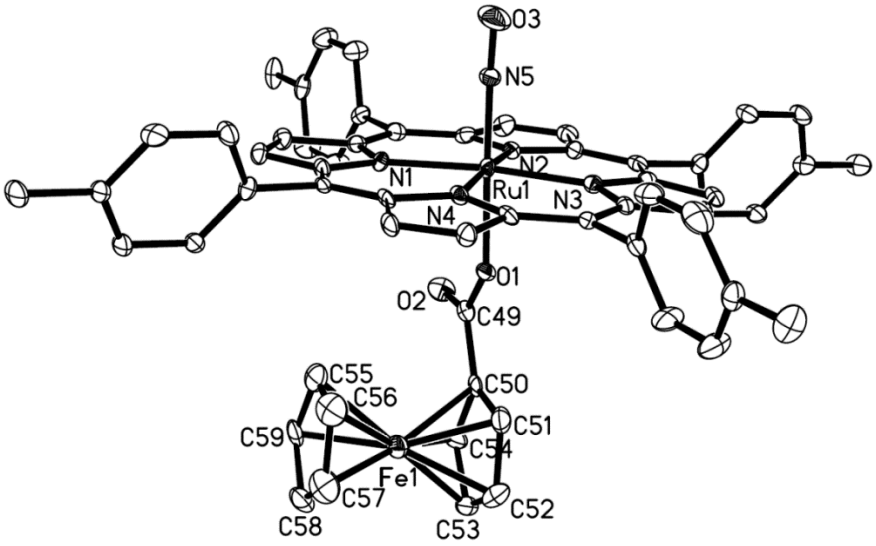

Figure 2.7. Molecular structure of compound **6**. Hydrogen atoms have been omitted for clarity.

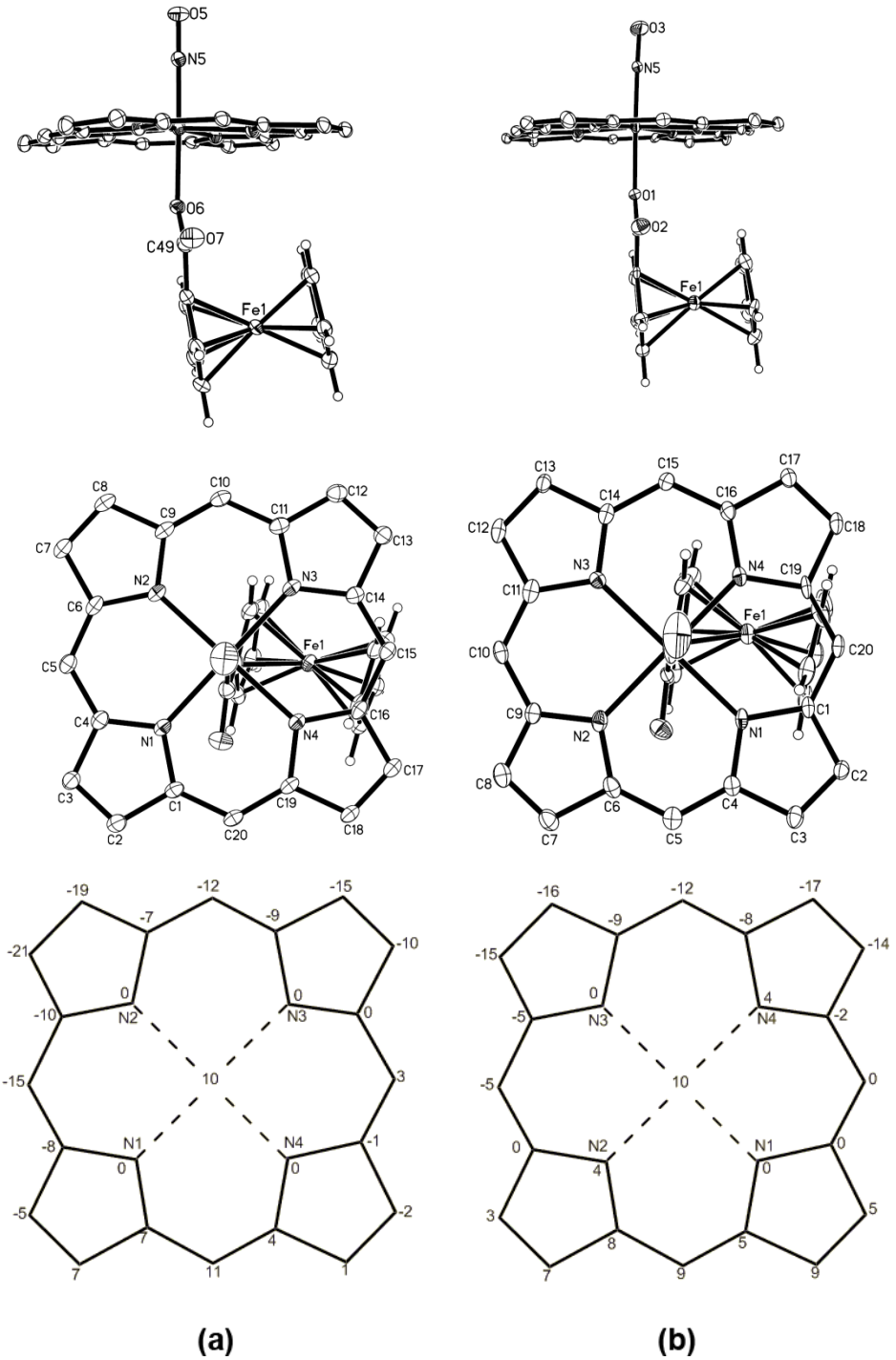

Figure 2.8. Top: Side view; Middle: Top view from NO side; Bottom: Perpendicular atom displacements (in Å × 100) of the porphyrin core from the 4N mean planes. (T(*p*-OMe)PP)Ru(NO)(OC(=O)Fc) (**5**) (Left) and (TTP)Ru(NO)(OC(=O)Fc) (**6**) (Right). The phenyl rings and porphyrin hydrogens are omitted for clarity.

(a)

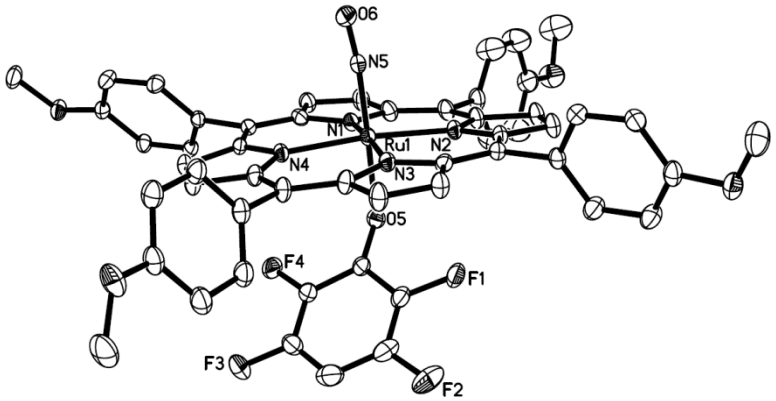

(b)

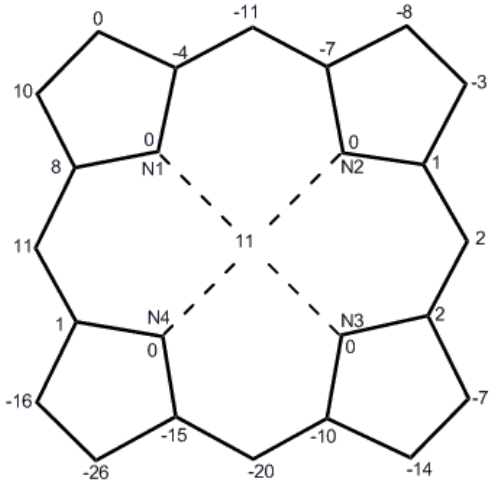

Figure 2.9. (a) Molecular structure of compound **7**. Hydrogen atoms have been omitted for clarity. (b) Perpendicular atom displacements (in Å × 100) of the porphyrin core from the 4-N mean planes of the porphyrin macrocycle.

Other structural features of the compounds are worthy of note. First, the axial carboxylate ligands are bonded to Ru via via one of its oxygens in a η^1-O fashion. Second, Ru−O bond lengths in the aliphatic carboxylate complexes **1** (1.909 (10) Å) and **2** (1.805 (11) Å) are shorter than those of the more bulky and better σ-donating

ferrocenecarboxylate coordinated complexes, **5** (1.9959(19) Å) and **6** (1.971(5) Å. These Ru−O bond lengths are relatively shorter than that **7** (2.000(3)); and relatively longer than that of **8** (1.773(11) Å) due to the more electron-donating ability of the aryloxide ligand than the carboxylate ligands for backdonation into the RuNO moiety. Conversely, the Ru−N(O) bond lengths in compounds **1** (1.850(12) Å) and **2** (1.874(15) Å) are longer than those of **7** (1.739(3) Å) [32] and (T(*p*-OMe)PP)Ru(NO)Cl (1.790(17) Å)[27] due to the same reasons discussed above. We note that the Ru−O bond lengths in **5** and **6** are shorter than those of the related *bis*-η^1-O_2CFc tin(IV) porphyrin complexes (TPP)Sn(OC(=O)Fc)$_2$ (2.0730(16) Å)[48] and (OEP)Sn(OC(=O)Fc)$_2$[47] (2.0731(16) Å).

Crystal structures of some η^2-OC(=O)Fc coordinated Ru non-porphyrin complexes including those of [Ru(η^2-OC(=O)Fc)(CH=CH$_2$)(CO)(PPh$_3$)$_2$],[50] [Ru(η^2-O_2CFc)(dppm)$_2$](PF$_6$), [Ru(η^2-O_2CFc)(dppp)$_2$](PF$_6$), [Ru(η^2-O_2CFc)(dppe)$_2$](PF$_6$)·2MeOH, [Ru(η^2-O_2CCH$_3$)(dppm)$_2$](PF$_6$), [Ru(η^2-O_2CCH$_3$)(dppe)$_2$](PF$_6$)·2H$_2$O, [Ru(η^2-O_2CCH$_3$)(dppp)$_2$](PF$_6$)·MeOH,[51] and [Ru(η^2-O_2CRc)(dppe)$_2$](PF$_6$)[52] have Ru−O bond lengths >2 Å. The rather short axial Ru−O bond length of 1.9959(19) and 1.971(5) Å in **5** and **6**, respectively as compared to the (por)Sn(OC(=O)Fc)$_2$ complexes (> 2 Å) may be due to the inverse *trans* influence of NO (compared to FcC(=O)O) at the axial position bearing in mind that they contain different metals in different oxidation states.

We note that the Ru atom in compounds **2** (Fig. 2.4b) and **8** (Fig. 2.5b) lie in the plane of the porphyrin 4N atom plane. However, in compounds **1** (Fig. 2.3b) and **7** (Fig. 2.9b) the Ru atom is displaced away from the plane towards N of NO by 0.04 Å and

0.11 Å, respectively. Furthermore, the porphyrin macrocycles of compounds **1**, **2**, **7** and **8** are each distorted from the porphyrin 4N plane.

The X-ray crystal structures of **5** and **6** show non-planar porphyrin macrocycles (bottom of Fig. 2.8) with the Ru atom displaced towards NO by 0.10 Å from the mean porphyrin 4N plane in **5** and **6**. A comparison of the solid state molecular geometry of **5** and **6** show that the ferrocenyl moiety is more tilted towards the porphyrin plane in **5** than it is in **6** (Fig. 2.8 Top). In particular, the substituted cyclopentadienyl ring, Cp' is slightly tilted away from the center of the porphyrin ring in **5**, and the Cp' plane almost bisects the porphyrin ring in **6** (Fig. 2.8, Middle). The Cp plane in compound **5** is at an angle ~90° with the porphyrin plane at C15 and C16 and is close to the *meso*-carbon. Although this difference in structure of **5** and **6** appear insignificant in the solid state structure, however, in solution, it is possible that the FcC(=O)O ligand in these groups may be oriented in different positions relative to the porphyrin plane such that the Cp-*H* experience different porphyrin ring effect and thus, different ^{1}HNMR chemical shifts.

2.3.6 Electrochemistry

2.3.6.1 Cyclic Voltammetry (CV)

The redox behavior of compounds **1**-**8** were investigated by cyclic voltammetry experiments. Fig. 2.10 shows the cyclic voltammogram of **7** in CH_2Cl_2 with 0.1 M NBu_4PF_6 as support electrolyte at a scan rate of 200 mV/s. Fig. 2.10 reveals that **7** undergoes a reversible one-electron oxidation at $E^{\circ\prime}$ = +0.59 V *vs.* the Fc/Fc^+ couple to generate the monocation $[\mathbf{7}]^+$. This $E^{\circ\prime}$ value for the first oxidation of **7** is more positive

by 20 mV than that determined for the related (T(*p*-OMe)PP)Ru(NO)Cl (+0.57 V) under similar experimental conditions.[27]

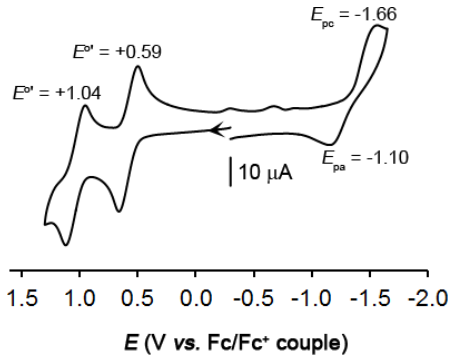

Figure 2.10 Cyclic voltammogram of **7** showing two oxidations and one reduction. Conditions: 1 mM analyte, 200 mV/s scan rate, 0.1 M NBu_4PF_6 support electrolyte, room temperature.

Further, compound **7** undergoes a second one-electron oxidation at $E^{o'}$ = +1.04 V *vs.* the (Fc/Fc^+) couple and this potential is 30 mV larger than that determined for the second oxidation of the compound (T(*p*-OMe)PP)Ru(NO)Cl[27] and this difference in the second oxidation potentials is attributed to the difference in electrondonating abilities of the axial ligands. The ligand C_6HF_4O in compound **7** is overall more electron-donating than Cl in (T(*p*-OMe)PP)Ru(NO)Cl. One implication of the difference in the second oxidation potential is that the axial ligands in these systems are still bound to the ruthenium center after second oxidation which rules out the possibility of axial ligand dissociation.

Similarly, compound **8** undergoes a reversible one-electron first oxidation at $E^{o'}$ = +0.62 V *vs.* Fc/Fc^+ (Fig. 2.11, Bottom). Compound **8** undergoes a second oxidation at a potential of $E^{o'}$ = +1.04 V. The compound **8** also displays a reduction peak at E_{pc} =

−1.66 V (Fig. 2.11) which exhibits poor chemical reversibility; a corresponding weak return peak was observed at $E_{pa} = -1.17$ V.

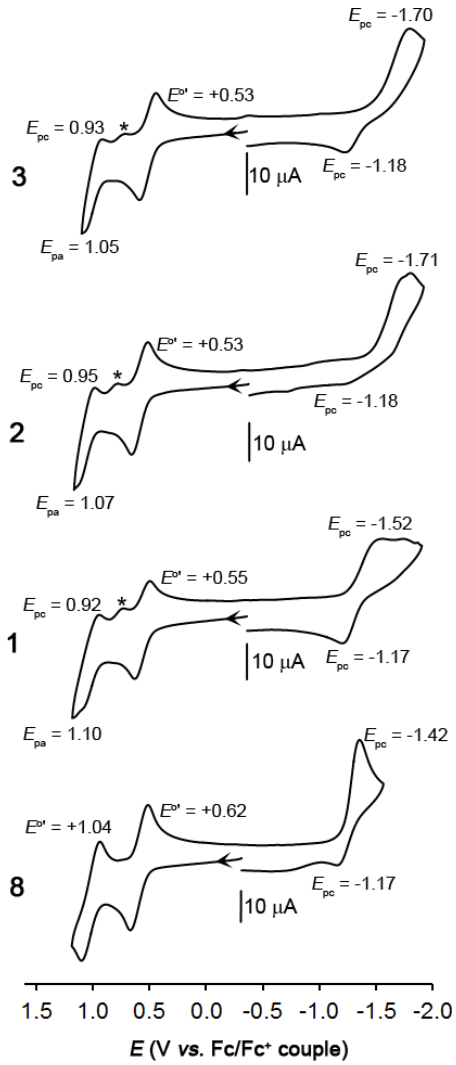

Figure 2.11. Cyclic voltammogram of compounds **1**-**3** and **8** (1 mM) in CH_2Cl_2 containing 0.1 M NBu_4PF_6 support electrolyte and at a scan rate of 200 mV/s at room temperature.

We note that the cyclic voltammograms of compounds **1**, **2**, and **3** (Fig. 2.11) obtained in CH_2Cl_2 with 0.1 M NBu_4PF_6 as support electrolyte at a scan rate of 200 mVs^{-1} and at room temperature show similar redox behavior as those of compound **8**.

Thus, the aliphatic carboxylate complexes have reversible first oxidations at $E^{\circ\prime}$ = +0.55, +0.54 and +0.53 V for compounds **1**, **2** and **3**, respectively. Their respective second oxidations were observed at E_{pa} = 1.10, 1.07 and 1.05 V. Note that a small return peak (labelled *) was observed at *ca.* 0.72 V after second oxidation which we tentatively associate with the return peak of the product generated following dissociation of a fraction of the axial carboxylate ligand.

The three other aliphatic carboxylate complexes **1**, **2** and **3** each displayed poor chemically reversible reduction peaks at $E_{pc} \sim -1.5$ to -1.7 V and $E_{pa} \sim -1.2$ (Table 2. 4). Among the aliphatic carboxylate complexes, in general, the redox potentials parallel the pK_as of their corresponding RC(=O)OH precursors. Compound **8** (pK_a of $CF_3C(=O)OH$ = 0.5)[41] is overall less electron rich than the other aliphatic complexes **1**, **2** and **3** (pK_as ~ 4.8 in water)[53] and thus, has a more positive oxidation potential and a less negative reduction potential. However, it was observed that substitution of the hydrogen atoms with a methyl group in the axial ligands of the aliphatic complexes had little effect on the redox potentials (Table 2.4, entries 2 and 3), consistent with the observation that substitution of hydrogen with a methyl group did not significantly change the pK_as of the precursor carboxylic acids (pK_a of $CH_3C(=O)OH$ and $(CH_3)_2CHC(=O)OH$ are 4.9 and 5.0, respectively).

Table 2.4. Electrochemical potentials[a] for the compounds **1**, **2**, **3**, **4**, **7**, and **8** in CH_2Cl_2.

Compound	1st oxid./ $E^{\circ\prime}$	2nd oxid./ $E^{\circ\prime}$	Red.[c] E_{pc}/ E_{pa}
1	0.55 (135)	1.10/ 0.92[c]	−1.52/ −1.17
2	0.53 (134)	1.07/ 0.95[c]	−1.71/ −1.18
3	0.53 (124)	1.05/ 0.93[c]	−1.70/ −1.18
4	0.59 (153)	1.03 (155)	−1.53/ −1.19
7	0.59 (150)[b]	1.04 (152)	−1.66/ −1.11 [b]
8	0.62 (167) [b]	1.04 (164)	−1.42/ −1.17 [b]

[a] Potentials are in volts, and are referenced to the Fc/Fc^+ set at 0.00 V. Experimental conditions: 1 mM analyte, 200 mV/s scan rate, 0.1 M NBu_4PF_6. The numbers in parenthesis represent the ΔE_p values (in mV) for the redox couples which compare with those of Fc/Fc^+. [b] Also reported in ref. [32] [c] E_{pa}/ E_{pc} potentials. [d] E_{pa}/ E_{pc} potentials.

The cyclic voltammograms of compound **4** in CH_2Cl_2 with 0.1 M NBu_4PF_6 as support electrolyte at a scan rate of 200 mVs^{-1} is shown in Fig. 2.12.

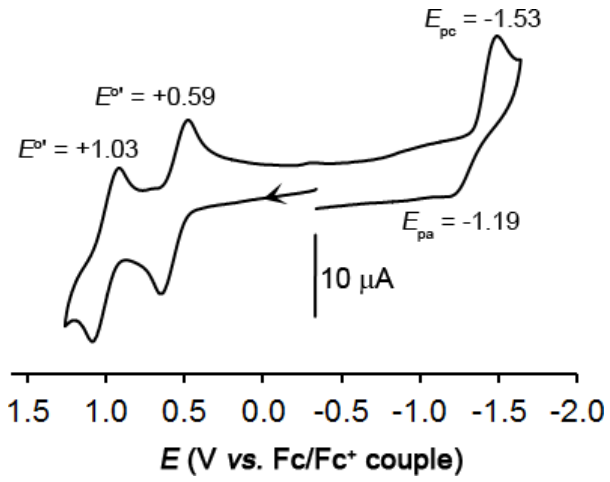

Figure 2.12 . Cyclic voltammogram of **4**. Conditions: 1 mM analyte, 200 mV/s scan rate, 0.1 M NBu_4PF_6 support electrolyte, room temperature.

The voltammogram reveals that compound **4** undergoes a reversible first oxidation at $E^{\circ\prime}$ = 0.59 V *vs.* the Fc/Fc^+ couple to generate the monocation $[\mathbf{4}]^+$. This potential compares with that obtained for **7**, also at $E^{\circ\prime}$ = 0.59 V *vs.* the Fc/Fc^+ couple. A

reversible second oxidation was observed at a higher potential of $E°'$ = 1.03 V and a chemically irreversible reduction was observed at E_{pa} = −1.53 and E_{pc} = −1.19 V for compound **4**.

We note that first oxidations of **1**, **2**, **3**, **4**, **7** and **8** each have cathodic-to-anodic peak ratios (i_{pa}/i_{pc}) of ~1.0. Furthermore, plots of i_{pa} *vs.* the square root of the scan rate ($\nu^{1/2}$) for the first oxidations of these compounds and the second oxidations of **4**, **7** and **8** show a linear relationship over a scan rate range 0.05 – 1.6 V/s indicating diffusion-controlled processes, and the peak separation $\Delta E_p = \left| E_{pa} - E_{pc} \right|$ of the these oxidations compare with those of the Fc/Fc^+ (Table 2.4).

The redox behaviors of the ferrocenecarboxylate compounds **5** and **6** were also investigated by cyclic voltammetry. Fig. 2.13a and 2.13b show the cyclic voltammogram of compounds **5** and **6**, respectively, in CH_2Cl_2 with 1 mM acetylferrocene and 0.1 M $NBuPF_6$ as support electrolyte at a scan rate of 200 mVs^{-1}.

The voltammogram of **5** (Fig. 2.13a) shows four one-electron reversible redox waves at E^o_1' = +0.058 V, E^o_r' = + 0.28 V, E^o_2' = +0.66 V, and E^o_3' = + 1.03 V (*vs.* Fc/Fc^+ couple) (Table 2.5). The potential E^o_r' = +0.28 V is the redox potential of acetylferrocene-acetylferrocenium couple referenced to Fc/Fc^+ at 0.00 V. Similarly, compound **6** displayed oxidations at E^o_1' = +0.056 V, E^o_2' = +0.37 V, and E^o_3' = + 0.83 V (*vs.* Fc/Fc^+) (Fig. 2.13b).

Table 2.5. Electrochemical data[a] for compounds **5** and **6**.

Compound	1st oxid./ E^{o}_{1}'	2nd oxid./ E^{o}_{2}'	3rd oxid./ E^{o}_{3}'	Red. (E_{pc})/ E_{pa}
5	0.058 (120)	0.66 (120)	1.03 (128)	−1.79
6	0.056 (158)	0.37 (125)	0.83 (154)	−1.65/ −1.16

[a] Potentials are in volts, and are referenced to the Fc/Fc^{+} couple set at 0.00 V. Experimental conditions: 1 mM analyte, 200 mV/s scan rate, 0.1 M NBu_4PF_6. The numbers in parenthesis represent the ΔE_p values (in mV) for the redox couples which compare with those of Fc/Fc^{+}.

We note here that the oxidation wave due to acetylferrocene and the second oxidation wave of **6** overlapped. This explains why the peak separation (ΔE_p = 234 mV) is ~2× those of the first and the second oxidations as observed in the overlaid CVs of **5** without AcFc (dash lines) and with AcFc (solid lines) (Fig. 2.13b).

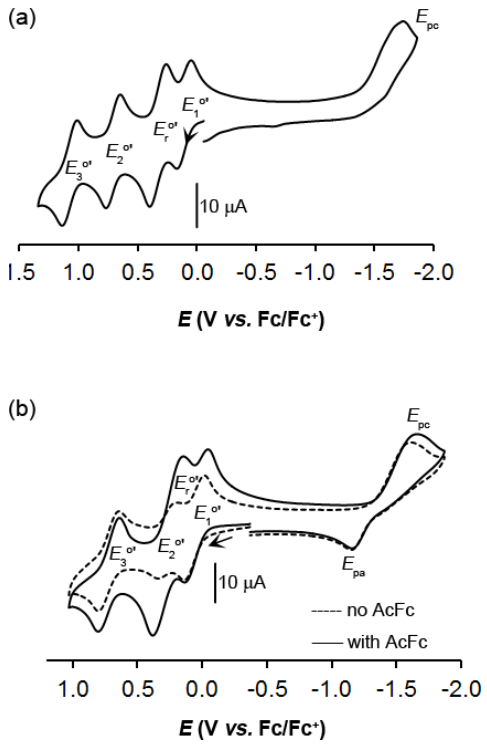

Figure 2.13. Cyclic voltammogram of (a) **5** (1 mM) with acetylferrocene in CH_2Cl_2 (b) **6** (1 mM) with 1 mM AcFc (—), and without AcFc (----) in CH_2Cl_2. Support electrolyte: 0.1 M $NBuPF_6$ at a scan rate of 200 mVs^{-1} at room temperature.

We assign the site of first oxidation to the iron center of the ferrocene carboxylate ligands. The first oxidation potentials of both **5** and **6** *vs.* Fc/Fc^+ couple compare with those of ferrocenylacetic acid ($E_{1/2}$ = +0.05 V in 1,2-dichloroethane),[54] *p*-bromophenylferrocene ($E_{1/2}$ = +0.09 V in CH_3CN), phenylferrocene (+0.03 V in CH_3CN), octaphenylferrocene ($E_{1/2}$ = +0.03 V in CH_3CN) and vinylferrocene ($E_{1/2}$ = + 0.02 V in CH_3CN).[55] However, these first oxidation potentials of **5** and **6** are lower than those reported for the free ferrocenecarboxylic acid ($E_{1/2}$ = +0.234 V in 1,2-dichloroethane), 3-ferrocenyl-2-propenoic acid ($E_{1/2}$ = +0.127V in 1,2-dichloroethane),[54] acetylferrocene ($E_{1/2}$ = +0.27 V in CH_3CN,[55] and ($E_{1/2}$ =+0.28 V in CH_2Cl_2 in this work). We attribute reason for these lower first oxidation potentials of **5** and **6** to an overall electron-donation from the porphyrins to the ferrocene carboxylate ligands. Thus, the site of first oxidation in **5** and **6** is the FcC(=O)O ligand to generate the species $[(por)Ru(NO)(OC(=O)Fc)]^{\bullet+}$ (por = T(*p*-OMe)PP, TTP) where the site of oxidation is the ferrocenyl Fe (i.e., the Fe^{2+}/Fe^{3+} couple). Cyclic voltammetry measurements of the non-porphyrin complexes $[Ru(\eta^2\text{-}O_2CFc)(L_2)]$ (L = dppm, dppe, dppp) in 1,2-dichloroethane show $E_{1/2}$ (*vs.* Fc/Fc^+ couple) of +0.218 V, +0.192 V and +0.245 V, respectively which were also confirmed by OSWV measurements.[51] The authors assigned the Fe centers of these compounds as the site of oxidation (i.e Fe^{2+}/Fe^{3+}). In the complex $(TPP)Sn(OC(=O)Fc)_2$ the authors reported a reversible oxidation at $E_{1/2}$ = +0.11 V (*vs.* Fc/Fc^+ in THF) due to the FcC(=O)O ligand.[48]

We attribute the site of the second oxidations ($E^o{}_2'$= +0.66 V for **5** and $E^o{}_2'$ = +0.37 V for **6** *vs*. Fc/Fc^+) to the porphyrin center leading to the generation of the π-radical cation $[(T(p\text{-}OMe)PP)Ru(NO)(OC(=O)Fc)]^{2+}$. The site of third oxidation is

assigned to the porphyrin macrocyle in both **5** and **6**. Meyer and Whitten, have reported that Ru^{II} porphyrin complexes containing π-acids such as CO have the propensity to display two porphyrin-centered one electron oxidations.[56] Based on the CV data alone we ascribe the second oxidation (E^{o}_{2}') and third oxidation (E^{o}_{2}') of compounds **5** and **6** as porphyrin-centered oxidations.

2.3.6.2 Infrared Spectroelectrochemistry

We performed IR spectroelectrochemical experiments[37,57] to gain insight into the chemical identities of the electrogenerated products of the compounds. In each of these experiments, the electrode was typically held at a potential slightly more positive than the peak potential (E_{pa}), or slightly more negative than the peak potential for reduction (E_{pc}), to accumulate sufficient quantities of the electrogenerated products. Prior to collecting FTIR spectra for the redox products, the IR spectra of the starting materials were used as backgrounds for the respective experiments. The difference IR spectra obtained during first electrooxidation of compound **7** is shown in Fig. 2.14a.

The ν_{NO} band of **7** at 1850 cm^{-1} is consumed and a corresponding new band at 1870 cm^{-1} is observed in the difference spectrum (Fig. 2.14a). This small ν_{NO} shift of +20 cm^{-1} from its original position in neutral (T(*p*-OMe)PP)Ru(NO)(OC_6HF_4) is attributed to a porphyrin-centered oxidation.[37] The new band at 1598 cm^{-1} was associated with an enhancement in intensity of a vibration in the porphyrin macrocycle[25] that appeared not to be directly associated with the 1607 cm^{-1} band of the starting material.

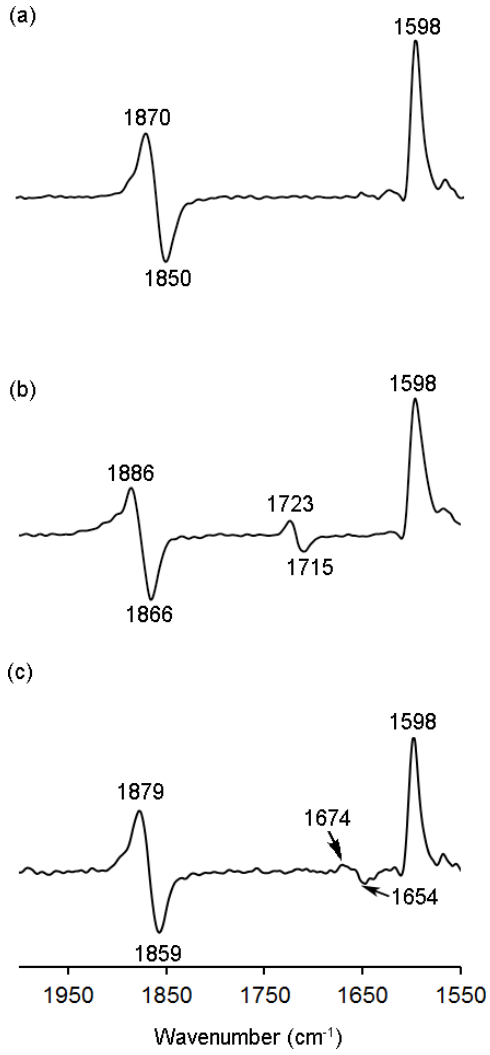

Figure 2.14. Difference IR spectra of (a) **7**, (b) **8** and (c) **4** showing the formation of products during first oxidations.

We also observed that the electrogenerated product of the first oxidation of compound **8** had a ν_{NO} band at 1886 cm^{-1} in the difference spectrum (Fig. 2.14b). This ν_{NO} shift of +20 cm^{-1} from the initial 1866 cm^{-1} band of the starting starting compound was similarly attributed to a porphyrin-centered oxidation. The new band at 1723 cm^{-1} was assigned to ν_{CO} which represented a shift of +8 cm^{-1} from its original position at 1715 cm^{-1} and suggests that the $CF_3C(=O)O$ group is still bound to ruthenium after the first oxidation. The characteristic bands for porphyrin radical cations in TPP-derived

macrocycles are in the 1270-1295 cm^{-1} range[58] which, unfortunately, are outside of the spectral window. Based on the cyclic voltammetric data and the IR spectroelectrochemical data, we conclude that the first oxidation process of **8** involve transfer of a single electron from the porphyrin macrocycle to generate the (T(*p*-OMe)$PP^{\bullet+}$)Ru(NO)(OC(=O)CF_3) radical cation.

The electrogenerated product after second oxidation of **7** has a new ν_{NO} band 1892 cm^{-1} in the difference IR spectrum and another at 1870 cm^{-1} due to the first oxidation product (Fig. 2.15a) and Δ_{NO} of each of these bands is less than 100 cm^{-1}, thus, implying both first and second oxidations of **7** are porphyrin-centered. Thus, during second oxidation of **7** both (T(*p*-OMe)PP^{2+})Ru(NO)(OC_6HF_4) and (T(*p*-OMe)$PP^{\bullet+}$)Ru(NO)(OC_6HF_4) are produced with the former being the least stable as evidenced by the weakness of their ν_{NO} bands (Fig. 2.15a).

The difference IR spectrum of compound **8** during first and second oxidations similarly showed new ν_{NO} bands at 1886 cm^{-1} ($\Delta\nu_{NO}$ = +20 cm^{-1}) and 1916 cm^{-1} $\Delta\nu_{NO}$ = +50 cm^{-1}). Their respective ν_{CO} bands are 1723 cm^{-1} ($\Delta\nu_{CO}$ = +8 cm^{-1}) and 1800 cm^{-1} ($\Delta\nu_{CO}$ = +85 cm^{-1}) (See Fig. 2.14 and 2.15) and the small $\Delta\nu_{NO}$ shifts are indicative of porphyrin-centered oxidations.

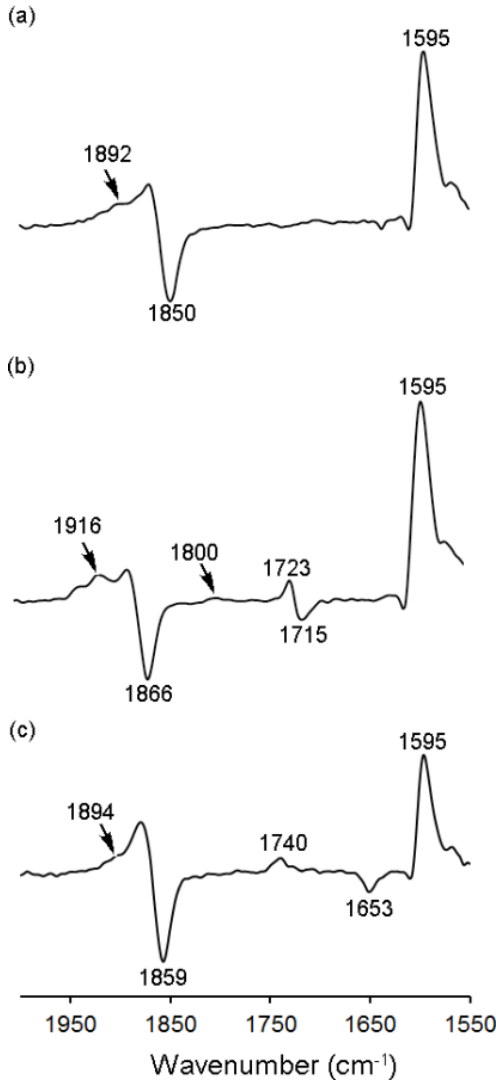

Figure 2.15. Difference IR spectra of (a) **7**, (b) **8** and (c) **4** showing the formation of products during second oxidations.

The other aliphatic carboxylate complexes (**1**, **2** and **3**) (not shown) and compound **4** (Fig. 2.14c and 2.15c) showed shifts in their respective ν_{NO} and ν_{CO} bands after first and second oxidations (Table 2.6) and each of them displayed two porphyrin-centered one-electron oxidations.

Table 2.6. IR (CH_2Cl_2)/ cm^{-1} values of the *O*-bound ruthenium nitrosyl porphyrin compounds and their redox products.

Compound	IR (Initial)		IR (1st oxid.)		IR (2nd oxid.)		IR (red.)
	ν_{NO}	ν_{CO}	ν_{NO} ($\Delta\nu_{NO}$)	ν_{CO} ($\Delta\nu_{CO}$)	ν_{NO} ($\Delta\nu_{NO}$)	ν_{CO} ($\Delta\nu_{CO}$)	ν_{CO}
1	1852	1647, 1654 sh	1873 (+21)	1665 (+18)	1880 (+28), 1892 sh (+40)	1758 (+111)	1579
2	1850	1637, 1642 sh	1871 (+21)	1661 (+24)	1882 (+32)	1746 (+109), 1732 (+100)	1567
3	1849	1637	1870 (+21)	1657 (+17)	1881 (+32)	1741 (+104)	1568
4	1859	1653	1879 (+20)	1674 (+20)	1879 1894 sh (+35)	1740 (+87)	1589
5	1852	1634	1867 (+15)	1665 (+31)	1881 (+29)	1751 (+117)	1578
6	1850	1665	1865 (+15)	1665 (+31)	1882 (+32)	1750 (+116)	1578
7	1850		1870 (+20)		1892 (+42)		1634
8	1866	1715	1886 (+20)	1723 (+8)	1916 (+50)	1800 (+89)	1687[a]

[a] due to ν_{ArO}

Based on the cyclic voltammetry data and the IR spectroelectrochemical data, we conclude that the first and second oxidation processes of **1**, **2**, **3**, **7** and **8** involve transfer of electrons from the porphyrin macrocycle to generate (T(*p*-OMe)$PP^{\bullet+}$)Ru(NO)(*O*-ligand) and (T(*p*-OMe)PP)Ru(NO)(*O*-ligand)]$^{2+}$, respectively.

We then turned our attention to the study of the behavior of **1**, **2**, **3**, **7**, **8** and **4** during reduction. The difference IR spectrum of the product formed after reduction of **7** is shown in Fig. 2.16a. The initial ν_{NO} band at 1850 cm^{-1} is consumed and a new (small)

band at 1634 cm^{-1} is observed. Kaim and coworkers have shown a lower energy shift in ν_{NO} (~300 cm^{-1}) upon reduction of some $[(por)Ru(NO)(L)]^{+}$ complexes.[59]

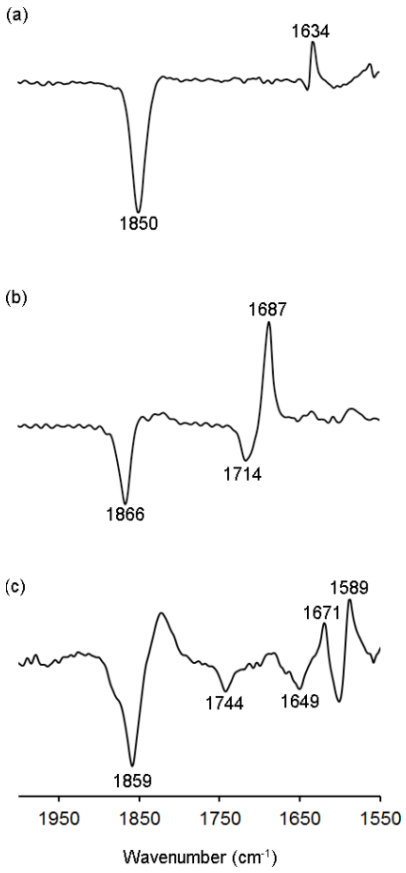

Figure 2.16. Difference IR spectra of (a) **7**, (b) **8** and (c) **4** showing the formation of products during reductions.

However, in a control experiment, we determined that this band at 1634 cm^{-1} is in an identical position to that obtained for the sodium salt of the tetrafluorophenoxide ($NaOC_6F_4H$) in 15-crown-5/CH_2Cl_2/NBu_4PF_6. We thus conclude that this band is due to the dissociation of the tetrafluorophenoxide ion ($C_6F_4HO^{-}$) upon electroreduction of **7**.

The difference IR spectrum obtained during reduction of **8** is shown in Fig. 2.16b, and reveals the loss of the starting ν_{NO} at 1866 cm^{-1}. Further, there is a loss of a band at 1714 cm^{-1} (due to ν_{CO} of **8**) and generation of a new band at 1687 cm^{-1}. We hypothesize that this band results from the dissociated trifluoroacetate anion $CF_3C(=O)O$ after reduction. Indeed, an IR spectrum of $NaOC(=O)CF_3$ in 15-crown-5/CH_2Cl_2/NBu_4PF_6 solution revealed an identical band at 1687 cm^{-1}.[32] Note that the compounds **1**, **2** and **3** have similar difference spectra as **8** and thus, produce similar redox products after reduction.

The difference IR spectrum obtained for **4** after reduction is shown in Fig. 2.16c reveals the loss of the starting ν_{NO} at 1859 cm^{-1} and a loss of the ν_{CO} band at 1649 cm^{-1}. The loss of the band at 1649 cm^{-1} resulted in the new band at 1671 cm^{-1} and was assigned to the dissociated *p*-NO_2-$C_6H_4C(=O)O$ ligand. Thus, electroreductions of **1**, **2**, **3**, **7**, and **8** result in the dissociation of the axial *O*-ligand generating the unstable (T(*p*-OMe)PP)Ru(NO) byproduct.

Using the information obtained above, we then proceeded to identify in comprehensive form, the redox products generated after the first and second oxidations, and the reductions of **5** and **6**. The difference IR spectra obtained after first oxidation of **5** and **6** are shown in Fig. 2.17a (left and right, respectively).

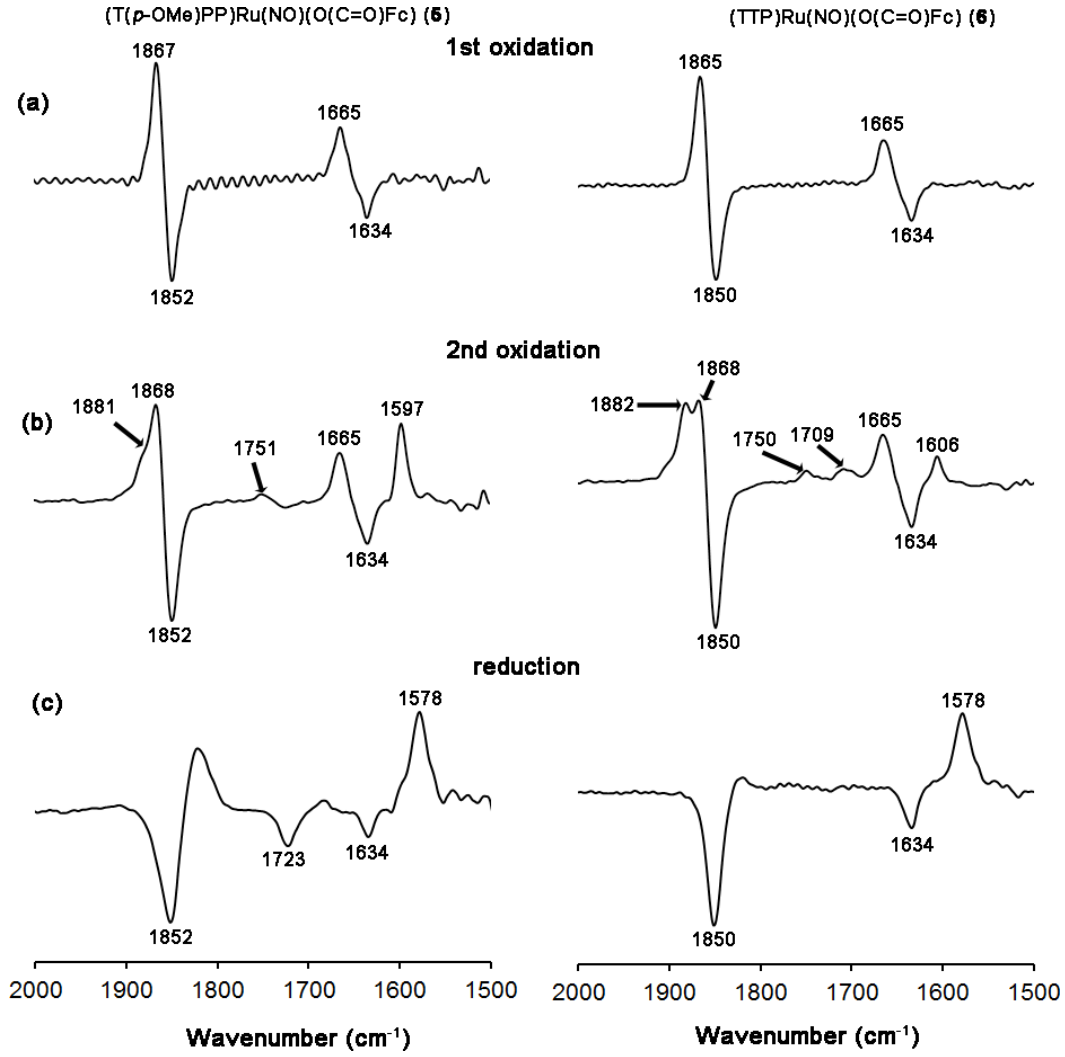

Figure 2.17. Difference IR spectra of (T(*p*-OMe)PP)Ru(NO)(OC(=O)Fc) (**5**) (left) and (TTP)Ru(NO)(OC(=O)Fc) (**6**) (right) showing the formation of products after (**a**) first oxidation, (**b**) second oxidation, and (**c**) reduction.

The electrogenerated product of the first oxidation of **5** has a ν_{NO} band at 1867 cm^{-1} in the difference spectrum (Fig. 2.17a, left) representing a shift of + 15 cm^{-1}. The new band at 1665 cm^{-1} is assigned to the ν_{CO} ($\Delta\nu_{CO}$ = + 31 cm^{-1}) of FcC(=O)O ligand, and suggests that the ligand is still bound to Ru in solution. Similarly, compound **6** displays a new ν_{NO} band at 1865 cm^{-1} upon first oxidation which represents a shift of +15 cm^{-1} from its original position at 1850 cm^{-1}, and a new ν_{CO} band at 1665 cm^{-1} ($\Delta\nu_{CO}$

= + 31 cm^{-1}). These shifts are consistent with ligand-centered oxidations and we assign the FcC(=O)O as the ligand undergoing oxidation when a potential of E^o = 58 mV was applied. We conclude that during the first oxidations, the compounds are converted to (por)Ru(NO)(OC(=O)Fc^{+}) (Eq. 2.4). The difference IR spectra of **5** and **6**, during the first oxidation, lack the 1598 cm^{-1} band usually associated with an enhancement in intensity of a vibration in the porphyrin macocycle,[25] an indication that the site of first oxidation is somewhere other than the porphyrin macrocycle, thus, our assignment of a ligand-centered oxidation.

$$\text{(por)Ru(NO)(OC(=O)Fc)} + e^- \rightleftharpoons \text{(por)Ru(NO)(OC(=O)Fc}^{+}\text{)} \qquad (\mathbf{2.4})$$

The difference spectrum of the product formed after second oxidation of **5** and **6** are shown in Fig. 2.17b (left and right, respectively). The difference spectrum of compound **5** after second oxidation shows a new ν_{NO} band at 1868 cm^{-1}. This shift of +16 cm^{-1} is comparative to the ν_{NO} shifts observed in the (T(*p*-OMe)PP)Ru(NO)(OC(=O)R) complexes, and thus, suggestive of a porphyrin-centered oxidation. A new ν_{CO} band was also observed at 1665 cm^{-1} ($\Delta\nu_{CO}$ = + 31 cm^{-1}) and a small band at 1751 cm^{-1} ($\Delta\nu_{CO}$ = + 117 cm^{-1}). We assign the 1751 cm^{-1} peak to the ν_{CO} of FcC(=O)O in the electrogenerated product, (T(*p*-OMe)$PP^{+\cdot}$)Ru(NO)(OC(=O)Fc).

The compound **6** similarly undergoes a porphyrin-centered second oxidation to generate the product ($TTP^{+\cdot}$)Ru(NO)(OC(=O)Fc) which has new ν_{NO} and ν_{CO} bands at 1882 and 1750 cm^{-1}, respectively.

We hypothesize that during the second oxidation process, a mixture of (por$^{+\bullet}$)Ru(NO)(OC(=O)Fc) and (por)Ru(NO)(OC(=O)Fc$^{+\bullet}$) are formed, the latter forming from the former by delocalization of the radical cation into the Cp ring of the FcC(=O)O ligand (Eq. 2.5), a process that needs to be investigated further.

(por$^{\bullet+}$)Ru(NO)(OC(=O)Fc) $\rightleftharpoons$ (por)Ru(NO)(OC(=O)Fc$^{\bullet+}$) (**2.5**)

Furthermore, the associated porphyrin macrocyle bands observed between 1597 cm^{-1} and 1606 cm^{-1} are not as enhanced as those observed for the porphyrin-centered first oxidation of the carboxylate complexes, (por)Ru(NO)(OC(=O)Fc), which supports our proposed mixed (por$^{\bullet+}$)Ru(NO)(OC(=O)Fc) and (por)Ru(NO)(OC(=O)Fc$^{+\bullet}$) after second oxidation of (por)Ru(NO)(OC(=O)Fc).

The electrogenerated ferrocenyl products after reductions of **5** and **6** were also studied by IR spectroelectrochemistry. The difference IR obtained during reduction are shown in Fig. 2.17c (left and right), respectively for (T(*p*-OMe)PP)Ru(NO)(OC(=O)Fc) and (TTP)Ru(NO)(OC(=O)Fc). The difference IR spectrum of (T(*p*-OMe)PP)Ru(NO)(OC(=O)Fc) after reduction shows the loss of the starting ν_{NO} and ν_{CO} bands at 1852 cm^{-1} and 1634 cm^{-1}, respectively and the generation of a new band at 1578 cm^{-1} assigned to (FcC(=O)O^{-}). Fig. 2.17c(left) also reveals the loss of a band at 1723 cm^{-1} and may be attributed to the loss of the (Fc$^{+\bullet}$C(=O)O^{-}) generated after oxidations (Eq. 2.6 and 2.7). Thus, the reduced products, like those of **1**, **2**, **3**, **4**, **7** and **8** are the unstable byproduct (por)Ru(NO).

(por)Ru(NO)(OC(=O)Fc) + e^{-} → (por)RuNO + FcC(=O)O^{-} (**2.6**)

$$(por)Ru(NO)(OC(=O)Fc^{+\cdot}) + e^{-} \rightarrow (por)RuNO + Fc^{+\cdot}C(=O)O^{-} \quad (\mathbf{2.7})$$

2.4 Conclusion

In conclusion, we have prepared and spectroscopically characterized the compounds (T(*p*-OMePP)Ru(NO)(OC_6HF_4) (**7**), (T(*p*-OMe)PP)Ru(NO)(OC(=O)R) (R = CH_3 (**1**), $CH(CH_3)_2$ (**2**), $C(CH_3)_3$ (**3**), *p*-NO_2-C_6H_4 (**4**), CF_3 (**8**)) and (por)Ru(NO)(OC(=O)Fc) (por = T(*p*-OMe)PP (**5**), TTP (**6**)). X-ray crystallographic data obtained for these $\{RuNO\}^6$ species reveal linear RuNO linkages. Cyclic voltammetry and IR spectroelectrochemistry reveal reversible oxidations centered on the porphyrin rings in **1**, **2**, **3**, **4**, **7** and **8**. In compounds **5** and **6** the first oxidation is ferrocenyl-centered resulting in the generation of the species $(por)Ru(NO)(OC(=O)Fc^{+\cdot})$. The electrochemical experiments also revealed that the second oxidations of the compounds (**1**-**8**) as porphyrin-centered. The electrochemical reductions result in the eventual dissociation of the axial *O*-ligands with concomitant generation of the putative and unstable (T(*p*-OMe)PP)Ru(NO) byproduct.

2.5 References

(1) Nicholls, P.; Fita, I.; Loewen, P. C. In *Adv. Inorg. Chem.*; Academic Press: 2000; Vol. 51, p 51-106.

(2) Maté, M. J.; Murshudov, G.; Bravo, J.; Melik-Adamyan; Loewen, P. C.; Fita, I. *Handbook of Metalloporphyrins;* Messerschmidt, A., Huber, R., Wieghardt, K., Poulos, T. Eds; John Wiley & Sons, Chichester, 2001

(3) Jepkorir, G.; Rodríguez, J. C.; Rui, H.; Im, W.; Lovell, S.; Battaile, K. P.; Alontaga, A. Y.; Yukl, E. T.; Moënne-Loccoz, P.; Rivera, M. *J. Am. Chem. Soc.* **2010**, *132*, 9857-9872.

(4) Gaudin, C. F. M.; Grigg, J. C.; Arrieta, A. L.; Murphy, M. E. P. *Biochemistry* **2011**, *50*, 5443-5452.

(5) Pulsinelli, P. D.; Perutz, M. F.; Nagel, R. L. *Proc. Natl. Acad. Sci. U S A* **1973**, *70*, 3870-3874.

(6) Perutz, M. F.; Pulsinelli, P. D.; Ranney, H. M. *Nat. New Biol.* **1972**, *237*, 259-263.

(7) Percy, M. J.; McFerran, N. V.; Lappin, T. R. J. *Blood Rev.*, *19*, 61-68.

(8) van Staveren, D. R.; Metzler-Nolte, N. *Chem. Rev.* **2004**, *104*, 5931-5986.

(9) Lal, B.; Badshah, A.; Altaf, A. A.; Khan, N.; Ullah, S. *Appl. Organomet. Chem.* **2011**, *25*, 843-855.

(10) Scutaru, D.; Tataru, L.; Mazilu, I.; Vata, M.; Lixandru, T.; Simionescu, C. *Appl. Organomet. Chem.* **1993**, *7*, 225-231.

(11) Edwards, E. I.; Epton, R.; Marr, G. *J. Organomet. Chem.* **1976**, *122*, C49-C53.

(12) Sawamura, M.; Sasaki, H.; Nakata, T.; Ito, Y. *Bull. Chem. Soc. Jpn.* **1993**, *66*, 2725-2729.

(13) Biot, C.; Glorian, G.; Maciejewski, L. A.; Brocard, J. S.; Domarle, O.; Blampain, G.; Millet, P.; Georges, A. J.; Abessolo, H.; Dive, D.; Lebibi, J. *J. Med. Chem.* **1997**, *40*, 3715-3718.

(14) Dive, D.; Biot, C. *ChemMedChem* **2008**, *3*, 383-391.

(15) Salas, P. F.; Herrmann, C.; Orvig, C. *Chem. Rev.* **2013**, *113*, 3450-3492.

(16) Top, S.; Vessières, A.; Leclercq, G.; Quivy, J.; Tang, J.; Vaissermann, J.; Huché, M.; Jaouen, G. *Chem. – Eur. J.* **2003**, *9*, 5223-5236.

(17) Di Gleria, K.; Nickerson, D. P.; Hill, H. A. O.; Wong, L.-L.; Fülöp, V. *J. Am. Chem. Soc.* **1998**, *120*, 46-52.

(18) Di Gleria, K.; Hill, H. A. O.; Wong, L. L. *FEBS Lett.* **1996**, *390*, 142-144.

(19) Clark, D.; Durner, J.; Navarre, D. A.; Klessig, D. F. *Mol. Plant Microbe In.* **2000**, *13*, 1380-1384.

(20) Purwar, N.; McGarry, J. M.; Kostera, J.; Pacheco, A. A.; Schmidt, M. *Biochemistry* **2011**, *50*, 4491-4503.

(21) Xu, N.; Goodrich, L. E.; Lehnert, N.; Powell, D. R.; Richter-Addo, G. B. *Angew. Chem. Int. Ed.* **2013**, *52*, 3896-3900.

(22) Yi, G.-B.; Khan, M. A.; Richter-Addo, G. B. *Inorg. Chem.* **1997**, *36*, 3876-3885.

(23) Bruker-AXS *Data Collection: SMART Software Reference Manual* **1998**.

(24) Bruker-AXS *Data Reduction: SAINT Software Reference Manual* **1998**.

(25) Xu, N.; Lilly, J.; Powell, D. R.; Richter-Addo, G. B. *Organometallics* **2012**.

(26) Xu, N.; Lee, J.; Powell, D. R.; Richter-Addo, G. B. *Inorg. Chim. Acta* **2005**, *358*, 2855-2860.

(27) El-Attar, M. A.; Xu, N.; Awasabisah, D.; Powell, D. R.; Richter-Addo, G. B. *Polyhedron* **2012**, *40*, 105-109.

(28) Nesmeyanov, A. N.; Baukova, T. V.; Grandberg, K. I.; Ustynyuk, Y. A.; Gubin, S. P.; Perevalova, É. G. *B. Acad. Sci. USSR, CH+* **1969**, *18*, 658-659.

(29) De Santis, G.; Fabbrizzi, L.; Licchelli, M.; Pallavicini, P. *Inorg. Chim. Acta* **1994**, *225*, 239-244.

(30) Pendin, A. A.; Leont'evskaya, P. K.; L'vova, T. I.; Nikol'skii, B. P. *Doklady Akademii Nauk SSSR* **1969**, *189*, 115-118.

(31) Cheng, L.; Richter-Addo, G. B. *The Porphyrin Handbook; Kadish, K. M., Smith, K. M., Guilard, R., Eds.; Academic Press: New York, 2000; Vol. 4, Ch. 33 (Biochemistry and Binding: Activation of Small Molecules), pp 219-291*.

(32) Awasabisah, D.; Xu, N.; Sharmah Gautam, K. P.; Powell, D. R.; Shaw, M. J.; Richter-Addo, G. B. *Dalton Trans.* **2013**, *42*, 8537-8540.

(33) Warhausen, A. *Dissertation, University of Oklahoma* **2012**.

(34) Lee, J.; Yi, G.-B.; Khan, M. A.; Richter-Addo, G. B. *Inorg. Chem.* **1999**, *38*, 4578-4584.

(35) Antipas, A.; Buchler, J. W.; Gouterman, M.; Smith, P. D. *J. Am. Chem. Soc.* **1978**, *100*, 3015-3024.

(36) Scott Bohle, D.; Goodson, P. A.; Smith, B. D. *Polyhedron* **1996**, *15*, 3147-3150.

(37) Carter, S. M.; Lee, J.; Hixson, C. A.; Powell, D. R.; Wheeler, R. A.; Shaw, M. J.; Richter-Addo, G. B. *Dalton Trans.* **2006**, 1338-1346.

(38) Buchler, J.; Kokisch, W.; Smith, P. In *Novel Aspects*; Springer Berlin Heidelberg: 1978; Vol. 34, p. 79-134.

(39) Yoshida, M.; Katagiri, Y.; Zhu, W.-B.; Shishido, K. *Org. Biomol. Chem.* **2009**, *7*, 4062-4066.

(40) Cheng, L.; Powell, D. R.; Khan, M. A.; Richter-Addo, G. B. *Inorg. Chem.* **2001**, *40*, 125-133.

(41) Gokel, G. W. In *Dean's Handbook of Organic Chemistry***.** The McGraw-Hill Companies, Inc., New York, USA, 2004.

(42) Yi, G.-B.; Khan, M. A.; Richter-Addo, G. B. *Inorg. Chem.* **1996**, *35*, 3453-3454.

(43) Boekelheide, V.; Hollins, R. A. *J. Am. Chem. Soc.* **1970**, *92*, 3512-3513.

(44) Ponomarev, G. V.; Borovkov, V. V.; Sugiura, K.-i.; Sakata, Y.; Shul'ga, A. M. *Tetrahedron Lett.* **1993**, *34*, 2153-2156.

(45) Senge, M. O.; Gerzevske, K. R.; Vicente, M. G. H.; Forsyth, T. P.; Smith, K. M. *Angew. Chem. Int. Edit.* **1993**, *32*, 750-753.

(46) Senge, M. O.; Vicente, M. G. H.; Gerzevske, K. R.; Forsyth, T. P.; Smith, K. M. *Inorg. Chem.* **1994**, *33*, 5625-5638.

(47) Maeda, D.; Shimakoshi, H.; Abe, M.; Fujitsuka, M.; Majima, T.; Hisaeda, Y. *Inorg. Chem.* **2010**, *49*, 2872-2880.

(48) Kim, H. J.; Jeon, W. S.; Lim, J. H.; Hong, C. S.; Kim, H.-J. *Polyhedron* **2007**, *26*, 2517-2522.

(49) Enemark, J. H.; Feltham, R. D. *Coord. Chem. Rev.* **1974**, *13*, 339-406.

(50) Matas, L.; Moldes, I.; Soler, J.; Ros, J.; Alvarez-Larena, Á.; Piniella, J. F. *Organometallics* **1998**, *17*, 4551-4555.

(51) Wyman, I. W.; Burchell, T. J.; Robertson, K. N.; Cameron, T. S.; Aquino, M. A. S. *Organometallics* **2004**, *23*, 5353-5364.

(52) Wyman, I. W.; Robertson, K. N.; Cameron, T. S.; Swarts, J. C.; Aquino, M. A. S. *Organometallics* **2005**, *24*, 6055-6058.

(53) Bordwell, F. G. *Acc. Chem. Res.* **1988**, *21*, 456-463.

(54) Cooke, M. W.; Cameron, T. S.; Robertson, K. N.; Swarts, J. C.; Aquino, M. A. S. *Organometallics* **2002**, *21*, 5962-5971.

(55) Geiger, W. E. *J. Organomet. Chem. Libr.* **1990**, *22*, 142-172.

(56) Brown, G. M.; Hopf, F. R.; Ferguson, J. A.; Meyer, T. J.; Whitten, D. G. *J. Am. Chem. Soc.* **1973**, *95*, 5939-5942.

(57) Shaw, M. J.; Henson, R. L.; Houk, S. E.; Westhoff, J. W.; Jones, M. W.; Richter-Addo, G. B. *J. Electroanal. Chem.* **2002**, *534*, 47-53.

(58) Shimomura, E. T.; Phillippi, M. A.; Goff, H. M.; Scholz, W. F.; Reed, C. A. *J. Am. Chem. Soc.* **1981**, *103*, 6778-6780.

(59) Singh, P.; Das, A. K.; Sarkar, B.; Niemeyer, M.; Roncaroli, F.; Olabe, J. A.; Fiedler, J.; Záliš, S.; Kaim, W. *Inorg. Chem.* **2008**, *47*, 7106-7113.

Chapter 3: Synthesis, Characterization, and Spectroelectrochemistry of O-bound Five-coordinate Porphyrin Complexes; Reactivity with Nitric Oxide and Potential Structural Consequences.

3.1 Introduction

Ferric heme complexes, (por)Fe^{III}(X) (X = anionic, neutral) are relevant in biological systems and have received a great deal of attention.[1] For example, as mentioned in Chapter 2, (por)Fe(O-aryl) complexes have been used as models for heme catalase[2] and hemoglobin M variants.[3] Also, bacterial ferricytochromes *c*' possess ferric heme prosthetic groups with varying spin-states, a property necessary for its catalytic action.[4,5]

The relationship between the spin-state and stereochemistry of (por)FeX complexes is relatively well established in the literature**.** Hoard, Scheidt and others have detailed this relationship using X-ray crystallographic data.[6,7] A general trend has been inferred for the Fe−N(por) and the Fe−X(X = imidazole) bond lengths as well as the out-of-plane iron atom displacement from the mean 24-atom porphyrin cores (Δ_{por}Fe) of (por)FeX complexes. For example, in five-coordinate (por)FeX complexes, Fe−N(por) bond lengths of 2.060-2.087 Å and 1.994-2.001 Å have been observed for high-spin and admixed intermediate spins, respectively. Also, Δ_{por}Fe values of five-coordinate intermediate spins complexes lie between those of low-spin (<0.11 Å) and high-spin complexes (>0.39 Å).[7]

It is now known that the ligand field provided by the nature of the axial ligand and the porphyrin macrocycle control the spin states of metalloporphyrins. For example, whereas (TPP)FeCl is a high-spin complex, the related (TPP)Fe($OClO_3$) species has admixed intermediate spin properties. Also, the cationic complex [(TPP)Fe$(THF)_2$]ClO_4

has admixed spin state properties, but the analogous complexes $[(OETPP)Fe(THF)_2]ClO_4$ and $[(T^{i}prPP)Fe(THF)_2]ClO_4$ are pure intermediate-spin state species.[8,9] The deformation of the porphyrin core due to steric overcrowding is known to stabilize pure intermediate spin states in iron porphyrins.[10]

In this chapter, I explore the relationship between the stereochemistry and spin-states of some (por)Fe(OR) (R = aryl, aliphatic) complexes using X-ray crystallography. I also examine whether a relationship exists between the electronic properties of the axial OR ligand (and/or porphyrin macrocycle) and the spin states of their iron porphyrin derivatives. The overall goal is to be able to identify whether the spin states of the (por)Fe(OR) complexes have any correlation with nitric oxide (NO) binding to give the (por)Fe(NO)(OR) products. I anticipated that if the six-coordinate (por)Fe(NO)(OR) derivatives could be formed from the five-coordinate (por)Fe(OR) precursors, the spectral and structural comparisons would help to explain the *trans* influence of NO on the axial O-bound ligands (Fe−O) in the six-coordinate (por)Fe(NO)(OR) complexes, a phenomenon, which unlike the *cis* influence[11] has not been well explored.Our group has previously observed that the *trans* NO ligand in the complex (TPP)Fe(NO)(OC(=O)CF_3) exhibited a negative *trans* influence as evidenced by a shortening by 0.03 Å of the Fe−O bond in the six-coordinate (TPP)Fe(NO)(OC(=O)CF_3).[12] In this work I use a combination of spectroscopy, X-ray crystallography, electrochemistry and theoretical calculations to explore the chemistry of (por)Fe(OR) compounds.

3.2 Experimental Section

All reactions were performed under an atmosphere of nitrogen using standard Schlenk glassware and/ or in an Innovative Technology Labmaster 100 Dry Box unless stated otherwise. Solvents for reactions were collected under a nitrogen atmosphere from a solvent purification system (Innovative Technology, Inc. Newburyport, MA, USA, PS-400-5MD) using a glass syringe.

3.2.1 Chemicals

The free base porphyrins (por)H_2 (por = TPP, T(*p*-OMe)PP, TTP,[13] TMP,[14] $T_{piv}PP$,[15] TF_8PP, and OETPP[16] were synthesized by published procedures. Metalloporphyrins (por)FeCl (por = TPP, T(*p*-OMe)PP, TTP, TMP, $T_{piv}PP$, TF_8PP, and OETPP) were prepared by the standard Alder-Longo method.[17] The compound (OEP)FeCl was purchased from Mid-Century Chemicals and used as received. The compounds $[(por)Fe]_2O$ (por = TPP, T(*p*-OMe)PP, TTP, OEP),[18-21] $[(T_{piv}PP)Fe]_2O$[15] and (por)Fe(OMe)[22] were prepared by published procedures. The compounds, 2,3,5,6-tetrafluorophenol (C_6HF_4OH, 98%), *p*-fluorophenol (*p*-F-C_6H_4OH, 99%), *p*-nitrophenol (*p*-NO_2-C_6H_4OH, 99%), potassium trimethylsilanolate ($KOSiMe_3$, 90%), sodium methoxide (NaOMe, 95%), ferrocene (Fc, 98%) and tetrabutylammonium hexafluorophosphate (NBu_4PF_6, ≥99%) were purchased from Aldrich Chemical company and used as received. Cobaltocene (Cp_2Co, 98%) was purchased from Aldrich Chemical company and purified by sublimation.[23] Trimethylsilylmethanol (Me_3SiCH_2OH, > 97%) was purchased from TCI Chemicals Company and used as received. Chloroform-*d* ($CDCl_3$, 99.96 atom %D) was purchased from Cambridge

Isotope Laboratories and purified by three freeze-pump-thaw cycles, and stored over 4Å molecular sieves. Nitric oxide (NO, 98%, Matheson Gas) was passed through a double KOH pellet trap and a cold trap (dry ice/ acetone) to remove higher nitrogen oxides.

3.2.2 Instrumentation/ Spectroscopy

Infrared spectra were recorded on a Bio-Rad FT-155 and/ or a Tensor 27 FTIR spectrometer. UV-vis spectra were recorded on a Hewlett-Packard model 8453 diode array instrument. ^{1}H NMR spectra were obtained on a Varian 300 MHz spectrometer at room temperature and the signals referenced to the residual signal of the solvent employed ($CHCl_3$ at 7.24 ppm). The effective magnetic moments of the complexes, μ_{eff} were obtained by the Evans method[24,25] and calculated using the equation $\mu_{eff} = 2.84\sqrt{(\chi_M T)}$, where T is the temperature in Kelvin , and χ_M is the molar paramagnetic susceptibility given by: $\chi_M = [(\chi_O M_{(solute)}/M_{(solvent)})] + [3000(\Delta\nu/4\pi\nu_0 C)]$.[25,26] $\Delta\nu$ is the frequency difference between the CH_2Cl_2 signal in the inner tube and the outer tube, χ_0 is the diamagnetic susceptibility of pure $CDCl_3$ solvent,[27] M is the molecular weight, C is concentration of sample in mol/L, ν_0 is the frequency of the 300 MHz instrument. Elemental analyses were obtained by the staff of Atlantic Microlab, Norcross, GA.

Cyclic voltammetry was performed using a BAS CV 50W instrument (Bioanalytical Systems, West Lafayette, IN). In all the electrochemical experiments, a three-electrode cell was utilized and consisted of a 3.0-mm diameter Pt disk working electrode, a Pt wire counter electrode, and a Ag/AgCl reference electrode. Solutions were deaerated before electrochemical experiments were performed by passing a stream of N_2 gas through the solution for a minimum of 10 min. A blanket of N_2 was

maintained over the solution while performing the experiments. The electrochemical experiments were performed in solutions containing 0.1 M NBu_4PF_6 and 1.0 mM of the analyte. Ferrocene, (Fc, 1.0 mM) was used as standard for the electrochemical experiments of compounds where potentials were referenced to the Fc/Fc^+ couple set at 0.00 V. A Bruker Tensor 27 FTIR spectrometer equipped with a mid-IR fiber-optic dip probe and liquid nitrogen cooled MCT detector (RemSpec Corporation, Sturbridge, MA, USA) was used for the infrared spectroelectrochemistry. The electrochemical experiments were performed in triplicates. X-ray diffraction data were collected using a diffractometer with a Bruker APEX ccd area detector[28,29] and graphite-monochromated Mo Kα radiation (λ = 0.71073 Å).

Density functional calculations (B3LYP/ DGDVZP) were performed using Gaussian-09[30] through the WebMO interface (https://webmo.oscer.ou.edu). Geometric optimizations were performed on the five coordinate (porphine)Fe($OSiMe_3$) (S = 5/2) and the six-coordinate (porphine)Fe(NO)($OSiMe_3$) (S=0), followed by vibrational frequency calculations and molecular orbital calculations.

3.2.3 Syntheses

3.2.3.1 Preparation of the (por)Fe(O-aryl) Complexes

The five-coordinate ferric aryloxide porphyrin complexes (por)Fe(O-*aryl*) were prepared by treating dichloromethane solutions of the complex $[(por)Fe]_2(\mu\text{-O})$ or (por)Fe(OMe) with the aryl alcohol. The following reaction is representative:

(TPP)Fe(OC_6HF_4). To a dichloromethane solution (10 mL) of $[(TPP)Fe]_2(\mu\text{-O})$ (32.3 mg, 0.024 mmol) in a Schlenk tube was added excess 2,3,5,6-tetrafluorophenol

(40.7 mg, 0.240mmol). The mixture was stirred overnight at room temperature during which time the color of the solution changed from green to red-brown. The solvent was then reduced under vacuum to *ca.* 3 mL and hexane (10 mL) was added. The resulting brown precipitate was filtered, washed with hexane, and dried in vacuo to give 37.8 mg (0.045 mmol, 95 % isolated yield based on [(TPP)Fe]$_2$(μ-O)) of the product. IR (KBr, cm^{-1}): 3079 w, 3058 w, 3023 w, 2963 vw, 2928 vw, 2857 vw, 1820 w, 1640 m, 1600 m, 1532 s, 1506 s, 1477 s, 1442 m, 1401 w, 1340 m, 1276 w, 1202 m, 1176 (sh) w, 1169 m, 1090 s, 1077 s, 1005 s, 996 s, 932 s, 804 s, 754 s, 718 m, 704 s, 661 m, 573 w, 524 w, 490 m, 437 m. UV-vis (CH_2Cl_2, λ/ nm): 345, 415, 574. Anal. Cald for $C_{50}H_{29}N_4F_4OFe{\cdot}0.1CH_2Cl_2$: C, 71.45; H, 3.49; N, 6.65. Found: C, 71.67; H, 3.95; N, 6.65. Magnetic susceptibility measurements by Evans method: μ_{eff} = 5.34 BM at 294 K. X-ray quality crystals of (TPP)Fe(OC_6HF_4) were obtained by slow evaporation of a 1:1 dichloroethane/ cyclohexane solution of the compound.

(T(*p*-OMe)PP)Fe(OC_6HF_4): (T(*p*-OMe)PP)Fe(OC_6HF_4) was prepared as described for (TPP)Fe(OC_6HF_4) by treating a CH_2Cl_2 solution of [(T(*p*-OMe)PP)Fe]$_2$(μ-O) with excess C_6HF_4OH. Isolated yield: 93 %. IR (KBr, cm^{-1}): 3072 vw, 3032 vw, 3002 vw, 2957 w, 2934 w, 2908 w, 2837 w, 1655 w, 1637 w, 1607 m, 1575 w, 1531 m, 1506 s, 1796 m, 1476 (sh) m, 1440 m, 1411 w, 1336 m, 1290 m, 1249 s, 1175 s, 1097 m, 1035 m, 998 s, 934 m, 848 w, 807 s, 781m, 729 w, 717 m, 640 w, 602 m, 569 w, 539 w, 481 w, 423 w. Anal. Cald for $C_{54}H_{37}N_4F_4O_5Fe{\cdot}0.2CH_2Cl_2$: C, 67.06; H, 3.88; N, 5.77. Found: C, 67.01; H, 3.93; N, 5.79.

(TTP)Fe(OC_6H_4-*p*-F): This compound was prepared as described for (TPP)Fe(OC_6HF_4) by reacting [(TTP)Fe]$_2$(μ-O) with *p*-F-C_6H_4OH. Isolated yield: 94 %.

IR (KBr, cm^{-1}): 3126 vw, 3048 vw, 3024 w, 2919 w, 2863 vw, 1910 vw, 1819 vw, 1630 vw, 1528 w, 1509 w, 1490 s, 1449 w, 1404 vw, 1335 m, 1249 w, 1204 s, 1183 m, 1110 w, 1071 w, 1000 s, 832 m, 801 s, 768 m, 723 m, 562 w, 524 w, 511 w, 426 w. Anal. Cald for $C_{54}H_{40}N_4OFe \cdot CH_2Cl_2$: C, 71.75; H, 4.60; N, 6.09. Found: C, 72.25; H, 4.66; N, 5.93. X-ray quality crystals of (TTP)Fe(OC_6H_4-*p*-F) were obtained by slow evaporation of a 2:1 dichloromethane/ hexane solution of the compound.

(OEP)Fe(OC_6HF_4): This compound was prepared as described for (TPP)Fe(OC_6HF_4) by reacting [(OEP)Fe]$_2$(μ-O) with C_6HF_4OH . Isolated yield: 97 %. IR (KBr, cm^{-1}): 2966 m, 2933 w, 2872 w, 1654 m, 1636 m, 1648 w, 1616 w, 1531 s, 1502 s, 1473 s, 1457 m, 1449 m, 1419 w, 1402 m, 1374 w, 1370 w, 1362 w, 1315 m, 1275 m, 1269 m, 1217 w, 1167 s, 1147 s, 1222 w, 1110 m, 1089 s, 1083 s, 1075 s, 1064 m, 1054 s, 1016 s, 980 m, 957 s, 936 s, 924 s, 860 w, 850 w, 844 s, 917 s, 799 m, 747 m, 732 w, 729 w, 714 s, 705 w, 698 w, 683 w, 669 w, 586, w, 578 w, 564 w. Magnetic susceptibility measurements by Evans method: μ_{eff} = 5.64 BM at 290 K. Anal. Cald for $C_{42}H_{45}N_4F_4OFe$: C, 66.93; H, 6.02; N, 7.43. Found: C, 66.25; H, 6.00; N, 7.43. X-ray quality crystals of (OEP)Fe(OC_6HF_4) were obtained by slow evaporation of a 1:1 dichloromethane/ hexane solution of the compound.

(TMP)Fe(OC_6H_4-*p*-F): This compound was prepared as described for (TPP)Fe(OC_6HF_4) using the precursors (TMP)FeOMe and *p*-F-C_6H_4OH. Isolated yield: 90%. IR (KBr, cm^{-1}): 2952 w, 2918 w, 2855 w, 1633 w, 1611 w, 1509 m, 1493 m, 1445 w, 1382 w,1258 m, 1218 m, 1203 m, 1154 m, 1086 w, 1063 w, 999 s, 867 w, 852 w, 831 m, 804 m, 782 w, 747 w, 726 w, 639 w, 559 w, 510 m, 419 w.

(OETPP)Fe(OC_6HF_4): This was prepared as described for (TMP)Fe(OC_6H_4-*p*-F) using (OETPP)FeOMe as precursor. Isolated yield: 89 %. Anal. Cald for $C_{66}H_{61}N_4OF_4Fe{\cdot}0.8CH_2Cl_2$: C, 71.25; H, 5.60; N, 4.98. Found: C, 71.03; H, 6.10; N, 4.69. X-ray quality crystals of (OETPP)Fe(OC_6HF_4) were obtained by slow evaporation of a 2:1 dichloromethane/ hexane solution of the compound. UV-vis at room temperature (CH_2Cl_2, λ, nm): 392, 441, 476, 570, 705. Magnetic susceptibility measurements by Evans method: μ_{eff} = 4.6 BM at 294 K.

(T_{piv}PP)Fe(OC_6HF_4): This compound was prepared as described for (TPP)Fe(OC_6HF_4) using the precursor [(T_{piv}PP)Fe]$_2$(μ-O) . Isolated yield: 89 %. IR (KBr, cm^{-1}): 3435 m, 3372 w, 3064 w, 2961 m, 2936 w, 2909 w, 2869 w, 1825 w, 1695 s, 1638 w, 1605 w, 1583 s, 1510 s, 1477 s, 1455 s, 1441 s, 1396 w, 1366 w, 1332 w, 1301 m, 1254 w, 1205 w, 1159 m, 1100 m, 1085 m, 1074 m, 1000 s, 807 m, 800 m, 761 s, 720 m, 657 w, 562 w, 494 w, 466 w. UV-vis (CH_2Cl_2, λ, nm): 355, 415, 502, 573. Magnetic susceptibility measurements by Evans method: μ_{eff} = 5.35 BM at 294 K.

(T_{piv}PP)Fe(OC_6H_4-*p*-F): This compound was prepared as described for (TPP)Fe(OC_6HF_4) using [(T_{piv}PP)Fe]$_2$(μ-O) as the precursor. Isolated yield: 93 %. IR (KBr, cm^{-1}): 3431 m. 3360 w, 2961 w, 2869 w, 1691 m, 1682 m, 1668 m, 1582 m, 1510 s, 1492 m, 1455 m, 1443 m, 1302 w, 1220 m, 1204 m, 1559 m, 999 s, 833 m, 807 m, 761 m, 749 m. Anal. Cald for $C_{70}H_{68}N_8O_5FFe{\cdot}2.5CH_2Cl_2$: C, 62.71; H, 5.30; N, 8.07. Found: C, 62.47; H, 4.98; N, 7.53.

(T_{piv}PP)Fe(OC_6H_4-*p*-NO_2): This compound was prepared as described for (TPP)Fe(OC_6HF_4) by reacting [(T_{piv}PP)Fe]$_2$(μ-O) with *p*-NO_2-C_6H_4OH. Isolated yield: 92 %. IR (KBr, cm^{-1}): 3429 s, 3060 vw, 2959 m, 2907 w, 2869 w, 1692 s, 1581 s, 1515

s, 1479 m, 1455 m, 1438 m, 1396 w, 1365 w, 1333 w, 1300 m, 1253 w, 1205 w, 1158 m, 1071 w. 998 s, 924 w, 807 m, 796 w, 760 m, 722 w, 657 w, 565 w.

$(TF_8PP)Fe(OC_6HF_4)$: This compound was prepared as described for $(TPP)Fe(OC_6HF_4)$ using $(TF_8PP)Fe(OMe)$ as precursor. Isolated yield: 95 %. IR (KBr, cm^{-1}): 3090 vw, 2956 vw, 2854 vw, 2745 vw, 1638 w, 1624 m, 1583 m, 1534 vw, 1508 m, 1479 m, 1465 s, 1366 vw, 1328 m, 1276 m, 1237 m, 1206 m, 1167 m, 1102 m, 1077 m, 1001 s, 935 m, 887 w, 800 m, 782 m, 745 w, 715 m, 662 w, 579 m, 538 w, 509 w, 494 w, 474 w, 420 w. UV-vis (CH_2Cl_2, λ, nm): 330, 407, 495, 560, 615. Magnetic susceptibility measurements by Evans method: μ_{eff} = 5.77 BM at 294 K.

3.2.3.2 Preparation of the (por)Fe(O(CH2)nSiMe3) (n = 0, 1) complexes

$(TPP)Fe(OCH_2SiMe_3)$: This compound was prepared as described for $(TPP)Fe(OC_6HF_4)$ by treating $[(TPP)Fe]_2(\mu\text{-}O)$ or (TPP)Fe(OMe) with trimethylsilylmethanol (Me_3SiCH_2OH). Isolated yield: 93%. IR (KBr, cm^{-1}): $\delta_{Si\text{-}Me}$ = 1243 m, $\nu_{Si\text{-}C}$ = 853 s, 844 (sh) s. also; 3054 w, 3023 w, 2951 w, 2897 w, 2822 w, 2773 w, 1813 w, 1629 w, 1597 m, 1487 m, 1440 m, 1411 m, 1338 m, 1202 m, 1777 w, 1556 w, 1071 m, 1003 s, 995 s, 800 s, 752 m, 719 m, 701 s, 660 w, 573 w, 520 w, 435 w. UV-vis (CH_2Cl_2, λ, nm): 336, 415, 574, 632. Anal. Cald for $C_{48}H_{39}N_4OSiFe{\cdot}2.5CH_2Cl_2$: C, 61.63; H, 4.51; N, 5.69. Found: C, 61.89; H, 4.25; N, 5.77. X-ray quality crystals of $(TPP)FeO(CH_2SiMe_3)$ were obtained by slow evaporation of a 1:1 dichloromethane/ cyclohexane solution of the compound.

$(OEP)Fe(OSiMe_3)$: To a stirred THF (10 mL) solution of (OEP)FeCl (50.1 mg, 0.080 mmol) was added 1.2 equiv. of $KOSiMe_3$ (13.7 mg). The mixture was stirred for

1 h during which time the color of the solution changed from pink to red. After 1 hr of stirring the solvent was removed under vacuum and the resulting solid redissolved with toluene, filtered and then dried to give the (TPP)Fe($OSiMe_3$) product. Isolated yield: 92%. IR (KBr, cm^{-1}): $\delta_{Si\text{-}Me}$ = 1240 s, $\nu_{Si\text{-}O}$ = 958 s, 831 (sh) s; also. 2967 vs, 2931 m, 2871 m, 2780 w, 1687 w, 1629 w, 1468 m, 1450 m, 1375 w, 1317 w, 1269 m, 1216 m, 1146 s, 1111 w, 1056 s, 1016 s, 981 m, 915 m, 831 s, 748 m, 732 w, 698 m, 475 m. UV-vis (CH_2Cl_2, λ, nm): 347, 395, 465, 582, 656.

(TPP)Fe($OSiMe_3$): This compound was prepared as described for (OEP)Fe($OSiMe_3$) using (TTP)FeCl as precursor. Isolated yield: 90%. IR (KBr, cm^{-1}): $\delta_{Si\text{-}Me}$ = 1240 m, $\nu_{Si\text{-}O}$ = 961 s, 949 (sh) s; also, 3054 w, 3021 w, 2948 w, 1597 m, 1487 m, 1441 m, 1339 s, 1263 w, 1202 m, 1176 m, 1156 w, 1070 s, 1003 s, 995 s, 833 s, 800 s, 749 s, 730 w, 718 m, 699 s, 660 m, 572 w, 523 w. X-ray quality crystals (TPP)Fe($OSiMe_3$) were obtained by slow evaporation of a 1:2 dichloromethane/ hexane solution of the compound.

(OEP)Fe(OCH_2SiMe_3): This compound was prepared as described for (TPP)Fe(OCH_2SiMe_3) using [(OEP)Fe]$_2$(μ-O) as precursor. Isolated yield: 93%. IR (KBr, cm^{-1}): $\delta_{Si\text{-}Me}$ = 1241 m, $\nu_{Si\text{-}C}$ = 855 s; also, 2963 m, 2931 m, 2871 m, 2773 w, 1469 m, 1450 m, 1373 w, 1319 w, 1270 w, 1216 w, 1147 s, 1111 w, 1056 m, 1015 s, 981 m, 958 s, 916 w, 841 s, 749 m, 731 w, 719 w, 699 m, 586 m. UV-vis (CH_2Cl_2, λ/ nm): 384, 547. Magnetic susceptibility measurements by Evans method: μ_{eff} = 5.85 at 294 K. Anal. Cald for $C_{40}H_{55}N_4OSiFe{\cdot}0.4CH_2Cl_2$: C, 66.86; H, 7.75; N, 7.72. Found: C, 66.82; H, 7.12; N, 7.88.

(T_{piv}PP)Fe(OCH_2SiMe_3): This compound was prepared as described for (TPP)Fe(OCH_2SiMe_3) using [(T_{piv}PP)Fe]$_2$(μ-O) as precursor. Isolated yield: 87%. IR (KBr, cm^{-1}): $\delta_{Si\text{-}Me}$ = 1246 m, $\nu_{Si\text{-}C}$ = 855 s, 844 (sh) s; also, 3434 s, 3061 w, 2958 m, 2905 w, 2869 w, 1694 s, 1582 m, 1517 s, 1479 m, 1455 m, 1440 m, 1333 w, 1302 m, 1257 m, 1157 m, 1071 m, 998 s, 806 m, 798 m, 760 s, 755 (sh) s, 722 m, 562 w. UV-vis (CH_2Cl_2, λ/ nm): 315, 415, 568, 656. Magnetic susceptibility measurements by Evans method: μ_{eff} = 5.84 BM at 294 K. Anal. Cald for $C_{68}H_{75}N_8O_5SiFe{\cdot}0.2CH_2Cl_2$: C, 69.11; H, 6.41; N, 9.45. Found: C, 69.17; H, 6.36; N, 9.94.

(T_{piv}PP)Fe($OSiMe_3$): This compound was prepared as described for (OEP)Fe($OSiMe_3$) using (T_{piv}PP)FeCl as precursor. Isolated yield: 89%. IR (KBr, cm^{-1}): $\delta_{Si\text{-}Me}$ = 1242 m, $\nu_{Si\text{-}O}$ = 956 s, 939 (sh) s. Also, 3433 m, 3364 w, 3059 w, 2957 m, 2907 w, 2868 w, 1695 s, 1582 s, 1517 s, 1477 m, 1457 m, 1439 m, 1395 w, 1364 w, 1332 w, 1301 m, 1226 w, 1206 w, 1156 s, 1105 w, 1070 m, 998 s, 923 m, 833 m, 807 m, 796 m, 759 s, 751 m, 722 w, 669 w, 657 w, 638 w, 561 w. UV-vis (CH_2Cl_2, λ/ nm): 328, 415, 511, 571. Magnetic susceptibility measurements by Evans method: μ_{eff} = 5.60 BM at 293 K. Anal. Cald for $C_{67}H_{73}N_8O_5Fe{\cdot}CH_2Cl_2$: C, 65.91; H, 6.10; N, 9.04. Found: C, 65.72; H, 5.66; N, 9.38. X-ray quality crystals (T_{piv}PP)Fe($OSiMe_3$) were obtained by slow evaporation of a 1:10 dichloromethane/ hexane solution of the compound.

3.2.3.3 Reaction of the (por)Fe(OR) compounds with NO and IR Data Collection

The following manipulations were performed under strict nitrogen atmosphere in a glovebox. Powdered samples of the five-coordinate (por)Fe(OR) compound (~5

mg) were carefully transferred into a vial and the vial and its contents were sealed with an air-tight septum. NO (~10 equiv. by volume) was transferred into the vial through the septum using an air-tight Hamilton Syringe/ needle. The mixture was carefully agitated by shaking the vial for 1 min and the sealed vial and its contents were allowed to stand at room temperature for 1 h. (*Note: These reactions are often accompanied by change in color of the powdered samples, typically from brown to red)*. After the 1 h reaction time, the septum was removed. Approximately 2 mg of the sample was taken from the vial and cautiously mixed with KBr and pressed into a pellet (Solid IR Cell). The KBr cell was quickly transferred to the IR spectrometer and IR spectral data was collected. The reactions of the single crystal samples of the (por)Fe(OR) were done by a similar procedure.

3.3 Results and discussion

3.3.1 Synthesis and structural characterization

The five coordinate (por)Fe(OR) (R = aryl, $SiMe_3$, CH_2SiMe_3) complexes were prepared by one of the following three methods: (**i**) treatment of the μ-oxo-dimer complex[(por)Fe]$_2$(μ-O) with an "alcohol" (ROH)[31] (Eq. 3.1), (**ii**) by "alkoxide" ($R'O^-$) exchange (Eq. 3.2), and (**iii**) by treating (por)FeCl with the "metal alkoxide" (MOR) (K or Na) (Eq. 3.3).

$$[(por)Fe]_2(\mu\text{-}O) + 2ROH \rightarrow 2(por)Fe(OR) + H_2O \quad (\mathbf{3.1})$$

$$(por)Fe(OR') + ROH \rightarrow (por)Fe(OR) + R'OH \quad (\mathbf{3.2})$$

$$(por)FeCl + MOR \rightarrow (por)Fe(OR) + MCl \quad (\mathbf{3.3})$$

The aryloxide complexes (por)Fe(OC_6HF_4) (por = TPP, T(*p*-OMe)PP, OEP, TF_8PP, OETPP, $T_{piv}PP$), (por)Fe(OC_6H_4-*p*-F) (por = TTP, TMP, $T_{piv}PP$), and ($T_{piv}PP$)Fe(OC_6H_4-*p*-NO_2) were prepared either by method (**i**) (Eq. 3.1) or method (**ii**) (Eq. 3.2). I found method (**i**) a more convenient method considering the precursor [(por)Fe]$_2$(μ- O) complex could be readily purified by column chromatography and due to the fact that the progress of the reaction could easily be monitored by IR spectroscopy. The disappearance of the IR bands in the 870-880 cm^{-1} region due to the Fe−O−Fe stretch[18,32-34] of the [(por)Fe]$_2$(μ- O) precursors in the IR spectra were indicative of completion of the reaction. Also, the [(por)Fe]$_2$(μ-O) or (por)Fe(OMe) solutions gradually changed color upon addition of the ROH reagent. For example, during the reaction of [(TPP)Fe]$_2$(μ-O) with 2,3,5,6-tetrafluorophenol (C_6HF_4OH) in CH_2Cl_2, the color of the solution changed from green to red-brown, generating, after workup, the product in 95% isolated yield. The IR spectrum of the final product did not show the Fe−O−Fe band of the precursor at ~ 875 cm^{-1}. The bands due to the axial aryloxide ligands in the spectrum were difficult to assign as they have relatively weak intensities that may also have overlapped with the porphyrin IR bands. In the (OEP)Fe(O-*aryl)* complexes, however, the infrared spectral bands due to the $\nu_{C=C}$ of aryloxide ligand were observed in the 1600 cm^{-1} region.

The (por)Fe(O-*aliphatic*) compounds were prepared by methods (**i**), (**ii**) or (**iii**). For example, the reaction of [(TPP)Fe]$_2$O(μ-O) or (TPP)Fe(OMe) with Me_3SiCH_2OH produced (TPP)Fe(OCH_2SiMe_3), and the reaction of (TPP)FeCl with $KOSiMe_3$ produced (TPP)Fe($OSiMe_3$). The IR spectra of the resulting (por)Fe($O(CH_2)_nSiMe_3$) (por = OEP, TPP, $T_{piv}PP$, n = 0, 1) complexes displayed strong bands at ~1243 cm^{-1} and

~855 cm^{-1} due to Si−C−H (of $SiMe_3$) bending ($\delta_{Si\text{-}Me}$) and C−$SiMe_3$ stretch ($\nu_{Si\text{-}C}$), respectively when n =1 (Table 3.1).[35]

Table 3.1. Selected IR (KBr, cm^{-1}) data of the (por)Fe($O(CH_2)_nSiMe_3$) (n = 0, 1) complexes.

	(TPP)Fe(OR)	(OEP)Fe(OR)	(T_{piv}PP)Fe(OR)	(P)Fe(OR)*
R = $SiMe_3$	1240	1240	1242	1308
	961 (949 sh)	958 (831 sh)	956, (936 sh)	962 (877 sh)
R = CH_2SiMe_3	1243	1241	1246	
	853 (844 sh)	855	855 (844 sh)	

*Obtained by calculation where P is porphine.

In the case of (por)Fe($OSiMe_3$), (i.e., n = 0), medium intensity $\delta_{Si\text{-}C}$ bands were observed at ~1242 cm^{-1}, and a strong band due to $\nu_{Si\text{-}O}$ observed at ~960 cm^{-1}.[35] For example, in the complex (T_{piv}PP)Fe($OSiMe_3$) these bands were observed at 1242 cm^{-1} and 956 (936 sh) cm^{-1}, respectively. The assignment of the IR bands in (por)Fe($OSiMe_3$) were confirmed by DFT calculations using B3LYP/ DGDZVP for the model compound (P)Fe($OSiMe_3$) (P = unsubstituted porphine ring) (Table 3.1). Furthermore, the bands due to the $Me_3Si(CH_2)_nO$ fragment in the (por)Fe($O(CH_2)_nSiMe_3$) complexes were observed at lower frequencies than in the corresponding precursors Me_3SiCH_2OH and $KOSiMe_3$, indicative of ligand binding to the iron center.

The effective magnetic moments (μ_{eff}) of compounds (OEP)Fe(OC_6HF_4), (OEP)Fe(OCH_2SiMe_3), (T_{piv}PP)Fe(OCH_2SiMe_3), (T_{piv}PP)Fe($OSiMe_3$) and (TF_8PP)Fe(OC_6HF_4), as determined by Evans method[24] are 5.64, 5.85, 5.84, 5.60 and 5.77 BM, respectively. These are in the same range as those determined for other five-coordinate high-spin (S = 5/2) (por)Fe(OR) complexes,[31,36] In contrast, the compound

(TPP)Fe(OC_6HF_4) was found to exhibit admixed spin state properties[36] in solution, with a μ_{eff} = 5.34 BM; a value quite close to the μ_{eff} = 5.19 BM obtained for the related admixed spin-state (TPP)Fe($OClO_3$) compound.[37] Weak field axial ligand binding to Fe, as in the case of the latter compound, a smaller iron displacement from the mean porphyrin plane[7] and the deformation of the porphyrin macrocycle (*vide infra*)[8,38] are some of the factors that contribute to influencing the spin-state of iron porphyrin complexes. I expect these factors to contribute to the observed magnetic susceptibilities of the compounds. Note that the compounds (T_{piv}PP)Fe(OC_6HF_4) (μ_{eff} = 5.35) and (OETPP)Fe(OC_6HF_4) (μ_{eff} = 4.60) seem to possess admixed spin-state properties in solution. Furthermore, the μ_{eff} values of 5.85, 5.60 and 5.84 for (OEP)Fe(OCH_2SiMe_3), (T_{piv}PP)Fe($OSiMe_3$) and (T_{piv}PP)Fe(OCH_2SiMe_3), respectively, show that these complexes are also essentially high-spin species.

UV-vis spectral data of some of the compounds in CH_2Cl_2 are shown in Table 3.2. All the complexes have at least one peak with $\lambda_{max} \leq 400$ nm, and the absorption bands compare well with those of other high-spin ferric (TPP)Fe(OR) complexes reported by Shaffer and Straub (Table 3.2).[39]

Table 3.2. UV-vis spectra of some (por)Fe(OR) compounds.

Compound	Peak position, λ (nm)	Reference
(TPP)Fe(OC_6HF_4)	345, 415, 574	this work
(TPP)Fe(OC_6H_2-2,4,6-Me)	330, 418, 487, 582, 632	[39]
(TPP)Fe(OC_6H_5)	335, 418, 495, 558, 635, 840	[39]
(TPP)Fe(OC_6H_4-*p*-Me)	332, 418, 500, 567, 638	[39]
(TPP)Fe(OC_6H_4-*p*-NO_2)	362, 418, 503, 565, 640, 670, 840	[39]
(TPP)Fe(OC_6H_4-2,4-NO_2)	356, 417, 508, 575, 654, 683, 860	[39]
(TF_8PP)Fe(OC_6HF_4)	330, 407, 495, 560, 615	this work
(T_{piv}PP)Fe(OC_6HF_4)	355, 415, 502, 573	this work
(PPIXDME)Fe(OC_6H_4-*p*-NO_2)	400, 501, 529, 620	[31]
(OEP)Fe(OC_6HF_4)	367, 394, 504, 534, 623	this work
(TPP)Fe(OCH_2SiMe_3)	336, 415, 574, 632	this work
(OEP)Fe($OSiMe_3$)	347, 395, 465, 582, 656	this work
(OEP)Fe(OC_6H_5)	391, 488, 515, 602	[40]
(OETPP)Fe(OC_6H_5)	392, 441, 476, 570, 705	this work
(T_{piv}PP)Fe($OSiMe_3$)	328, 415, 511, 571	this work
(TPP)Fe($OCMe_3$)	344, 418, 510, 573, 610, 694, 775	[39]
(OEP)Fe(OCH_2SiMe_3)	384, 547	this work
(T_{piv}PP)Fe(OCH_2SiMe_3)	315, 415, 568, 656	this work
(T_{piv}PP)Fe(OMe)	353, 416, 512, 624, 680	this work
(TPP)Fe(OMe)	344, 419, 500, 581, 632, 765	[39]
(OETPP)Fe(OMe)	377, 438, 486	this work

Importantly, the position of the Soret band is dependent on the substitution on the porphyrin macrocycle, and the dependence of the Soret band on the axial ligand (pK_a) has already been noted in the literature.[41] It has been known for decades that *para*-substituted electron donor groups at the *meso* position of free base and acid-cations of tetraphenylporphyrins tend to shift the UV-vis bands to lower wavelengths[4,42] and the electronic effects on the redox potentials of *meso*-substituted porphyrins have been extensively demonstrated by electrochemistry.[43,44] For example, *para*-substituted electron-withdrawing groups on the aryl groups of *meso*-tetraaryl porphyrins increase the oxidation potentials of the iron porphyrin complexes.[44]

The UV-vis spectrum is, however, different for the di-*ortho*-substituted tetraaryl porphyrin compound, (TF_8PP)Fe(OC_6HF_4), where there is a blue shift of the Soret band

to 407 nm (*cf.* Soret band at 415 nm in the unsubstituted (TPP)Fe(OC_6HF_4) compound). It is not clear why this shift occurs, but one can infer the reasons being the inductive effect of the strong electron withdrawing F atoms (×8) on the phenyl ring as well as steric hindrance to co-planarity of the aryl group with the porphyrin plane (*vide infra*). Blue shifts have been observed in the free base porphyrin compounds T(*o*-CH_3)PPH_2 and T(*o*-CH_2CH_3)PPH_2, and have been attributed to direct steric interaction between the *ortho*-substituents and the porphyrin ring which tend to distort the porphyrin macrocycle.[42] Note that in (T_{piv}PP)Fe($OSiMe_3$), (T_{piv}PP)Fe(OCH_2SiMe_3), (T_{piv}PP)Fe(OC_6HF_4) and (TPP)Fe(OCH_2SiMe_3) where the porphyrins may have comparable electronic properties and less steric hindrance in the vicinity of the axial ligands, their Soret bands were observed at 415 nm (Figure 3.1).

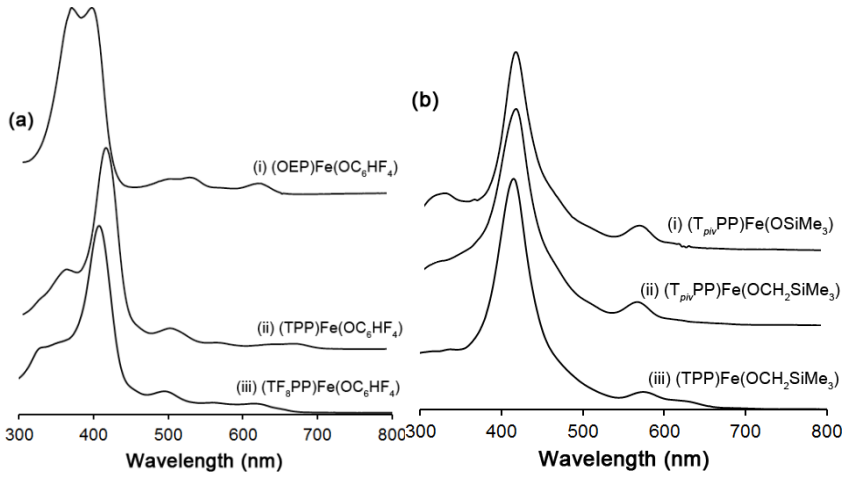

Figure 3.1. UV-vis spectra of (a) (por)Fe(*O-aryl*): (i) (OEP)Fe(OC_6HF_4), (ii) (TPP)Fe(OC_6HF_4), (iii) (TF_8PP)Fe(OC_6HF_4); and (b) por)Fe(*O-alkyl*): (i) (T_{piv}PP)Fe($OSiMe_3$), (ii) (T_{piv}PP)Fe(OCH_2SiMe_3), (iii) (TPP)Fe(OCH_2SiMe_3), in CH_2Cl_2.

Furthermore, the 407 nm Soret band observed in the UV-vis spectrum of the compound (TF_8PP)Fe(OC_6HF_4) is lower than that reported for (TF_8PP)FeCl (411 nm),[45]

and the difference may be attributed to the different electronic properties of the axial ligand; $C_6HF_4O^-$ being a better σ-donor than chloride. Even more striking is the difference in the location of the Q-bands in these complexes. In the compound $(TF_8PP)Fe(OC_6HF_4)$ the Q bands were observed at lower wavelengths (560 nm), but at relatively higher wavelengths in $(TPP)Fe(OC_6HF_4)$ (574 nm) and $(T_{piv}PP)Fe(OC_6HF_4)$ (573 nm) probably due to similar reason discussed above. In general, the maximum absorbances of the wavelengths in the UV spectra are less than 1. In addition, the UV-vis spectra of the (por)Fe(OR) compounds are consistent with other ferric (por)FeX (and not ferrous) systems in literature and they support that they are essentially high-spin species.

Diffraction quality single crystals of some of the five-coordinate complexes were obtained and subjected to X-ray crystallographic studies. Molecular structures of the aryloxide complexes $(TPP)Fe(OC_6HF_4)$, $(OEP)Fe(OC_6HF_4)$, $(OETPP)Fe(OC_6HF_4)$, $(TF_8PP)Fe(OC_6HF_4)$ and $(TTP)Fe(OC_6H_4$-*p*-F) are shown in Figure 3.2, Figure 3.3, Figure 3.4, Figure 3.5 and Figure 3.6, respectively (Table 3.3).

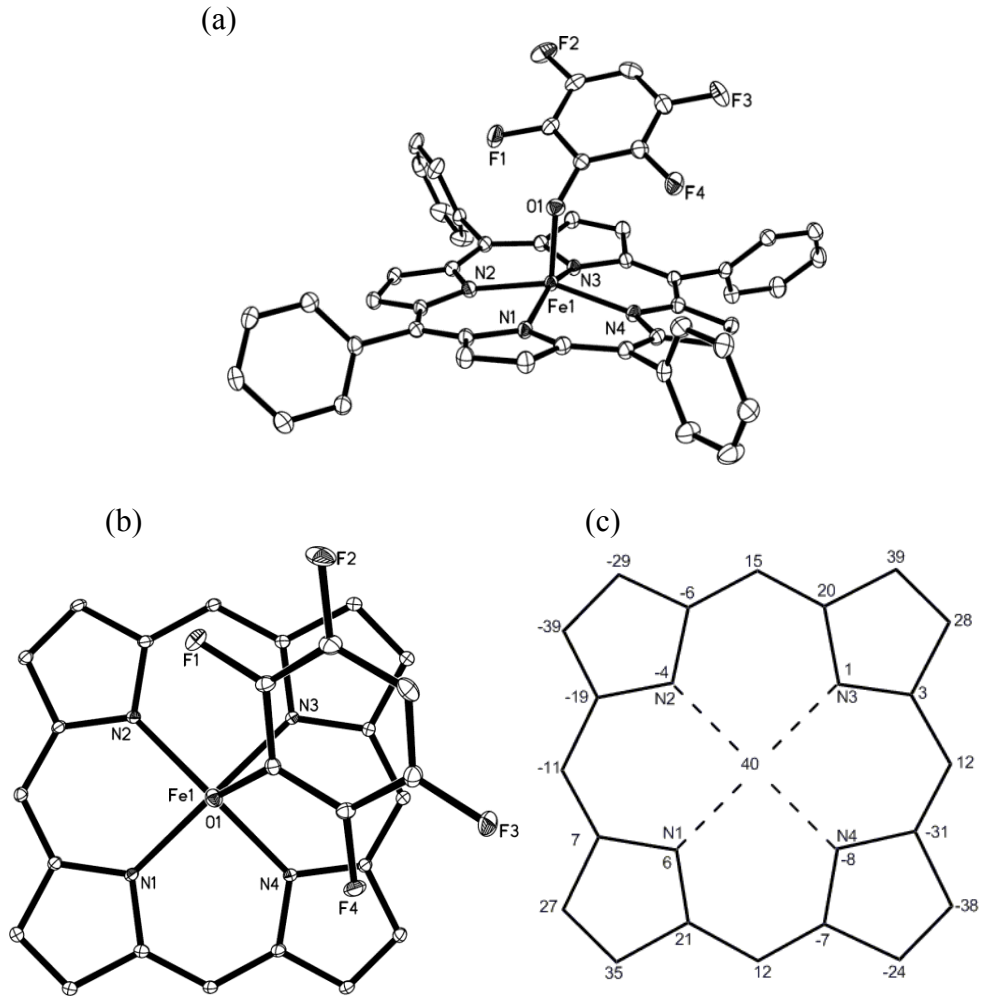

Figure 3.2 (a) Molecular structure of (TPP)Fe(OC_6HF_4). Hydrogen atoms and disordered components have been omitted for clarity. (b) View of the axial C_6HF_4O ligand relative to the porphyrin, with view along the O(1)−Fe(1) bond. (c) Perpendicular atom displacements (in Å × 100) of the porphyrin core from the 24-atom mean planes of the porphyrin of (TPP)Fe(OC_6HF_4).

Table 3.3. The (por)Fe(O-aryl) complexes characterized by X-ray crystallography.

Compound	Figure Number
(TPP)Fe(OC_6HF_4)	Figure 3.2
(OEP)Fe(OC_6HF_4)	Figure 3.3
(OETPP)Fe(OC_6HF_4)	Figure 3.4
(TF_8PP)Fe(OC_6HF_4)	Figure 3.5
(TTP)Fe(OC_6H_4-*p*-F)	Figure 3.6

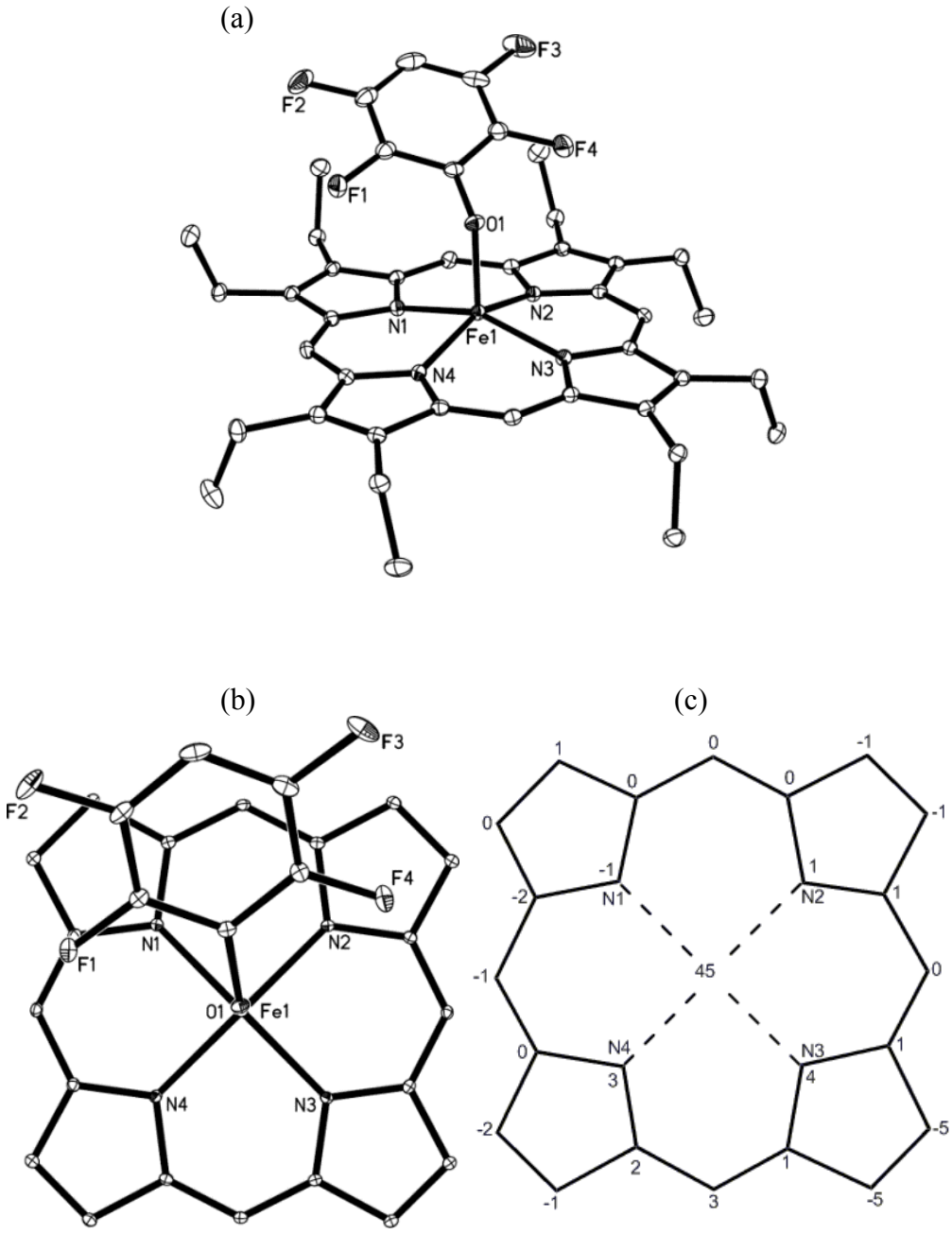

Figure 3.3. (a) Molecular structure of (OEP)Fe(OC_6HF_4). Hydrogen atoms and disordered components have been omitted for clarity. (b) View of the axial C_6HF_4O ligand relative to the the porphyrin, with view along the O(1)−Fe(1) bond. (c) Perpendicular atom displacements (in Å × 100) of the porphyrin core from the 24-atom mean planes of the porphyrin of (OEP)Fe(OC_6HF_4).

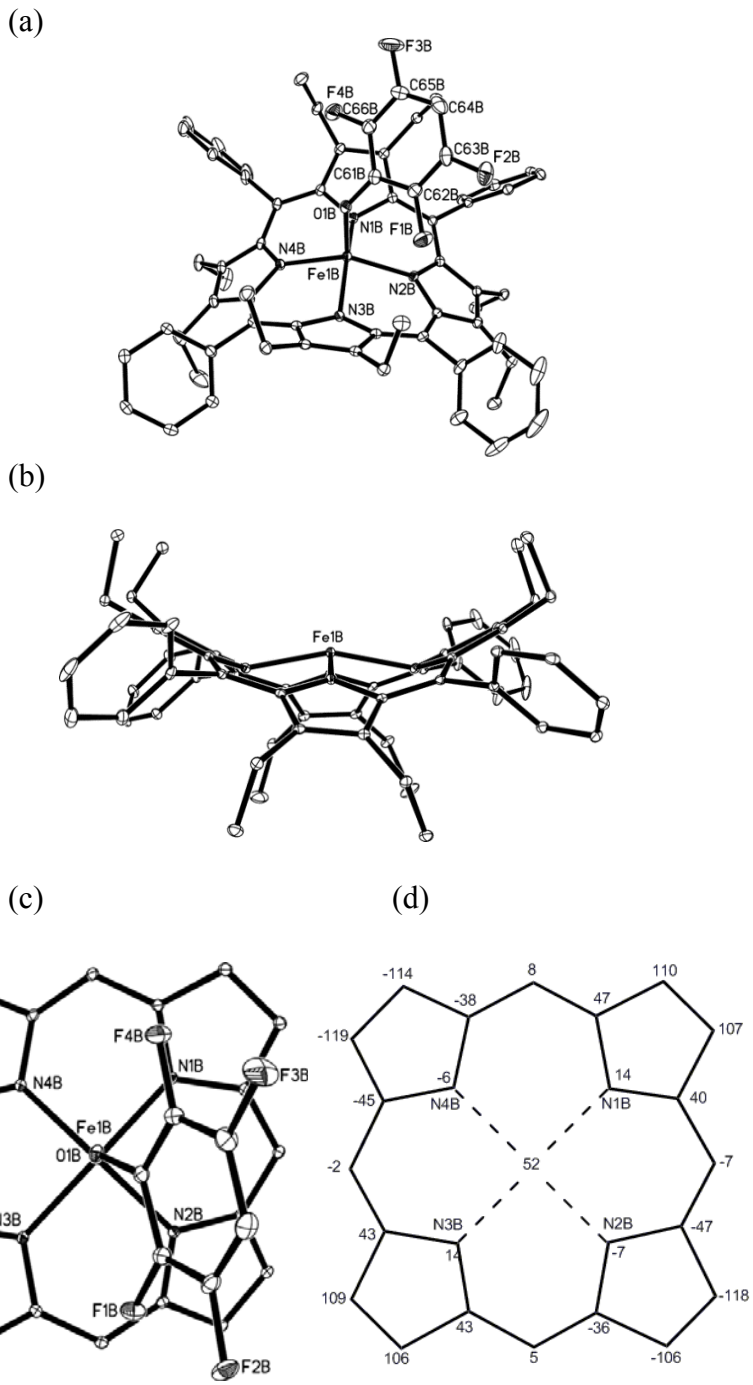

Figure 3.4. (a) Molecular structure of (OETPP)Fe(OC_6HF_4) and (b) molecular structure showing the saddled nature of the porphyrin macrocycle. Hydrogen atoms and disordered components have been omitted for clarity. (c) View of the axial C_6HF_4O ligand relative to the the porphyrin, with view along the O1(B)−Fe1(B) bond. (d) Perpendicular atom displacements (in Å × 100) of the porphyrin core from the 24-atom mean planes of the porphyrin of (OETPP)Fe(OC_6HF_4).

(a)

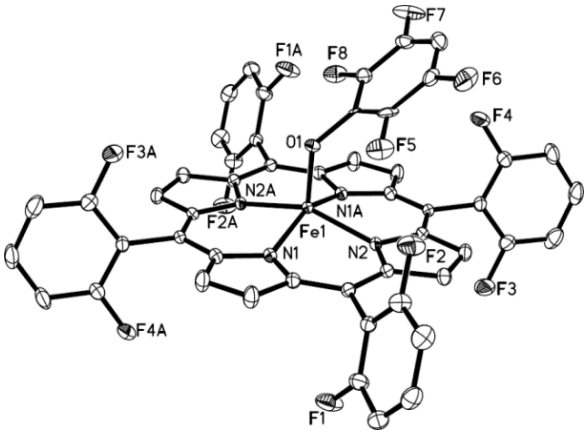

(b)

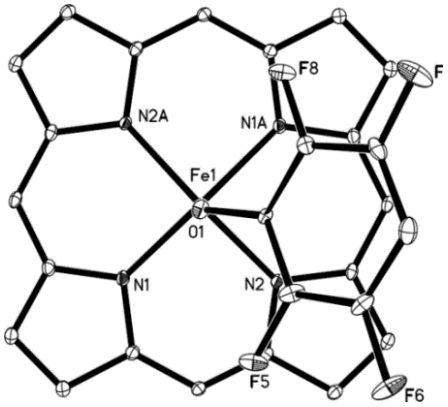

(c)

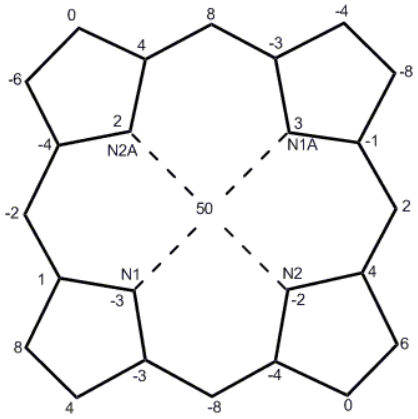

Figure 3.5. (a) Molecular structure of $(TF_8PP)Fe(OC_6HF_4)$. Hydrogen atoms and disordered components have been omitted for clarity. (b) View of the axial C_6HF_4O ligand relative to the the porphyrin, with view along the O(1)−Fe(1) bond. (c) Perpendicular atom displacements (in Å × 100) of the porphyrin core from the 24-atom mean planes of the porphyrin of $(TF_8PP)Fe(OC_6HF_4)$.

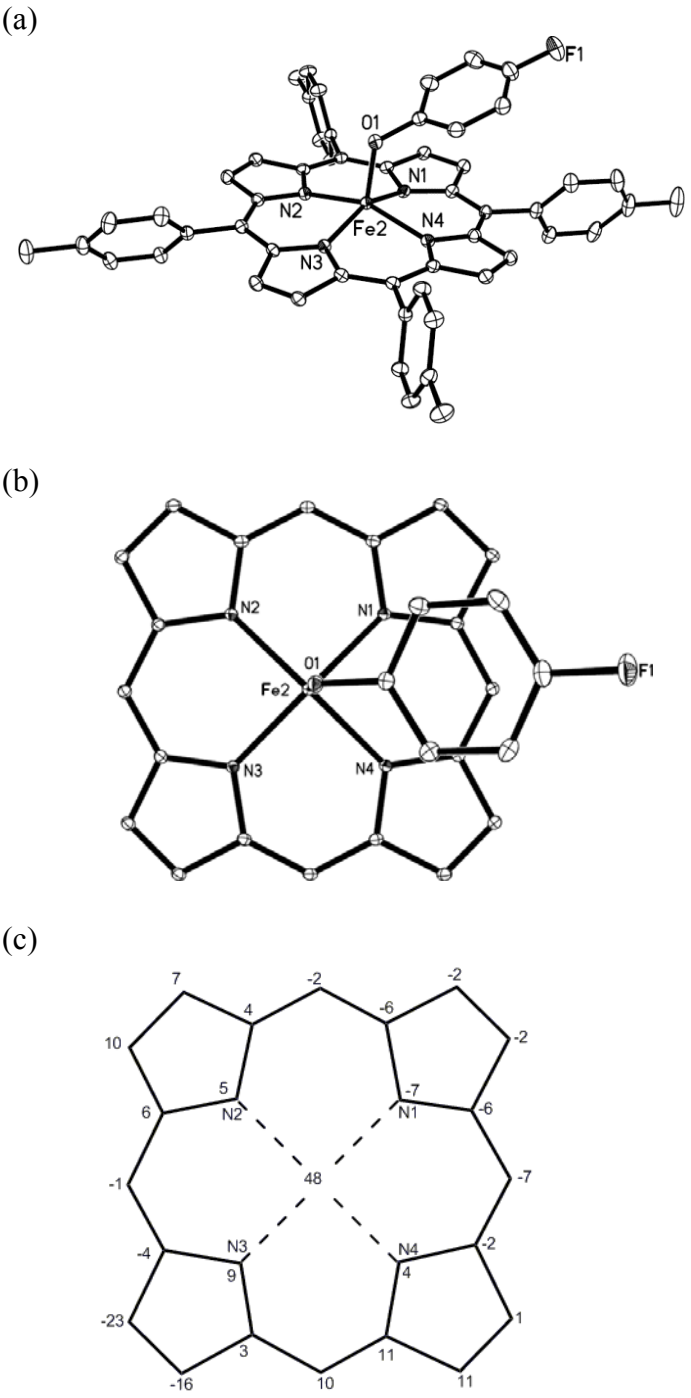

Figure 3.6. (a) Molecular structure of (TTP)Fe(OC_6H_4-*p*-F). Hydrogen atoms and disordered components have been omitted for clarity. (b) View of the axial *p*-F-C_6H_4O ligand relative to the the porphyrin, with view along the O(1)−Fe(2) bond. (c) Perpendicular atom displacements (in Å × 100) of the porphyrin core from the 24-atom mean planes of the porphyrin of (TTP)Fe(OC_6H_4-*p*-F).

Scheidt has provided a "nomenclature" for describing porphyrin plane distortions. He used idealized depictions of the out-of-plane core distortions to describe the plane of porphyrins and metalloporphyrin. The depictions are shown in Figure 3.7 where the filled and open circles represent atoms with displacement on opposite sides of the porphyrin mean plane.[46] The types of distortions are saddle (*sad*), wave (*wav*), ruffled (*ruf*) and domed-shape (*dom*) (Figure 3.7), and these terminologies have been used to describe the porphyrin core in this work.

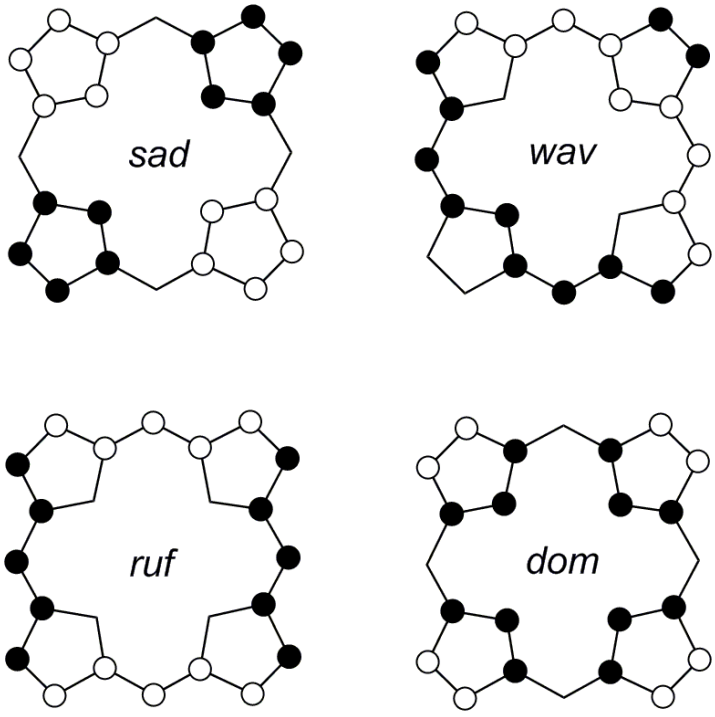

Figure 3.7. Idealized depictions of the out-of-plane core distortions that are found in porphyrin and metalloporphyrin species. Adapted from ref. [46]

The porphyrin planes of the *meso*-tetraaryl-substituted porphyrin complex (TPP)Fe(OC_6HF_4) (Fig. 3.2c) are severely distorted and they compared with that already reported for (T(*p*-OMe)PP)Fe(OC_6HF_4).[47] Furthermore, whereas the porphyrin

plane in the compound (TPP)Fe(OC_6HF_4) (Fig. 3.2c) appears to be saddled in shape, the porphyrin plane in the related (OEP)Fe(OC_6HF_4) is relatively planar (Fig. 3.3c), and the porphyrin plane in (TF_8PP)Fe(OC_6HF_4) (Fig.3.5c) is only slightly distorted. Similarly, the porphyrin macrocycle in (TTP)Fe(OC_6H_4-*p*-F) is saddled (Fig. 3.6c). The deformation of the porphyrin macrocyle often results in shortening of the Fe−N(por), and thus, the larger Fe displacement from the 24-mean porphyrin atom plane (Δ_{por}Fe) and concomitant destabilization of the ($d_{x^2-y^2}$) orbitals.[48,49] Consequently, these factors contribute in determining the spin state of the complexes. For instance, severe deformation of the porphyrin macrocycle in the compound (TPP)Fe(OC_6HF_4) may be responsible for its admixed spin-state properties (μ_{eff} = 5.34 BM) in solution.

Selected bond lengths and bond angles for the crystal structures are listed in Table 3.4 The Fe−O bond lengths in the aryloxide complexes characterized in this study lie in the 1.8 -1.9 Å range, with the Fe−N(por) lengths of ~2 Å being typical of high-spin Fe(III) porphyrin complexes (Table 3.4).[7]

Table 3.4. Selected bond distances (Å), bond angles (°), and displacement of Fe above porphyrin plane, (Δ_{por}Fe and Δ_NFe (Å))

Compound	Fe−N	Fe−O	FeO−C or FeO−Si	∠FeOC or ∠FeOSi	Δ_{por}Fe (Δ_NFe)	Ref
(TPP)Fe(OC_6HF_4)	2.055(3)-2.066(3)	1.886(2)	1.352(4)	127.90(19)	0.398 (0.411)	this work
(T(*p*-OMe)PP)Fe-(OC_6HF_4)	2.048(2)-2.056(2)	1.883(2)	1.321(3)	130.46(17)	0.364	[47]
(OEP)Fe(OC_6HF_4)	2.0553(15)-2.0597(15)	1.9053(13)	1.330(2)	122.97(11)	0.453 (0.435)	this work
(OETPP)Fe(OC_6HF_4)	2.0492(19)-2.0571(18)	1.9253(17)	1.281(3)	138.89(16)	(0.478)	this work
(TF_8PP)Fe(OC_6HF_4)	2.036(4)-2.067(4)	1.819(5)	1.403(10)	131.7(2)	0.497 (0.497)	this work
(TTP)Fe(OC_6H_4-*p*-F)	2.0700(14)-2.0746(14)	1.8611(13)	1.351(2)	122.71(12)	0.480 (0.454)	this work
(OEP)Fe(OC_6H_5)	2.061[a]	1.848(4)	142.2(3)		0.467	[50]
(OEP)Fe(O-2,4,6-(NO_2)$_3$-C_6H_2)	2.034(2)-2.062(3)	1.930(1)		123.87(12)	0.40	[51]
(OEP)Fe(OCH_3)	2.0706(12)-2.0734(12)	1.8460(10)	1.3915(18)	125.6(4)	0.512 (0.460)	this work
(OEP)Fe(OCH_3)	2.065(3)-2.081(3)	1.843(2)	1.415(5)	125.3(3)	0.53	[52]
(TF_8PP)Fe(OCH_3)	2.051(4)-2.131(4)	1.788(5)	1.409(10)	128.3(5)	(0.485)	[53]
(PPIXDME)Fe(OCH_3)	2.072(6)-2.074(6)	1.842(4)	1.367	125.9	0.49	[54]
(TPP)Fe(OCH_2SiMe_3)	2.025(4)-2.150(4)	1.814(6)	1.421(12)	132.4(5)	0.457 (0.459)	this work
(TPP)Fe($OSiMe_3$)	2.0639(19)-2.0689(18)	1.8206(17)	1.6044(18)	148.20(11)	0.491 (0.485)	this work
(OEP)Fe($OSiMe_3$)	2.0792(16)-2.0830(19)	1.8269(16)	1.6275(16)	141.17(10)	0.556 (0.507)	this work
(T_{piv}PP)Fe($OSiMe_3$)	2.058(4)-2.081(4)	1.819(3)	1.543(6)	144.0(3)	0.595 (0.525)	this work

[a] average

Importantly, the shortest Fe−O bond distance of 1.819(5) Å was observed in the compound containing the most electron-poor porphyrin moiety (i.e., (TF_8PP)Fe(OC_6HF_4)), and the longest Fe−O bond distances were observed in the most electron-rich porphyrins (por)Fe(OC_6HF_4) (por = OETPP (1.9253(17) Å), OEP (1.9053(13) Å) probably due to the *cis*-effect on the Fe−O interaction.[11,55,56] In addition, the Fe−O−C bond angles of the aryloxide complexes are 122.71(12)° for

(TTP)Fe(OC_6H_4-*p*-F), 122.97(11)° for (OEP)Fe(OC_6HF_4), 127.90(19)° for (TPP)Fe(OC_6HF_4), 131.7(2) Å for (TF_8PP)Fe(OC_6HF_4) and 138.89(14)° for (OETPP)Fe(OC_6HF_4) (Table 3.4). The Fe−O−C bond angles appear to increase with increasing distortion in the porphyrin plane, which is necessary in order for the porphyrin macrocycle to minimize direct contact with the axial ligand atoms. The consequence of this is lengthening of the Fe−O bond as in the case of the compound (OEP)Fe(O-2,4,6-$(NO_2)_3C_6H_2$) (1.930(1) Å).[51] Consistent with this view is in the most severely distorted compound, i.e. the ruffled (OETPP)Fe(OC_6HF_4) compound (Fig. 3.4d), has a Fe−O bond length of 1.9253(17) Å which is comparable to that of compound (OEP)Fe(O-2,4,6-$(NO_2)_3C_6H_2$) (1.930(1) Å). Furthermore, the ∠FeOC of 138.89(16)° in (OETPP)Fe(OC_6HF_4) is the largest of the (por)Fe(O-*aryl*) complexes probably due to the extra distortion observed in the complex. The molecular structures of the "aliphatic alkoxides" (Table 3.5) are shown in Fig. 3.8, Fig. 3.9, Fig. 3.10, Fig. 3.11 and Fig. 3.12 for (TPP)Fe(OCH_2SiMe_3), (TPP)Fe($OSiMe_3$), (OEP)Fe($OSiMe_3$), (T_{piv}PP)Fe($OSiMe_3$) and (OEP)Fe(OMe), respectively.

Table 3.5. The (por)Fe(O-*alkoxide*) complexes characterized by X-ray crystallography.

Compound	Figure Number
(TPP)Fe(OCH_2SiMe_3)	Figure 3.8
(TPP)Fe($OSiMe_3$)	Figure 3.9
(OEP)Fe($OSiMe_3$)	Figure 3.10
(T_{piv}PP)Fe($OSiMe_3$)	Figure 3.11
(OEP)Fe(OMe)	Figure 3.12

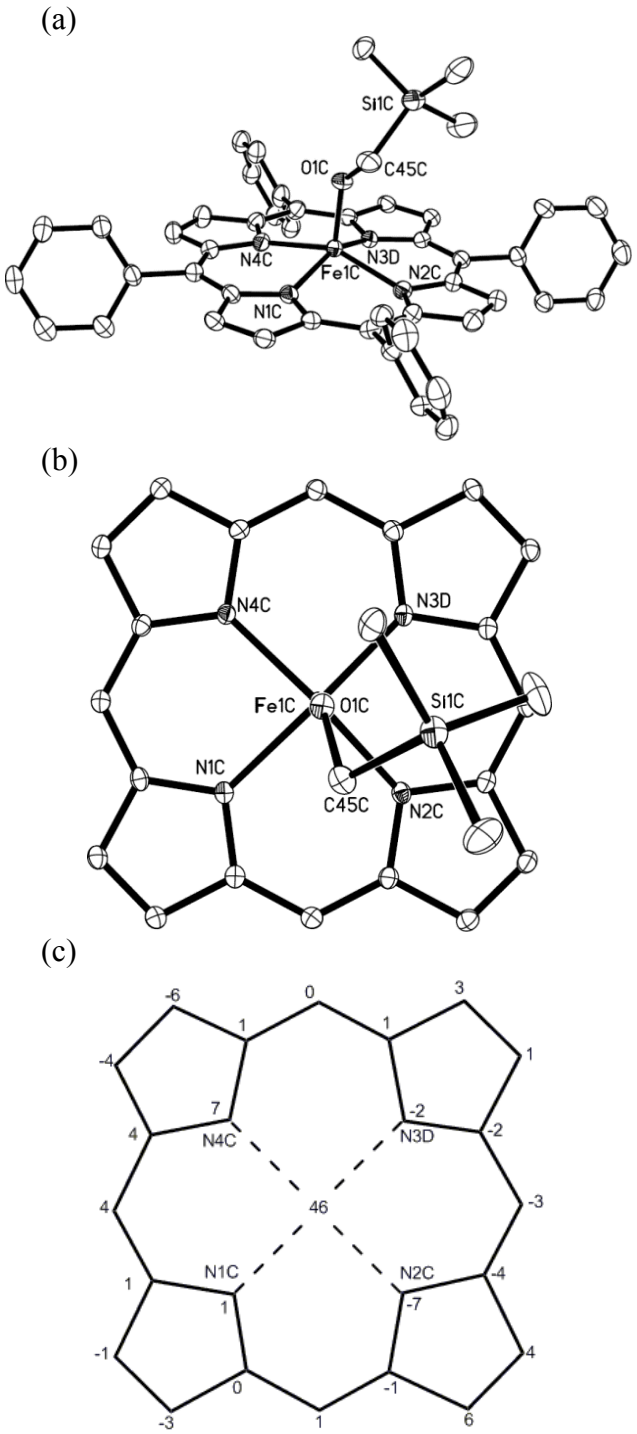

Figure 3.8. (a) Molecular structure of (TPP)Fe(OCH_2SiMe_3). Hydrogen atoms and disordered components have been omitted for clarity. (b) View of the axial Me_3SiCH_2O ligand relative to the the porphyrin, with view along the O1(C)−Fe1(C) bond. (c) Perpendicular atom displacements (in Å × 100) of the porphyrin core from the 24-atom mean planes of the porphyrin of (TPP)Fe(OCH_2SiMe_3).

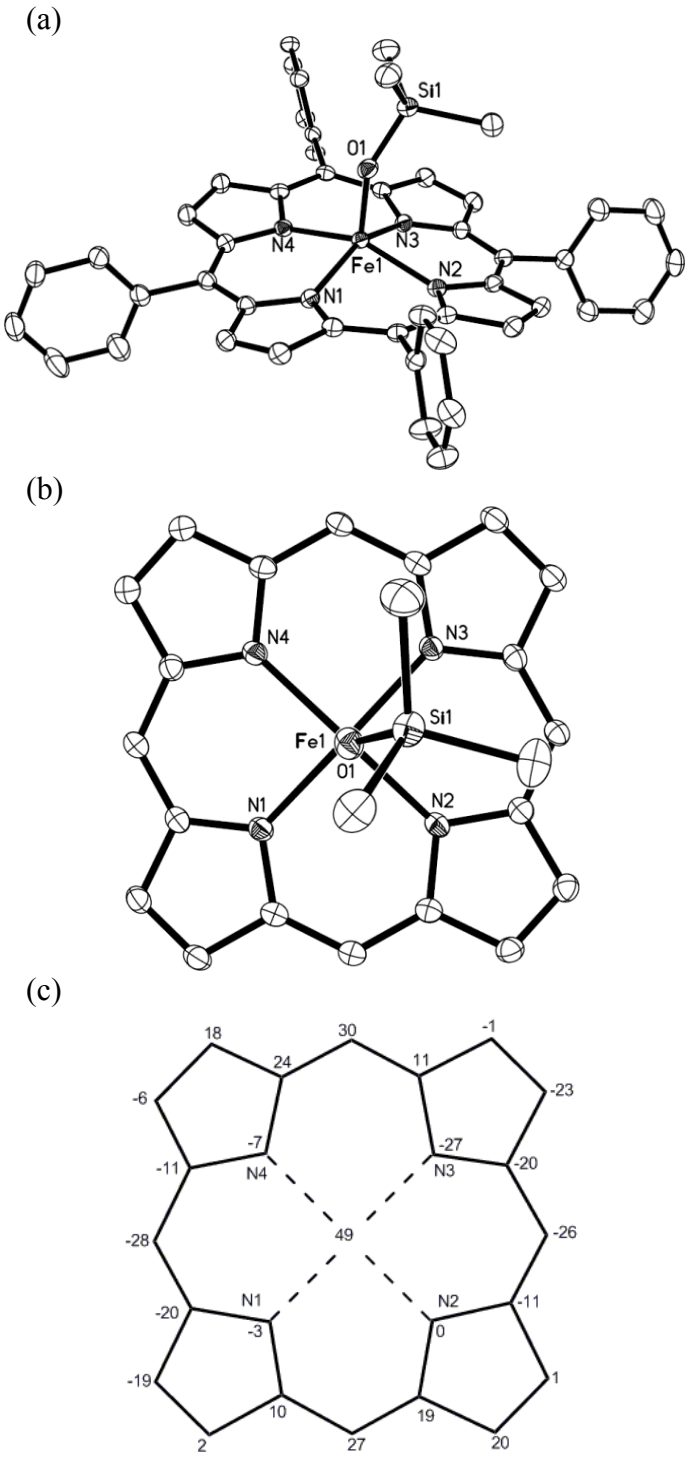

Figure 3.9. (a) Molecular structure of (TPP)Fe($OSiMe_3$). Hydrogen atoms and disordered components have been omitted for clarity. (b) View of the axial Me_3SiO ligand relative to the the porphyrin, with view along the O(1)−Fe(1) bond. (c) Perpendicular atom displacements (in Å × 100) of the porphyrin core from the 24-atom mean planes of the porphyrin of (TPP)Fe($OSiMe_3$).

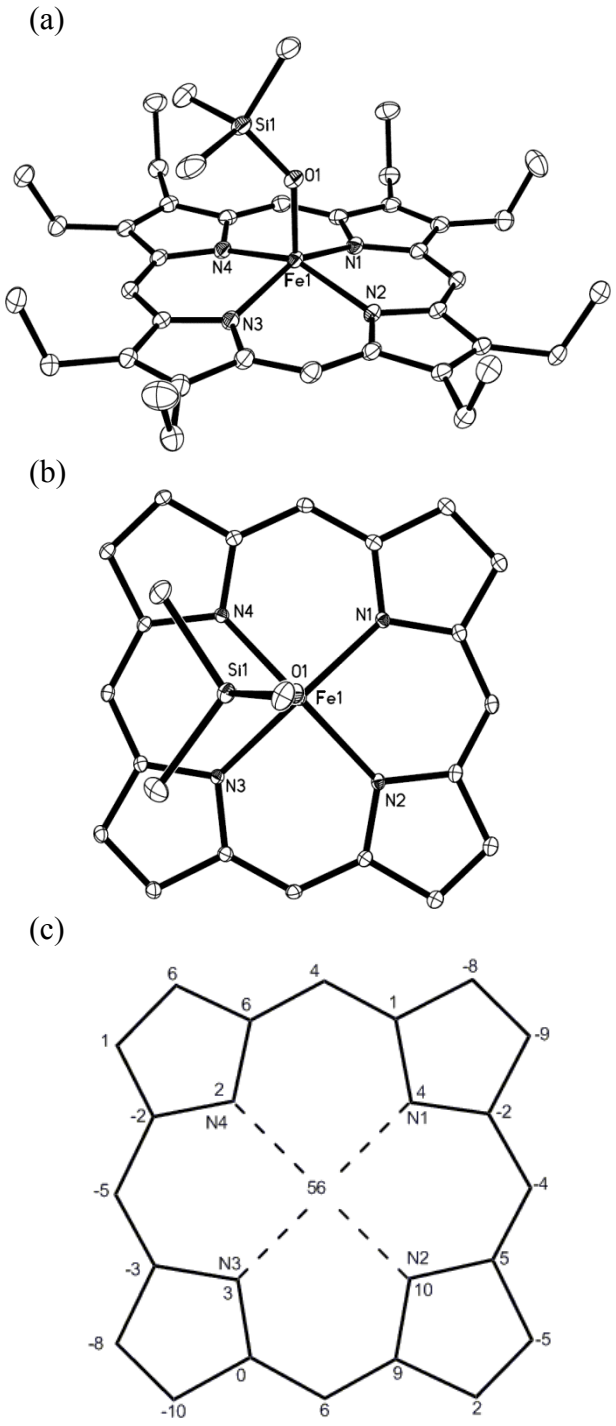

Figure 3.10. (a) Molecular structure of (OEP)Fe(OSiMe$_3$). Hydrogen atoms and disordered components have been omitted for clarity. (b) View of the axial Me$_3$SiO ligand relative to the the porphyrin, with view along the O(1)−Fe(1) bond. (c) Perpendicular atom displacements (in Å × 100) of the porphyrin core from the 24-atom mean planes of the porphyrin of (OEP)Fe(OSiMe$_3$).

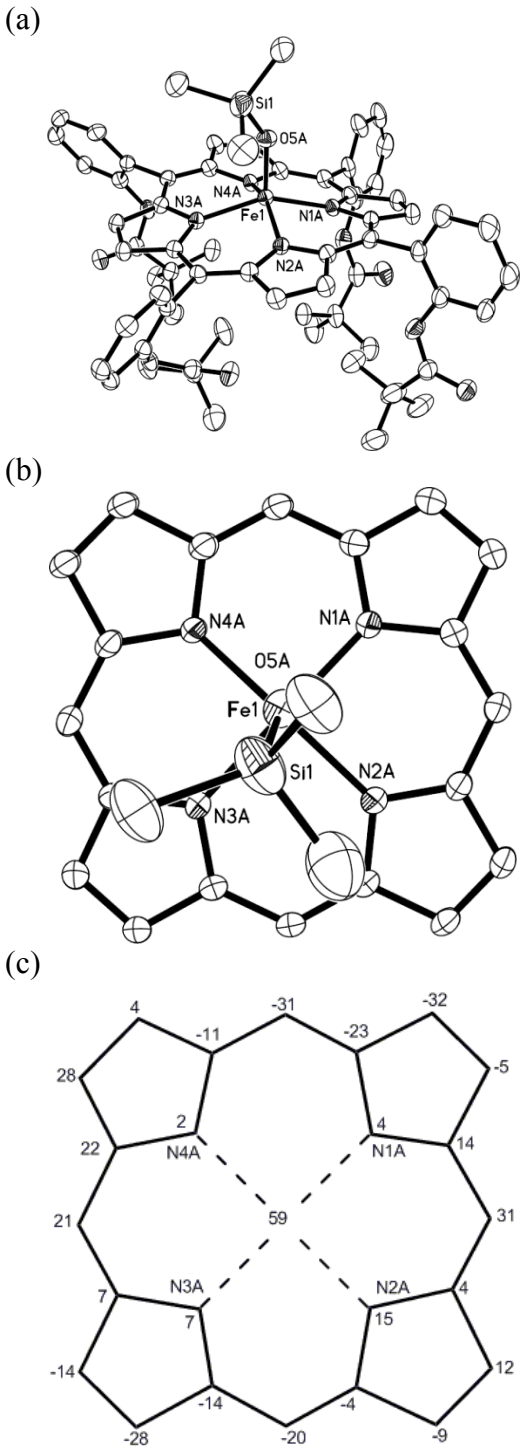

Figure 3.11. (a) Molecular structure of (T_{piv}PP)Fe(OSiMe$_3$). Hydrogen atoms and disordered components have been omitted for clarity. (b) View of the axial Me$_3$SiO ligand relative to the the porphyrin, with view along the O(1)−Fe(1) bond. (c) Perpendicular atom displacements (in Å × 100) of the porphyrin core from the 24-atom mean planes of the porphyrin of (T_{piv}PP)Fe(OSiMe$_3$).

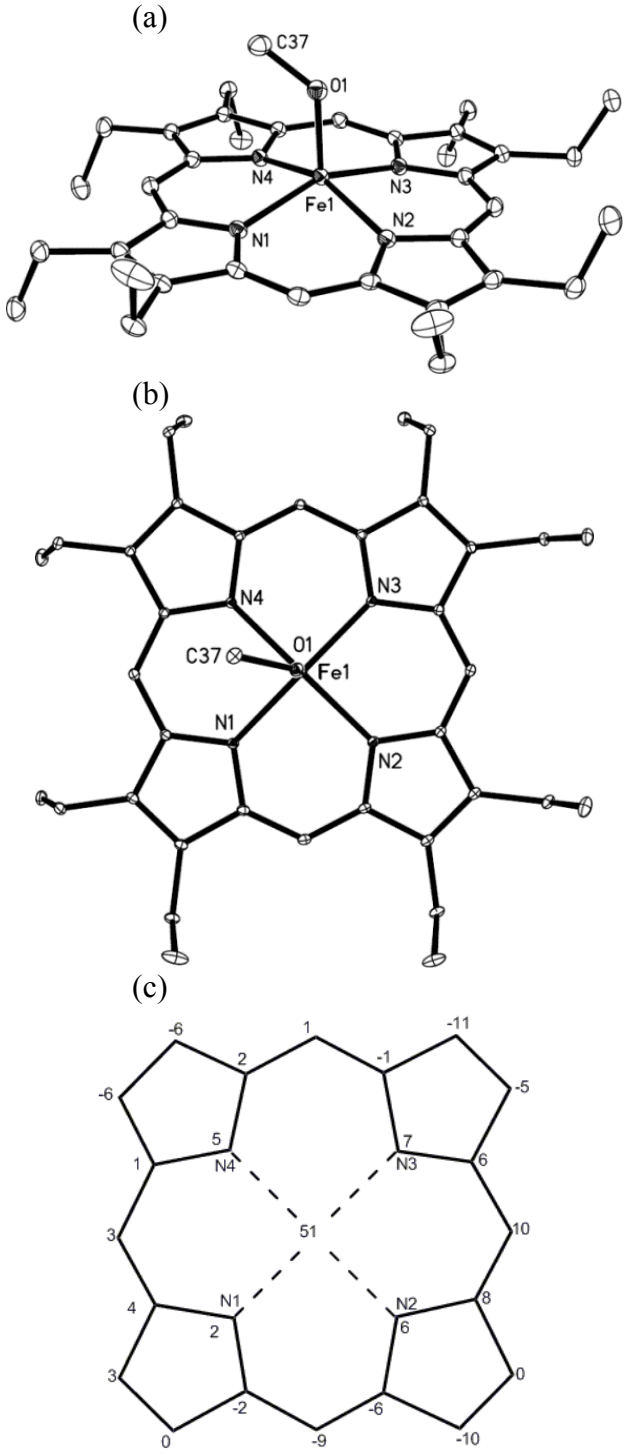

Figure 3.12. (a) Molecular structure of (OEP)Fe(OMe). Hydrogen atoms and disordered components have been omitted for clarity. (b) View of the axial Me_3SiO ligand relative to the the porphyrin, with view along the O(1)−Fe(1) bond. (c) Perpendicular atom displacements (in Å × 100) of the porphyrin core from the 24-atom mean planes of the porphyrin of (OEP)Fe(OMe).

The porphyrin plane in the compounds (TPP)Fe(OCH_2SiMe_3) (Fig. 3.8c) and (TPP)Fe($OSiMe_3$) (Fig. 3.9c) are ruffled with the plane in the latter being the most distorted among the (por)Fe(O-*aliphatic*) compounds, which is necessary to avoid the steric interaction between the more bulky Me_3SiO group and the porphyrin macrocycle. In fact, the porphyrin atoms around N2 and N3 in (TPP)Fe($OSiMe_3$) are pushed further away from the vicinity of the axial trimethylsilyoxide ligand, thus severely deforming the porphyrin macrocycle (Fig. 3.9). This phenomenon was also observed in the compounds (OEP)Fe($OSiMe_3$) (Fig. 3.10) and ($T_{piv}PP$)Fe($OSiMe_3$) (Fig. 3.11), although in the former the distortion is less severe probably because of the absence of the porphyrin *meso*-substituents. Note that, by replacing the axial ligand Me_3SiO in (TPP)Fe($OSiMe_3$) with Me_3SiCH_2O to form (TPP)Fe(OCH_2SiMe_3) (i.e controlling sterics), the porphyrin macrocycle becomes less deformed as shown in Fig. 3.8.

The (por)Fe(O-*aliphatic*) compounds similarly have Fe−N(por) bond lengths of ~2 Å, but have relatively shorter Fe−O bond (~1.8 Å) than those of the aryloxide complexes (Table 3.4). For example, whereas (TPP)Fe(OC_6HF_4) has Fe−N(por) bond lengths of 2.055(3) – 2.066(3) Å and an Fe−O bond length of 1.886(2) Å, the related (TPP)Fe(OCH_2SiMe_3) compound has Fe−N bond lengths of 2.025(4) – 2.150(4) Å and an Fe−O distance of 1.814(6) Å. However, the Fe−O−Si bond angles are relatively larger than those of the aliphatic and aromatic complexes, probably due to the larger size of Si (1.1 Å; *cf* C = 0.7 Å).[57] For instance, (TPP)Fe($OSiMe_3$) has ∠FeOSi of 148.20(11)° and ($T_{piv}PP$)Fe($OSiMe_3$) has ∠FeOSi of 144.0(3)°, but (TPP)Fe(OC_6HF_4) has ∠FeOC = 127.090(19)°. The ∠FeOC in (TPP)Fe(OCH_2SiMe_3) (132.4(5)°) is comparable to those of the aryloxides complexes and (OEP)Fe(OMe) (125.64(9)°)

obtained in this work. Notice that in the picket-fence porphyrin complex (T_{piv}PP)Fe(OSiMe$_3$) (Fig. 3.11) the axial trimethylsilyloxide ligand is opposite the "protected side" of the porphyrin. This is relevant for the reversible binding of small molecules in the pocket.[15,58]

Worthy of mention in the crystal structures of these compounds are the out of plane perpendicular iron atom displacements above the 24-atom mean porphyrin planes (Δ_{por}Fe) (Table 3.4, column 6). The Δ_{por}Fe values obtained from the crystal structures are >0.3 Å consistent with the complexes being mainly high-spin species as solids,[7] thus paralleling the μ_{eff} values in solution. For the same porphyrin macrocycle, the trimethylsilyloxide complexes gave the largest Δ_{por}Fe. In the complex (TPP)Fe(OC_6HF_4), for example, a Δ_{por}Fe of 0.40 Å was obtained, whereas in (TPP)Fe(OSiMe$_3$) a larger Δ_{por}Fe of 0.49 Å was obtained. These Δ_{por}Fe values are in congruence with those obtained for the related (TPP)Fe(SSi^{i}Pr$_3$) (0.56 Å) and (TMP)Fe(SSi^{i}Pr$_3$) (0.64 Å) compounds and the large Δ_{por}Fe values in the complexes (por)Fe(OSiMe$_3$) and (por)Fe(SSi^{i}Pr$_3$) most likely a consequence of the steric interaction between the silyloxide (or silanethiolate) ligand and the *meso* substituents of the porphyrin.[59] Notice that a lower Δ_{por}Fe value of 0.46 Å was obtained in (TPP)Fe(OCH_2SiMe_3) compound due to less steric encumbrance introduced by the methylene group between the oxygen and SiMe$_3$ in the axial OCH_2SiMe_3 ligand. However, in (OEP)Fe(OMe) a Δ_{por}Fe of 0.51 (*cf.* 0.53 Å already reported[52]) was obtained, and in (T_{piv}PP)Fe(OSiMe$_3$), Δ_{por}Fe was found to be 0.60 Å. Thus, it appears that electronics may also be involved in the difference in the Δ_{por}Fe values. A similar trend was observed in the perpendicular iron atom displacement above the 4N-atom

mean planes Δ_NFe, and for (OETPP)Fe(OC_6HF_4) which is ruffled in shape, for which the Δ_NFe displacement is 0.48 Å.

Some intermolecular features are worthy of note. Values between 3.5 and 5.3 Å were obtained for the distances between the two closest porphyrin (Δ_{mp}) macrocycles. Also, the lateral displacement (Δ_{LD}) of one porphyrin macrocycle from another was calculated for some of the compounds and values range from 3.5 to 11.1 Å (Table 3.6).

Table 3.6. Intermolecular features of some of the (por)Fe(OR) complexes.

Compound	Figures	Δ_{mp} (Å)	Lateral displ. (Å)
(OEP)Fe(OCH_3)	Fig. 3.13	3.5	3.4
(TF_8PP)Fe(OC_6HF_4)	Fig. 3.14	5.3	8.4
(TPP)Fe(OCH_2SiMe_3)	Fig. 3.15	4.9	11.1
(TPP)Fe(OC_6HF_4)	Fig. 3.16	4.2	3.5
(OEP)Fe(OC_6HF_4)	Fig. 3.17	4.9	7.4
(TPP)Fe($OSiMe_3$)	Fig. 3.18	3.8	7.4
(OEP)Fe($OSiMe_3$)	Fig. 3.19	5.0	9.4

Both the Δ_{mp} and the Δ_{LD} values are predicted to play a role in our attempt at heterogeneous NO crystal soaking reactions to produce the six-coordinate (por)Fe(NO)(OR) compounds[12] (*vide infra*). Note that the smallest Δ_{mp} = 3.5 Å was observed in (OEP)Fe(OMe) (Fig. 3.13), and (TF_8PP)Fe(OC_6HF_4) gave the largest Δ_{mp} of 5.3 Å (Fig. 3.14). Furthermore, the largest lateral neighboring porphyrin displacement of 11.1 Å was observed in the compound (TPP)Fe(OCH_2SiMe_3) (Fig. 3.15) and smallest lateral porphyrin displacement of 3.4 Å was observed in (OEP)Fe(OMe) (Fig. 3.13).

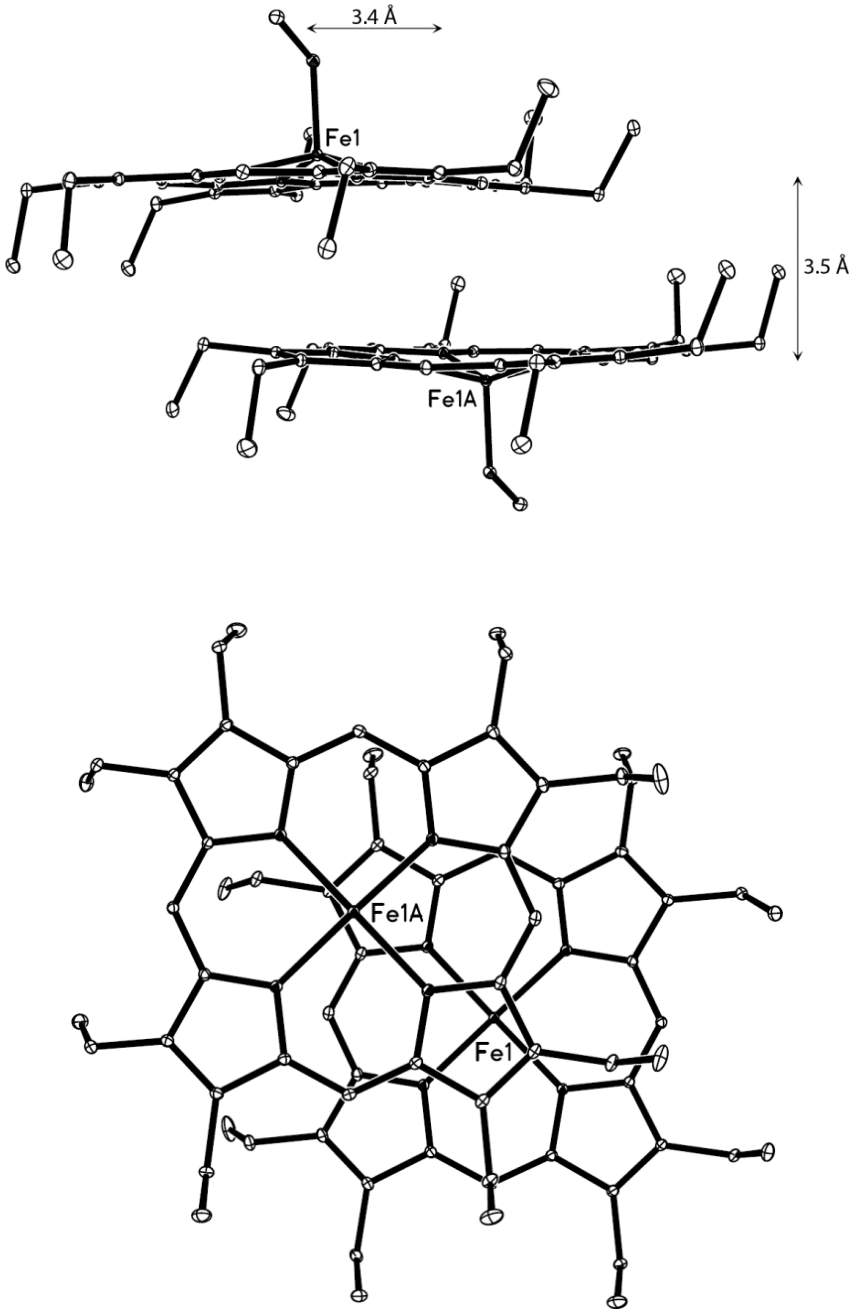

Figure 3.13. (Top) Side view and (Bottom) top view of two neighbouring porphyrin molecules of (OEP)Fe(OMe) in a unit cell.

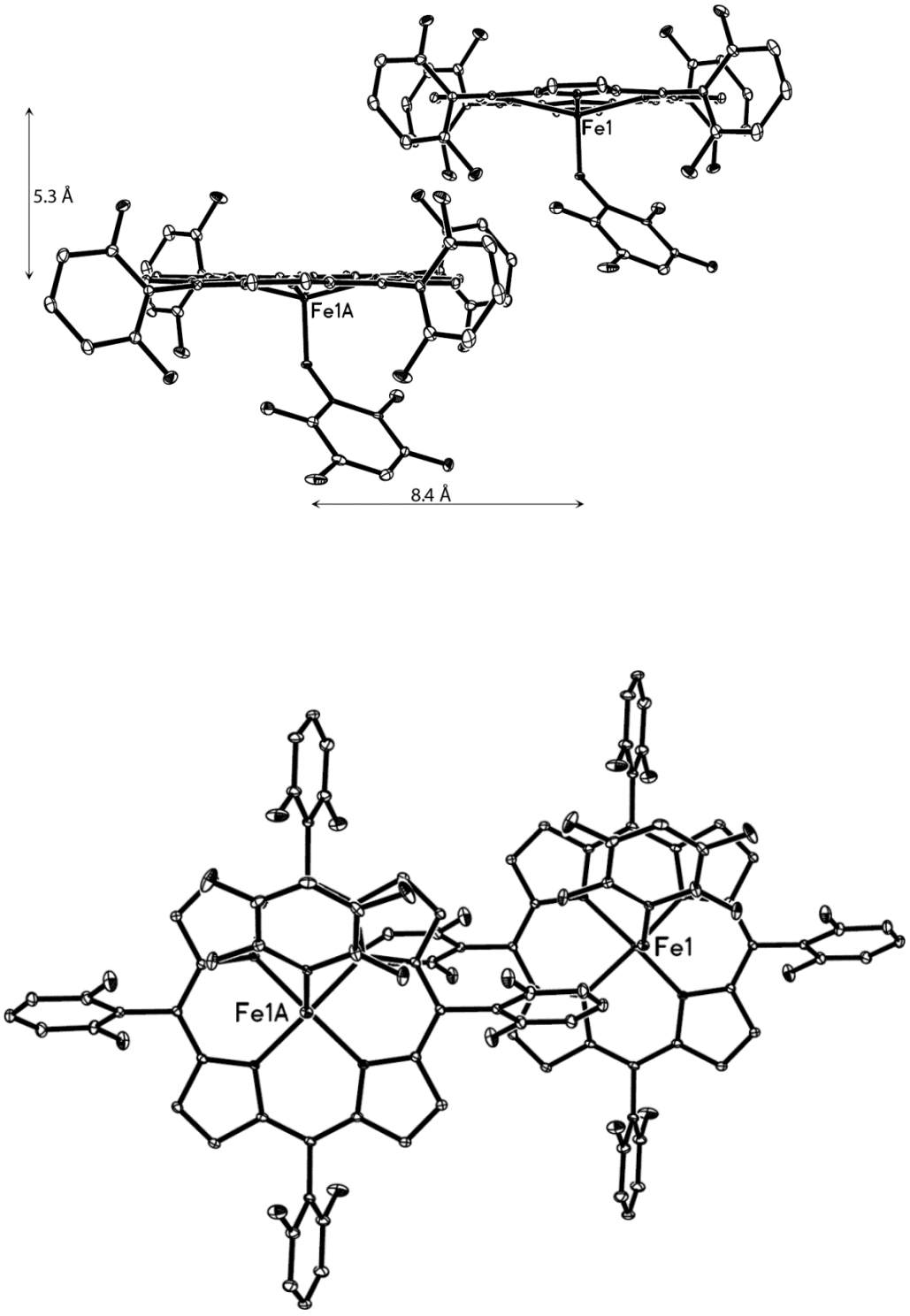

Figure 3.14. (Top) Side view and (Bottom) top view of two neighbouring porphyrin molecules of $(TF_8PP)Fe(OC_6HF_4)$ in a unit cell.

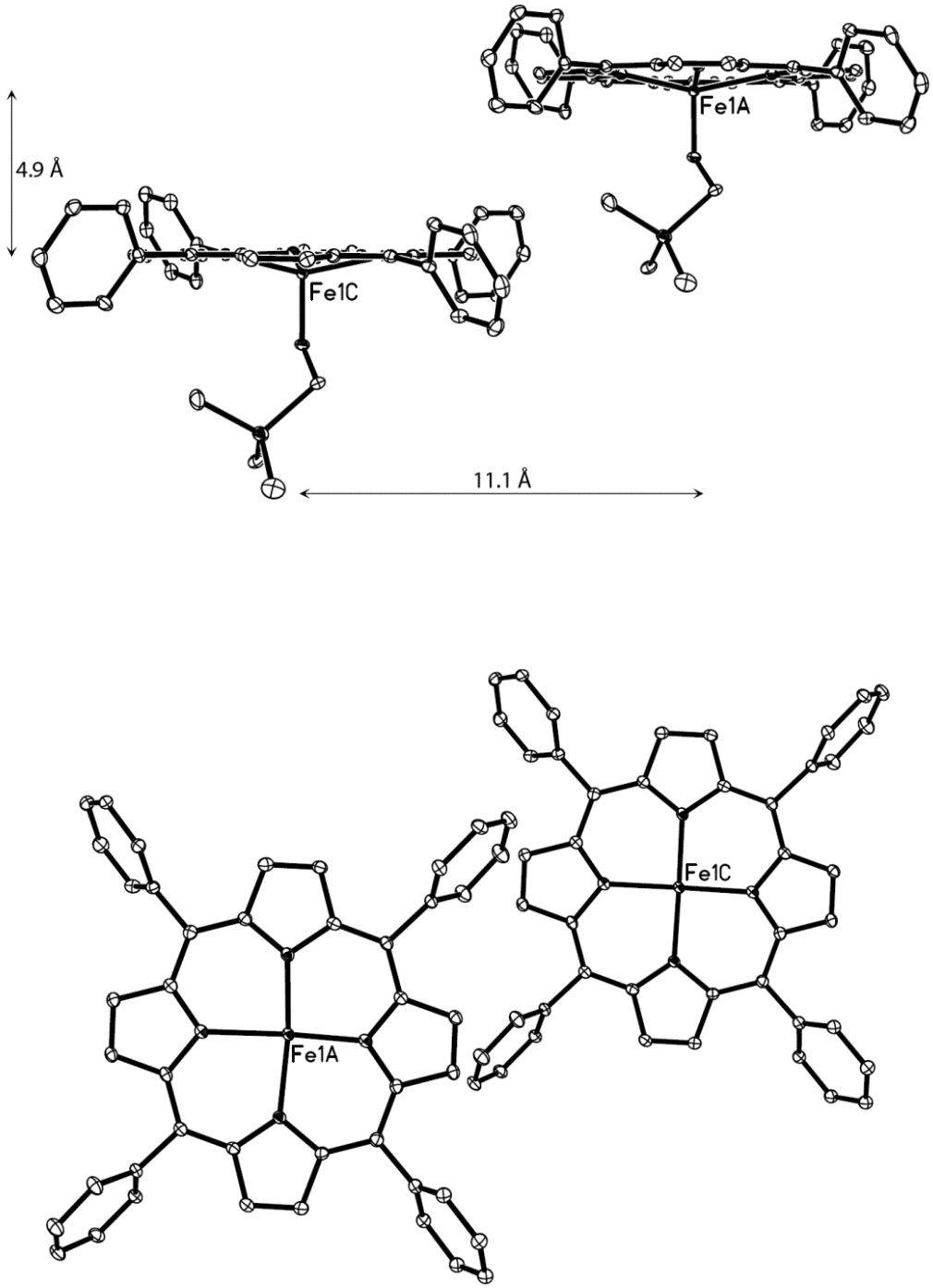

Figure 3.15. (Top) Side view and (Bottom) top view of two neighbouring porphyrin molecules of (TPP)Fe(OCH_2SiMe_3) in a unit cell.Axial ligands in the figure on the bottom have been omitted for clarity.

The molecular structures showing the intermolecular features of the other complexes as listed in Table 3.6 are shown below and they follow the order below of appearance in Table 3.6 (i.e. Fig. 3.16, Fig. 3.17, Fig. 3.18 and Fig. 3.19)

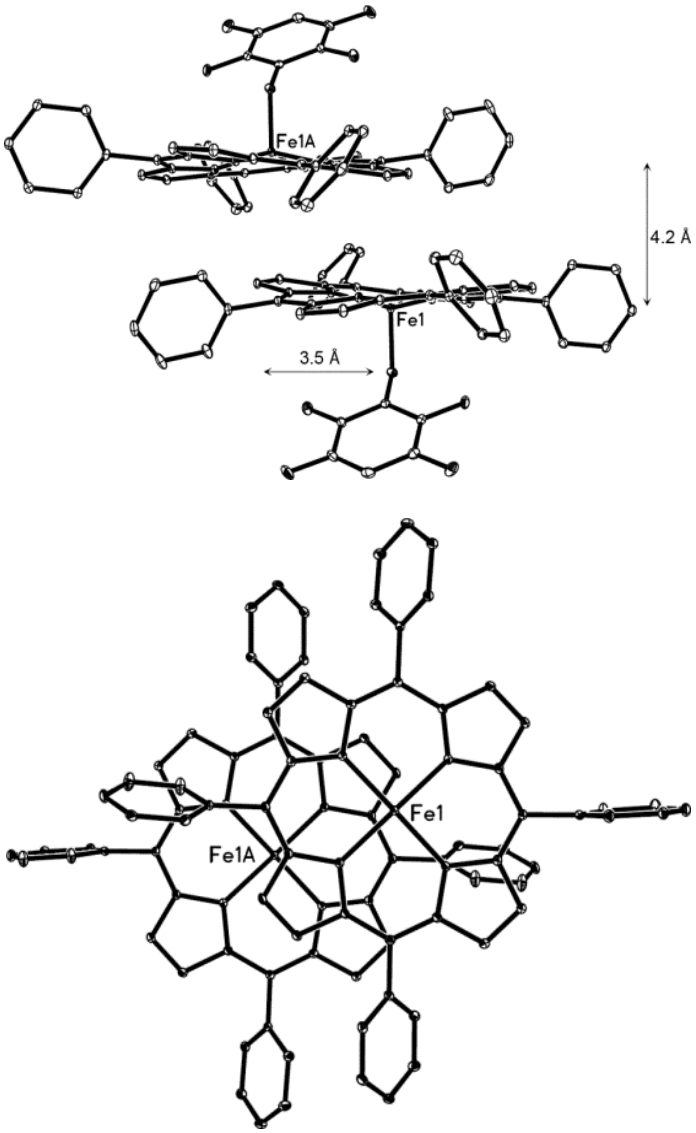

Figure 3.16. (Top) Side view and (Bottom) top view of two neighbouring porphyrin molecules of (TPP)Fe(OC_6HF_4) in a unit cell. Axial ligands in the bottom figure have been omitted for clarity.

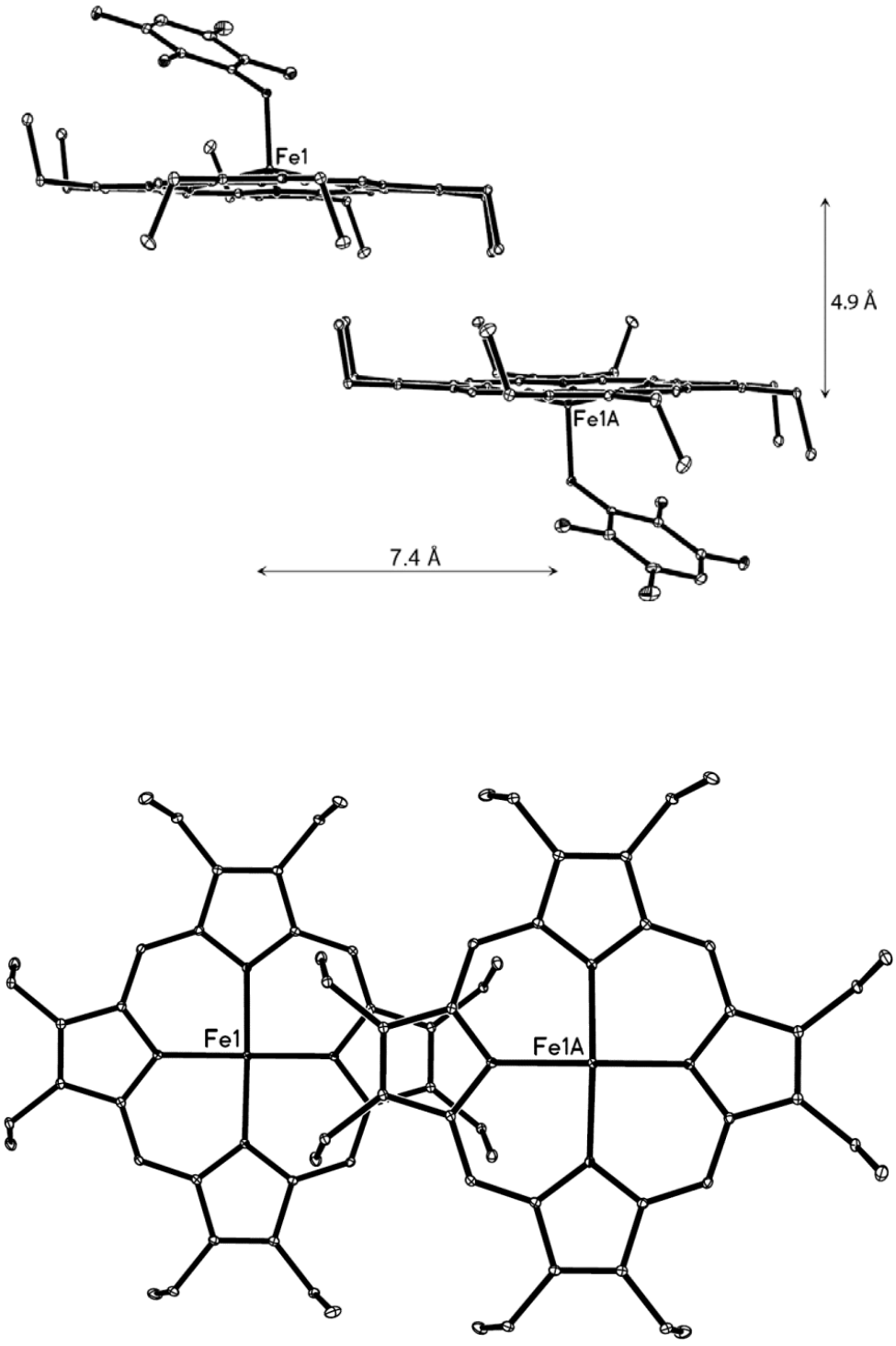

Figure 3.17. (Top) Side view and (Bottom) top view of two neighbouring porphyrin molecules of (OEP)Fe(OC_6HF_4) in a unit cell. Axial ligands in the bottom figure have been omitted for clarity.

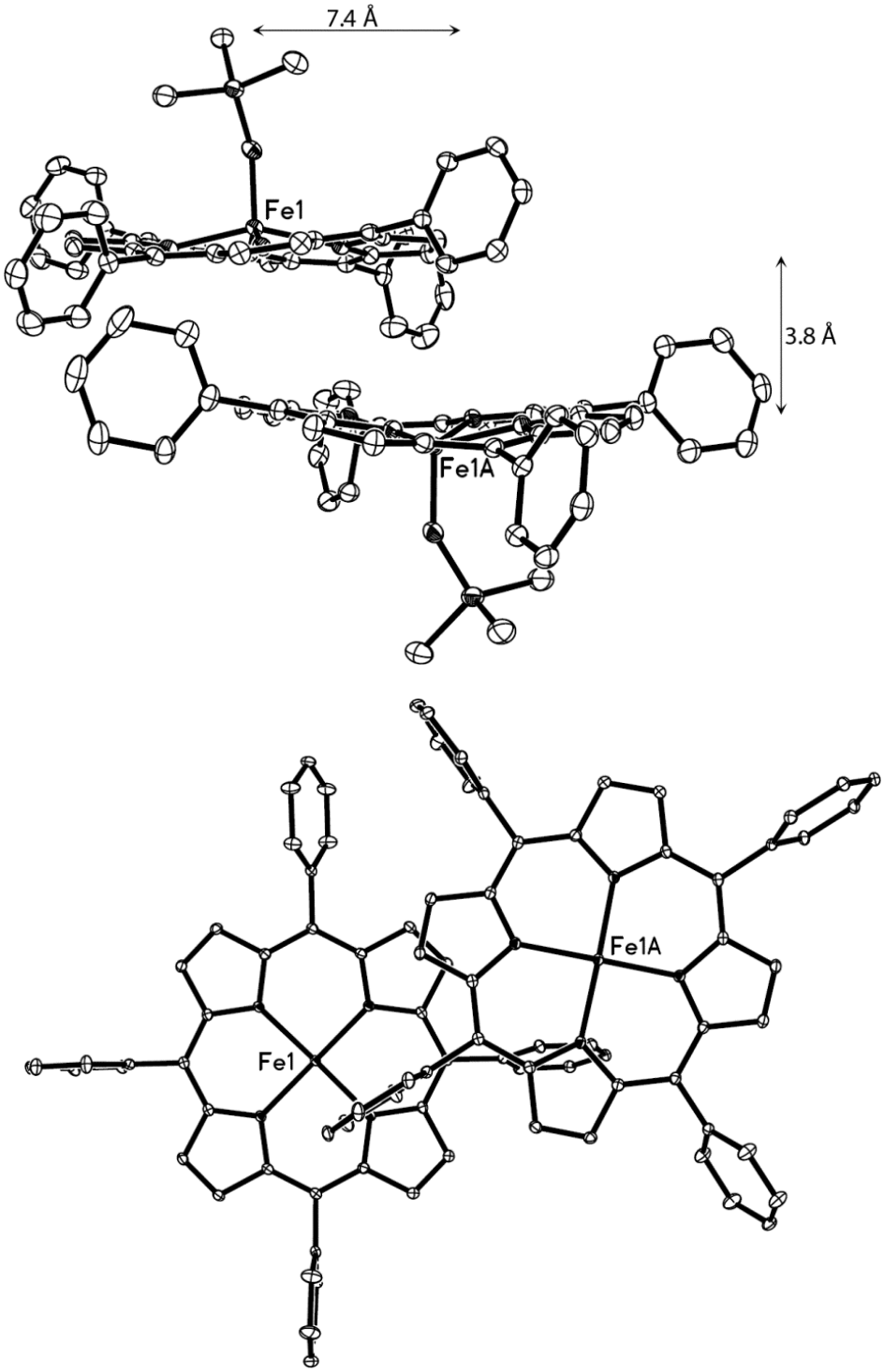

Figure 3.18. (Top) Side view and (Bottom) top view of two neighbouring porphyrin molecules of (TPP)Fe($OSiMe_3$) in a unit cell. Axial ligands in the bottom figure have been omitted for clarity.

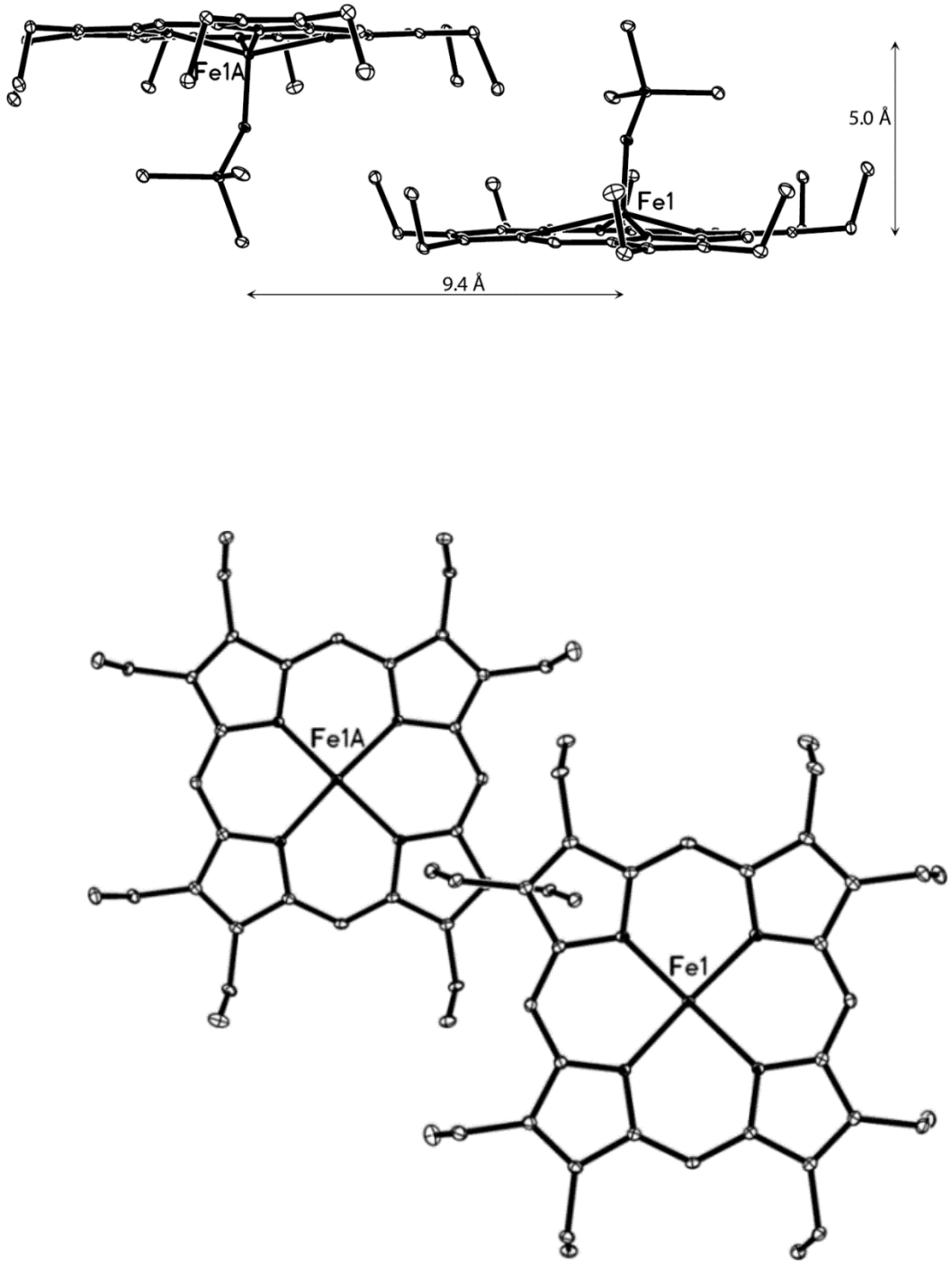

Figure 3.19. (Top) Side view and (Bottom) top view of two neighbouring porphyrin molecules of (OEP)Fe($OSiMe_3$) in a unit cell. Axial ligands in the bottom figure have been omitted for clarity.

The relative orientation of the neighboring molecules of (TTP)Fe(OC_6H_4-*p*-F) in a unit cell as shown in Fig. 3.20.

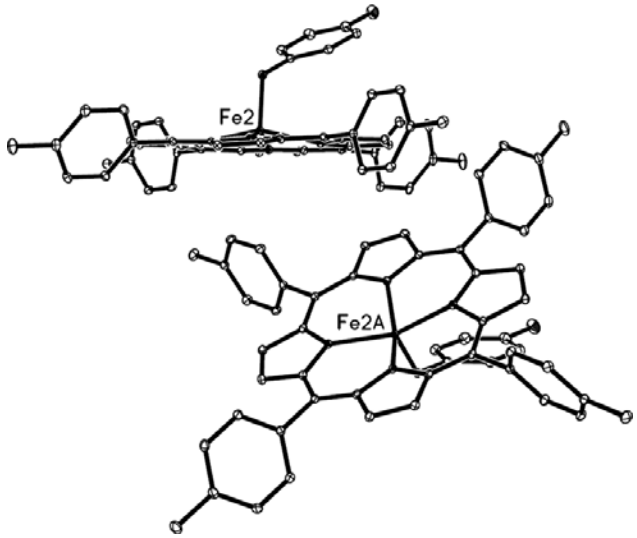

Figure 3.20. Side view of two neighbouring porphyrin molecules of (TTP)Fe(OC_6H_4-*p*-F) in a unit cell.

3.3.2 Electrochemistry of the (por)Fe(OR) complexes

3.3.2.1 Cyclic Voltammetry (CV)

The electrochemistry of the compounds (T(*p*-OMe)PP)Fe(OR) (R = C_6H_5, C_6H_4-*p*-NO_2) have previously been studied in our laboratory by Adam Warhausen. He performed CV experiments on the compounds and observed two reversible oxidations in the compound (T(*p*-OMe)PP)Fe(OC_6H_5) at $E^{\circ\prime}$ = 0.47 V and 0.90 V (*vs.* Fc/Fc^+).[60] In (T(*p*-OMe)PP)Fe(OC_6H_4-*p*-NO_2), in addition to two reversible oxidations at 0.53 V and 0.95 V, he observed a reversible reduction at −0.89 V in the CV.[60] Richard and coworkers have previously studied the redox behavior of other five-coordinate compounds (TTP)Fe(OR) (R = alkyl, aryl, acyl) by CV and observed that the $E^{\circ\prime}$ for the Fe(III) → Fe(II) reduction increased linearly with the pK_a of the axial RO^- ligand over a

pK_a range of 0.7-10.[61] I examined whether the redox potentials of the compounds (por)Fe(OC_6HF_4) (por = OEP, T(*p*-OMe)PP) would be affected by changing the porphyrin macrocycle. Indeed, the CV experiment shows that the compound (T(*p*-OMe)PP)Fe(OC_6HF_4) (Figure 3.21a) undergoes two reversible oxidations at relatively higher potentials, $E^{\circ\prime}$ = 0.55 V (ΔE_p = 0.19 V) and $E^{\circ\prime}$ = 0.96 V (i_{pc}/i_{pa} ~1, ΔE_p = 0.27 V) and their ΔE_ps are in good agreement with the ΔE_p = 0.22 V obtained for the Fc/Fc^+ couple under the same conditions.[62,63]

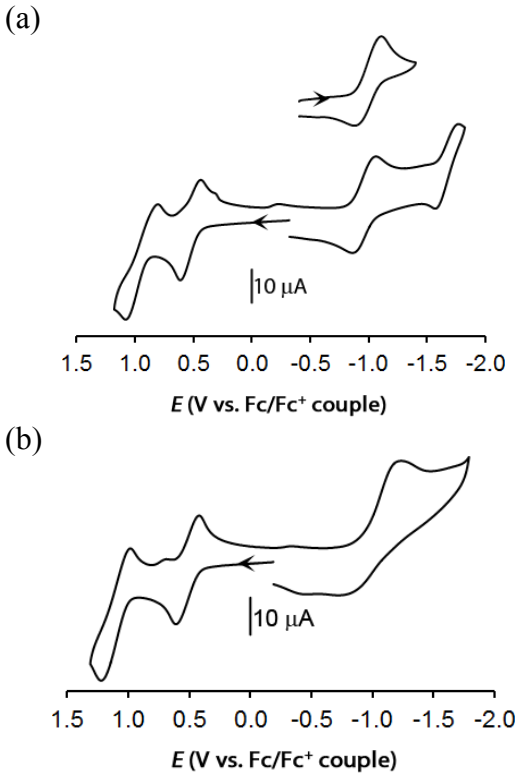

Figure 3.21. Cyclic voltammograms of (T(*p*-OMe)PP)Fe(OC_6HF_4) (a) and (OEP)Fe(OC_6HF_4) (b) at 200 mV/s, 1mM analyte, 0.1 M NBu_4PF_6 at room temperature. Potentials are referenced to Fc/Fc^+ set to 0.00 V.

The cathodic-to-anodic peak (i_{pc}/i_{pa}) ratio at 200 mVs^{-1} for the first and second oxidation of (T(*p*-OMe)PP)Fe(OC_6HF_4) are 1.0 and 0.8, respectively suggesting that the

oxidations each are chemically reversible one electron transfer processes as shown in Eq. 3.4.

$$(\text{por})\text{Fe}(\text{OC}_6\text{HF}_4) \rightleftharpoons [(\text{por})\text{Fe}(\text{OC}_6\text{HF}_4)]^+ + e^- \quad \text{(por = T(}p\text{-OMe)PP, OEP)} \qquad \textbf{(3.4)}$$

Plots of the i_{pa} values versus the corresponding (scan rate)$^{1/2}$ over the 0.05 V to 1.5 V range are linear indicating diffusion-controlled processes for both the first and second oxidations. In addition, (T(*p*-OMe)PP)Fe(OC_6HF_4) undergoes a chemically reversible one-electron reduction at $E^{\circ\prime} = -0.95$ V ($i_{pa}/i_{pc} \sim 1$, $\Delta E_p = 0.17$ V) and a less-defined second reduction at −1.82 V. The first and second oxidation potentials of (T(*p*-OMe)PP)Fe(OC_6HF_4) are higher than those of (T(*p*-OMe)PP)Fe(OC_6H_4-*p*-NO_2), correlating with the fact that $C_6HF_4O^-$ (pK_a of C_6HF_4OH = 5.53)[64] is overall a weaker σ-donor than *p*-NO_2-$C_6H_4O^-$ (pK_a of *p*-NO_2-C_6H_4OH = 7.15).[65] The compound (OEP)Fe(OC_6HF_4) similarly undergoes two reversible oxidations at $E^{\circ\prime} = 0.52$ V (i_{pa}/i_{pc} 0.9, $\Delta E_p = 0.20$ V) and $E^{\circ\prime} = 1.09$ V (i_{pa}/i_{pc} 0.8, $\Delta E_p = 0.26$ V) (cf. $\Delta E_p = 0.19$ V for Fc/Fc^+), and an irreversible reduction at $E_{pc} = -1.18$ V. Furthermore, the second oxidation potentials in the (T(*p*-OMe)PP)Fe(OC_6HF_4) and (OEP)Fe(OC_6HF_4) are ~ 400 mV more positive than their corresponding first oxidations, a phenomenon typical of the CVs of non-oxo iron porphyrin complexes.[66]

I also wanted to study the redox behavior of the five-coordinate (por)Fe(OR) complex, where OR is a more electron-rich σ-donor ligand. Complexes bearing the axial ligands $Me_3Si(CH_2)_nO$ (n = 0, 1) were used, partly because there is limited information in the literature on the electrochemical behavior of these compounds and

because of the structural differences (X-ray crystallography) obtained for these compounds which I anticipated may play a role in its reaction with NO to yield the six-coordinate (por)Fe(NO)(OR) derivatives (*vide infra*). Thus, I selected the two complexes (T_{piv}PP)Fe($OSiMe_3$) and (T_{piv}PP)Fe(OCH_2SiMe_3) for study.

The cyclic voltammograms of the complexes (T_{piv}PP)Fe($OSiMe_3$) and (T_{piv}PP)Fe(OCH_2SiMe_3) are shown in Fig. 3.22a and Fig. 3.22b, respectively.

(a)

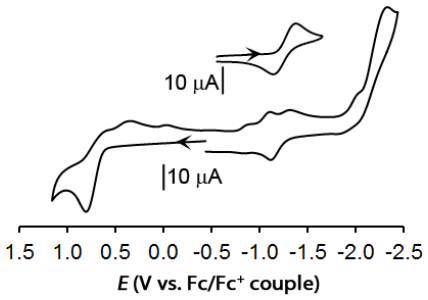

(b)

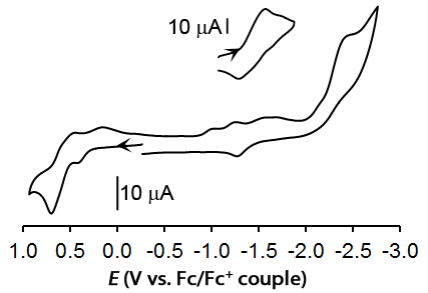

Figure 3.22. Cyclic voltammogram of (a) (T_{piv}PP)Fe($OSiMe_3$) and (b) (T_{piv}PP)Fe(OCH_2SiMe_3) in CH_2Cl_2 at 200 mV/s. Conditions: 1mM analyte, 0.1 M NBu_4PF_6, room temperature. Insert: scanning in the negative direction showing the reversibility and partial reversibility, respectively, after first reduction. Potentials are referenced to Fc/Fc^+ set to 0.00 V.

The compound (T_{piv}PP)Fe($OSiMe_3$) undergoes an irreversible oxidation at E_{pa} = +0.87 V, a reversible reduction at $E^{o'} = -1.17$ V (i_{pc}/i_{pa} ~1, $\Delta E_p = 0.20$; *cf.* $\Delta E_p = 0.17$ V for Fc/Fc^+), and a second irreversible reduction at $E_{pc} = -2.30$ V. Note that the first

reduction of (T_{piv}PP)Fe($OSiMe_3$) is reversible only when the CV is scanned from 0.00 V (*vs*. Ag/AgCl) in the negative (reduction) direction (insert in Fig. 3.22a).

The CV of (T_{piv}PP)Fe(OCH_2SiMe_3) (Fig. 3.22b), reveals an unexplainable pre-wave at E_{pa} = 0.61 V and an irreversible oxidation at E_{pa} = +0.91 V. In addition, one partially reversible reduction (scanning in negative direction from 0.00 V; see insert of Fig. 3.22b) was observed at E_{pc} = −1.03 V and an irreversible reduction was observed at E_{pc} = −2.21 V. The redox potentials determined for the (por)Fe(OR) complexes by CV are listed in Table 3.7.

Table 3.7. Redox potential (in V) of the (por)Fe(OR) compounds in CH_2Cl_2.

	E°' (V)			
Compound	1st Ox.	2nd Ox.	1st Red.	2nd Red.
(T(*p*-OMe)PP)Fe(OC_6HF_4)	0.55	0.96	−0.95	−1.82
(T(*p*-OMe)PP)Fe(OC_6H_5)[a]	0.47[a]	0.90[a]		
(T(*p*-OMe)PP)Fe(OC_6H_4-*p*-NO_2)[a]	0.53[a]	0.95[a]	−0.89[a]	
(OEP)Fe(OC_6HF_4)	0.52	1.09	−1.18*	
(T_{piv}PP)Fe($OSiMe_3$)	0.87*		−1.17	−2.30*
(T_{piv}PP)Fe(OCH_2SiMe_3)	0.91*		−1.03*	−2.21

Potentials are in volts, and are referenced to the Fc/Fc^+ couple set at 0.00V. Analytes are 1mM analyte, 0.1 M NBu_4PF_6 at room temperature and scan rate of 200 mV/s. [a] Obtained from ref. [60] *These E_{pa} and E_{pc} values are due to irreversibility.

The CVs of the related four-coordinate (T_{piv}PP)Zn and (T_{piv}PP)Cu compounds revealed similar irreversible first oxidations at 1.00 and 1.28 V (*vs*. SCE), respectively.[67] Further, each of these compounds displayed reversible first reductions at −1.06 V ((T_{piv}PP)Zn) and −1.59 V ((T_{piv}PP)Cu). Both the first oxidations and the first reductions were attributed to porphyrin-centered electron transfer processes. Their second reductions, however, were irreversible at E_{pc} = −1.49 V ((T_{piv}PP)Zn) and

(T_{piv}PP)Cu (E_{pc} = −1.59 V) and were attributed to an irreversible process from a chemical reaction of the dianion with the solvent (CH_2Cl_2).[67]

3.3.2.2 Infrared Spectroelectrochemistry

In order to spectroscopically characterize the redox products generated at the electrode surfaces in the CV experiments, I employed IR spectroelectrochemistry similar to that described in Chapter 2. The IR spectroelectrochemical experiments were performed on compounds (T_{piv}PP)Fe($OSiMe_3$) and (T_{piv}PP)Fe(OCH_2SiMe_3). The first oxidation of (T_{piv}PP)Fe($OSiMe_3$) held at a potential, E_{pa} = +0.88 V led to the disappearance of the ν_{CO} band due to the *t*-butylamido group at 1688 cm^{-1} and the appearance of a new IR band at 1651 cm^{-1} in the difference IR spectrum (Fig. 3.23).

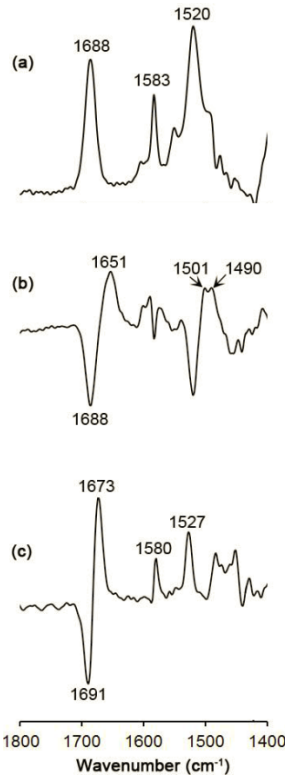

Figure 3.23. (a) FTIR spectrum (in CH_2Cl_2) of (T_{piv}PP)Fe($OSiMe_3$). Difference FTIR spectra (in CH_2Cl_2) of (T_{piv}PP)Fe($OSiMe_3$) after (b) oxidation; (c) reduction.

The latter ν_{CO} band corresponds to a downward shift ($-$ 37 cm^{-1}) from that of the neutral starting compound suggesting a porphyrin-centered oxidation. Note that the bands at ~1580 cm^{-1} and ~1520 cm^{-1} are also due to *t*-butylamido group vibrations and they were found to disappear during oxidations. The first oxidation product can be formulated as $[(T_{piv}PP^{\bullet+})Fe(OSiMe_3)]$ (Eq. 3.5a).

$$(T_{piv}PP)Fe(OSiMe_3) \rightarrow [(T_{piv}PP^{\bullet+})Fe(OSiMe_3)] + e^- \qquad (\mathbf{3.5a})$$

The difference IR spectrum of the product after first oxidation of $(T_{piv}PP)Fe(OCH_2SiMe_3)$ (Fig. 3.24b) when the potential was held at E_{pa} = 1.01 V has ν_{CO} bands downshifted by (~ $-$32 cm^{-1}) from that of the neutral starting compound, and may also be assigned to porphyrin-centered oxidations (Eq. 3.5b).

$$(T_{piv}PP)Fe(OCH_2SiMe_3) \rightarrow [(T_{piv}PP^{\bullet+})Fe(OCH_2SiMe_3)] + e^- \qquad (\mathbf{3.5b})$$

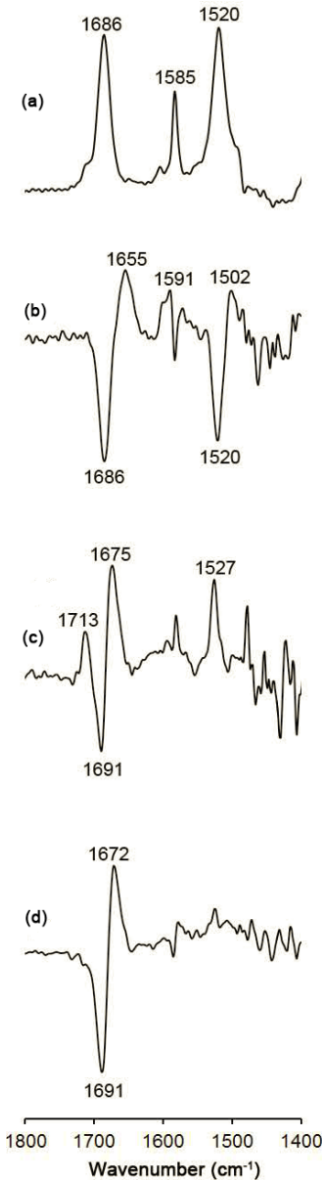

Figure 3.24. (a) FTIR spectrum (in CH_2Cl_2) of (T_{piv}PP)Fe(OCH_2SiMe_3). Difference FTIR spectra (in CH_2Cl_2) of (T_{piv}PP)Fe(OCH_2SiMe_3) after (b) 1st oxidation; (c)1st reduction; (d) 2nd reduction.

The reduction of (T_{piv}PP)Fe($OSiMe_3$) at a potential $E_{pc} = -1.28$ V yielded a product with a downward ν_{CO} band shift (-18 cm^{-1}) from the initial 1691 cm^{-1} band to 1673 cm^{-1} (Fig. 3.23c). Note that the "negative" IR band of the starting compound was observed at 1691 cm^{-1} (not 1688 cm^{-1}) after reduction and the difference was calculated from this

band. This small ν_{CO} shift was initially ignored considering the IR instrument has a resolution of 4 cm^{-1}. This shift, however, was reproducible and it was not observed during oxidations. Furthermore, a similar shift was observed in the first oxidation and reduction products of the related (T_{piv}PP)Fe(OCH_2SiMe_3) compound (*vide infra*). Based on this result alone, three hypotheses were made:

(1) During reduction, the axial ligand dissociates, leading to the (T_{piv}PP)Fe complex (Eq. 3.6).

$$(T_{piv}PP)Fe(O(CH_2)_nSiMe_3) + e^- \rightarrow (T_{piv}PP)Fe + Me_3Si(CH_2)_nO^- \quad (\mathbf{3.6})$$

(2) Reduction leads to a change in spin state of the complex via Charge Transfer-Induced Spin-Transitions (CTIST).[68-70]

(3) Conformational change of the porphyrin macrocycle due to change in the electronics of the porphyrin macrocycle after first oxidation and after reduction.

The first hypothesis, at first consideration, seems plausible considering that a similar shift in the ν_{CO} ($\Delta\nu_{CO}$ = 18 cm^{-1}) was observed in both (T_{piv}PP)Fe($OSiMe_3$) and (T_{piv}PP)Fe(OCH_2SiMe_3) compounds after reduction. The bands due to the dissociated $Me_3(CH_2)_nSiO$ axial ligands were not detected. Thus, it is possible that these bands may have shifted to lower wavenumbers in the undetectable regions (< 1500 cm^{-1}) of our IR spectroelectrochemical configuration.[62,63] However, this hypothesis does not explain why both oxidation and reduction lead to downward shifts of the ν_{CO} bands and why the first reduction of (T_{piv}PP)Fe(OCH_2SiMe_3) generated species with higher ν_{CO} bands.

Oxidations are usually responsible for upward shifts of the IR bands due to increase in positive charge.

The second hypothesis, *viz*, change in spin state of the redox products is also probable. This is evidenced by the fact that both the reduced and oxidized products unexpectedly have wavenumbers shifted to lower frequencies. Doctorovich and Kaim have studied the IR spectroelectrochemical behavior of $(TFPPBr_8)Fe(NO)$ (ν_{NO} = 1715 cm^{-1}) and have found the complexes to undergo a first reversible reduction to a product which has a downward shifted ν_{NO} band of 1550 cm^{-1}.[71,72] The compound $(TFPPBr_8)Fe(NO)$ was also found to undergo a second reversible reduction, which, surprisingly, yielded a product with a higher ν_{NO} band than the starting complex and they characterized the redox product as a high-spin species. Their experimental results were confirmed by DFT calculations and the authors attributed these surprising ν_{NO} shifts to changes in spin states.[72] I speculate that the $(T_{piv}PP)Fe(OSiMe_3)$ and $(T_{piv}PP)Fe(OCH_2SiMe_3)$ compounds used in this study similarly undergo changes in spin state during reduction. Note that during the first reduction of $(T_{piv}PP)Fe(OCH_2SiMe_3)$ the difference IR spectrum shows a positive shift of ν_{CO} from 1691 cm^{-1} to 1713 cm^{-1}, as well as a negative shift to 1672 cm^{-1} (Fig. 3.24c). During the second reduction, however, only the downward shift band (1673 cm^{-1}) was observed (Fig. 3.24d).

The third hypothesis which is merely due to conformational change is the most probable. It has been known for decades that the phenyl group in a diacid tetraphenylporphyrin makes a dihedral angle of 21° (*cf.* 70° in the neutral $TPPH_2$) with the porphyrin macrocycle to allow stronger interaction between the phenyl ring and the

porphyrin π system [73] so there can be delocalization of the charge. For example, the crystal structure of radical cation ($TPP^{+\cdot}$)FeCl shows a saddled-shaped porphyrin macrocycle and it exhibits strong antiferromagnetic coupling between the S =5/2 iron and the S = 1/2 porphyrin radical, an indication of non-planarity. However, unlike TPP, "picket-fenced" porphyrins are more rigid due to the presence of the bulky *pivalamido* groups at the *ortho* positions. Addition of an extra electron (reduction) to, or removal of an electron (oxidation) from the 18π aromatic porphyrin macrocycle yields an antiaromatic system, thus, destabilizing it. To stabilize the antiaromatic system in the $T_{piv}PP$ the system, the porphyrin undergoes a conformational change to allow delocalization of the charge. I speculate that the complex ($T_{piv}PP$)Fe($OSiMe_3$) similarly undergoes conformational change during oxidation and reduction to generate species with lower ν_{CO}. As already discussed, conformational change in porphyrin macrocycle affects the spin state, and as such the second and third hypothesis could be related.

The *in situ* chemical reduction of the ($T_{piv}PP$)Fe($OSiMe_3$) to [($T_{piv}PP$)Fe($OSiMe_3$)]Cp_2Co was performed using cobaltocene. In this experiment, I treated a CD_2Cl_2 solution of ($T_{piv}PP$)Fe($OSiMe_3$) in an NMR tube with 1.1 eq of Cp_2Co and detected a singlet at 3.9 ppm in the ^{1}HNMR spectrum. This signal was assigned to Cp_2Co^+ generated after the reduction and is 1 ppm lower than that detected in the ^{1}H NMR spectrum of the [(TFPPBr_8)Fe(NO)]Cp_2Co adduct generated after Cp_2Co reduction of (TFPPBr_8)Fe(NO).[72]

The UV-vis spectrum of the reduced compound [($T_{piv}PP$)Fe($OSiMe_3$)]Cp_2Co shows a decrease in the band at 415 nm giving rise to a new Soret band 443 nm (Fig. 3.25). The red shift of this Soret band was observed in the UV-vis spectra (in

chlorobenzene) of some reduced picket-fenced porphyrins including those of $[(T_{piv}PP)Fe(OR)]^-$ (R = Me, $C(=O)CH_3$, C_6H_5) in which the Soret bands shifted to ~ 450 nm.[74]

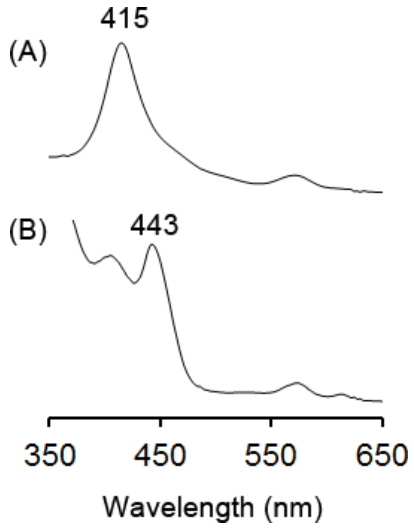

Figure 3.25. UV-vis spectrum of $(T_{piv}PP)Fe(OSiMe_3)$ (A) and $[(T_{piv}PP)Fe(OSiMe_3)]Cp_2Co$ (B).

3.3.3 Reactivity Studies of the (por)Fe(OR) compounds with NO

The (por)Fe(OR) compounds were found to be reactive with nitric oxide. In CH_2Cl_2, all the five coordinate (por)Fe(OR) compounds react with nitric oxide to form one or more of the three compounds: (por)Fe(NO), (por)Fe(NO)(OR) and (por)Fe(NO)(NO_2)[75] (Eq. 3.7) (Table 3.8).

(por)Fe(OR) + NO → (por)Fe(NO) and/or (por)Fe(NO)(OR) and/ or (por)Fe(NO)(NO_2) (**3.7**)

Table. 3.8. IR ν_{NO} (cm^{-1}) data of some six-coordinate (por)Fe(NO)(OR) complexes produced by reacting the five-coordinate (por)Fe(OR) compound (both as solid and in CH_2Cl_2 solution) with NO.

Five-coordinate precursor	IR ν_{NO} (cm^{-1})	
	KBr[a]	CH_2Cl_2
(T_{piv}PP)Fe($OSiMe_3$)	1880	1893
(T_{piv}PP)Fe(OCH_2SiMe_3)	1881	1893
(T_{piv}PP)Fe(OC_6HF_4)	1884	
(T_{piv}PP)Fe(OC_6H_4-*p*-NO_2)	1883	1896
(T_{piv}PP)Fe(OCH_2CF_3)	1882	
(T_{piv}PP)Fe(OC_6H_5)	1886	
(TPP)Fe(OC_6HF_4) [b]	1880, 1870 sh	
(T(*p*-OMe)PP)Fe(OC_6HF_4)	ND	1888
(OEP)Fe(OCH_2SiMe_3)[b]	1876, 1858	1889, 1883
(OEP)Fe($OSiMe_3$) [b]	1880, 1862	
(OEP)Fe(OC_6HF_4)	ND	1849, 1890

[a] reaction in solid form. ND = not detected. [b] linkage isomers

In a typical reaction, the (por)Fe(OR) complex is dissolved in anhydrous dichloromethane under N_2 atmosphere, and ~3× excess NO(g) is slowly bubbled through via an air-tight Hamilton syringe. On standing at room temperature for about 10 minutes, the (por)Fe(NO)(OR) in CH_2Cl_2 decomposes to (por)Fe(NO) based on the solution IR spectrum.

Furthermore, powdered samples of the (por)Fe(*O*-alkyl) complexes react with NO to give a mixture of (por)Fe(NO)(O-*alkyl*), and (por)Fe(NO) complexes. For example, in the reaction of (OEP)Fe(OCH_2SiMe_3) with NO, three ν_{NO} bands were observed at 1667, 1858 and 1876 cm^{-1} in the IR (KBr) spectrum and these species have apparent intensity ratios of 2:1:1, respectively (Fig. 3.26).

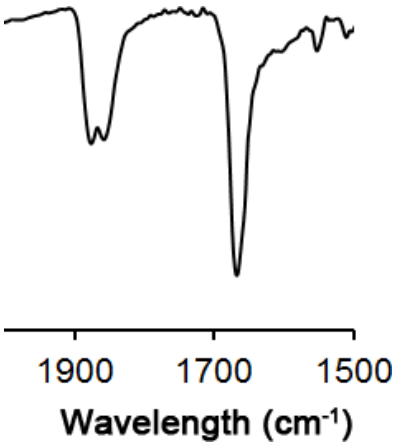

Figure 3.26. IR (KBr) spectrum of the product mixture obtained from the reaction of solid samples of (OEP)Fe(OCH_2SiMe_3) with NO(g) at room temperature. These bands are assigned to (OEP)Fe(NO)(OCH_2SiMe_3) (ν_{NO} = 1859 and 1876 cm^{-1}) and (OEP)Fe(NO) (ν_{NO} = 1667 cm^{-1}).[76]

The large intensity band at 1667 cm^{-1} is due to the five-coordinate (OEP)Fe(NO) complex.[76] The almost equal intensity bands at 1858 and 1876 cm^{-1} lie in the region of the ν_{NO} of a neutral six-coordinate iron nitrosyl porphyrin complex.[77] I note that the (por)Fe(NO)(NO_2) complex may be formed by the reaction of (por)Fe(NO) with higher NO_x species (e.g., as impurities in NO gas).[78,79] However, the complex (OEP)Fe(NO)(NO_2) (ν_{NO} = 1883 cm^{-1})[75] was not detected in the KBr sample during the reaction of powdered samples of (OEP)Fe(OCH_2SiMe_3) and NO, implying the sixth axial ligand is a ligand other than a nitrite, possibly, Me_3SiCH_2O. Hence, the ν_{NO} band at 1859 and 1876 cm^{-1} are assigned to the ν_{NO} of (OEP)Fe(NO)(OCH_2SiMe_3) and the splitting of the ν_{NO} bands is due to solid-state effect[80] and/ or existence of linkage isomers; the lower ν_{NO} = 1858 cm^{-1} band is assigned to a slightly bent NO-linkage and the 1876 cm^{-1} band assigned to the linear NO-linkage (see later).[81]

Furthermore, the IR bands due to the Me_3SiCH_2O ligands shifted to higher wavenumbers of 1296 and 991 cm^{-1} representing $\delta_{Si\text{-}Me}$ and $\nu_{Si\text{-}C}$, respectively, probably

implying that the $Me_3SiH_2C{-}O$ bond length became shorter, in which case NO would be expected to exert a positive *trans* influence on the axial $Me_3SiCH_2O^-$ ligand. Note that a ν_{NO} of 1850 cm^{-1} and a bent FeNO linkage ($\angle FeNO = 159.6$ °) was observed in the related (OEP)Fe(NO)(S-2,6-$(CF_3CONH)_2C_6H_3$) complex, with an accompanying shift in ν_{CO} to a higher wavenumber.[82] I predict that the Fe−O bond distance in the six-coordinate (OEP)Fe(NO)(OCH_2SiMe_3) compound to be longer than that in the five-coordinate (OEP)Fe(OCH_2SiMe_3) compound due to the positive *trans* influence of NO on the axial ligand.

Similarly, powder samples of (T_{piv}PP)Fe($OSiMe_3$) react with NO to produce the six-coordinate (T_{piv}PP)Fe(NO)($OSiMe_3$) compound identified by a new band at 1882 cm^{-1} due to ν_{NO} (Fig. 3.27).

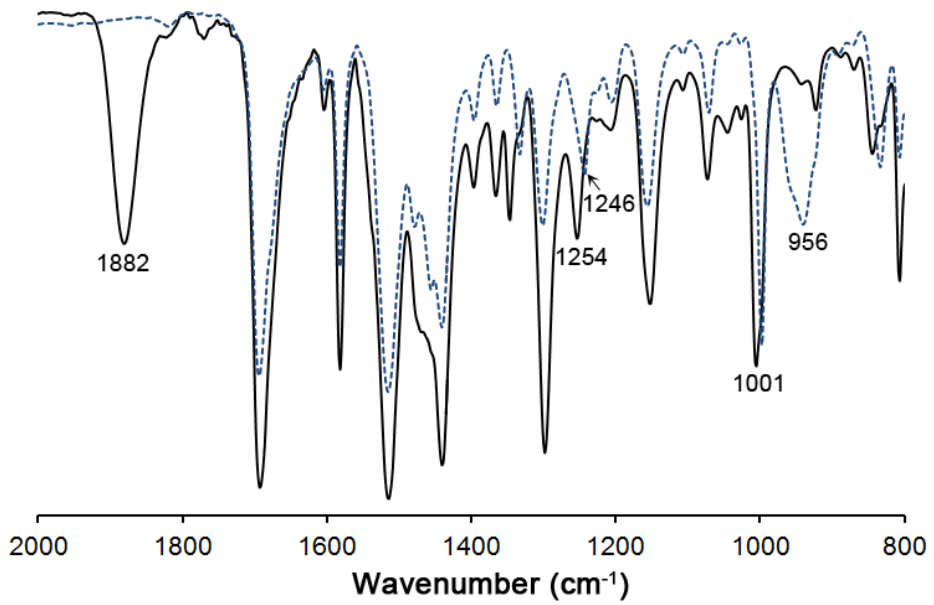

Figure 3.27. IR (KBr) spectrum of (T_{piv}PP)Fe(NO)($OSiMe_3$) (solid black line; ν_{NO} = 1882 cm^{-1} $\nu_{Si\text{-}O}$ = 1004 cm^{-1} and $\nu_{Si\text{-}C}$ = 1254 cm^{-1}) overlaid against (T_{piv}PP)Fe($OSiMe_3$) (dashed blue line; $\nu_{Si\text{-}O}$ = 956 cm^{-1} and $\nu_{Si\text{-}Me}$ = 1246 cm^{-1})

A comparison of the IR spectrum of (T_{piv}PP)Fe($OSiMe_3$) with that of (T_{piv}PP)Fe(NO)($OSiMe_3$) shows that the band due to $\nu_{Si\text{-}O}$ is shifted from 956 cm^{-1} in the former to 1004 cm^{-1} in the latter representing a $\Delta\nu_{Si\text{-}O}$ = 48 cm^{-1}. On the other hand the band due to $\delta_{Si\text{-}Me}$ shifted only by 8 cm^{-1} from 1246 cm^{-1}- in (T_{piv}PP)Fe($OSiMe_3$) to 1254 cm^{-1} in (T_{piv}PP)Fe(NO)$OSiMe_3$) (Fig. 3.24) The *trans* influence of NO on the axial trimethylsilyloxide ligand is responsible for the higher shift in the IR frequencies which predictably lengthens the Fe–O bond.

It is interesting to note that only the *meso*-substituted (por)Fe(*O*-aryl) complexes in the powder form reacted with NO to give the five- or six-coordinate nitrosyl derivatives. Furthermore, amongst these, only (TPP)Fe(OC_6HF_4) and the picket-fence porphyrin complexes yielded the six-coordinate compound. The six-coordinate (TPP)Fe(NO)(OC(=O)CF_3) complex was previously prepared and characterized by crystallography by NO soaking of a crystal samples of the five-coordinate (TPP)Fe(O(=O)CF_3) complex.[12] Thus, there is probably an interesting feature of the TPP porphyrin macrocycle that allows the weak NO binding[83] at the sixth coordination site. For example, powdered samples of (TPP)Fe(OC_6HF_4) reacted with NO to form (TPP)Fe(NO)(OC_6HF_4) which displays a new ν_{NO} band at 1880 cm^{-1} (1870 cm^{-1} (sh)) in the IR (KBr) spectrum (*cf.* ν_{NO} = 1901 cm^{-1} in the compound (TPP)Fe(NO)(OC(=O)CF_3)[12]). Not surprising, higher ν_{NO} vibrations are observed in the complexes that have weaker σ-donor axial OR groups and vice versa for stronger σ-donor group, similar to the related (T(*p*-OMe)PP)Ru(NO)(OR) (R = C_6HF_4, $CF_3C(=O)O$) complexes (Chapter 2).[84] Note that the pK_as of $CF_3C(=O)OH$ and C_6HF_4OH are 0.5[65] and 5.53,[64] respectively.

I speculated that the six-coordinate picket-fenced porphyrin complexes (T_{piv}PP)Fe(NO)(OR) may be obtained by utilizing the ability of the *pivalamido* group in the picket-fence porphyrin to protect small molecules as in the case of the six-coordinate (T_{piv}PP)Fe(O_2)(1-MeIm).[58,85] I previously obtained crystal structures of (T_{piv}PP)FeCl[86] and (T_{piv}PP)FeBr (unpublished) in which the axial halide ligands are coordinated to iron in the protected site of the "picket-fence" porphyrin.

The binding capabilities of these two five-coordinate porphyrin complexes (TPP)Fe(OR) and (T_{piv}PP)Fe(OR) with NO were investigated further to see if it would be possible to generate crystal samples of the six-coordinate complexes by NO(g) diffusion into single crystals of the five coordinate complexes.

Based on previous success in the formation of crystal samples of (TPP)Fe(NO)(OC(=O)CF_3),[12] and the reactivity of the powdered samples of the complex (TPP)Fe(OC_6HF_4) with NO to form (TPP)Fe(NO)(OC_6HF_4) in this work, it seemed that the porphyrin macrocyle TPP may be a good candidate for the NO soaking reactions in this work. However, several repeated attempts at producing crystal samples of the six-coordinate (TPP)Fe(NO)(OC_6HF_4) by this procedure were not successful. An examination of the molecular structure of (TPP)Fe(OC_6HF_4) (Fig. 3.16) shows relatively "tight" crystal packing (mean-plane porphyrin-porphyrin separation, Δ_{mp} = 4.2 Å, and lateral shift of 3.5 Å) which probably explains their non-reactivity in the crystal. The complex (TPP)Fe($OSiMe_3$) similarly has "tight" crystal packing (mean-plane porphyrin-porphyrin separation, Δ_{mp} = 3.8 Å, and lateral shift of 7.4 Å) (Fig. 3.18) and also failed to form the desired six-coordinate (TPP)Fe(NO)($OSiMe_3$) compound upon reaction with NO with crystalline (TPP)Fe($OSiMe_3$). The molecular structure of

the related (TPP)Fe(OCH_2SiMe_3) complex has a Δ_{mp} and lateral shift of 4.9 Å and 11.1 Å, respectively (Fig. 3.15) and seemed to have a favorable crystal packing but it did not produce the six-coordinate complex on reaction with NO.

In one instance, crystalline samples of the complex (OEP)Fe(OCH_2SiMe_3) were obtained and then exposed to NO. The crystals instantly turned orange, but unfortunately with associated crystal cracking during the reaction. The IR (KBr) spectrum of this orange sample showed a band at 1667 cm^{-1} related to the ν_{NO} of the final five-coordinate (OEP)Fe(NO) complex.

To take advantage of the protecting capability of the *t*-butylamido group (in $T_{piv}PP$) with small molecules[58,85] and the favorable crystal space in the five-coordinate ($T_{piv}PP$)Fe($OSiMe_3$) compound (Fig. 3.28), I exposed crystal samples of the five-coordinate ($T_{piv}PP$)Fe($OSiMe_3$) with NO.

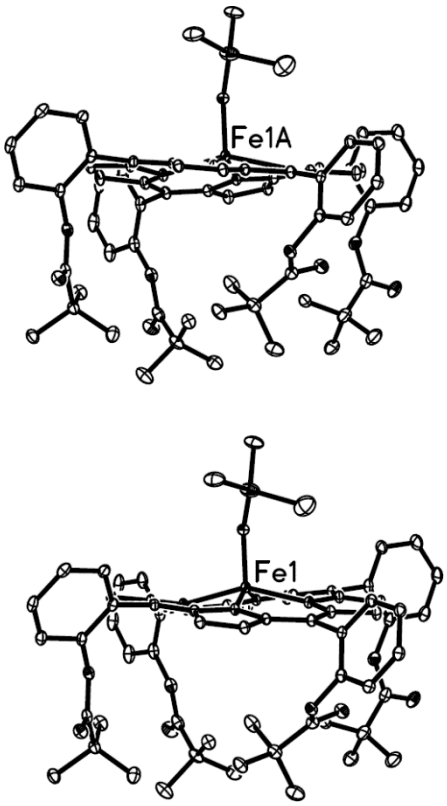

Figure 3.28. Side view of the two neighboring porphyrin molecules of (T_{piv}PP)Fe($OSiMe_3$) in a unit cell.

The reaction of crystalline samples of (T_{piv}PP)Fe(OR) with NO has not thus far yielded the desired (T_{piv}PP)Fe(NO)(OR) compound, although the five-coordinate (T_{piv}PP)Fe(NO) was obtained on exposure with NO at longer reaction times. It also appears that crystal packing alone may not be the only determining factor for solid state NO binding to (por)Fe(OR) to generate the six-coordinate (por)Fe(NO)(OR), but the electronic properties of the axial and equatorial ligands (donor- and acceptor properties) may play a direct role.

3.3.4 Electrochemistry of generated ($T_{piv}PP$)Fe(NO)($OSiMe_3$)

The nitrosyl compound ($T_{piv}PP$)Fe(NO)($OSiMe_3$), prepared by solid-gas phase reaction between the five-coordinate ($T_{piv}PP$)Fe($OSiMe_3$) and NO, was subjected to IR spectroelectrochemical studies. Fig. 3.29 shows the cyclic voltammogram of the generated ($T_{piv}PP$)Fe(NO)($OSiMe_3$) in dichloromethane which shows an irreversible first oxidation at E_{pa} = 0.56 V (*vs* Fc/Fc^+ couple) with a corresponding return peak at E_{pc} = 0.44 V.

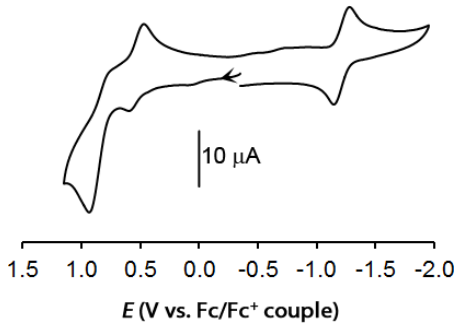

Figure 3.29. The cyclic voltammogram of generated ($T_{piv}PP$)Fe(NO)($OSiMe_3$) compound at 200 mV/s, 1mM analyte, 0.1 M NBu_4PF_6 at room temperature. Potentials are referenced to Fc/Fc^+ set to 0.00 V.

The intensity of the first oxidation wave is lower than that of the second oxidation probably due to the weak NO binding to ferric centers (Fig. 3.29).[83] The electrogenerated products were unstable in solution. This made it difficult to obtain unambiguous IR spectra data for the redox products. The cyclic voltammogram also shows an irreversible second oxidation at E_{pa} = 0.93 V and a reversible reduction at E_{pa} = −1.21 V.

3.4 Theoretical Consideration

To gain insight into the electronic behavior of the (T_{piv}PP)Fe(OSiMe$_3$) reactions, electron density maps of the frontier molecular orbitals (FMO) of the model compound (P)Fe(OSiMe$_3$) were calculated using density functional calculations (Gaussian 09[30] with B3LYP/ DGDZVP). In the ground state, the electron density in the HOMO (Fig. 3.31a) is concentrated on the porphyrin macrocycle along the four porphine nitrogen core and the *meso*-positions, with the latter positions carrying greater electron density. The LUMO of the model compound (P)Fe(OSiMe$_3$) (Fig. 3.31b) shows that the addition of an electron would potentially be held in the plane of the porphyrin. Thus, the DFT supports the experimental observation that both oxidation and reduction of (T_{piv}PP)Fe(OSiMe$_3$) are porphyrin-centered redox reactions.

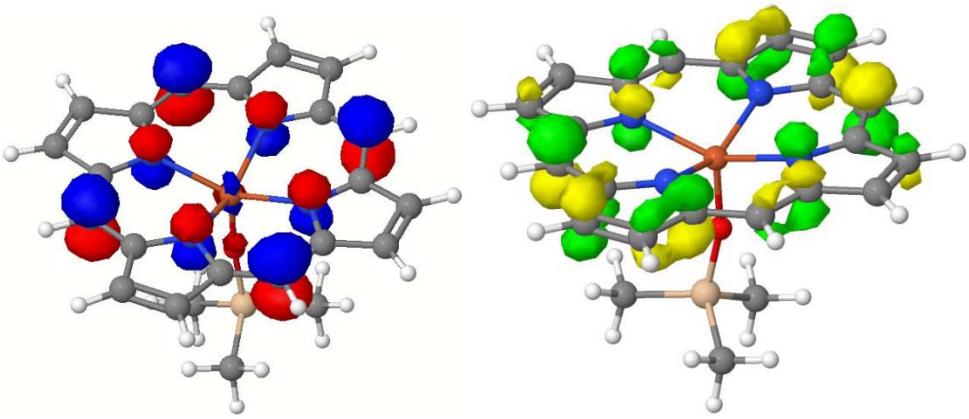

(a) (b)

Figure 3.31.The FMO orbitals of (P)Fe(OSiMe$_3$): (a) HOMO (b) LUMO

Bonding parameters of the model compound (P)Fe(NO)(OSiMe$_3$) (S = 0) were also obtained by DFT calculations using the same method and basis set as for the five-coordinate (P)Fe(OSiMe$_3$) compound. Fig. 3.32 shows the calculated structures of (P)Fe(OSiMe$_3$) and (P)Fe(NO)(OSiMe$_3$).

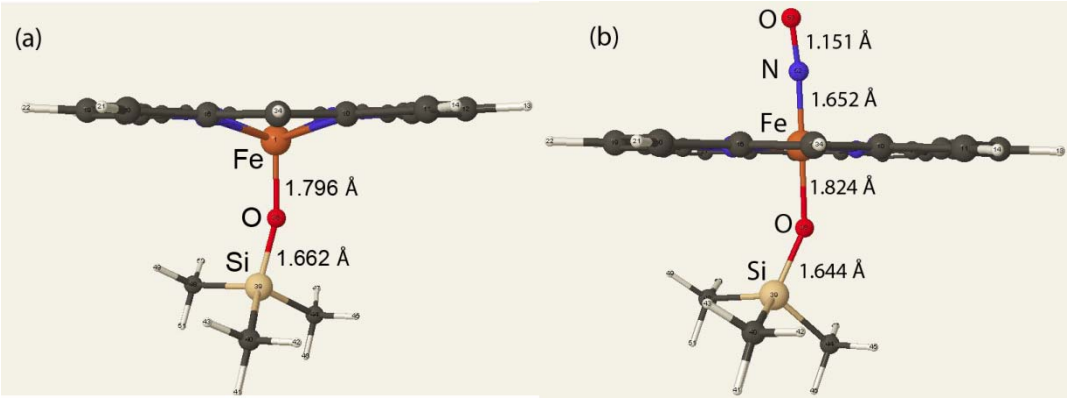

Figure 3.32. Calculated structures of the five-coordinate (P)Fe($OSiMe_3$) (a) and six-coordinate (P)Fe(NO)($OSiMe_3$) (b) obtained by DFT calculations. The Fe−O bond lengthens by 0.028 Å after coordination with NO, and Fe is centered in the plane of the porphine macrocycle in the nitrosyl product.

The Fe−N distances are 2.109-2.110 Å and 2.030-2.033 Å for the model compounds (P)Fe($OSiMe_3$) and (P)Fe(NO)($OSiMe_3$), respectively. The shortening of these bonds are accompanied by a centering of the Fe atom in the plane of the porphine macrocyle. Importantly, the Fe−O bond was lengthened by 0.028 Å in the six-coordinate (P)Fe($OSiMe_3$) in contrast to the experimentally observed scenario for (TPP)Fe($OC(=O)CF_3$) where Fe−O bond became shorter.[12] Further, the Si−O bond length became shorter and this parallels the higher $\nu_{Si\text{-}O}$ (KBr) vibrational frequency obtained in the (por)Fe(NO)($OSiMe_3$) compound compared with its non-nitrosyl precursor. It appears, based on the DFT calculations that NO exhibits a negative *trans* effect on the Fe−O and this probably explains why the (por)Fe(NO)($OSiMe_3$) decomposed to the five-coordinate (por)Fe(NO) compound over a period of time.

3.5 Conclusion

In conclusion, the complexes (por)Fe(O-*aryl*), (OEP)Fe(OMe) and (por)Fe(O$(CH_2)_n$SiMe$_3$) complexes have been synthesized in high yields. The magnetic susceptibility data as obtained by Evans method shows that the complexes are mainly high-spin species and that distortion of the porphyrin macrocycles due to steric interaction with the axial ligands could influence the spin-states. X-ray crystal structures of the five-coordinate complexes show that the compounds are pyramidal with the axial O-bound ligands in the axial position. The Fe−O bond lengths are ~1.9 Å and the Fe−N bonds are ~2 Å. In general, the Fe−O($(CH_2)_n$SiMe$_3$) bonds are longer than the Fe−O(*aryl*) bonds because of sterics in the former. Furthermore, the *cis*-influence of the porphyrin macrocycle is more defined in these five-coordinate complexes.

The redox behaviors of the five-coordinate compounds were studied by CV and IR spectroelectrochemistry which shows porphyrin-centered oxidations in the (por)Fe(OR) compounds. In the (por)Fe(O-*aryl*) complexes two reversible oxidations were obtained. The compounds and (T_{piv}PP)Fe(OSiMe$_3$) and (T_{piv}PP)Fe(OCH$_2$SiMe$_3$) each undergo one irreversible oxidation. The compound (T(*p*-OMe)PP)Fe(OC_6HF_4) and (T_{piv}PP)Fe(OSiMe$_3$) undergo chemically and electrochemical reversible reductions. IR spectroelectrochemistry data suggests that electroreduction of (T_{piv}PP)Fe(OSiMe$_3$) is accompanied by conformational change and spin-state changes resulting in shifts of the ν_{CO} band to lower wavenumbers. Chemical reduction using cobaltocene and ^{1}H NMR and UV-vis characterization support the formation of the reduced [(T_{piv}PP)Fe(OSiMe$_3$)]$^-$ product.

In addition, CH_2Cl_2 solutions of the five-coordinate (por)Fe(OR) compounds react with NO to form (por)Fe(NO), and/ or (por)Fe(NO)(NO_2) and/ or (por)Fe(NO)(OR). Furthermore, some of the five coordinate (por)Fe(O-aryl) and (por)Fe(*O*-alkyl) complexes in the powdered form react with NO to form (por)Fe(NO)(OR) and (por)Fe(NO). A comparison of the IR data of the five-coordinate (por)Fe(OR) and six-coordinate (por)Fe(NO)(OR) shows the possibility of *trans* influence of NO on the axial ligand and this has been examined by DFT calculations. Attempts to obtain crystals of the six-coordinate (por)Fe(NO)(OR) complex have, however, not been successful.

Finally, CV of the six-coordinate (T_{piv}PP)Fe(NO)($OSiMe_3$) compound shows an irreversible first oxidation at E_{pa} = 0.56 V with a corresponding return peak at E_{pc} = 0.44 V. DFT calculations of the five-coordinate complexes support the porphyrin-centered oxidations.

3.6 References

(1) Walker, F. A.; Simonis, U. In *Encyclopedia of Inorganic and Bioinorganic Chemistry*; John Wiley & Sons, Ltd: 2011.

(2) Ainscough, E. W.; Addison, A. W.; Dolphin, D.; James, B. R. *J. Am. Chem. Soc.* **1978**, *100*, 7585-7591.

(3) Arasasingham, R. D.; Balch, A. L.; Cornman, C. R.; De Ropp, J. S.; Eguchi, K.; La Mar, G. N. *Inorg. Chem.* **1990**, *29*, 1847-1850.

(4) Smith, D. W.; Williams, R. J. P. In *Struct. Bond.*; Springer Berlin Heidelberg: 1970; Vol. 7, p 1-45.

(5) Weiss, R.; Gold, A.; Terner, J. *Chem. Rev.* **2006**, *106*, 2550-2579.

(6) Hoard, J. L. *Science* **1971**, *174*, 1295-1302.

(7) Scheidt, W. R.; Reed, C. A. *Chem. Rev.* **1981**, *81*, 543-555.

(8) Barkigia, K. M.; Renner, M. W.; Fajer, J. *J. Porphyr. Phthalocya.***2001**, *5*, 415-418.

(9) Sakai, T.; Ohgo, Y.; Ikeue, T.; Takahashi, M.; Takeda, M.; Nakamura, M. *J. Am. Chem. Soc.* **2003**, *125*, 13028-13029.

(10) Nakamura, M. *Coord. Chem. Rev.* **2006**, *250*, 2271-2294.

(11) Buchler, J.; Kokisch, W.; Smith, P. In *Novel Aspects*; Springer Berlin Heidelberg: 1978; Vol. 34, p 79-134.

(12) Xu, N.; Goodrich, L. E.; Lehnert, N.; Powell, D. R.; Richter-Addo, G. B. *Angew. Chem. Int. Ed.* **2013**, *52*, 3896-3900.

(13) Adler, A. D.; Longo, F. R.; Finarelli, J. D.; Goldmacher, J.; Assour, J.; Korsakoff, L. *J. Org. Chem.* **1967**, *32*, 476-476.

(14) Lindsey, J. S.; Wagner, R. W. *J. Org. Chem.* **1989**, *54*, 828-836.

(15) Collman, J. P.; Gagne, R. R.; Reed, C.; Halbert, T. R.; Lang, G.; Robinson, W. T. *J. Am. Chem. Soc.* **1975**, *97*, 1427-1439.

(16) Barkigia, K. M.; Berber, M. D.; Fajer, J.; Medforth, C. J.; Renner, M. W.; Smith, K. M. *J. Am. Chem. Soc.* **1990**, *112*, 8851-8857.

(17) Adler, A. D.; Longo, F. R.; Kampas, F.; Kim, J. *J. Inorg. Nucl. Chem.* **1970**, *32*, 2443-2445.

(18) Fleischer, E. B.; Srivastava, T. S. *J. Am. Chem. Soc.* **1969**, *91*, 2403-2405.

(19) La Mar, G. N.; Eaton, G. R.; Holm, R. H.; Walker, F. A. *J. Am. Chem. Soc.* **1973**, *95*, 63-75.

(20) Cheng, B.; Hobbs, J. D.; Debrunner, P. G.; Erlebacher, J.; Shelnutt, J. A.; Scheidt, W. R. *Inorg. Chem.* **1995**, *34*, 102-110.

(21) Helms, J. H.; Ter Haar, L. W.; Hatfield, W. E.; Harris, D. L.; Jayaraj, K.; Toney, G. E.; Gold, A.; Mewborn, T. D.; Pemberton, J. E. *Inorg. Chem.* **1986**, *25*, 2334-2337.

(22) Kobayashi, H.; Higuchi, T.; Kaizu, Y.; Osada, H.; Aoki, M. *Bull. Chem. Soc. Jpn.* **1975**, *48*, 3137-3141.

(23) King, R. B. *Organomet. Synth.* **1965**, *1*, 70-71.

(24) Schubert, E. M. *J. Chem. Educ.* **1992**, *69*, 62.

(25) Sur, S. K. *J. Magn. Reson.***1989**, *82*, 169-173.

(26) Yatsunyk, L. A.; Walker, F. A. *Inorg. Chem.* **2004**, *43*, 757-777.

(27) Bain, G. A.; Berry, J. F. *J. Chem. Educ.* **2008**, *85*, 532.

(28) Bruker-AXS *Data Collection: SMART Software Reference Manual* **1998**.

(29) Bruker-AXS *Data Reduction: SAINT Software Reference Manual* **1998**.

(30) Frisch, M. J.; Trucks, G. W.; Schlegel, H. B.; G. E. Scuseria; Robb, M. A.; Cheeseman, J. R.; Scalmani, G.; Barone, V.; Mennucci, B.; Petersson, G. A.; Nakatsuji, H.; Caricato, M.; Li, X.; Hratchian, H. P.; Izmaylov, A. F.; Bloino, J.; Zheng, G.; Sonnenberg, J. L.; Hada, M.; Ehara, M.; Toyota, K.; Fukuda, R.; Hasegawa, J.; Ishida, M.; Nakajima, T.; Honda, Y.; Kitao, O.; Nakai, H.; Vreven, T.; Montgomery, J., J. A. ; Peralta, J. E.; Ogliaro, F.; Bearpark, M.; Heyd, J. J.; Brothers, E.; Kudin, K. N.; Staroverov, V. N.; Keith, T.; Kobayashi, R.; Normand, J.; Raghavachari, K.; Rendell, A.; Burant, J. C.; Iyengar, S. S.; Tomasi, J.; Cossi, M.; Rega, N.; Millam, J. M.; Klene, M.; Knox, J. E.; Cross, J. B.; Bakken, V.; Adamo, C.; Jaramillo, J.; Gomperts, R.; Stratmann, R. E.; Yazyev, O.; Austin, A. J.; Cammi, R.; Pomelli, C.; Ochterski, J. W.; Martin, R. L.; Morokuma, K.; Zakrzewski, V. G.; Voth, G. A.; Salvador, P.; Dannenberg, J. J.; Dapprich, S.; Daniels, A. D.; Farkas, O. J.; Foresman, B.; Ortiz, J. V.; Cioslowski, J.; Fox, D. J.; Gaussian, I., Wallingford CT, 2010., Ed.

(31) Tang, S. C.; Koch, S.; Papaefthymiou, G. C.; Foner, S.; Frankel, R. B.; Ibers, J. A.; Holm, R. H. *J. Am. Chem. Soc.* **1976**, *98*, 2414-2434.

(32) Sadasivan, N.; Eberspaecher, H. I.; Fuchsman, W. H.; Caughey, W. S. *Biochemistry* **1969**, *8*, 534-541.

(33) Cohen, I. A. *J. Am. Chem. Soc.* **1969**, *91*, 1980-1983.

(34) O'Keeffe, D. H.; Barlow, C. H.; Smythe, G. A.; Fuchsman, W. H.; Moss, T. H.; Lilienthal, H. R.; Caughey, W. S. *Bioinorg. Chem.* **1975**, *5*, 125-147.

(35) Wright, N.; Hunter, M. J. *J. Am. Chem. Soc.* **1947**, *69*, 803-809.

(36) Figgis, B. N.; Lewis, J. M*odern Coordination Chemistry: Magnetochemistry of complex compounds*; Wiley.M: New York, 1960.

(37) Reed, C. A.; Mashiko, T.; Bentley, S. P.; Kastner, M. E.; Scheidt, W. R.; Spartalian, K.; Lang, G. *J. Am. Chem. Soc.* **1979**, *101*, 2948-2958.

(38) Nakamura, M.; Ikeue, T.; Ohgo, Y.; Takahashi, M.; Takeda, M. *Chem. Commun.* **2002**, 1198-1199.

(39) Shaffer, C. D.; Straub, D. K. *Inorg. Chim. Acta* **1989**, *158*, 167-180.

(40) Sugimoto, H.; Ueda, N.; Mori, M. *Bull. Chem. Soc. Jpn.* **1982**, *55*, 3468-3472.

(41) Uno, T.; Hatano, K.; Nishimura, Y.; Arata, Y. *Inorg. Chem.* **1990**, *29*, 2803-2807.

(42) Meot-Ner, M.; Adler, A. D. *J. Am. Chem. Soc.* **1975**, *97*, 5107-5111.

(43) Kadish, K. M.; Morrison, M. M. *Bioinorg. Chem.* **1977**, *7*, 107-115.

(44) Kadish, K. M.; Morrison, M. M.; Constant, L. A.; Dickens, L.; Davis, D. G. *J. Am. Chem. Soc.* **1976**, *98*, 8387-8390.

(45) Ghiladi, R. A.; Kretzer, R. M.; Guzei, I.; Rheingold, A. L.; Neuhold, Y.-M.; Hatwell, K. R.; Zuberbühler, A. D.; Karlin, K. D. *Inorg. Chem.* **2001**, *40*, 5754-5767.

(46) Scheidt, W. R. *The Porphyrin Handbook; Kadish, K. M., Smith, K. M., Guilard, R., Eds.; Academic Press: New York, 2000; Vol. 3, Chapter 16 (*Systematics of the Stereochemistry of Porphyrins and Metalloporphyrin)*, pp. 49-112*.

(47) Xu, N.; Powell, D. R.; Richter-Addo, G. B. *Acta Cryst. E* **2013**, *69*, m530-m531.

(48) Cheng, R.-J.; Chen, P.-Y.; Gau, P.-R.; Chen, C.-C.; Peng, S.-M. *J. Am. Chem. Soc.* **1997**, *119*, 2563-2569.

(49) Sakai, T.; Ohgo, Y.; Hoshino, A.; Ikeue, T.; Saitoh, T.; Takahashi, M.; Nakamura, M. *Inorg. Chem.* **2004**, *43*, 5034-5043.

(50) Kanamori, D.; Yamada, Y.; Onoda, A.; Okamura, T.-a.; Adachi, S.; Yamamoto, H.; Ueyama, N. *Inorg. Chim. Acta* **2005**, *358*, 331-338.

(51) Bhowmik, S.; Dey, S.; Sahoo, D.; Rath, S. P. *Chem. – Eur. J.* **2013**, *19*, 13732-13744.

(52) Hatano, K.; Uno, T. *Bull. Chem. Soc. Jpn.* **1990**, *63*, 1825-1827.

(53) Kim, Y.; Nam, W.; Lim, M. H.; Jin, S. W.; Lough, A. J.; Kim, S.-J. *Acta Cryst. C* **2001**, *57*, 556-557.

(54) Hoard, J. L.; Hamor, M. J.; Hamor, T. A.; Caughey, W. S. *J. Am. Chem. Soc.* **1965**, *87*, 2312-2319.

(55) Coe, B. J.; Glenwright, S. J. *Coord. Chem. Rev.* **2000**, *203*, 5-80.

56) Appleton, T. G.; Clark, H. C.; Manzer, L. E. *Coord. Chem. Rev.* **1973**, *10*, 335-422.

(57) Kaftory, M.; Kapon, M.; Botoshansky, M. In *The Chemistry of Organic Silicon Compounds*; John Wiley & Sons, Ltd: 2003, p 181-265.

(58) Collman, J. P.; Gagne, R. R.; Reed, C. A.; Robinson, W. T.; Rodley, G. A. *Proc. Nat. Acad. Sci.***1974**, *71*, 1326-1329.

(59) Meininger, D. J.; Muzquiz, N.; Arman, H. D.; Tonzetich, Z. J. *J. Porphyr. Phthal.* **2014**, *18*, 416-423.

(60) Warhausen, A. *Dissertation, University of Oklahoma* **2012**.

(61) Richard, M. J.; Shaffer, C. D.; Evilia, R. F. *Electrochim. Acta* **1982**, *27*, 979-983.

(62) Shaw, M. J.; Henson, R. L.; Houk, S. E.; Westhoff, J. W.; Jones, M. W.; Richter-Addo, G. B. *J. Electroanal. Chem.* **2002**, *534*, 47-53.

(63) Carter, S. M.; Lee, J.; Hixson, C. A.; Powell, D. R.; Wheeler, R. A.; Shaw, M. J.; Richter-Addo, G. B. *Dalton Trans.* **2006**, 1338-1346.

(64) Kipper, K.; Herodes, K.; Leito, I. *J. Chromatogr. A* **2011**, *1218*, 8175-8180.

(65) Gokel, G. W. In *Dean's Handbook of Organic Chemistry*, The McGraw-Hill Companies, Inc., New York, 2004.

(66) Lee, W. A.; Calderwood, T. S.; Bruice, T. C. *Proc. Nat. Acad. Sci.* **1985**, *82*, 4301-4305.

(67) Leondiadis, L.; Momenteau, M. *J. Org. Chem.* **1989**, *54*, 6135-6138.

(68) Dunbar, K. R.; Achim, C.; Shatruk, M. In *Spin-Crossover Materials*; John Wiley & Sons Ltd: 2013, p 171-202.

(69) Murray, K. S. In *Spin-Crossover Materials*; John Wiley & Sons Ltd: 2013, p 1-54.

(70) Sato, O.; Tao, J.; Zhang, Y.-Z. *Angew. Chem. Int. Ed.* **2007**, *46*, 2152-2187.

(71) Pellegrino, J.; Hübner, R.; Doctorovich, F.; Kaim, W. *Chem. – Eur. J.* **2011**, *17*, 7868-7874.

(72) Pellegrino, J.; Bari, S. E.; Bikiel, D. E.; Doctorovich, F. *J. Am. Chem. Soc.* **2009**, *132*, 989-995.

(73) Fleischer, E. B. *Acc. Chem. Res.* **1970**, *3*, 105-112.

(74) Nasri, H.; Fischer, J.; Weiss, R.; Bill, E.; Trautwein, A. *J. Am. Chem. Soc.* **1987**, *109*, 2549-2550.

(75) Ellison, M. K.; Schulz, C. E.; Scheidt, W. R. *Inorg. Chem.* **1998**, *38*, 100-108.

(76) Ellison, M. K.; Scheidt, W. R. *J. Am. Chem. Soc.* **1997**, *119*, 7404-7405.

(77) Cheng, L.; Richter-Addo, G. B. *The Porphyrin Handbook; Kadish,K. M., Smith, K. M., Guilard, R., Eds.; Academic Press: New York, 2000; Vol. 4, Chapter 33 (Biochemistry and Binding: Activation of Small Molecules), pp 219-291*.

(78) Lorković, I.; Ford, P. C. *J. Am. Chem. Soc.* **2000**, *122*, 6516-6517.

(79) Lorković, I. M.; Ford, P. C. *Inorg. Chem.* **2000**, *39*, 632-633.

(80) Srivastava, T. S.; Hoffman, L.; Tsutsui, M. *J. Am. Chem. Soc.* **1972**, *94*, 1385-1386.

(81) Awasabisah, D.; Richter-Addo, G. B. In *Adv. Inorg. Chem.*; Rudi van, E., José, A. O., Eds.; Academic Press: 2015; Volume 67, p 1-86.

(82) Xu, N.; Powell, D. R.; Cheng, L.; Richter-Addo, G. B. *Chem. Commun.* **2006**, 2030-2032.

(83) Lim, M. D.; Lorkovic, I. M.; Ford, P. C. *J. Inorg. Biochem.* **2005**, *99*, 151-165.

(84) Awasabisah, D.; Xu, N.; Sharmah Gautam, K. P.; Powell, D. R.; Shaw, M. J.; Richter-Addo, G. B. *Dalton Trans.* **2013**, *42*, 8537-8540.

(85) Collman, J. P.; Gagne, R. R.; Halbert, T. R.; Marchon, J. C.; Reed, C. A. *J. Am. Chem. Soc.* **1973**, *95*, 7868-7870.

(86) Awasabisah, D.; Powell, D. R.; Richter-Addo, G. B. *Acta Crystallogr.E* **2015**, *71*, m42-m43.

Chapter 4: Iridium Phosphine Complexes and their reactivity

4.1 Introduction

The chemistry of NO is linked to that of other species that contain the NO fragment. A notable class of such species are the alkyl nitrites (R-O-N=O; R = alkyl). Some alkyl nitrites, such as amyl nitrite, are known to interact with biological heme proteins to either release NO or to oxidize the heme protein via as yet unknown mechanisms.[1,2] Such RONO compounds have been used as nitrosylating agents in coordination chemistry.[3] In the previous two chapters, I reported on the preparation and characterization of various group 8 metal nitrosyl alkoxides M(NO)(OR). I this chapter, I explored the possible formation of the other coordination isomer M{N(=O)OR} (Fig. 4.1). Surprisingly, the latter compounds have been elusive, and thus remain of interest to chemists examining the broader reaction chemistry of NO.

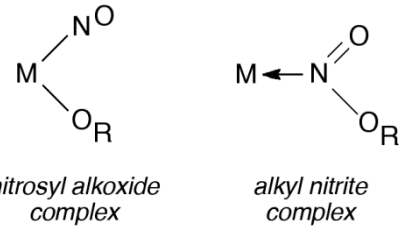

Figure 4.1. The coordination isomers of M{N(=O)OR}considered in this dissertation.

The discovery of Vaska's reagent[4,5] and the report on oxidation of triphenylphosphine by Vaska's reagent, first investigated by Teranishi,[6] was historically groundbreaking in the field of iridium-catalyzed reactions. Since then, there has been a rising interest in the chemistry of iridium complexes, for example, in the area of organic synthesis.[7] The use of metal-nitrosyl complexes to activate other small molecules is

well-established in the literature. For example, the dinitrosyl iridium complex $[Ir(NO)_2(PPh_3)]^+$reacts with CO to generate CO_2 and N_2O.[8]

Endogenous NO is oxidized by HbO_2 to nitrate, and a mechanistic review on this topic and other metal-mediated NO_x reactions have been reviewed previously.[9] In this chapter, I examine the reactivity of Ir(III) phosphine complexes with other molecules. The reaction of $IrCl_3(PPh_3)_2$ with *n*-BuONO produces the compound $IrCl_3$(*n*-BuONO)$(PPh_3)_2$ which reacts further with O_2 to generate the nitrate complex $IrCl_3(\eta^2\text{-}O_2NO)(PPh_3)_2$.

4.2 Experimental Section

General Procedures. Unless otherwise stated, all reactions and manipulations were performed under an atmosphere of nitrogen using standard Schlenk glassware and/ or in an Innovative Technology Labmaster 100 Dry Box. Solvents for reactions were collected under a nitrogen atmosphere from a solvent purification system (Innovative Technology, Inc. Newburyport, MA, PS-400-5MD) using a glass syringe.

4.2.1 Chemicals

The compound iridium(III) chloride tetrahydrate ($IrCl_3 \cdot 3H_2O$) was purchased from Aldrich and used as received. Chloroform-*d* ($CDCl_3$, 99.96 atom %D) and Chloroform-d_2 (CD_2Cl_2, 99.9 atom %D) were purchased from Cambridge Isotope Laboratories, deaerated by a three cycle freeze-pump-thaw and dried under a 4 Å molecular sieves. Butyl nitrite was prepared as reported in literature.[10] Ethyl nitrite (10-20 wt% in EtOH) and triphenyl phosphine (PPh_3, 99%) were purchased form Aldrich

and used as received. Diethyl ether was purchased from Aldrich. $IrHCl_2(PPh_3)_3$ was prepared by a modified method in the literature (see experimental).[11]

Chlorine gas was prepared as follows: *CAUTION. Corrosives and oxidizing agents. Wear protective gloves and goggles*. A flask equipped with a condenser, a dropping funnel and a gas delivery tube was charged with $KMNO_4$ (~1 g). Concentrated HCl was delivered dropwise into the flask via the dropping pipette to generate the yellow-green Cl_2 gas.[12] The Cl_2 gas that was generated was bubbled through another flask containing water via the delivery tube, which was in turn bubbled through a concentrated solution of H_2SO_4 and finally delivered into the reacting vessel. Occasionally, it was necessary to gently heat the mixture of HCl and $KMnO_4$ to generate the Cl_2 gas.

4.2.2 Instrumentation

Infrared spectra were recorded on a Bio-Rad FT-155 and/or a Tensor 27 FTIR spectrometer. ^1H NMR and ^{31}P NMR spectra were obtained on a Varian 300 MHz spectrometer at room temperature and the signals referenced to the residual signal of the solvent employed ($CHCl_3$ at 7.24 ppm, CH_2Cl_2 at 5.32 ppm). ESI mass spectra were obtained on a Micromass Q-TOF mass spectrometer by Dr. Steven Foster. Elemental analyses were obtained by the staff of Atlantic Microlab, Norcross, GA. X-ray diffraction data were collected by Dr. Douglas R. Powell using a diffractometer with a Bruker APEX ccd area detector[13,14] and graphite-monochromated Mo Kα radiation (λ = 0.71073 Å).

Cyclic voltammetry measurements were performed using a BAS CV 50W instrument (Bioanalytical Systems, West Lafayette, IN). In all the electrochemical experiments, a three-electrode cell was utilized and consisted of a 3.0-mm diameter Pt disk working electrode, a Pt wire counter electrode, and a Ag/AgCl reference electrode. Solutions were deaerated before use by passing a stream of N_2 gas through the solution for a minimum of 10 min. A blanket of N_2 was maintained over the solution while performing the experiments. The electrochemical experiments were performed in solutions containing 0.1 M NBu_4PF_6 and 1.0 mM of the analyte.

A Bruker Vector 22 and/ or a Tensor 27 FTIR spectrometer equipped with a mid-IR fiber-optic dip probe and liquid nitrogen cooled MCT detector (RemSpec Corporation, Sturbridge, MA, USA) was used for the infrared spectroelectrochemistry.

4.2.3 Syntheses of *cis,mer*-$IrHCl_2(PPh_3)_3$ (1)

The compound *cis,mer*-$IrHCl_2(PPh_3)_3$ (**1**) was prepared by a slight modification of the method reported by Morris and coworkers.[11] In this synthesis, a 50 mL two-neck round bottom flask equipped with a magnetic stir bar and a condenser was charged with $IrCl_3 \cdot 3H_2O$ (0.750 g, 2.13 mmol) and PPh_3 (4.02 mg, 15.48 mmol). Isopropanol (25 mL) was added to the flask and the mixture was refluxed under nitrogen for 36 h during which time the color of the solution changed from brown-green to yellow. After the 36 h reaction time, the mixture was allowed to cool to room temperature and the solvent was reduced to ~4 mL under vacuum. Diethyl ether (15 mL) was added resulting in precipitation of the product, which was filtered from the solution to give a yellow powder. Further purification of the solid product was achieved by triturating the solid

residue with Et_2O (two 10 mL portions) and then filtering the solid under vacuum to give a yellow powder of the *cis*, *mer*-$IrHCl_2(PPh_3)_3$ (**1**) isomer (2.1 g, 94 % isolated yield). IR (KBr, cm^{-1}): ν_{Ir-H} = 2189 m. Also: 3057 m, 1482 s, 1434 s, 1192 m, 1160 w, 1091 s, 1000 m, 742 s, 696 s, 523 s, 500 s, 465 w. IR (Nujol, cm^{-1}): ν_{Ir-H} = 2184 m. ^1H NMR (CD_2Cl_2, 300 MHz): δ 7.59−6.86 (m, 45H, phenyl H), −19.15 (dt, $^2J(HP_A)$ = 13.8 Hz, $^2J(HP_B)$ = 15.6 Hz, IrH). $^{31}P\{^1H\}$ NMR (CD_2Cl_2, 121 MHz): δ −2.31 (dd, ^2J(PP) = 12.9 Hz, ^2J(PP) = 2.8 Hz, 2P, P_A), −7.50 (dd, ^2J(PP) = 14.8 Hz, ^2J(PP) =15.7 Hz, 1P, P_B).

4.2.4 Reactivity Studies

*4.2.4.1 Reactivity of cis,mer-$IrHCl_2(PPh_3)_3$ (**1**) with NO*

A 50 mL Schlenk tube was charged with $IrHCl_2(PPh_3)_3$ (100 mg, 0.095 mmol) and CH_2Cl_2 (10 mL) and the mixture was stirred at room temperature to give a yellow solution. NO was slowly bubbled through the solution for 20 min during which time the color of the solution changed from yellow to yellow-brown. After the 20 min reaction time, anhydrous ethanol (10 mL) was added and the mixture was stirred for 1 min. The tube and its contents were then allowed to stand for 3 days at room temperature. After 3 days yellow microcrystalline solids were deposited on inner surfaces of the tube and the crystals were filtered and dried under vacuum to give the product $IrCl_2(NO)(PPh_3)_2$ (**2**) (65 mg, 83% isolated yield). IR(KBr, cm^{-1}): ν_{NO} = 1561 s, 1577(sh) m. Also: 3062 w, 3043 w, 3023 w, 1482 m, 1436 s, 1385 w, 1263 w, 1186 w, 1163 w, 1096 s, 1073 w, 745 m, 707 m, 521 s, 511 s. ESI mass spectrum (TOF): *m/z* 782.1166 $(M-Cl)^+$. X-ray

diffraction-quality crystals of **2** were obtained by slow evaporation of a CH_2Cl_2/ EtOH (1:1) solution of the compound.

*4.2.4.2 Reaction of **1** with Cl_2*

Chlorine gas (excess) was slowly bubbled through a benzene (25 mL) suspension of $IrHCl_2(PPh_3)_3$ (500 mg, 0.48 mmol) in a 50 mL Schlenk tube for 5 min. At this point the mixture became more homogenous. The tube was then sealed under the Cl_2 atmosphere and allowed to stand at room temperature for three days. During this period, the color of the solution gradually turned dark purple. After 3 days, micro-crystalline solids were deposited on the bottom of the tube, and the solid was separated from the dark-purple solution by filtration. The collected product was washed with benzene (three 5 mL portions) and then dried under vacuum to give an orange powder of $IrCl_3(PPh_3)_2$ (**3**) (152 mg, 39% isolated yield). ^{1}H NMR ($CDCl_3$, 300 MHz): δ 7.48−7.32 (m, 15H, phenyl H), 7.18−7.12 (m, 15H, phenyl H). $^{31}P\{^1H\}$ NMR ($CDCl_3$, 121 MHz): −27.45 (s, 2P). ESI mass spectrum (TOF): *m/z* 787.0818 $[M-Cl]^+$.

4.2.4.3 Reactivity of $IrCl_3(PPh_3)_2$ with Alkyl Nitrites

Reaction with butyl nitrite (*n*-BuONO): To a CH_2Cl_2 (10 mL) solution of $IrCl_3(PPh_3)_2$ (50 mg, 0.061 mmol) at 0 °C (ice bath) was added freshly prepared *n*-BuONO (0.1 mL, 0.85 mmol). The color of the solution immediately changed from yellow to pale-yellow. After stirring for 15 min, the ice bath was removed and the solution was stirred for 12 h at room temperature in the dark. After 12 h of stirring the solution was reduced to ~ 5 mL, then hexane (10 mL) was added. The solvent was slowly removed under vacuum to give a residue that was manually transferred by a

spatula to give 48 mg (85% unoptimized yield) of the yellow $IrCl_3$(*n*-BuONO)$(PPh_3)_2$ compound (**4**). IR (KBr, cm^{-1}): ν_{NO} = 1625 m. Also: 3064 m, 2960 w, 2930 w, 2872 w, 1484 s, 1434 s,1385 m, 1316 w, 1288 w, 1190 s, 1000 w, 934 w, 844 w, 745 s, 695 s. ^{1}H NMR ($CDCl_3$, 300 MHz): δ 7.45−7.36 (m, 15H, phenyl *H*), 7.17−7.14 (m, 15H, phenyl *H*), 3.58 (*app* dd, 2H, *J* = 6.3 Hz, *J* = 4.2, C*H*$_2$), 1.40 (m, 2H, *J* = 7.5, C*H*$_2$), 1.28 (m, 2H, *J* = 7.5 Hz, C*H*$_2$), 0.86 (t, 3H, *J* = 7.2 Hz, C*H*$_3$). ^{31}P{^{1}H} NMR ($CDCl_3$, 121 MHz): δ −26.9 (s, 1P), −27.7 (s, 1P). Anal. Cald for $C_{40}H_{39}Cl_3NO_2P_2Ir \cdot 0.5CH_2Cl_2$: C, 50.21; H, 4.16; N, 1.45. Found: C, 50.15; H, 4.19; N, 0.21.

Reaction with ethyl nitrite (EtONO): To a CH_2Cl_2 (8 mL) solution of $IrCl_3(PPh_3)_2$ (10 mg, 0.012 mmol) in a Schlenk tube at room temperature was added EtONO (0.01 mL) resulting in an immediate change in the color of the solution from yellow to pale-yellow. The mixture was stirred for 1h in the dark and then hexane (10 mL) was added. The solvent was slowly removed under vacuum to give a pale-yellow residue that was manually transferred by a spatula to give a 8.3 mg (77% unoptimized yield of $IrCl_3$(EtONO)$(PPh_3)_2$ (**5**). (Note: This reaction is reversible and high vacuum can remove the coordinated EtONO and reconvert the $IrCl_3$(EtONO)$(PPh_3)_2$ compound to $IrCl_3(PPh_3)_2$. Care should be taken when removing solvent under vacuum in this experiment). IR (KBr, cm^{-1}): ν_{NO} = 1627. Also: 3065 m, 3056 m, 3005 w, 2958 w, 2929 w, 2869 w, 1573 w, 1562 w, 1484 s, 1434 s, 1395 m,1317 w, 1265 w, 1190m, 1162 w, 1093 s, 1028 m, 1001 w, 869 w, 746 s, 696 s. ^{1}H NMR ($CDCl_3$, 300 MHz): δ 7.43−7.29 (m, 15H, *J* = 7.2 Hz, phenyl *H*), 7.17−7.12 (m, 15H, *J* = 7.8 Hz), 3.70 (t, 2H, *J* = 6.6 Hz, C*H*$_2$), 1.21 (t, 3H, *J* = 7.5 H, C*H*$_3$).

*4.2.4.4 Synthesis of $IrCl_2(\eta^2\text{-}O_2NO)(PPh_3)_2$ (**6**)*

The compound $IrCl_2(\eta^2\text{-}O_2NO)(PPh_3)_2$ (**6**) was obtained by exposure of a CH_2Cl_2 (5 mL) solution of $IrCl_3(n\text{-BuONO})(PPh_3)_2$ (**4**) (3 mg, 0.0036 mmol) to air and laboratory light resulting in the solution gradually changing color from pale-yellow to orange. A slow evaporation of CH_2Cl_2 solution of **4** over a three-day period afforded crystals of the compound $IrCl_2(\eta^2\text{-}O_2NO)(PPh_3)_2$ (1.5 mg, 48%). IR (KBr, cm^{-1}): ν_{NO3} = 1561 s, 1532 s, 1261 m, 1223 m. Also: 3066 w, 3053 w, 2964 w, 1483 m, 1392 w, 1319 w, 1191 w, 1164 w, 1091 s, 1029 w, 1002 m, 802 m, 763 m, 748 s, 705 s, 692 s, 547.

4.3 Results and Discussion

4.3.1 Syntheses and Characterization

The preparation of the *mer*- and *fac*-$IrHCl_2(PPh_3)_3$ compounds have previously been reported.[4,11,15-17] A modification of method by Morris and coworkers was used in this work as it provides a single isomer, *viz.* the *cis,mer*-$IrHCl_2(PPh_3)_3$ product.[18] In a typical reaction, a mixture of $IrCl_3{\cdot}3H_2O$ and PPh_3 was refluxed in ^{i}PrOH for 36 h (Scheme 4.1). It is critical that the reaction be stopped after 36 h to prevent the formation of the *trans,mer*-isomer.

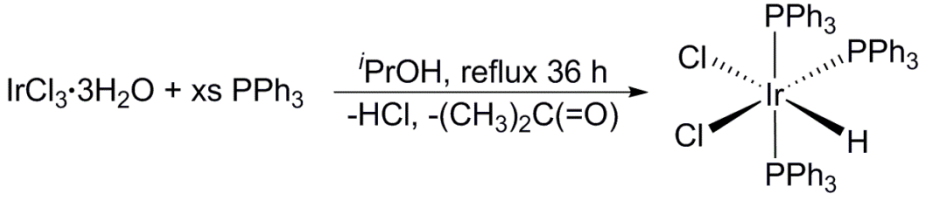

Scheme 4.1 Direct synthesis of compound **1** from readily available $IrCl_3{\cdot}3H_2O$

Synthesis by this modified procedure provided 82% isolated yield of only the *cis,mer*-$IrHCl_2(PPh_3)_3$ isomer as judged by ^{1}H NMR and ^{31}P NMR spectroscopy. The

^{1}H NMR spectrum of the product generated by this modified method displayed one signal due to Ir−*H* at −19.15 ppm (*cf.* −14.00 ppm in the *trans,mer*-$IrHCl_2(PPh_3)_3$ isomer).[11] The ^{31}P NMR spectrum of this pure *cis,mer*-$IrHCl_2(PPh_3)_3$ displays two signals at −2.13 and −7.5 ppm (*cf.* −7.5 and −29.7 ppm in the *trans,mer*-$IrHCl_2(PPh_3)_3$).[11] IR (KBr) samples of the pure *cis,mer*-$IrHCl_2(PPh_3)_3$ prepared in this work displayed a band at 2189 cm^{-1} (2184 cm^{-1}, as Nujol) due to ν_{Ir-H} and is consistent with that reported previously (Table 4.1). [4,11,15-17] The compound **1** is air-stable as a solid at room temperature for several months as judged by IR and ^{1}H NMR spectroscopy.

Table 4.1 IR spectral data of some neutral iridium hydride complexes

Compound	Ir−H	Reference
$IrHCl(NO)(PPh_3)_2$	2070	[19]
$IrHCl_2(PPh_3)_3$ (1)	2189	this work
$IrH_5(PPh_3)_2$	1950	[11]
$IrHCl_2[PPh(OEt)_2](PPh_3)_2$	2116	[17]
$IrHCl_2[P(OEt)_3](PPh_3)_2$	2073	[17]
$IrHCl_2[PPh(OEt)_3](AsPh_3)_2$	2065	[17]
$IrHCl_2[P(OEt)_3](AsPh_3)_2$	2051	[17]

4.3.2 Reactivity of *cis,mer*-$IrHCl_2(PPh_3)_3$ (1)

*4.3.2.1 Reaction of **1** with hydrides and chlorine gas*

It has been reported that the compound $IrHCl_2(PPh_3)_3$ reacted with H_2 (75 atm, 100 °C) in the presence of KH to produce the pentahydrido bis-triphenylphosphine compound, $IrHCl_5(PPh_3)_2$.[11] The PPh_3 group in $IrHCl_2(PPh_3)_3$ would then be displaced by phosphites. For example, $IrHCl_2(PPh_3)_3$ reacts with $P(OEt)_3$ to generate both $IrHCl_2[PPh(OEt)_2](PPh_3)_2$ and $IrHCl_2[P(OEt)_3](PPh_3)_2$ at 60% yield.[17] The final

products of these reactions showed a shift of the ν_{Ir-H} band to lower frequencies (Table 4.1).

Compound **1** also reacts with chlorine gas to produce the compound $IrCl_3(PPh_3)_2$ (**2**) in moderate yields (Scheme 4.2).[20] A major impurity in this reaction is the compound $IrHCl_4(PPh_3)_2$.

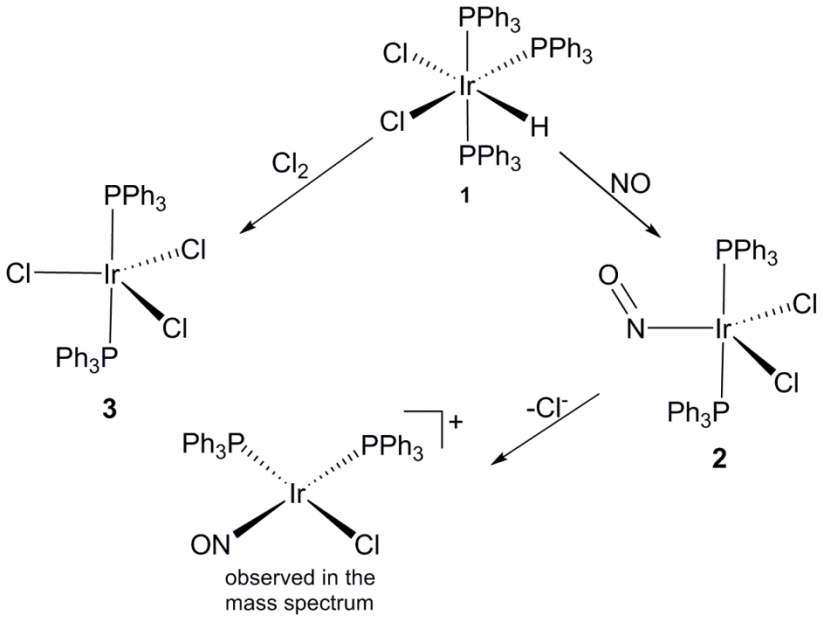

Scheme 4.2. Reactivity of *cis,mer*-$IrHCl_2(PPh_3)_3$ with Cl_2 and NO.

I have found that the yields of the desired compound **3** may be improved by reducing the exposure time of the $IrHCl_2(PPh_3)_3$ precursor to Cl_2 to 3 days. The impurity is soluble in benzene, and trace quantities of $IrHCl_4(PPh_3)_2$ were removed from the desired compound **3** by trituration of the product with benzene. Compound **3** is stable in air as a solid. The IR (KBr) spectrum of **3** lacked the ν_{Ir-H} signal due to the precursor Ir-H, and no trace of the polyhydrido complexes were detected, thus implying

formation of pure **3**. The ESI mass spectral data of **3** show a peak at 787.08 assigned to the fragment $IrCl_2(PPh_3)_2^+$ (i.e. $[M-Cl]^+$) peak.

The ^1H NMR spectrum of **3** shows that this compound is diamagnetic and it displayed proton signals at ~7.3 ppm for P-*Ph* group with no trace of ^1H NMR signal due to Ir-*H* of the $IrHCl_2(PPh_3)_3$ precursor. The ^{31}P NMR spectrum displayed a singlet at −27.45 ppm suggesting that the two PPh_3 groups are in the same chemical environment. Based on this observation, it is likely that PPh_3 groups in compound **3** are *trans* to each other in a trigonal bipyramidal arrangement as shown in Scheme 4.2.

*4.3.2.2 Reactions of **1** with NO*

In view of our laboratory's long standing interest in the chemistry of NO_x and related compounds, I investigated the reactivity of compound **1** with NO. The reaction of a CH_2Cl_2 solution of compound **1** with NO(g) at room temperature, followed by treatment with anhydrous ethanol produced the known compound $IrCl_2(NO)(PPh_3)_2$ (**2**)[19] in 83% isolated yield. Not surprisingly, **2** lacked the ν_{Ir-H} band at 2189 cm^{-1}, but displayed a strong ν_{NO} band at 1561 cm^{-1}, similar to the 1560 cm^{-1} band previously reported for the same compound.[19] Note that this procedure of preparing **2** is more efficient and requires fewer synthetic steps as opposed to the previous procedure that require several synthetic steps.[21]

The ESI mass spectrum of **2** shows a peak at m/z = 782.12 assigned to $[IrCl(NO)(PPh_3)_2]^+$ ($[M-Cl]^+$). It is likely that the chloride was lost during mass spectrometry analysis of **2**. Note that the compound $[IrCl(NO)(PPh_3)_2]^+$ (ν_{NO} = 1890 cm^{-1}) is a nitrosyl analogue of Vaska's complex[5] and it was previously found to react with

halides to generate the neutral $IrX_2(NO)(PPh_3)_2$ (e.g., the $IrCl_2(NO)(PPh_3)_2$ species as shown in Scheme 4.2).[19,22] It may be argued that both $IrCl_2(NO)(PPh_3)_2$ and $[IrCl(NO)(PPh_3)_2]^+$ do co-exist in the sample, and that the former was generated during IR (KBr) sample preparation where Br^- from KBr reacts with $[IrCl(NO)(PPh_3)_2]^+$ to produce the neutral $IrClBr(NO)(PPh_3)_2$ with ν_{NO} ~1560 cm^{-1}. This prompted us to obtain an X-ray crystal structure to confirm our proposed structure of **2**.

The X-ray crystal structure of **2** confirms that the compound is indeed $IrCl_2(NO)(PPh_3)_2$; a similar crystal structure was previously reported by Ibers.[23] The solid-state structure of our compound **2** is shown in Fig.4.1 and it reveals a near-trigonal bi-pyramidal structure with the PPh_3 groups in the *trans* positions and NO and the two chlorides as atoms in the trigonal plane.

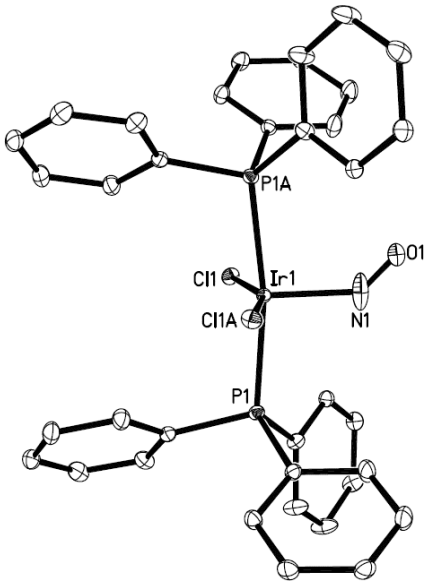

Figure 4.2. The solid-state structure of compound **2**.

The Ir−N−O linkage is bent with a bond angle of 136.26(17)°. Note that this bond angle is larger than the 123(2)° obtained previously by Mingos in 1973 for the same compound.[24] The ∠N−Ir−Cl is 101.325(10)° and is smaller than ∠Cl−Ir−Cl (157.35(2)) but all three angles around the Ir(Cl/NO) plane all add up to 360°. The Ir−N bond length in compound **2** is 1.910(2) Å and the Ir−P and Ir−Cl bond lengths are 2.3456(4) and 2.3579(4) Å, respectively. The Ir−Cl bond distance is shorter than that obtained in $[IrCl(CO)(NO)(PPh_3)_2]$ BF_4 (2.343(3) Å)[25] and the Ir−I (2.666(3) Å) in $[IrI(CO)(NO)(PPh_3)_2]BF_4$[26] (Table 4.2)

Table 4.2. Selected bond distances (Å) and bond angles (°) in some iridium phosphine nitrosyl complexes.

Compound	Ir−N (Å)	Ir−X(Å)	Ir−P (Å)	∠IrNO(°)	∠NIrX	Ref.
$IrCl_2(NO)L_2$ (2)	1.910(2)	2.3579(4)	2.3456(4)	136.26(17)	101.325(10)	this work
$[IrCl(CO)(NO)L_2]^+Y$	1.97(1)	2.343(3)	2.407(3)	124(1)	101.3(3)	[25]
$[IrI(CO)(NO)L_2]^+Y$	1.89(2)	2.666(3)	2.35(1)	125(3)	101(1)	[26]

$L = PPh_3$

4.3.3 Reaction of $IrCl_3(PPh_3)_2$ with Alkyl nitrites

Compound **3** was found to be reactive with alkyl nitrites, *n*-BuONO and EtONO, producing the alkyl nitrite adducts, compounds $IrCl_3$(*n*-BuONO)$(PPh_3)_2$ (**4**) and $IrCl_3(EtONO)(PPh_3)_2$ (**5**), respectively. Reactions of compound **3** with the alkyl nitrites were performed in CH_2Cl_2 solutions and both IR and ^1H NMR suggest that these adducts are of the $IrCl_3(RONO)(PPh_3)$ formulation. For example, the reaction of $IrCl_3(PPh_3)_2$ with *n*-BuONO produced the compound **4** which has an IR (KBr) band at 1625 cm^{-1} assigned to ν_{NO}. The assignment of this ν_{NO} band was supported by DFT calculations (B3LYP/LANL2DZ) on the model compound $IrCl_3(CH_3ONO)(PPh_3)_2$

(calculated ν_{NO} = 1645 cm^{-1}) (Fig. 4.3). The reaction of $IrCl_3(PPh_3)_2$ with EtONO similarly yielded compound (**5**) with ν_{NO} = 1627 cm^{-1}. These IR bands are in the region of those of *trans* alkyl nitrites[27] and are close to the ν_{NO} = 1612 cm^{-1} band obtained for $[Pd_2Cl_2(C_{10}H_{12}ONO]$[28] (Fig. 4.4). Surprisingly, the compound $[Pd_2Cl_2(C_{10}H_{12}ONO)]$ is the only metal-(RONO) compound whose crystal structure is known.[29]

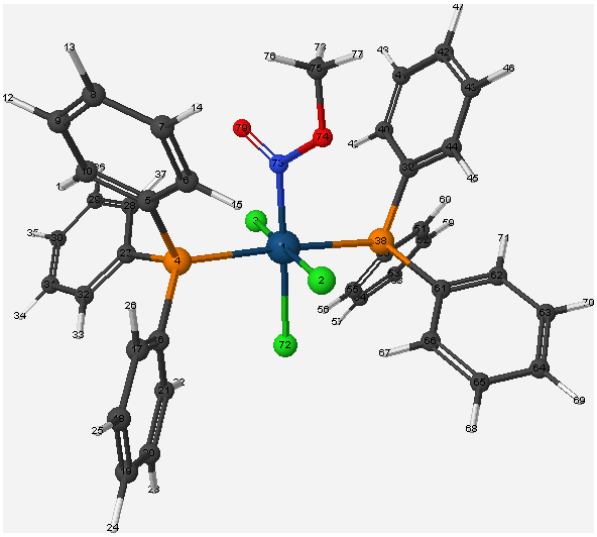

Figure 4.3. The calculated molecular structure of $IrCl_3(CH_3ONO)(PPh_3)$. The vibrational frequency calculation shows ν_{NO} = 1645 cm^{-1}.

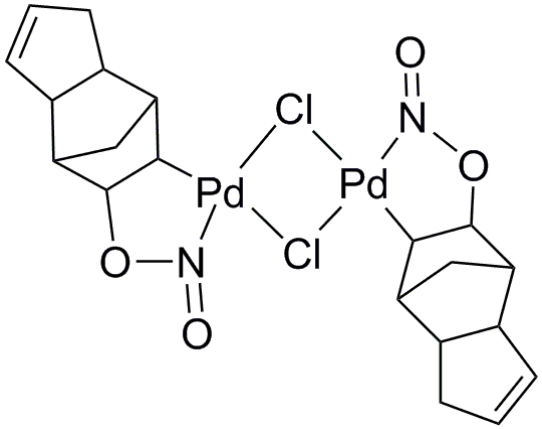

Figure 4.4. The first and only published metal-RONO adduct whose X-ray structure is known.[28]

The ^{1}H NMR spectrum of compound of **5** displays the peaks due to the phenyl groups at 7.43−7.12 ppm. Furthermore, a triplet was observed at 3.70 ppm and a quartet at 1.21 ppm for the C*H*$_3$ and C*H*$_2$ protons, respectively. These signals are shifted upfield from those of the uncoordinated EtONO ligand at 5.1 ppm and 2.3 ppm, respectively,[30] suggesting EtONO ligand coordination to the Ir center. Similarly, the phenyl proton signals of **4** were observed as apparent multiplets at ~7.4 ppm and 7.2 ppm. The signals due to the coordinated *n*-BuONO ligand in **2** were observed at the following positions: 3.58 ppm (C*H*$_3$), 1.40 ppm (C*H*$_2$), 1.28 ppm (C*H*$_2$), and 0.86 ppm (C*H*$_2$). It is worth noting that the adducts $IrCl_3(PPh_3)_2(RONO)$ (R= Me, Et, Pr) were previously suggested to form via alkoxide-ion attack at the nitrosyl group of $[IrCl_3(NO)(PPh_3)_2]^+$, and that the adducts were found to react with other ligands such as CO, NH_3 and pyridine to displace the RONO ligand (Scheme 4.3). I note that the $IrCl_3(PPh_3)_2(RONO)$ adducts decomposed at 80°C to produce $IrCl_3(PPh_3)_2$.

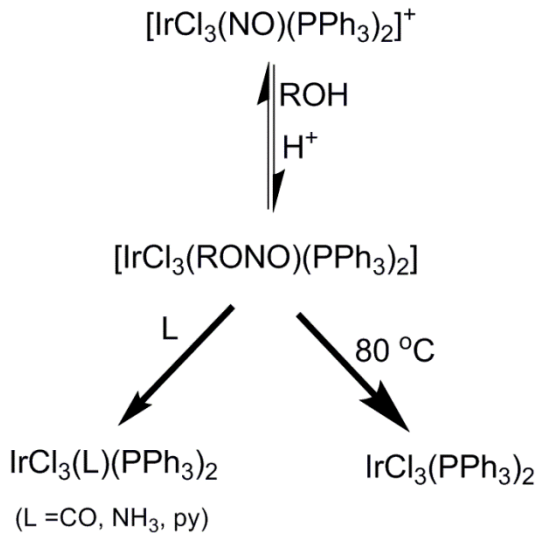

Scheme 4.3. Alternate route for preparation of $IrCl_3(PPh_3)_2$, its reactivity and decomposition pathways. *Adapted from ref.*[21]

A CH_2Cl_2 solution of **4** exposed to air for several days resulted in the conversion of **4** to the nitrate compound **6**. The IR (KBr) of compound **6** displayed strong IR bands at 1561, 1532, 1261 and 1223 cm^{-1}, and these bands are due to the coordinated η^2-nitrato group. The higher frequency bands are assigned to the asymmetric ν_{NO2} and the lower frequency bands are assigned to the symmetric ν_{NO2}.[31]

Several attempts at crystallizing structure **4** were unsuccessful, instead orange crystals of $IrCl_2(\eta^2\text{-}O_2NO)(PPh_3)_2$ (**6**) were generated by a process probably involving the reaction of *n*-BuONO with O_2, and/ or PPh_3. Phosphorus reagents such as PPh_3 can deoxygenate organic nitrites.[32] Also, RONO could decompose to generate NO which can attack the $IrCl_3(PPh_3)_2$ precursor. However, the fact that the ^1H NMR of the octahedral complex $IrCl_3(RONO)(PPh_3)_2$ displayed the bands due to the coordinated RONO group suggests that the reaction pathway involving PPh_3 did not occur, but that *n*-BuONO donated NO to $IrCl_3(PPh_3)_2$ to generate $IrCl_3(NO)(PPh_3)_2$. Metal-coordinated RONO and related complexes are known to decompose in solution to generate metal-NO complexes.[33,34] For example, the reaction of (por)Ru(CO) complexes with *i*-$C_5H_{11}ONO$ produces (por)Ru(NO)(O-*i*-C_5H_{11}) via initial coordination of RONO to Ru via the internal O atom followed by cleavage of the RO−NO bond to generate (por)Ru(CO)(OR) and NO. NO then displaces CO to give (por)Ru(NO)(O-*i*-C_5H_{11}). A similar sequence of reaction mechanism may be involved in the production of **6** from **3**.

It is necessary to note here that the nitrosyl intermediate was not observed in the reaction of $IrCl_3(PPh_3)_2$ with RONO probably implying a fast decomposition of RONO. It is likely that $IrCl_3(NO)(PPh_3)_2$ is octahedral with NO *trans* to one of the chlorides,[35,36] and in the presence of trace oxygen is converted to the nitrato compound **6**. Stirred

oxygenated benzene solutions of $Ir(NO)_2(PPh_3)_2]^+$ and $IrCl_2(NO)(CO)(PPh_3)$ were previously converted to their nitrato compounds, $Ir(NO)(NO_3)(PPh_3)_2$ and $IrCl_2(CO)(NO_3)(PPh_3)$, respectively,[37] by O_2 attack on the coordinate NO group to generate a peroxynitrato group which then isomerized to the nitrato derivatives. It is likely that the exposure of a CH_2Cl_2 solution of $IrCl_3(n\text{-BuONO})(PPh_3)$ with O_2 would follow a similar pathway as shown in Scheme 4.4.

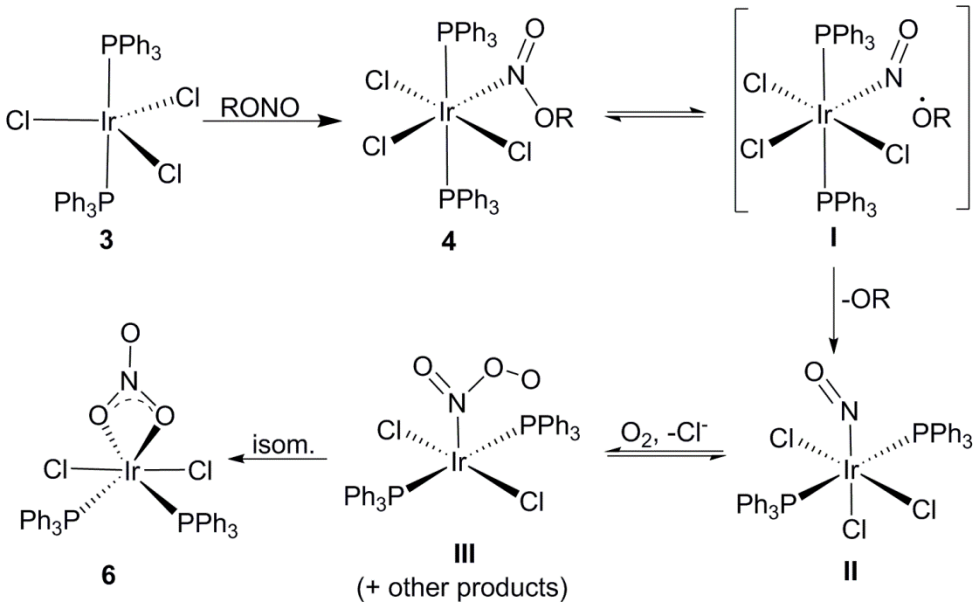

Scheme 4.4. Proposed mechanism of $IrCl_3(PPh_3)_2$-mediated reduction of RONO to NO_3.

The proposed mechanism for the RONO reaction with $IrCl_3(PPh_3)_2$ is likened to the proposed mechanism for oxidation of NO by oxyhemoglobin.[9] In this mechanism (Scheme 4.4), the RO−NO bond in **4** is cleaved to generate the intermediate **I** which is probably in equilibrium with **II**. The Cl ligand *trans* to NO dissociates due to the *trans* effect of NO, and in the presence of O_2 the peroxynitrate complex **III** is formed.

Complex **III** then isomerizes to give **6**. We were able to characterize the product **6** by X-ray crystallography.

The solid-state structure of **6** is shown in Fig. 4.5 (top). The calculated molecular structure (by DFT) is shown in Fig. 4.5 (bottom). The molecular structure shows that **6** is a pseudo-octahedral complex with the two chloride ions in the axial positions.

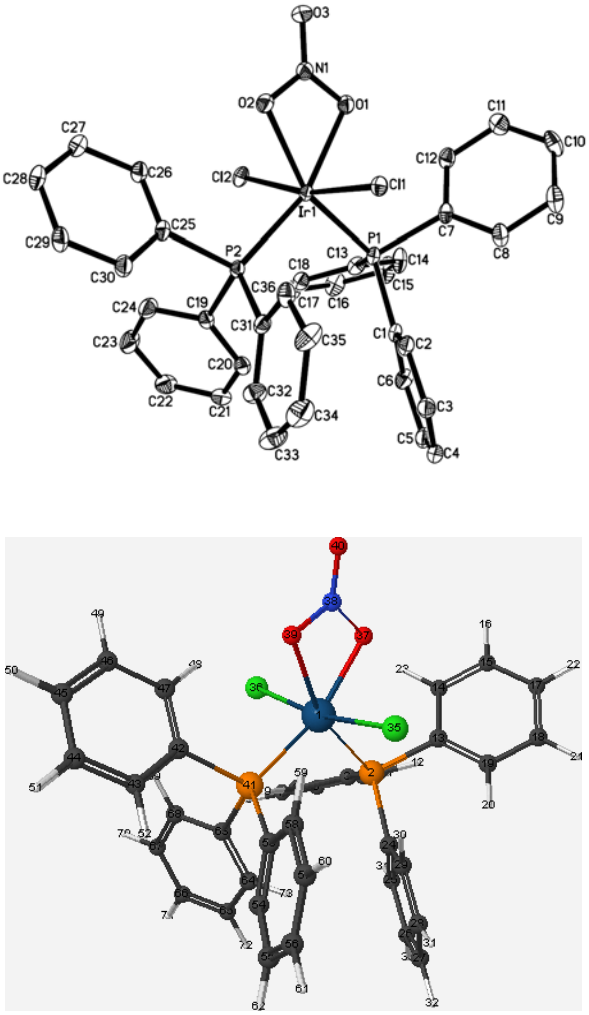

Figure 4.5. (Top) The X-ray crystal molecular structure of **6**. Hydrogen atoms have been omitted for clarity. (Bottom) DFT-calculated molecular structure of **6**.

The molecular structures also reveal that the nitrato ion is coordinated to Ir via two of its oxygens in an η^2-O_2NO fashion[38,39] with a bite angle of 60.02(9)°. Importantly, the nitrato ligand is symmetrically bound to Ir and has equal Ir−O bond lengths of 2.173(2) Å. Two of the N−O bonds, namely N−O(1) and N−O(2) have equal bond lengths (1.294(4) Å) and are longer than the N−O(3) bond (1.209(4) A) (Fig. 4.6), a feature that is not uncommon in nitrato structures (Table 4.3).[40]

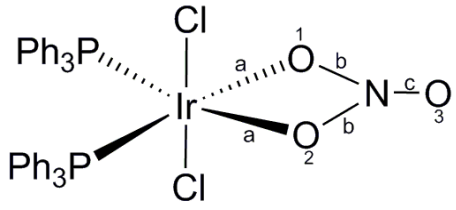

Figure 4.6. Symmetrical η^2-O_2NO coordination in **6**. Bond distances: a = 2.173(2) Å; b = 1.292(4) Å; c = 1.209(4) Å.

The bond angle, ∠O1−N−O2 = 114.5(3)° is less than those of ∠O1−N−O3 and ∠O2−N−O3 (122.7(3)°). Thus, the X-ray crystal structure confirms the structure of **4** and bonding parameters parallel those of other symmetrically coordinated η^2-O_2NO complexes.[39] Selected structural data of **6** and other η^2-O_2NO complexes are shown in Table 4.3. Note that the bonding parameters obtained for compound **6** by DFT calculations are similar to that obtained by X-ray crystallography (Table 4.3).

Table 4.3. Bond distances (Å) and bond angles (°) in selected η^2-O_2NO bound iridium complexes.

Compound	Ir−O	N−O	∠O−Ir−O	∠O−N−O	Ref
Cp*Ir(η^2-O_2NO)(ONO_2)	2.165(8)	1.25(1)	57.9(3)	121(1)	[41]
	2.184(8)	1.24(1)		122(1)	
		1.23(1)		115.2(9)	
[Ir(η^2-*ppy*)$_2$(η^2-O_2NO)]	2.2543	1.283	57.51	123.42	[42]
	2.2273	1.286		122.44	
				114.14	
[$IrAu_3(PPh_3)_5$(η^2-O_2NO)]$^+$	2.220	1.334	58.17	121.73	[43]
	2.264	1.264		124.08	
				114.10	
$IrCl_2$(η^2-O_2NO)$(PPh_3)_2$	2.173(2)	1.294(4)	60.02(9),	122.9(3)	this
	2.174(2)	1.291(4		122.6(3)	work
		1.209(4)		114.5(3)	
$IrCl_2$(η^2-O_2NO)$(PPh_3)_2$[a]	2.181	1.354	61.635	124.397	this
	2.182	1.352		124.231	work
		1.242		111.372	
[$IrAu_2(PPh_3)_4$(η^2-O_2NO)]$^+$	2.22(1)	1.33(2)	58.2(3)	124(1)	[43]
	2.22(1)	1.26(2)		122(1)	
		1.24(2)		114(1)	
[$IrAu_3$(η^2-O_2NO)$(PPh_3)_5$]$^+$	2.256	1.264	57.4	121.42	[44]
	2.324	1.276		120.03	
		1.23		118.5	

[a] obtained by DFT calculations

4.4 Electrochemistry

The redox behavior of compound **4** was investigated using cyclic voltammetry. The voltammogram of **4** in CH_2Cl_2 with 0.1 M NBu_4PF_6 as support electrolyte at scan rate of 200 mVs^{-1} and at room temperature is shown in Fig. 4.7.

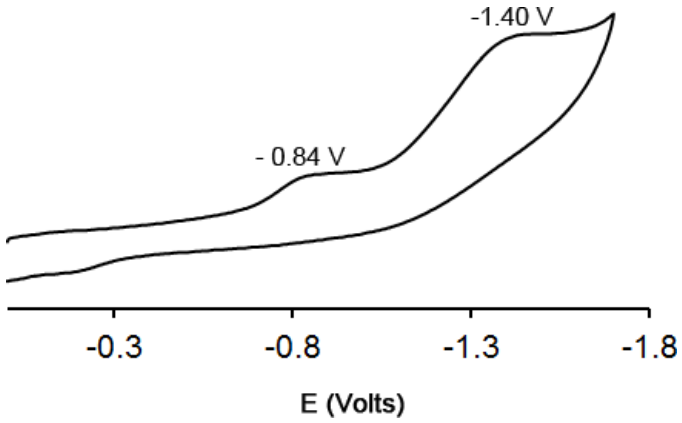

Figure 4.7. Cyclic voltammetry of $IrCl_3$(*n*-BuONO)$(PPh_3)_2$ (**4**) illustrating the reduction behavior. Conditions: 1 mM of analyte ,0.1 M NBu_4PF_6 ,scan rate of 0.2 V/s, room temperature.

The CV of **4** did not reveal any oxidation waves within the solvent limit, but displayed irreversible reduction peaks at −0.84 V and −1.40 V (*vs*. Ag/ AgCl). These reduction potentials are more negative than those obtained for $IrCl_3(PPh_3)_2L$ (L = 2-(phenylazo)pyridine, 2-(*o*-chlorophenylazo)pyridine) ($E_{1/2}$ = − 0.30 and −0.41 V, respectively).[45] Unlike **4**, the CVs of the first reductions of $IrCl_3(PPh_3)_2L$ are reversible. Note that first oxidations at ~1.5 V have been observed in the CVs of $[IrHCl_2(PPh_3)L]$ complexes.[45]

We then performed IR spectroelectrochemical experiments to gain insight into the chemical identities of the electrogenerated products at the electrode surface during the first reduction of $IrCl_3$(*n*-BuONO)$(PPh_3)_2$ (**4**). The difference IR spectra obtained during the first reduction shows a new band at 1712 cm^{-1}. This band is in the range of ν_{NO} of linear M−N−O compound. We assign this band to ν_{NO} and we propose the compound **II** (Scheme 4.4) as the electrogenerated product. Note that in the related $IrBr_3(NO)(PPh_3)$, a ν_{NO} = 1730 cm^{-1} was observed. Thus, during first reduction the N−O(R) bond is cleaved to generate **II**. The ν_{NO} of the proposed compound **II** is higher

than that of $[IrCl_2(NO)(PPh_3)_2]$ probably because Cl is *trans* to NO in **II**. As already discussed in Chapter 1 and 2, electron withdrawing groups *trans* to NO cause a shift of the ν_{NO} to higher wavenumbers.

DFT calculations (B3LYP/LANL2DZ) of the frontier orbitals in the model compound $IrCl_3(CH_3ONO)(PPh_3)_2$ were performed to confirm the site of reduction in compound **4**. The LUMO of the model compound (Fig. 4.8, Left) suggests that an added electron during reduction would potentially occupy the IrN−O(R) region of the antibonding orbital, thus, cleaving the N−O(R) as already proposed in Scheme 4.4. The HOMO, on the other hand, shows high electron density around the two *trans* chloride ligands and oxidations may be outside those needed to oxidize the $Ir(CH_3ONO)$ moiety.

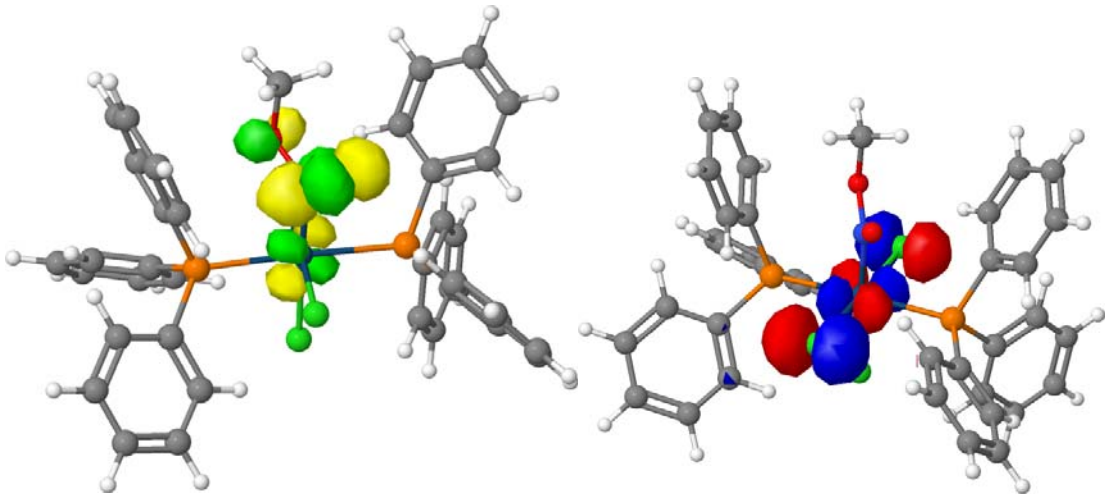

Figure 4.8. Calculated FMO (a) LUMO and (b) HOMO of the model compound $IrCl_3(CH_3ONO)(PPh_3)_2$.

4.5 Conclusion

In conclusion, the reactivity of the iridium(III) complex *cis,mer*-$IrHCl_2(PPh_3)$ with NO has been investigated, and has shown to produce the previously reported $IrCl_2(NO)(PPh_3)_2$ (**2**). Also, *cis,mer*-$IrHCl_2(PPh_3)$ reacts with Cl_2 to generate $IrCl_3(PPh_3)_2$. The latter complex reacts with alkyl nitrites to generate the $IrCl_3(RONO)(PPh_3)_2$ derivatives which react with molecular oxygen to generate the nitrato iridium(III) complex, $IrCl_2(\eta^2\text{-}O_2NO)(PPh_3)_2$ that has been characterized by IR spectroscopy and X-ray crystallography. This mechanism of RONO oxidation is likely similar to the proposed mechanism of action of NO oxidation by HbO_2. IR spectroelectrochemistry of $IrCl_3(n\text{-BuONO})(PPh_3)_2$ reveals reductions centered on the *n*-BuONO ligand to generate the $IrCl_3(NO)(PPh_3)_2$ intermediate. DFT calculations (B3LYP/LANL2DZ) support the proposed reduction site.

4.6 References

(1) Doyle, M. P.; Pickering, R. A.; da Conceição, J. *J. Biol. Chem.* **1984**, *259*, 80-87.

(2) Lee, J.; Chen, L.; West, A. H.; Richter-Addo, G. B. *Chem. Rev.* **2002**, *102*, 1019-1066.

(3) Richter-Addo, G. B.; Legzdins, P. In *Metal Nitrosyls*. Oxford University Press: New York, 1992, pp. 1-369.

(4) Vaska, L. *J. Am. Chem. Soc.* **1961**, *83*, 756-756.

(5) Vaska, L.; DiLuzio, J. W. *J. Am. Chem. Soc.* **1962**, *84*, 4989-4990.

(6) Takao, K.; Fujiwara, Y.; Imanaka, T.; Teranishi, S. *Bull. Chem. Soc. Jpn.* **1970**, *43*, 1153-1157.

(7) Suzuki, T. *Chem. Rev.* **2011**, *111*, 1825-1845.

(8) Johnson, B. F. G.; Bhaduri, S. *J. Chem. Soc., Chem. Commun.* **1973**, 650b-651.

(9) Ford, P. C.; Lorkovic, I. M. *Chem. Rev.* **2002**, *102*, 993-1018.

(10) Noyes, W. A. *n-Butyl Nitrite*; Wiley: New York, 1943; Vol. Coll. Vol. 2.

(11) Landau, S. E.; Groh, K. E.; Lough, A. J.; Morris, R. H. *Inorg. Chem.* **2002**, *41*, 2995-3007.

(12) Brown, F.; Gillies, A.; Stevens, W. H. *Can. J. Chem.* **1953**, *31*, 768-768.

(13) Bruker-AXS *Data Collection: SMART Software Reference Manual* **1998**.

(14) Bruker-AXS *Data Reduction: SAINT Software Reference Manual* **1998**.

(15) Park, S.; Lough, A. J.; Morris, R. H. *Inorg. Chem.* **1996**, *35*, 3001-3006.

(16) Hayter, R. G. *J. Am. Chem. Soc.* **1961**, *83*, 1259-1259.

(17) Albertin, G.; Antoniutti, S.; Bordignon, E.; Menegazzo, F. *J. Chem. Soc., Dalton Trans.* **2000**, 1181-1189.

(18) Taylor, R. C.; Young, J. F.; Wilkinson, G. *Inorg. Chem.* **1966**, *5*, 20-25.

(19) Reed, C. A.; Roper, W. R. *J. Chem.Soc. Chem. Commun.***1969**, 155-155.

(20) Bennett, M. A.; Milner, D. L. *J. Am. Chem. Soc.* **1969**, *91*, 6983-6994.

(21) Reed, C. A.; Roper, W. R. *J. Chem. Soc., Dalton Trans.* **1972**, 1243-1246.

(22) Reed, C. A.; Roper, W. R. *J. Chem. Soc. Chem. Commun.s* **1969**, 1459-1460.

(23) Ibers, J. A.; Mingos, D. M. P. *Inorg. Chem.* **1971**, *10*, 1035-1042.

(24) Mingos, D. M. P. *Inorg. Chem.* **1973**, *12*, 1209-1211.

(25) Hodgson, D. J.; Payne, N. C.; McGinnety, J. A.; Pearson, R. G.; Ibers, J. A. *J. Am. Chem. Soc.* **1968**, *90*, 4486-4488.

(26) Hodgson, D. J.; Ibers, J. A. *Inorg. Chem.* **1969**, *8*, 1282-1287.

(27) Nyquist, R. A. In *Interpreting Infrared, Raman, and Nuclear Magnetic Resonance Spectra*; Academic Press: San Diego, 2001, p 173-230.

(28) Andrews, M. A.; Chang, T. C. T.; Cheng, C. W. F.; Emge, T. J.; Kelly, K. P.; Koetzle, T. F. *J. Am. Chem. Soc.* **1984**, *106*, 5913-5920.

(29) Xu, N.; Richter-Addo, G. B. In *Progress in Inorganic Chemistry: Volume 59*; John Wiley & Sons, Inc.: 2014, p 381-446.

(30) Brown, H. W.; Hollis, D. P. *J. Mol. Spectrosc.* **1964**, *13*, 305-312.

(31) Nakamoto, K. In *Infrared and Raman Spectra of Inorganic and Coordination Compounds*; John Wiley & Sons, Inc.: 2008, p 1-273.

(32) Boyer, J. H.; Woodyard, J. D. *J.Org. Chem.* **1968**, *33*, 3329-3331.

(33) McCleverty, J. A. *Chem. Rev.* **1979**, *79*, 53-76.

(34) Richter-Addo, G. B. *Acc. Chem. Res.* **1999**, *32*, 529-536.

(35) Kubota, M.; Blake, D. M. *J. Am. Chem. Soc.* **1971**, *93*, 1368-1373.

(36) Strope, D.; Shriver, D. F. *Inorg. Chem.* **1974**, *13*, 2652-2655.

(37) Kubota, M.; Phillips, D. A. *J. Am. Chem. Soc.* **1975**, *97*, 5637-5638.

(38) Awasabisah, D.; Richter-Addo, G. B. In *Adv. Inorg. Chem.*; Rudi van, E., José, A. O., Eds.; Academic Press: 2015; Vol. Volume 67, p 1-86.

(39) Addison, C. C.; Logan, N.; Wallwork, S. C.; Garner, C. D. *Q.Rev. Chem.Soc.* **1971**, *25*, 289-322.

(40) Allen, F. H.; Kennard, O.; Watson, D. G.; Brammer, L.; Orpen, A. G.; Taylor, R. *J. Chem.Soc. Perkin Trans. 2* **1987**, S1-S19.

(41) Ogo, S.; Nakai, H.; Watanabe, Y. *J. Am. Chem. Soc.* **2002**, *124*, 597-601.

(42) Sie, W.-S.; Jian, J.-Y.; Su, T.-C.; Lee, G.-H.; Lee, H. M.; Shiu, K.-B. *J. Organomet. Chem.* **2008**, *693*, 1510-1517.

(43) Casalnuovo, A. L.; Laska, T.; Nilsson, P. V.; Olofson, J.; Pignolet, L. H. *Inorg. Chem.* **1985**, *24*, 182-187.

(44) Casalnuovo, A. L.; Pignolet, L. H.; Van der Velden, J. W. A.; Bour, J. J.; Steggerda, J. J. *J. Am. Chem. Soc.* **1983**, *105*, 5957-5958.

(45) Panda, M.; Paul, N. D.; Joy, S.; Hung, C.-H.; Goswami, S. *Inorg. Chim. Acta* **2011**, *372*, 168-174.

Appendix A: List of Schemes

Appendix B: List of Abbreviations

$(Bim)_3$ tris(2-benzimidazolylmethyl)amine)

Bipy 2,2'-bipyridine

Cp cylopentadienyl

Cp* pentamethylcyclopentadienyl

Cyclam 1,4,8,11-tetraazacyclotetradecane

CV cyclic voltammetry

dcpe 1,2-bis(dicyclohexylphosphanyl)ethane

dmpe ethylenebis(dimethylphosphine)

dppe 1,2-bis(diphenylphosphino)ethane)

dppen 1,2-bis(diphenylphosphino)ethylene

dppf 1,1′-ferrocenediyl-bis(diphenylphosphine)

PPIX protoporphyrin IX

dppm 1,1-bis(diphenylphosphino)methane

DSC differential scanning calorimetry

dtc dimethyldithiocarbamate

en ethylenediamine

fac facial

Fc ferrocene

Hb hemoglobin

Hh horse heart

HOMO highest occupied molecular orbital

Hox oxalic acid

IR infrared

LUMO lowest unoccupied molecular orbital

Mb myoglobin

Mbc 5,7-dimethyl-6-benzylcyclam

Mer meridional

MPPa pyropheophorbide-*a* methyl ester

NBO natural bond orbital

NMR nuclear magnetic resonance

NRVS nuclear resonance vibrational spectroscopy

OEP octaethylporphyrin

OETPP 2,3,7,8,12,13,17,18-octaethyl-5,10,15,20-tetraphenylporphyrin

OSWV Osteryoung square wave voltammetry

Ox oxalate ion

pip piperidine

Pz porphyrazine

salen *N,N′*-ethylenebis(salicylideneaminato)

SNP sodium nitroprusside

TF_8PP 5,10,15,20-tetrakis(2,6-difluorophenyl)porphyrin

THF tetrahydrofuran

TMP 5,10,15,20-tetramesitylporphyrin

TPP 5,10,15,20-tetraphenylporphyrin

T(*p*-OMe)PP 5,10,15,20-tetra(*p*-methoxphenyl)porphyrin

$T^{i}prPP$ 5,10,15,20-tetraisopropylporphyrin

TTP 5,10,15,20-tetra-*p*-tolylporphyrin

Tpy 2,6-bis(2-pyridyl)pyridine

UV Ultra-violet